

# **Development of superconducting devices employing coherent Quantum Phase Slip**

## **Entwicklung supraleitender Bauelemente zur Untersuchung von kohärenten Quanten-Phasenschlupf Drähten**

Zur Erlangung des akademischen Grades eines  
DOKTORS DER NATURWISSENSCHAFTEN

von der KIT-Fakultät für Physik  
des Karlsruher Instituts für Technologie (KIT)

genehmigte

DISSERTATION

von

Dipl.-Phys. Sebastian Tobias Skacel

aus Karlsruhe

**Datum der mündlichen Prüfung:** 12.07.2019  
**Referent:** Prof. Dr. Alexey V. Ustinov  
**Korreferent:** Prof. Dr. Oleg V. Astafiev



# Contents

<b>1. Introduction</b>	<b>1</b>
<b>2. Theory</b>	<b>5</b>
2.1. Superconductivity . . . . .	6
2.1.1. Perfect conductivity and diamagnetism . . . . .	6
2.1.2. Flux quantization in a superconducting loop . . . . .	7
2.1.3. Kinetic inductance . . . . .	8
2.2. Superconductivity in one dimension . . . . .	10
2.2.1. Phase slip effect . . . . .	10
2.2.2. Quantum phase slip (QPS) . . . . .	12
2.3. Quantum phase slip and Josephson effect . . . . .	15
2.3.1. Quantum phase slip junction . . . . .	15
2.3.2. Josephson junction . . . . .	17
2.3.3. Duality . . . . .	20
2.4. Measuring coherent quantum phase slip . . . . .	27
2.4.1. Quantum phase slip flux qubit . . . . .	27
2.4.2. Superconducting microwave resonators . . . . .	30
2.4.3. Strong qubit-resonator coupling . . . . .	33
2.5. Recent experiments on quantum phase slip . . . . .	36
2.5.1. Superconducting loops with QPS junctions . . . . .	36
2.5.2. Superconducting nanorings . . . . .	37
<b>3. Experimental details</b>	<b>39</b>
3.1. Material . . . . .	40
3.1.1. Sputter deposited granular aluminium ( $\text{AlO}_x$ ) . . . . .	40
3.1.2. Atomic layer deposited niobium nitride (NbN) . . . . .	43
3.2. Fabrication . . . . .	46
3.2.1. Techniques . . . . .	46
3.2.2. Procedure . . . . .	49
3.2.3. Results . . . . .	51
3.3. Experimental setup . . . . .	53
3.3.1. Ultra-low temperature cryostats . . . . .	53
3.3.2. Microwave measurement setup . . . . .	54
3.3.3. Time domain setup . . . . .	58

<b>4. Results</b>	<b>61</b>
4.1. Capacitively coupled nanowire loop with large inductance . . . . .	62
4.1.1. Sample design and setup . . . . .	62
4.1.2. Microwave transmission spectroscopy . . . . .	66
4.1.3. Granular aluminium nanowire considered as QPS junction . . . . .	68
4.1.4. Granular aluminium nanowire considered as Josephson weak link	73
4.1.5. AC Stark effect . . . . .	83
4.1.6. Driven Rabi oscillations . . . . .	84
4.1.7. Qubit lifetimes . . . . .	87
4.1.8. Discussion and Conclusion . . . . .	91
4.2. Galvanically coupled constriction loop . . . . .	93
4.2.1. Sample design and measurement setup . . . . .	93
4.2.2. Frequency spectroscopy . . . . .	97
4.2.3. Magnetic field spectroscopy . . . . .	98
4.2.4. Coupling strength . . . . .	101
4.2.5. Transition spectroscopy . . . . .	104
4.2.6. Multiphoton transitions . . . . .	109
4.2.7. Conclusion . . . . .	113
4.3. A charge quantum interference device based on two constrictions in series	115
4.3.1. Sample design . . . . .	116
4.3.2. Frequency and magnetic field spectroscopy . . . . .	118
4.3.3. Transition spectroscopy . . . . .	119
4.3.4. Electric gate charge dependence . . . . .	122
4.3.5. Quasiparticles and charge parity . . . . .	125
4.3.6. Conclusion . . . . .	127
<b>5. Conclusions and Outlook</b>	<b>129</b>
<b>Bibliography</b>	<b>133</b>
<b>List of Publications</b>	<b>143</b>
<b>Appendix</b>	<b>145</b>
<b>A. Fabrication details</b>	<b>147</b>
A.1. Samples . . . . .	147
A.1.1. Chip A0102 . . . . .	147
A.1.2. Chip A0105 . . . . .	152
A.1.3. Chip A0109 . . . . .	156
A.2. General precautions . . . . .	160
<b>List of Figures</b>	<b>163</b>

<b>List of Tables</b>	<b>175</b>
<b>Acknowledgements</b>	<b>177</b>



# 1. Introduction

---

*"Measurements of the superconducting-to-normal transition in very-small-diameter ... wires ... suggest that the(ir) low-temperature behavior is dominated by quantum-mechanical tunneling through the free-energy barrier..."*

**Nicholas J. Giordano**

## Quantum phase slip in superconducting nanowires

Remarkably, a bulk superconducting wire can transport an electric current without dissipation [Kam11] due to the interaction of electrons forming the well-known Cooper pairs [BCS57]. Their interaction distance is determined by the material-dependent, superconducting coherence length. All Cooper pairs condense into a common ground state which is described by the superconducting order parameter, a complex single-valued wave function.

Intuitively, a narrow constriction along the superconducting wire limits the maximum supercurrent which the wire can carry. When the constriction is very small, i. e. it has a diameter and a length less than the wire's coherence length, the superconducting current through the constriction results from coherent tunnelling of Cooper pairs [Tin04]. The coherent tunnelling is determined by the overlap of the wavefunctions of the two wire branches. Since this phase coherence amplitude over the constriction is smaller than inside the wire branches, the constriction can form a superconducting *weak link* obeying the Josephson relations [Lik79].

A weak-link can also span over a distance that is longer than the coherence length. With its cross section of the order of the coherence length, it forms a (quasi-)one-dimensional superconducting channel [AGZ08]. For a dirty, weak superconductor, the coherence length is of the order of a few nm. Hence, a weak link made from such a dirty superconductor has to be narrowed to a few nm in cross-section and forms a *nanowire*. A system with reduced dimensions and high intrinsic disorder is usually more affected by fluctuations which can lead to the loss of phase coherence of the wavefunctions on both sides of the nanowire. The phase can then change by arbitrary values with an applied voltage. At temperatures much below the superconducting transition temperature of the nanowire, transient quantum fluctuations of the order parameter can reduce the accumulated phase over the nanowire. However, the single-valuedness of the superconducting order parameter of the nanowire only allows phase adjustments by multiples of  $2\pi$ ; the nanowire experiences *quantum phase slips (QPS)* [AGZ08]. The reduction of phase due to transient QPS means an appearance of voltage. Hence, the nanowire experiences a resistance in the superconducting state. This dissipative process is caused by *incoherent* QPS fluctuations.

QPS does not have to be dissipative [BGB04], however. The spatial interference of frequent QPS events at different spots along the nanowire can form a coherent superposition of quantum phase slips [Man+12]. During a QPS event, the superconducting order parameter of the nanowire is reduced to zero which permits tunnelling of magnetic fluxons across the nanowire. In case of coherent QPS, the nanowire can be considered a QPS junction which allows for coherent tunnelling of fluxons or phase respectively [MN06]. Since charge and phase are conjugate variables for superconductors, a QPS junction represents the dual to a Josephson weak link (or junction). From this point of view, QPS junctions represent a novel building block for superconducting electronics and quantum metrology, e.g. for quantum current standards [MN06].

## Coherent quantum phase slip observed in experiments

So far, mainly DC transport measurements of superconducting nanowires have been performed, in which the suppression of the superconducting transition for temperatures  $T \rightarrow 0$  have been observed [Gio88; BLT00a; Zgi+08; Leh+12; HZ12]. The appearance of dissipation in superconducting nanowires is a clear signal for incoherent quantum phase slips. However, the detection of coherent QPS proves to be difficult in DC transport measurements. In an alternative approach, a QPS junction is embedded into a superconducting loop [MH05]. Due to coherent QPS, the loop can form a two-level system with a superposition of adjacent fluxon states. This is called a *QPS flux qubit* [MH05]. In such a system made from an superconducting indium oxide ( $\text{InO}_x$ ) thin film, coherent QPS could be observed experimentally for the first time in 2012 [Ast+12]. Due to the highly disordered  $\text{InO}_x$ , superconducting phase coherence is reduced and QPS is favoured. The observation could be successfully repeated in QPS flux qubits made from highly-disordered superconducting niobium nitride (NbN) thin films [Pel+13]. However, the highly-disordered superconducting films utilized to realize QPS flux qubits, especially  $\text{InO}_x$ , proved to be unstable over time when kept at room temperature. Furthermore, only a qualitative scaling of the coherent phase slip amplitude with nanowire width could have been observed, so far.

## This Work

The goal of this thesis is to study coherent QPS physics in nanowires made from superconducting thin films which exhibit high-sheet resistances in their normal conducting state. Special attention is paid to *granular aluminium* which has not been used so far in this context. Granular aluminium can be fabricated with sheet resistances extending across a wide range from a few  $\Omega$  to hundreds of  $\text{k}\Omega$ , and it has been shown to be stable over time when kept at room temperature [Abe77]. This makes it very promising for QPS devices. It is compared with niobium nitride which has been shown to be compatible with QPS experiments as mentioned above. Beginning with the fabrication, characterization and optimization of granular aluminium thin films for the use in QPS devices, a technique is established to reproducibly fabricate wires from these thin films with widths of a few nm. Such nanowires are embedded into superconducting circuits. These circuits are designed such that QPS physics in the nanowires can be studied.

In Ch. 2, the theoretical background is discussed which is necessary to understand the performed experiments. It includes a brief look on superconductivity with a focus on one-dimensional superconducting systems and the QPS concept. It will be discussed why disorder is favourable for QPS and which prerequisites have to be fulfilled to realize coherent QPS. Attention is drawn to the close relation between QPS and Josephson effect and to measurement techniques utilized to investigate coherent QPS. Regarding the stability and homogeneity of the superconducting thin films, this work investigates sputtered,

superconducting granular aluminium  $AlO_x$  thin films as well as atomic layer deposited, superconducting niobium nitride thin films for their applicability for coherent QPS. The development of the  $AlO_x$  sputtering process and the characterization of the  $AlO_x$  thin film properties are explained in Ch. 3. Subsequently, the fabrication technique, which was optimized in order to obtain nanowires with dimensions in the several-nm range, is described. The chapter finishes with the description of the utilized microwave measurement methods performed at ultra-low temperatures. In Ch. 4, the experiments are described which are realized with the developed techniques. The first two experiments deal with nanowires made from superconducting  $AlO_x$  and NbN which are embedded into superconducting loops. In a further experiment, the dynamics given by the interference of two nanowires, which are embedded into a single superconducting loop, is explored.

## 2. Theory

---

*"The experiment left no doubt that, as far as accuracy of measurement went, the resistance disappeared. At the same time, however, something unexpected occurred. The disappearance did not take place gradually but abruptly. From 1/500 the resistance at 4.2 K, it could be established that the resistance had become less than a thousand-millionth part of that at normal temperature. Thus the mercury at 4.2 K has entered a new state, which, owing to its particular electrical properties, can be called the state of superconductivity."*

**Heike Kamerlingh Onnes**

The discovery of superconductivity in 1911 triggered a plethora of theoretical predictions in the following decades. While many of them have been deeply investigated by successful experiments, some still remain to be explored in greater detail. One of these topics is the quantum phase slip effect whose investigation is the topic of this thesis.

In Ch. 2, the theoretical background is discussed which is necessary to understand the described experimental results in Ch. 4. After summing up some basics of superconductivity in Sec. 2.1, which are important for the upcoming experiments, the focus is on the consequence of one-dimensionality on superconductivity in Sec. 2.2. Having introduced the quantum phase slip (QPS) concept in Sec. 2.2, the attention is drawn to its close relation to the well-known Josephson effect in Sec. 2.3 and to measurement techniques in Sec. 2.4, which will be used later on to investigate coherent QPS. Eventually, recent experiments on quantum phase slip are overviewed in Sec. 2.5 which are linked to the experiments performed in this thesis.

## 2.1. Superconductivity

Superconductivity is the effect fundamental to the experiments presented in this work. Below, its basic concepts are explained briefly to corroborate the subsequent notions of quantum phase slips. With the help of textbooks such as [Tin04; Sch97; Lik91], the reader might deepen the understanding of the basic principles of superconductivity.

### 2.1.1. Perfect conductivity and diamagnetism

As quoted in the beginning of this chapter, the electrical resistance of mercury - as well as of other certain materials - drops abruptly to zero below a critical temperature  $T_c$ . This was first discovered by H. K. Onnes in 1911 [Kam11]. Henceforth, such materials were called superconductors. This effect could be theoretically fully explained not until 1957. J. Bardeen, L. Cooper and J. R. Shrieffer [BCS57] postulated that conduction electrons of opposite spin and momentum form so-called Cooper pairs with zero spin. This is possible due to the interaction between the electrons and lattice phonons in superconductors. The maximum length scale over which the pairing can be maintained inside a superconductor is called superconducting coherence length  $\xi_{\text{BCS}}$ . The energy necessary to break up a Cooper pair at  $T = 0$  is

$$2\Delta_0 \approx 3.52k_{\text{B}}T_c. \quad (2.1)$$

Here,  $\Delta_0$  is the superconducting energy gap.

The Cooper pairs obey the Bose-Einstein statistics and can therefore condense into a macroscopic ground state in case the thermal energy is below  $k_{\text{B}}T_c$ . This allows to describe this ground state by a single wave function

$$\Psi(\vec{r}) = \sqrt{n_s}e^{i\phi(\vec{r})}, \quad (2.2)$$

where  $n_s$  is the Cooper pair density and  $\phi(\vec{r})$  the phase of the wave function.

Besides this macroscopic quantum phenomenon of ideal conductance, superconductivity exhibits the remarkable characteristic of ideal diamagnetism. Magnetic fields can penetrate superconductors above  $T_c$ . However, is a superconductor cooled through  $T_c$  in non-zero magnetic field, it expels the field from its core as soon as  $T_c$  is reached. This effect had already been observed by Meißner and Ochsenfeld in 1933 [MO33] and in 1935, F. and H. London [LL35] were able to phenomenologically describe it with <sup>1</sup>

$$\text{rot}(\Lambda\vec{j}_s) = -\vec{B}, \quad (2.3)$$

where  $\Lambda$  is given by

$$\Lambda = \frac{m_s}{n_s e_s^2}. \quad (2.4)$$

---

<sup>1</sup>Eq. (2.3) is called the 2<sup>nd</sup> London equation.

Here,  $m_s$ ,  $n_s$  and  $e_s$  are the mass, density and charge of superconducting charge carriers<sup>2</sup>. Eq. (2.3) shows clearly that the induced circulating current  $\text{rot}(\Lambda\vec{j}_s)$  cancels the magnetic field inside the superconductor.

An alternative theoretical description of superconductivity is given by the phenomenological Ginzburg-Landau (GL) theory. It had already been derived in 1950 describing the transition from normal to superconducting state as a second-order phase transition<sup>3</sup>. Introducing an order parameter  $\psi_{\text{GL}}$  which describes the superconducting electrons<sup>4</sup>, the GL theory expands the free energy in  $\psi_{\text{GL}}$  around a critical value  $T = T_c$  where the transition takes place. This leads to the well-known GL differential equation

$$\alpha\psi + \beta |\psi|^2 \psi + \frac{1}{2m_s} \left( \frac{\hbar}{i} \nabla - \frac{2e}{c} \vec{A} \right)^2 \psi = 0, \quad (2.5)$$

where  $\alpha$ ,  $\beta$  are expansion coefficients,  $c$  the speed of light and  $\vec{A}$  the vector potential. For the case of no fields and with a wavefunction normalized to  $f = \psi/\psi_\infty$ <sup>5</sup>, the GL equation becomes

$$\xi_{\text{GL}}^2 \frac{d^2 f}{dx^2} + f - f^3 = 0, \quad (2.6)$$

$$\xi_{\text{GL}} = \frac{\hbar^2}{2m_s |\alpha|}.$$

Here,  $\xi_{\text{GL}}$  is the GL coherence length which is  $\xi_{\text{GL}} = \xi_{\text{BCS}}$  for pure materials well below  $T_c$ .

### 2.1.2. Flux quantization in a superconducting loop

Let us consider a superconductor bent to a closed loop and penetrated by a magnetic field at  $T > T_c$ . As aforementioned, the magnetic field gets expelled from the interior of the superconductor when cooled through  $T_c$ . Inside the loop, a portion of magnetic field freezes out. The phase accumulated on a path  $\vec{s}$  around the loop has to be  $\Delta\phi = 2\pi n$  due to the condition that Eq. (2.2) must be single-valued

$$\oint \nabla\phi \cdot d\vec{s} = 2\pi n. \quad (2.7)$$

Using the canonical momentum of a Cooper pair

$$\vec{p} = \hbar\nabla\phi = \frac{m_s}{n_s e} \vec{j}_s + 2e\vec{A}, \quad (2.8)$$

<sup>2</sup> $e_s = 2e$  and  $m_s = 2m_e$ ; the concept of Cooper pairs had not been introduced at that time.

<sup>3</sup>This second-order phase transition concept has been proposed by L. Landau in 1937 and thus is called Landau theory.

<sup>4</sup>Cooper pairs as defined later.

<sup>5</sup> $\psi_\infty^2 = -\alpha/\beta > 0$ .

where  $\vec{j}_s = 0$  is the supercurrent density inside the superconductor and  $\vec{A}$  is the vector potential, Eq. (2.7) leads to

$$2\pi n = \frac{2e}{\hbar} \oint \vec{A} d\vec{s} = \frac{2e}{\hbar} \Phi, \quad (2.9)$$

$$\Phi = n \frac{\hbar}{2e} = n\Phi_0. \quad (2.10)$$

This means that the frozen flux  $\Phi$  inside the loop is generated by the supercurrent which flows at the inner surface of the ring and can only take multiples of  $\Phi_0 = 2.068 \times 10^{-15}$  Vs. It is therefore called the flux quantum. The flux quantization is hence a direct consequence of the quantization of the supercurrent and this supercurrent is called *persistent current*  $I_p$ .

### 2.1.3. Kinetic inductance

Although the magnetic field is expelled by a superconductor from its core, it still can penetrate the superconductor to some amount. The magnetic field decays exponentially from the surface to the core over a length

$$\lambda_L = \sqrt{\frac{m_s}{\mu_0 n_s e_s}}, \quad (2.11)$$

the so-called London penetration depth. In order to reduce the entered magnetic field, a screening supercurrent starts to flow close to the surface which also falls off with  $\lambda_L$  from the surface to the center. In a current carrying superconducting wire with a diameter  $d \ll \lambda_L$ , the current must circulate near the surface. From this it can be seen that the kinetic inductance  $L_{\text{kin}}$  of the wire which corresponds to the kinetic energy of the supercurrent charge carriers is

$$L_{\text{kin}} \propto \lambda_L, \quad (2.12)$$

or in other words, that  $\lambda_L$  characterizes the inertia of the superconducting charge carriers.

In electric fields alternating with frequency  $\omega$ , conduction electrons are perpetually accelerated and decelerated. Because they are massive particles, their response to a changing electric field is inertial. Within the framework of the Drude model, this is expressed by a complex conductivity

$$\sigma(\omega) = \sigma_1 - i\sigma_2 = \frac{ne^2\tau}{m(1 + \omega^2\tau^2)} - i\frac{ne^2\omega\tau^2}{m(1 + \omega^2\tau^2)}, \quad (2.13)$$

where the kinetic inductance  $L_{\text{kin}}$  arises from  $\sigma_2$ .  $n$  and  $e$  are density and charge of the electrons while  $\tau$  represents the time scale on which electrons collide with each other. For

normal conduction electrons with very small  $\tau$ <sup>6</sup>, frequencies in the range of some GHz - the typical frequency range this work deals with - result in a negligible kinetic inductance. However, for superconducting Cooper pairs, we assume  $\tau_s \rightarrow \infty$  giving a significant  $L_{\text{kin}}$  contribution.

Using the Mattis-Bardeen formula for a superconducting wire in the limit where  $\hbar\omega \ll k_B T_c$ ,  $\sigma_2$  can be written as

$$\frac{\sigma_2}{\sigma_n} = \frac{\pi\Delta_0}{\hbar\omega}. \quad (2.14)$$

Here,  $\sigma_n$  is the normal state conductivity. It can be expressed as  $\sigma_n = R_{\square}^{-1}$  in terms of the normal state sheet resistance  $R_{\square}$ .

Using Eq. (2.1) and  $L_{\text{kin},\square}^{-1} = \omega\sigma_2$ , Eq. (2.14) leads to

$$L_{\text{kin},\square} = 0.18 \frac{\hbar R_{\square}}{k_B T_c}. \quad (2.15)$$

$L_{\text{kin},\square}$  is the sheet kinetic inductance of a superconducting wire.

Eq. (2.15) implies that high kinetic inductances can be achieved by using superconducting wires with large sheet resistances in the normal conducting state. This fact is very important for this work.

---

<sup>6</sup> $\tau_e \sim 10^{-14}$  s.

## 2.2. Superconductivity in one dimension

In the 1960s, an intense theoretical effort was placed on how superconductivity is dependent on the dimensionality of the system. Fluctuations in amplitude or phase of the superconducting order parameter  $\psi$  might have an increasing effect in systems with decreasing dimensionality. In 1967, W. A. Little concluded from theoretical considerations that the persistent current in a *one-dimensional* superconducting loop is not necessarily suppressed by any fluctuations unless they drive the amplitude of  $\psi$  to zero on the complete loop surface [Lit67]. However, estimating the probability of such fluctuations, he stated that an infinitely sharp superconducting transition can only occur in an infinite three-dimensional system, while in finite one dimension, there will be a resistance due to fluctuations even well below  $T_c$ .

### 2.2.1. Phase slip effect

The condition for a superconducting system to be one-dimensional is that its transverse dimension is much smaller than its coherence length  $d \ll \xi$ . Thus from an energetic point of view, the variation of the superconducting order parameter  $\psi$  over the cross section is forbidden. This is expressed by

$$\psi = |\psi(x)| e^{i\phi(x)}. \quad (2.16)$$

Plotting  $\psi$  in the complex plane along the wire axis  $x$  shows helices with complete phase turns of  $2\pi$  (see Fig. 2.1a). As mentioned in Sec. 2.1.2, the phase difference  $\phi$  must be a multiple of  $2\pi$  due to the single-valuedness of Eq. (2.16) which is a stationary solution of the GL equation Eq. (2.5) representing a supercurrent in the wire at zero voltage.

The occurrence of a voltage means a change of the phase difference  $\varphi = \phi_1 - \phi_2$  between the ends of the wire  $\frac{d\varphi}{dt} = \frac{2e}{\hbar}V$  (see Eq. (2.38)). As shown in Fig. 2.1b, phase fluctuations as described in the beginning of this section force the amplitude of the order parameter  $\psi$  to zero at a spot along the wire. After re-establishing,  $\psi$  has lost a phase turn of  $2\pi$ ; one says the *phase slipped* by  $2\pi$  (see Fig. 2.1c). The annihilation of turns of the helix by such a *phase slip process* can maintain a steady state at zero voltage if the fluctuations happen at a rate that is equal to the one of adding turns. The energy added by the voltage is dissipated in heat and cannot be used to accelerate the Cooper pairs.  $\varphi$  increases with the applied voltage and can be imagined as a wrap of phase along  $x$ . Adding phase turns of  $2\pi$  tightens the helix until the critical current of the wire is reached and superconductivity gets suppressed.

J. S. Langer and V. Ambegaokar considered two uniform solutions Eq. (2.16) representing neighbouring numbers of phase turns and derived the lowest free energy barrier between

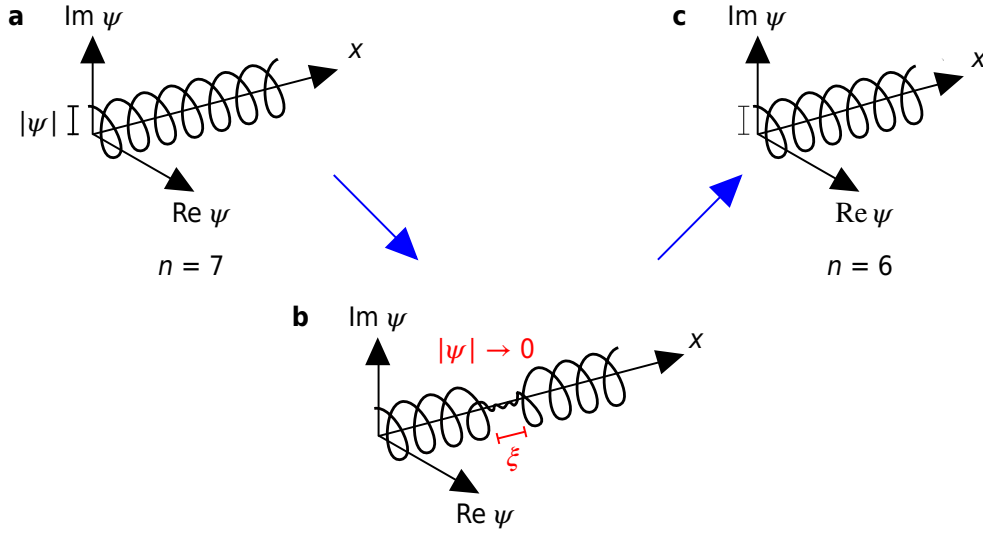


**Figure 2.1:** The superconducting order parameter  $\psi$  plotted in the complex plane along the wire axis  $x$ . Each turn of the helix represents a phase change by  $2\pi$ . **a** Before the event of a phase slip, the wire carries  $n$  phase turns (here  $n = 7$ ). **b** During the phase slip event, the amplitude of the order parameter  $|\psi|$  fluctuates to zero. A voltage drop occurs over the wire and thus the wire becomes resistive. **c** After re-establishing superconductivity, the nanowire only carries  $n-1$  phase turns (here  $n = 6$ ).

these two <sup>7</sup> [LA67]. As a result, the change in free-energy at this saddle-point is

$$\Delta F \propto \xi, \quad (2.17)$$

where  $\xi$  is the superconducting coherence length. Thus, at least on a length scale of  $\xi$  the phase coherence has to be disturbed to suppress superconductivity. The probability to observe a resistance in a one-dimensional superconductor is linked to the question at which rate  $\Gamma$  such fluctuations happen

$$\Gamma(T) = \Omega(T) \exp\left(-\frac{\Delta F(T)}{k_B T}\right). \quad (2.18)$$

Here,  $\Omega(T)$  is a temperature-dependent prefactor called attempt frequency,  $\Delta F(T)$  the free energy increment Eq. (2.17) and  $k_B$  the Boltzmann constant.

D. E. McCumber and B. I. Halperin refined the LA concept by utilizing the time-dependent GL theory and derived the prefactor of Eq. (2.18) to be [MH70]

$$\Omega(T) = \frac{\sqrt{3}}{2\pi^{3/2}} \frac{L}{\xi} \frac{1}{\tau_r} \left(\frac{\Delta F}{k_B T}\right)^{1/2}. \quad (2.19)$$

The fact that  $\Omega(T)$  scales with the ratio of wire length  $L$  and coherence length  $\xi$  sustains the concept Eq. (2.17) that the fluctuations take place on a length scale of  $\xi$ .  $1/\tau_r$  is the

<sup>7</sup>Their theory of phase slips is correspondingly called LA theory.

superconducting relaxation rate in the GL theory. The beauty of this *LAMH theory*<sup>8</sup> is that it agreed well with the resistance measurements of e.g. Newbower et al. [NBT72] in superconducting tin filaments close to  $T_c$ . According to Eq. (2.18), the theory predicts an exponentially decreasing phase slip rate for temperatures decreasing from  $T_c$  with vanishing phase slip probability well below  $T_c$ . This can be understood due to the validity of GL theory around  $T = T_c$  and shows that it deals with *thermally activated phase slips* (TAPS). It predicts a temperature dependent resistance

$$\begin{aligned} R_{\text{TAPS, LAMH}}(T) &= \frac{hR_q}{k_B T} \Gamma_{\text{QPS}}(T) \\ &= \frac{\sqrt{3}}{2\pi^{3/2}} \frac{hR_q}{k_B T} \frac{1}{\tau_r} \frac{L}{\xi} \left( \frac{\Delta F}{k_B T} \right)^{1/2} \exp\left( -\frac{\Delta F(T)}{k_B T} \right). \end{aligned} \quad (2.20)$$

In 2008, G. S. Golubev and A. Zaikin reanalyzed the TAPS problem by means of an effective action approach [GZ08]<sup>9</sup> which leads to a rate  $\Gamma$  that exceeds the one in Eq. (2.18) by a factor of  $(1 - T/T_c)^{-1}$ . It predicts a temperature-dependent resistance of a one-dimensional wire below  $T_c$  given as

$$R_{\text{TAPS, GZ}}(T) \approx 17 \frac{T_c}{T} R_q \frac{L}{\xi(T)} \sqrt{\frac{\Delta F}{k_B T}} \exp\left( -\frac{\Delta F}{k_B T} \right). \quad (2.21)$$

$R_q = h/(4e^2) \approx 6.45 \text{ k}\Omega$  is the quantum resistance. The general behaviour of an exponential decay of resistance with temperature is preserved.

### 2.2.2. Quantum phase slip (QPS)

In 1988, by measuring the resistance  $R$  of indium nanowires versus temperature, N. Giordano made the observation that  $R$  does not decrease exponentially for  $T \ll T_c$  [Gio88]. Because the thermal energy is not sufficient to activate phase slips, he drew the conclusion that the reason for this persisting resistance must be macroscopic quantum tunnelling (MQT) of the superconducting order parameter, and thus the process is called *quantum phase slip* (QPS). Instead of a thermally activated passage over the free-energy barrier Eq. (2.17), the order parameter tunnels through it. Giordano assumed that the energy which is therefore needed comes from quantum or "zero-point" fluctuations. Thus, he adapted the LAMH theory for QPS by replacing the thermal energy  $k_B T$  by the zero-point energy  $\hbar/\tau_r$  in regard to A. O. Caldeira and A. J. Leggett [CL81]

$$\Gamma_{\text{QPS, G}}(T) = \Omega_{\text{QPS}}(T) \exp\left( -\alpha \frac{\hbar}{\tau_r} \Delta F(T) \right), \quad (2.22)$$

$$\Omega_{\text{QPS, G}}(T) = \frac{\sqrt{3}}{2\pi^{3/2}} \frac{L}{\xi} \left( \frac{\tau_r}{\hbar} \Delta F(T) \right)^{1/2}. \quad (2.23)$$

<sup>8</sup>Extension of the LA theory by McCumber and Halperin and therefore called LAMH theory.

<sup>9</sup>A detailed explanation of this technique can be found in [Ott+99].

$\alpha$  was added as an unknown fitting parameter. This leads to an expression for the resistance

$$\begin{aligned} R_{\text{QPS,G}}(T) &= \sqrt{\frac{\pi}{3}} \beta R_{\text{q}} 2\pi \tau_{\text{r}} \Gamma_{\text{QPS}}(T) \\ &= \beta R_{\text{q}} \frac{L}{\xi} \left( \frac{\tau_{\text{r}}}{\hbar} \Delta F(T) \right)^{1/2} \exp \left( -\alpha \frac{\hbar}{\tau_{\text{r}}} \Delta F(T) \right), \end{aligned} \quad (2.24)$$

which agreed well with the measured data.  $\beta$  is like  $\alpha$  an unknown fitting parameter. Although there was some scepticism in Giordano's findings in the following years, a resistance well below  $T_{\text{c}}$  could be confirmed for superconducting nanowires by different experiments [BLT00b; Lau+01]. Already in 1989, S. Saito and Y. Murayama [SM89a; SM89b] worked out an effective action approach for an exact microscopic description of the quantum tunnelling in superconducting nanowires which was later revised by Zaikin et al. [Zai+97]. Examining influences of fields and dissipation carefully, the QPS rate and resistance become

$$\Gamma_{\text{QPS,GZ}} = \Omega_{\text{QPS,GZ}} \exp \left( -\alpha_{\text{GZ}} \frac{R_{\text{q}} L}{R_{\text{n}} \xi} \right), \quad (2.25)$$

$$\Omega_{\text{QPS,GZ}} = \beta_{\text{GZ}} \frac{\Delta}{\hbar} \frac{R_{\text{q}}}{R_{\text{n}}} \left( \frac{L}{\xi} \right)^2, \quad (2.26)$$

$$R_{\text{QPS,GZ}} = \beta_{\text{GZ}} 2\pi \frac{R_{\text{q}}^2}{R_{\text{n}}} \left( \frac{L}{\xi} \right)^2 \exp \left( -\alpha_{\text{GZ}} \frac{R_{\text{q}} L}{R_{\text{n}} \xi} \right). \quad (2.27)$$

Due to very small electron mean free paths  $l$  in the nanowires, the typical QPS length scale was assumed to be  $\xi \approx \sqrt{l \xi_{\text{BCS}}} \ll \xi_{\text{BCS}}$ , thus on the order of 10 nm for typical superconducting films used in experiments. Introducing the normal conducting resistance over a coherence length  $R_{\xi} = R_{\text{n}} \xi/L$ , Eq. (2.27) reads

$$R_{\text{QPS,GZ}} = \beta_{\text{GZ}} 2\pi \frac{R_{\text{q}}^2}{R_{\xi}} \frac{L}{\xi} \exp \left( -\alpha_{\text{GZ}} \frac{R_{\text{q}}}{R_{\xi}} \right). \quad (2.28)$$

Eq. (2.26) - Eq. (2.28) point out that the probability for quantum tunnelling rises with an increasing normal conducting resistance  $R_{\text{n}}$  comparable to the kinetic inductance of a superconducting wire as shown in Sec. 2.1.3. In particular, the ratio between  $R_{\text{n}}$  and the quantum resistance  $R_{\text{q}} = 6.45 \text{ k}\Omega$  quantifies the QPS manifestation in superconducting nanowires. This indicates that highly disordered superconducting films with sheet resistances in the  $\text{k}\Omega$  range are required for QPS rates in the GHz regime which is in the focus of this work. This is discussed in detail in Sec. 3.1.

## Wire inhomogeneities

In all aforementioned derivations of QPS rates, the nanowires are assumed homogeneous regarding their wire width. Various methods have been utilized to fabricate homogeneous wires [RB03; RB05; Mil+14; Mor+14; Bur+17] and the results show that variations in width along typical nanowires can be on the order of 10–20%. Thus in 2012, M. Vanevic and Y. V. Nazarov [VN12] examined the question how strong inhomogeneity influences the QPS rate. Since they deal with *coherently driven* QPS<sup>10</sup>, they use the term quantum amplitude  $E_s$ <sup>11</sup> rather than calling it a rate  $\Gamma_{\text{QPS}}$  of single events. In their model, the nanowire remains an ultra-thin wire with width  $d \ll \xi$  and length  $L \gg \xi$  into which a weak inhomogeneity or link is embedded. This link models a variation in the wire width which extends over a length  $l \ll \xi$ . This implies that the complete system has to fulfil the conditions that the resistance and inductance of the wire must not be dominated by the weak link. Otherwise, the dynamics of this contact between two superconductors is dominated by the interference of the two superconducting wavefunctions on both sides and can be described as a weak link Josephson junction (see Sec. 2.3.2).

For "short" (dissipative) wires as well as for "long" (superconducting) wires with a weak link constituting a slightly higher local resistance,  $E_s$  is dominated by the weak link and not by the wire. This is intuitively reasonable since  $E_s$  depends exponentially on the wire width. In both cases, the total QPS amplitude for a nanowire containing several weak links with spatial extension of  $l_c = 3.43 \xi$  and length  $L$  is derived as

$$E_{s, \text{VN}} = 0.32 \Delta \sqrt{\frac{R_q}{R_\xi}} \frac{L}{\xi} \exp\left(-0.36 \frac{R_q}{R_\xi}\right), \quad (2.29)$$

with the superconducting energy gap  $\Delta$  (see Eq. (2.1)). It is argued that going to one of the two mentioned regimes, it should be easier to control the QPS amplitude by only varying the width of the weak link or constriction, respectively.

---

<sup>10</sup>This will be discussed in detail in Sec. 2.5.

<sup>11</sup>Sec. 2.3 reveals the relation between  $E_s$  and  $E_j$  in Josephson junctions.

## 2.3. Quantum phase slip and Josephson effect

The tunnelling of the superconducting order parameter at  $T \ll T_c$  causing a quantum phase slip of  $2\pi$  can be considered dual to the tunneling of a Cooper pair in a Josephson junction (JJ) since phase and charge are conjugate quantum variables for a superconductor. As firstly suggested by Büchler et al. [BGB04], sequential QPS can be coherent. In 2006, J. E. Mooij and Y. V. Nazarov theoretically worked out the exact duality between coherent QPS (cQPS) and Josephson tunnelling [MN06]. By this, they proposed a new junction type dual to the Josephson junction, which subsequently will be called *quantum phase slip junction* (QPSJ). With the canonical transformation of charge and phase operators

$$(-\hat{\phi}/2\pi, 2\pi\hat{q})_{\text{QPSJ}} \leftrightarrow (\hat{q}, \hat{\phi})_{\text{JJ}}, \quad (2.30)$$

it is possible to transfer a QPSJ-based system into a JJ-based system as will be shown in the following.

### 2.3.1. Quantum phase slip junction

In a quantum phase slip junction, two superconducting leads are connected via a nanowire with width  $d \ll \xi$  and length  $L \gg \xi$  (see Fig. 2.2).

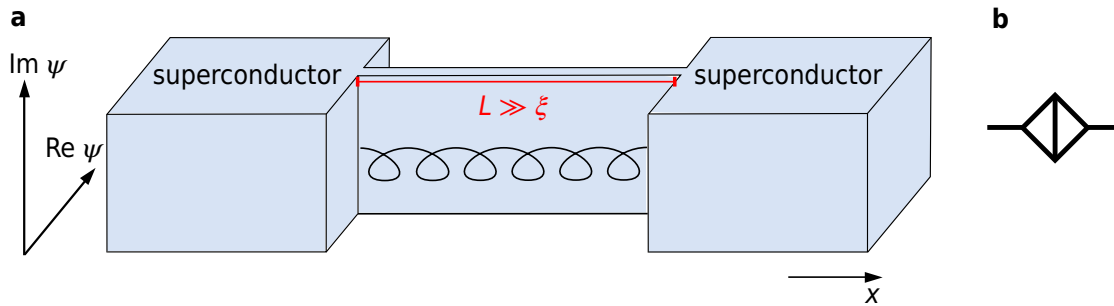


**Figure 2.2:** **a** Two superconducting electrodes (blue) connected by a superconducting nanowire forming a quantum phase slip (QPS) junction (not to scale). The amplitudes of the two superconducting wavefunctions do not overlap over the the nanowire because its length is bigger than the coherence length  $L \gg \xi$ . Under this condition, quantum phase slips can happen. The spiral represents the superconducting phase turns over the nanowire. **b** In an electrical circuit, a QPS junction is represented by a diamond with a bar.

Since the nanowire may carry a current or serve as a conducting channel between the leads, it forms an inductor and can be characterized by its *inductive energy*

$$E_L = \frac{\Phi_0^2}{2L}, \quad (2.31)$$

with the magnetic flux quantum  $\Phi_0$  and the wire inductance  $L$ . As discussed in Sec. 2.2.2, due to its one-dimensionality in regard to its coherence length, the nanowire forms a free energy barrier through which the superconducting order parameter can tunnel. This is characterized by the *phase slip energy*  $E_s$ . Hence,  $E_s$  and  $E_L$  determine the dynamics of a QPSJ.

The voltage over the junction depends on the charge difference  $Q$  of the two superconducting leads and is given by

$$V = V_c \sin\left(2\pi \frac{Q}{2e}\right). \quad (2.32)$$

Here,  $V_c$  is called the critical voltage, thus the maximum voltage which can be applied to the junction. This critical voltage is directly proportional to the phase slip energy  $E_s$ ,

$$V_c = \frac{2\pi}{2e} E_s, \quad (2.33)$$

since phase slips change the number of phase turns over the wire and the voltage, respectively.

The evolution of the charge with time manifests as current  $I$  carried by the junction,

$$\frac{dQ}{dt} = I. \quad (2.34)$$

### 2.3.2. Josephson junction

In a SIS Josephson junction (JJ), two superconductors (S) are separated by a thin <sup>12</sup> insulating (I) barrier which forms a weak link between the two "strong" superconductors (see Fig. 2.3). In 1962, B. D. Josephson postulated the possibility of tunnelling of Cooper pairs as well as normal electrons through such weak links when they are superconducting [Jos62]. This quantum tunnelling process becomes feasible because the amplitudes of the superconducting wavefunctions on both sides of the barrier decrease exponentially over the barrier (see Fig. 2.3).

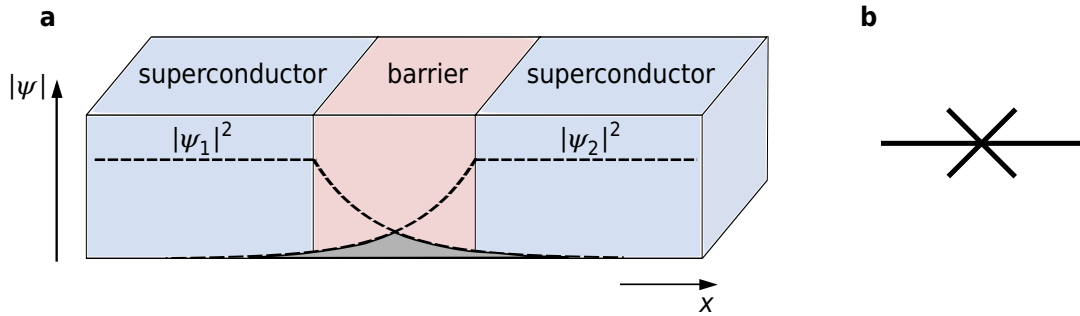


**Figure 2.3:** **a** Two superconducting electrodes (blue) separated by an isolating barrier (red) forming a Josephson junction (not to scale). The amplitudes of the two superconducting wavefunctions  $|\psi_{1,2}|^2$  decay exponentially over the barrier (dashed lines). Their overlap (grey) provides coupling between them. **b** In an electrical circuit, a Josephson junction is represented by a cross referring to its non-linear current properties.

Since the sandwich formed of two superconductors separated by a thin insulating layer forms a parallel plate capacitor, it can be characterized by its *charging energy*

$$E_C = \frac{(2e)^2}{2C}. \quad (2.35)$$

Since the barrier is thin enough to allow for an overlap of the wavefunctions, they can interfere with each other. This gives a probability for Cooper pairs on one side of the junction to exist also on the other side. The resulting Cooper pair tunnelling is characterized by the *Josephson energy*  $E_J$ . Hence,  $E_J$  and  $E_C$  determine the dynamics of a JJ.

The supercurrent through the junction is determined by the phase difference  $\varphi = \phi_1 - \phi_2$  of the two superconducting wavefunctions and is given by the *DC Josephson effect*

$$I_s = I_c \sin(\varphi). \quad (2.36)$$

Here,  $I_c$  is the so-called critical current, thus the maximum current a Josephson junction can carry without dissipation.  $I_c$  depends on the energy gaps of the two superconductors

<sup>12</sup>The thickness is on the order of a few nm.

and the normal state resistance of the barrier and is directly proportional to the Josephson energy  $E_J$

$$I_c = \frac{2\pi}{\Phi_0} E_J. \quad (2.37)$$

The *AC Josephson effect* describes the relation between the time evolution of the phase difference  $\varphi$  and the voltage  $V$  across the junction

$$\frac{d\varphi}{dt} = \frac{2e}{\hbar} V = \frac{2\pi}{\Phi_0} V, \quad (2.38)$$

where  $\Phi_0$  is the aforementioned flux quantum.<sup>13</sup>

Except by an insulating barrier as in a the *superconductor - insulator - superconductor* (SIS) junction, the separation of the two superconductors can be realized either by a normal conducting barrier forming a *superconductor - normalconductor - superconductor* (SNS) or by a very short and narrow bridge which forms a *weak link junctions*.

The junctions can also be classified into tunnel(-type) junctions and non-tunnel(-type) or direct conducting junctions. Then, SIS junctions belong to the first type while SNS and weak link junctions are of the second type. Eq. (2.36) and Eq. (2.38) are valid for all types of Josephson junctions.

### SNS junctions

In a SNS junction, the two superconductors are interrupted by a normal conducting layer forming a conducting and not a tunnel link. The reason why the superconducting wavefunctions from both sides can interfere even over a normal conducting gap is their ability to maintain their amplitude and phase inside the gap. Of course, the superconducting phase coherence gets destroyed inside the normalconductor but not instantaneously at the boundary. The effect that Cooper pairs can penetrate into a normalconductor on a length scale of  $\xi_N$  (coherence length in the normalconductor) is called *proximity effect*. Depending on the properties of the normal conducting film,  $\xi_N$  can be up to  $1 \mu\text{m}$  and hence a normal conducting barrier can be much longer than an insulating one.

### Weak link junctions

Josephson's theoretical considerations were originally motivated by the idea of quantum mechanical tunnelling of electrons from one superconductor to another through a non-conducting barrier layer. Nowadays, it is understood that the effects that Josephson derived from his considerations are more generally valid. As soon as two strong superconductors

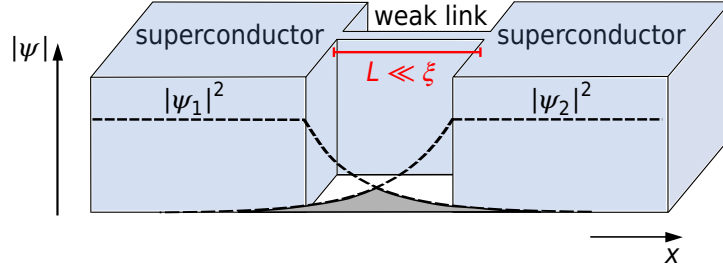


**Figure 2.4:** Two superconductors are weakly linked by a superconducting bridge. The length  $L$  of the link has to be smaller than the superconducting coherence length  $\xi$  in order to get an overlap of the superconducting wavefunctions  $\psi_{1,2}$ .

are connected by a weak link, the effects occur. The weak link can be realized in different ways. Here, the focus is on weak links as shown in Fig. 2.4.

The very short and narrow bridge<sup>14</sup> linking the two superconductors is assumed to be one-dimensional with a length  $L \ll \xi$ . In such a junction the Josephson effect occurs due to a spatial inhomogeneity in the superconducting state which is caused by the bridge. The GL theory introduced in Sec. 2.1.1 is particularly useful to describe such a situation. Only for the aforementioned condition of  $L \ll \xi$ , the first term in Eq. (2.6) dominates which leads to  $d^2 f/dx^2 = 0$ . In order to solve this, we use

$$f(x) = 1 - \frac{x}{L} + \frac{x}{L} e^{i\varphi}. \quad (2.39)$$

Using this ansatz, it can be shown that the current through the weak link junction is also given by Eq. (2.36) with the critical current proportional to the ratio of cross section  $A$  and length  $L$ ,  $I_c \propto A/L$ . With Eq. (2.39), the spatial dependence of the normalized order parameter  $f$  at the center of the bridge can be expressed as

$$|f|^2 = \cos^2(\varphi/2). \quad (2.40)$$

According to the second Josephson equation Eq. (2.38), the phase difference  $\varphi$  increases with increasing applied voltage  $V$ . For a Dayem bridge-like weak-link junction, this means an oscillation of the amplitude  $|f|^2$ .

<sup>13</sup>Eq. (2.36) and Eq. (2.38) are also called *first* and *second Josephson equation*.

<sup>14</sup>also called Dayem bridge.

### 2.3.3. Duality

Subsequently, the duality between QPSJ-based and JJ-based systems will be derived for different energetic regimes.

#### "Strong" tunnelling $E_s \gg E_L$ vs. $E_J \gg E_C$

In case of strong tunnelling where the phase slip energy is much bigger than the inductive energy of the junction, the quantum phase slip junction is in its *charge regime*. In order to understand the charge dynamics of such a junction, an equivalent circuit of a voltage-biased serial connection of a phase slip wire, inductance  $L$  and resistance  $R$  (see Fig. 2.5a) is considered [Moo+15]. This leads to a differential equation of the voltage over the system

$$\begin{aligned}
 V &= V_1 + V_2 + V_3, \\
 &= V_c \sin\left(2\pi \frac{Q}{2e}\right) + R \frac{dQ}{dt} + L \frac{d^2Q}{dt^2}, \\
 &= V_c \sin(2\pi q) + 2e R \frac{dq}{dt} + 2e L \frac{d^2q}{dt^2}.
 \end{aligned} \tag{2.41}$$

where  $q = Q/2e$  is the charge  $Q$  normalized in respect to a Cooper pair charge of  $2e$ .  $V_1$ ,  $V_2$  and  $V_3$  are the voltages over the different elements (see Fig. 2.5a).

Comparing this with the differential equation of a pendulum, one can describe the charge dynamics of a quantum phase slip junction with a particle of mass

$$m = (2e)^2 L \tag{2.42}$$

moving in a potential

$$U(2\pi q) = E_s \left( -\frac{V}{V_c} 2\pi q - \cos(2\pi q) \right), \tag{2.43}$$

$$E_s = \frac{2e}{2\pi} V_c. \tag{2.44}$$

The damping of the charge dynamics can be expressed by the parameter Eq. (2.49)

$$\beta_L = 2\pi \frac{V_c L}{2e R^2} = 2\pi^2 \frac{E_s}{E_L} \left( \frac{R_q}{R} \right)^2. \tag{2.45}$$

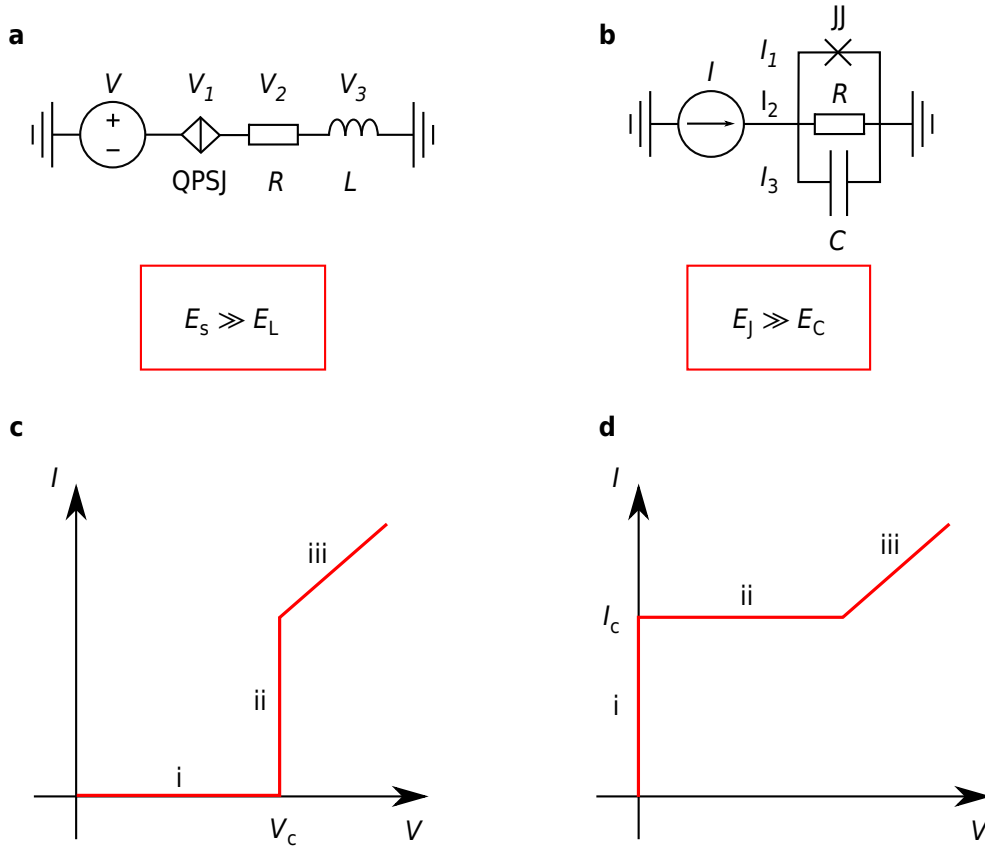


**Figure 2.5:** **a** A QPS junction (QPSJ) connected in series with a resistance  $R$  and an inductance  $L$ . The voltage  $V$  distributes over the different circuit elements ( $V_1$ ,  $V_2$ ,  $V_3$ ). **b** A Josephson junction (JJ) shunted by a resistance  $R$  and a capacitance  $C$ . The current  $I$  splits up into  $I_1$ ,  $I_2$  and  $I_3$  (see Eq. (2.46)) obeying Kirchhoff's current law. **c** Current-voltage characteristic of the voltage-biased QPS circuit shown in **a**. There is no current flowing through the junction for increasing applied voltage until a critical voltage  $V_c$  is reached and the junction becomes resistive. For more details on stages i, ii and iii please refer to the text. **d** Current-voltage characteristic of the current-biased Josephson junction circuit shown in **b**. There is no voltage drop over the junction for increasing current until a critical current  $I_c$  is reached and the junction becomes resistive. For more details on stages i, ii and iii please refer to the text.

In Fig. 2.5c, the current vs voltage (IV) curve of a quantum phase slip junction in the regime  $E_s \gg E_L$  is shown.

- i For an increasing bias voltage  $V$ , there is no current through the nanowire. Phase turns added by the applied voltage are canceled out by quantum phase slips. Thus, the applied energy is completely dissipated (see Fig. 2.5c). The junction is in the *isolating regime*.
- ii When the bias voltage reaches the critical voltage of the junction  $V = V_c$ , the Cooper pairs break up and a current starts to flow (see Fig. 2.5c) due to current transport

by electrons. The critical voltage is the point at which the rate of phase turns that are added by applying a voltage is equal to the rate of removing phase turns due to quantum phase slips.

- iii The slope in the IV characteristic for bias voltages  $V = V_c$  (see Fig. 2.5c) represents the ohmic behavior of the junction because here the current is carried by electrons, i.e. the junction is in the normal conducting regime.

For a Josephson junction, strong tunnelling means that its Josephson energy is larger than its charging energy. Then, the junction is in its *phase regime*. To describe the phase dynamics of such a Josephson junction, the *resistively and capacitively shunted junction* (RCSJ) model is commonly used. As depicted in Fig. 2.5b, the equivalent circuit of a current-biased Josephson junction contains a junction shunted by a resistance  $R$  and a capacitance  $C$ . Applying Kirchhoff's current law, the system current consists of the currents flowing through the three components of the circuit

$$\begin{aligned} I &= I_1 + I_2 + I_3 \\ &= I_c \sin(\varphi) + \frac{1}{R} \frac{\Phi_0}{2\pi} \frac{d\varphi}{dt} + C \frac{\Phi_0}{2\pi} \frac{d^2\varphi}{dt^2}. \end{aligned} \quad (2.46)$$

Comparing this differential equation with the one of a pendulum, one can describe the phase dynamics of a Josephson junction with a particle of mass

$$m = C \left( \frac{\Phi_0}{2\pi} \right)^2 \quad (2.47)$$

moving in a potential

$$U(\varphi) = E_J \left( -\frac{I}{I_c} \varphi - \cos(\varphi) \right). \quad (2.48)$$

The phase damping can be expressed by the Steward-McCumber parameter

$$\beta_c = \frac{2e}{\hbar} I_c R^2 C. \quad (2.49)$$

The typical current-voltage (IV) characteristics of the described Josephson junction can be seen in Fig. 2.5d.

- i For an increasing bias current  $I$ , there is no voltage drop over the junction. All electrons are condensed into Cooper pairs which carry the complete current according to Eq. (2.36) (see Fig. 2.5d). The junction is in the *superconducting regime*.
- ii When the bias current reaches the critical current of the junction  $I = I_c$ , the Cooper pairs break up and a voltage drop occurs (see Fig. 2.5d) due to current transport by electrons.
- iii The slope in the IV characteristic for bias currents  $I > I_c$  (see Fig. 2.5d) represents the ohmic behaviour of the junction because here the current is carried by electrons, i.e. that the junction is in the normal conducting regime.

**"Weak" tunnelling**  $E_s \ll E_L$  vs.  $E_J \ll E_C$

In the opposite energetic regime of weak tunnelling, the duality between quantum phase slip and Josephson junctions can be nicely seen by comparing the dynamics of the so-called *quantum phase slip flux qubit* (QPSFQ) which was proposed by J. E. Mooij and C. J. P. M. Harmans in 2005 [MH05] with the dynamics of the well-known Josephson junction based *Cooper pair box* (CPB).

The QPSFQ is made from a superconducting loop in which the magnetic field is quantized in discrete numbers of magnetic flux quanta as described in Sec. 2.1.2. The number of flux quanta inside the loop cannot change unless a quantum phase slip junction is embedded into the loop (see Fig. 4.6a). It allows fluxoids to tunnel in and out of the loop any time a phase slip reduces the superconducting order parameter to zero. In a QPSFQ, the phase slip energy  $E_s$  of the embedded nanowire is smaller than the total inductive energy  $E_L$  of the system where  $L_{\text{tot}} = L_{\text{loop}} + L_{\text{wire}}$ . Thus, the energy spectrum of a QPSFQ versus an externally applied magnetic flux  $\Phi$  or frustration  $f = \Phi/\Phi_0$  is determined by the quadratic dependence of  $E_L$  on  $\Phi$  as given by the parabolas in Fig. 4.6c. Each parabola represents a certain number of fluxoids in the loop. The fact that the phase slip junction acts as a flux shuttle and allows for a change of the fluxoid number in the loop is represented in the energy spectrum as lifting of the degeneracy of adjacent fluxoid states at half-integer values of the frustration  $f$  (see Fig. 4.6c). As a result, the system behaves as a two-level system or qubit with a ground  $|0\rangle$  and an excited state  $|1\rangle$ . Consecutive fluxoid states cause persistent currents in the loop with opposite direction and they are coherently coupled by QPS. The amplitude of this coherent coupling is  $E_s$  given by Eq. (2.29). The Hamiltonian which represents a QPSFQ is

$$H_{\text{QPSFQ}} = \sum_N E_L (f - N)^2 |N\rangle\langle N| - \frac{E_s}{2} \sum_N (|N+1\rangle\langle N| + |N\rangle\langle N+1|), \quad (2.50)$$

where  $N$  is the number of flux quanta in the loop. Therewith, the phase slip junction is here in its *phase regime*.

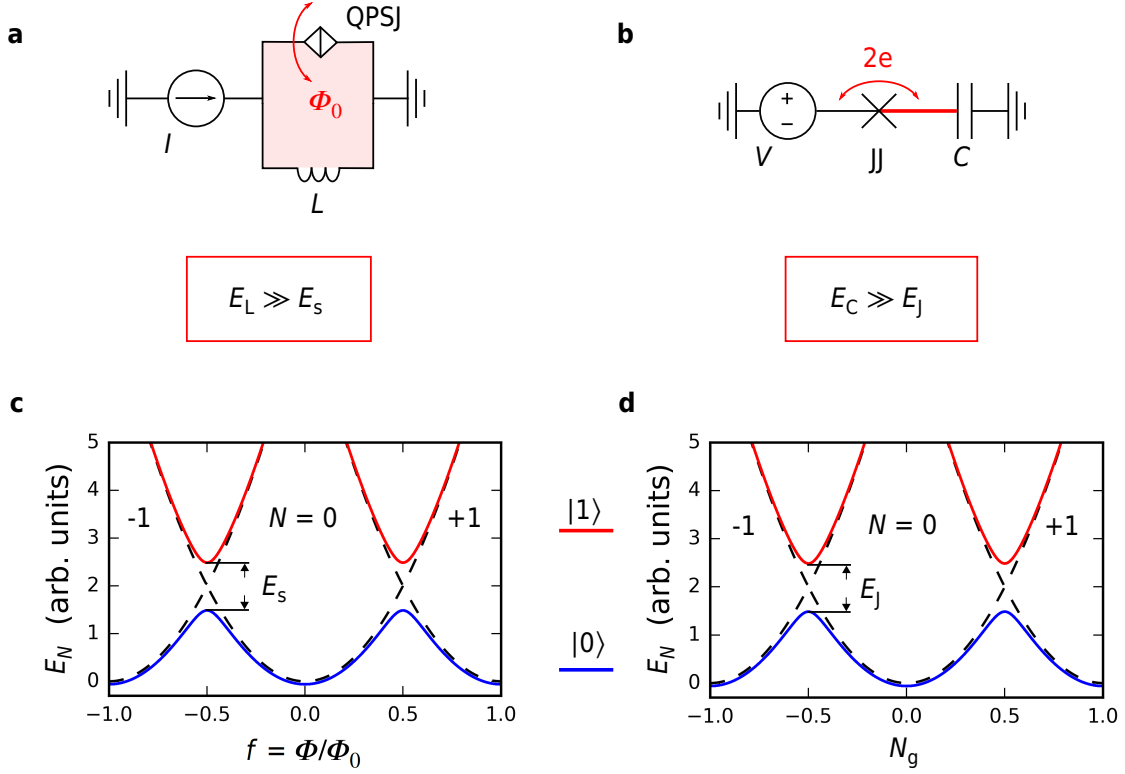


**Figure 2.6:** **a** Electrical circuit of the quantum phase slip flux qubit (QPSFQ). The number  $N$  of fluxoids ( $\Phi_0$ ) in the superconducting loop with inductance  $L$  and embedded QPS junction QPSJ can only change in discrete numbers under external flux bias. **b** Electrical circuit of the Cooper pair box (CPB). The number  $N$  of Cooper pairs ( $2e$ ) on the island (red) formed by gate capacitor  $C$  and the Josephson junction  $JJ$  can only change in discrete numbers under bias of the gate voltage  $V$ . **c** QPSFQ energy spectrum for  $N = -1, 0, +1$  fluxoids in the loop (dashed parabolae) as a function of magnetic frustration  $f = \Phi/\Phi_0$ . The QPS tunnelling  $E_s$  lifts the degeneracy at half-integer values of  $f$ . **d** CPB energy spectrum for  $N = -1, 0, +1$  Cooper pairs on the island (dashed parabolae) as a function of offset gate charge  $N_g = CV/2e$  in units of  $2e$ . The Josephson tunnelling  $E_J$  lifts the degeneracy at half-integer values of  $N_g$ . **c+d** In both cases, coherent tunnelling creates a two-level system with a ground state  $|0\rangle$  (blue) and an excited state  $|1\rangle$  (red).

The Josephson junction based dual of a QPSFQ for weak tunnelling is the Cooper pair box (CPB) as it is shown on Fig. 4.6b. In a CPB, a charge island (red in Fig. 4.6b) is formed between a gate capacitor with capacitance  $C$  and the Josephson junction which serves as connection to a superconducting reservoir. Weak tunnelling is realized when the Josephson energy  $E_J$  is smaller than the charging energy  $E_C$  where the total capacitance is given by the gate and the junction capacitance  $C = C_J + C_{\text{gate}}$ . The number of Cooper pairs on the island cannot change unless the Josephson junction allows for tunnelling of Cooper pairs from the reservoir to the island and vice versa. Then, the number of Cooper pairs

on the island can be controlled by the gate voltage  $V$  or the gate offset charge  $N_g$ , respectively. The energy spectrum of the system is determined by the quadratic dependence of the charging energy on  $N_g$  (see dashed parabolas in Fig. 2.7d). The parabolas represent certain numbers of Cooper pairs on the island. The tunnelling of Cooper pairs through the Josephson junction results in a lifting of the degeneracy of adjacent Cooper pair states at half-integer values of  $N_g$  by  $E_J$  (see Fig. 4.6d). This results in the formation of a two-level system or qubit, respectively, with ground and excited state  $|0\rangle$ ,  $|1\rangle$ . The CPB energy can be expressed by the Hamiltonian

$$H_{\text{CPB}} = \sum_N E_c (N_g - N)^2 |N\rangle\langle N| - \frac{E_J}{2} \sum_N (|N+1\rangle\langle N| + |N\rangle\langle N+1|), \quad (2.51)$$

where  $N$  now represents the number state of Cooper pairs on the island. Therefore, the Josephson junction is in its *charge regime*. It can nicely be seen that Eq. (2.51) is the dual of Eq. (2.50).

In Fig. 2.7, all important properties of the duality between Josephson und quantum phase slip junctions are displayed together.

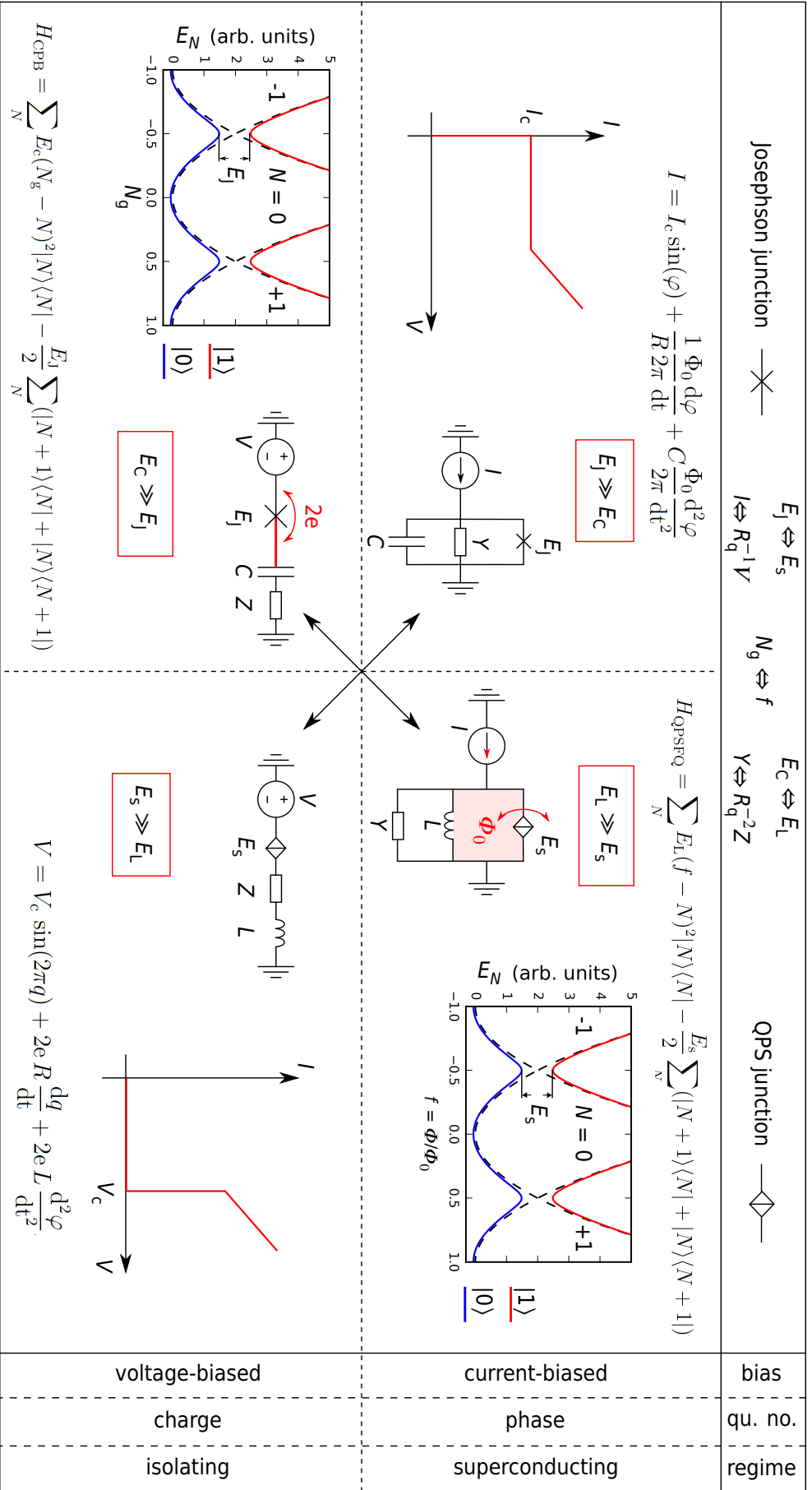


**Figure 2.7:** Complete duality picture for Josephson and quantum phase slip (QPS) junction recapturing the different energetic regimes and typical systems as discussed in this section.

## 2.4. Measuring coherent quantum phase slip

A possibility to investigate coherent quantum phase slip in experiment is to borrow well-known techniques from *quantum electrodynamics* (QED). QED deals with the interaction between matter and light. In cavity quantum electrodynamics (cQED), the interaction of interest is between single atoms and single electromagnetic field modes. These modes come from electromagnetic fields confined in cavities which can be expressed by quanta of the electromagnetic field called photons.

In 2004, A. Blais et al. proposed an implementation of cQED in a superconducting electrical circuit; therefore called *circuit QED* (cQED) [Bla+04]. In such a circuit, the electromagnetic field is quantized in field modes of a superconducting resonator. Typically, these resonators are designed to resonate in the lower GHz or *microwave* regime. Thus, the electromagnetic field is quantized into photons with microwave energies what is called *microwave photons*. The single natural atoms are replaced with artificial systems designed and made from superconducting circuits. The goal is to couple microwave photons from the resonator to quantized excitations of the artificial atom. Such an artificial atom can be the quantum phase slip flux qubit as described in Sec. 2.3.3.

### 2.4.1. Quantum phase slip flux qubit

Designed to be in the phase or flux regime, the only relevant degree of freedom of a quantum phase slip flux qubit (QPSFQ) is the number  $N$  of fluxoids in the loop. As shown in Fig. 4.6a, c, quantum phase slip leads to tunneling of fluxoids into and out of the loop. This creates a superposition of adjacent fluxoid states  $|N\rangle$  and  $|N + 1\rangle$  at half-integer values of the magnetic frustration  $f$ . Restricting the system on only one adjacent pair of fluxoid states describes a two-level system. These states are the clockwise and counter-clockwise circulating persistent current states in the loop which generate a magnetic field in the  $z$ -direction. Projecting the QPSFQ Hamiltonian Eq. (2.50) on these two states provides the matrix representation

$$\tilde{H}_{\text{QPSFQ}} = \frac{1}{2} E_L (2f - 1) \tilde{\sigma}_z - \frac{1}{2} E_s \tilde{\sigma}_x, \quad (2.52)$$

$$= \frac{1}{2} (2I_p \Phi_0 (f - 1/2) \tilde{\sigma}_z - E_s \tilde{\sigma}_x), \quad (2.53)$$

$$= \frac{1}{2} \begin{pmatrix} 2I_p \Phi_0 (f - 1/2) & -E_s \\ -E_s & -2I_p \Phi_0 (f - 1/2) \end{pmatrix}.$$

where  $\tilde{\sigma}_{x,z}$  are the Pauli operators in the persistent current basis and  $E_L$  is expressed by the persistent current  $I_p$ , the flux quantum  $\Phi_0$  and the frustration  $f = \Phi/\Phi_0$ . The qubit

eigenenergies close to the degeneracy point  $f = 1/2$  can be obtained by diagonalizing Eq. (2.53) by a unitary rotation of an angle  $\tan(2\theta) = E_s/(2I_p\Phi_0(f - 1/2))$  around the y-axis

$$U = \exp(i\theta\tilde{\sigma}_y) = \begin{pmatrix} \cos(\theta) & \sin(\theta) \\ -\sin(\theta) & \cos(\theta) \end{pmatrix}, \quad (2.55)$$

which leads to the Hamiltonian in the rotated qubit frame

$$\hat{H}_{\text{QPSFQ}} = U^\dagger \tilde{H}_{\text{QPSFQ}} U = \frac{1}{2} \sqrt{(2I_p\Phi_0(f - 1/2))^2 + E_s^2} \sigma_z = \frac{1}{2} \hbar\omega_q \sigma_z. \quad (2.56)$$

Here,  $\sigma_z$  is the Pauli operator in the rotated basis and  $\omega_q$  is the qubit transition frequency that shows a hyperbolic dependence on the magnetic flux  $\Phi$  or frustration  $f$ , respectively.

The qubit can be in any superposition state  $|\psi\rangle$  of  $|0\rangle$  and  $|1\rangle$ . An intuitive representation is that each state  $|\psi\rangle$  lies on the surface of the Bloch sphere (see Fig. 2.8). Hence,  $|\psi\rangle$  can be expressed in spherical coordinates

$$|\psi\rangle = \cos\left(\frac{\theta}{2}\right) |0\rangle + \sin\left(\frac{\theta}{2}\right) e^{i\phi} |1\rangle, \quad (2.57)$$

with the Euler angles  $\theta$  and  $\phi$ . In this representation, the ground state  $|0\rangle$  points in positive z-direction while the excited state  $|1\rangle$  points in negative z-direction. This representation is valid not only for flux qubits, but any other two-level type qubit exhibiting quantized states of charge or junction phase.

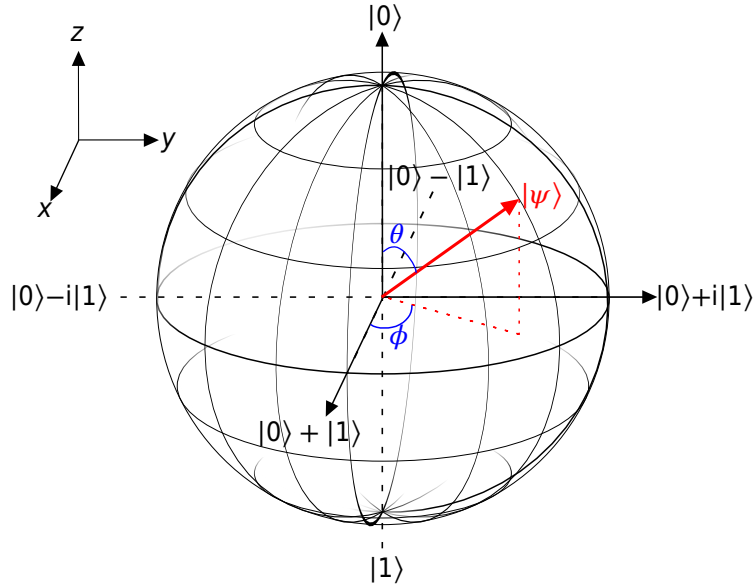


**Figure 2.8:** Bloch sphere representation of a two-level system or qubit, respectively. The ground state  $|0\rangle$  points in positive z direction while the excited state  $|1\rangle$  points to the opposite. Any qubit state  $\psi$  is represented as a point on the surface of the sphere given by spherical coordinates as in Eq. (2.57) with the Euler angles  $\theta$  and  $\phi$ .

## Qubit under drive

By coupling a quantum phase slip flux qubit to a microwave field represented by a resonator, the qubit transition can be coherently driven. The qubit will exhibit coherent oscillations between ground and excited states under this external drive when it is in resonance with the qubit. In the persistent current basis, the drive is

$$\tilde{H}_d = A \cos(\omega_d t + \varphi) \tilde{\sigma}_z, \quad (2.58)$$

with drive amplitude  $A$ , drive frequency  $\omega_d$  and phase offset  $\varphi$  coupled to the qubit via  $\tilde{\sigma}_z$ . It can be treated as a weak perturbation acting on the qubit Eq. (2.53). Rotating the drive into the qubit eigenbasis, leads to

$$\hat{H}_d = A \cos(\omega_d t + \varphi) \left( \frac{E_s}{\hbar \omega_q} \sigma_x + \frac{2I_p \Phi_0 (f - 1/2)}{\hbar \omega_q} \sigma_z \right), \quad (2.59)$$

Is the drive frequency in resonance with the qubit frequency, the rotation frequency of the Bloch vector is

$$\Omega_R = \frac{A_d}{\hbar^2} \frac{E_s}{\omega_q}, \quad (2.60)$$

called the *Rabi frequency* of the qubit under drive.

A detuning of qubit and drive frequencies results in a *generalized Rabi frequency*

$$\Omega_{R,g} = \sqrt{\left( \frac{A}{\hbar^2} \frac{E_s}{\omega_q} \right)^2 + (\omega_q - \omega_d)^2}. \quad (2.61)$$

The Rabi frequency is proportional to the amplitude of the drive signal and an off-resonant drive leads to a tilt of the rotation axis towards the  $z$  axis.

## Qubit relaxation

Relaxation processes of qubit states are conveniently considered in the Bloch-Redfield picture describing a weak coupling of noise to a qubit. For noise with short correlation times compared to the system dynamics, two important relaxation rates have to be considered:

$$\Gamma_1 \equiv \frac{1}{T_1}, \quad (2.62)$$

$$\Gamma_2 \equiv \frac{1}{T_2} = \frac{\Gamma_1}{2} + \Gamma_\varphi. \quad (2.63)$$

$\Gamma_1$  is the longitudinal relaxation rate and  $\Gamma_2$  is the transversal relaxation rate, which is limited by  $\Gamma_1$  in case of no dephasing  $\Gamma_\varphi = 0$ .

Longitudinal relaxation can be seen in the Bloch sphere as a depolarization of the qubit Bloch vector along the quantization axis  $z$ . It is caused by transversal noise which connects ground  $|0\rangle$  and excited states  $|1\rangle$  via off-diagonal elements in the interaction Hamiltonian and follows an exponential decay. Since typical superconducting qubit measurements take place at temperatures  $k_B T \ll \hbar\omega_q$ , longitudinal relaxation manifests only in a relaxation from the excited to the ground state.

Transversal relaxation is due to interaction with longitudinal noise leading to a variation of the qubit's precession on the equator. This, in turn, leads to dephasing (loss of phase coherence). Only during the longitudinal relaxation time, the qubit can be addressed by longitudinal noise which implicates that  $T_2$  has to be  $T_1$ -limited.

### 2.4.2. Superconducting microwave resonators

For the experiments performed in this thesis, different types of superconducting microwave resonators are used as cavities providing microwave photons. For a lumped element resonator, the geometric dimensions of its inductor  $L$ , capacitor  $C$  and resistor  $R$  are much smaller than its characteristic wavelength. Independent whether they are arranged in series or parallel, the resonator resonates at

$$f_{\text{res}} = \frac{1}{2\pi\sqrt{LC}}. \quad (2.64)$$

An important characteristic of a resonator is its quality factor  $Q$  which is defined as

$$Q = \frac{\text{energy stored in the resonator}}{\text{energy loss in the resonator}}. \quad (2.65)$$

Energy lost due to dissipation in the resonator is accounted by the *internal quality factor*  $Q_0$ . To readout a resonator, it has to be coupled to a transmission line. The coupling to this transmission line can be capacitive, inductive or galvanic and leads to an external loss because energy is lost into this coupling. This is accounted with the external or coupling quality factor  $Q_c$ . The combination of both loss factors leads to an overall loss, expressed in the loaded quality factor

$$\frac{1}{Q_1} = \frac{1}{Q_c} + \frac{1}{Q_0}. \quad (2.66)$$

A different type of resonator utilized in this work is a distributed resonator consisting of a piece of transmission line sufficiently long so that variations in current and voltage have to be taken into account. This is the case when the line has a length of a considerable fraction of the characteristic wavelength of the resonator. Capacitance and inductance are no longer confined but spread over the length of the transmission line resonator. When both ends are open or disconnected from any load or from electrical ground, standing waves can form with maximum charge and zero current at each end (see Fig. 2.9a). This condition

is fulfilled for any multiple of half the characteristic wavelength  $\lambda$  of the resonator<sup>15</sup> with corresponding frequency modes

$$f_{\text{res}} = \frac{1}{2l \sqrt{L'C'}}. \quad (2.67)$$

$l$  gives the length of the resonator and  $L'$  and  $C'$  are defined as the inductance and capacitance per unit length. If one end is connected to ground, a current node forms at this end. Together with a current antinode at the other end (see Fig. 2.9a), standing waves can form with multiples of quarter the characteristic wavelength  $\lambda$  of the resonator<sup>16</sup>. The corresponding frequency modes are given by

$$f_{\text{res}} = \frac{1}{4l \sqrt{L'C'}}. \quad (2.68)$$

For distributed resonators, Eq. (2.66) is also valid.

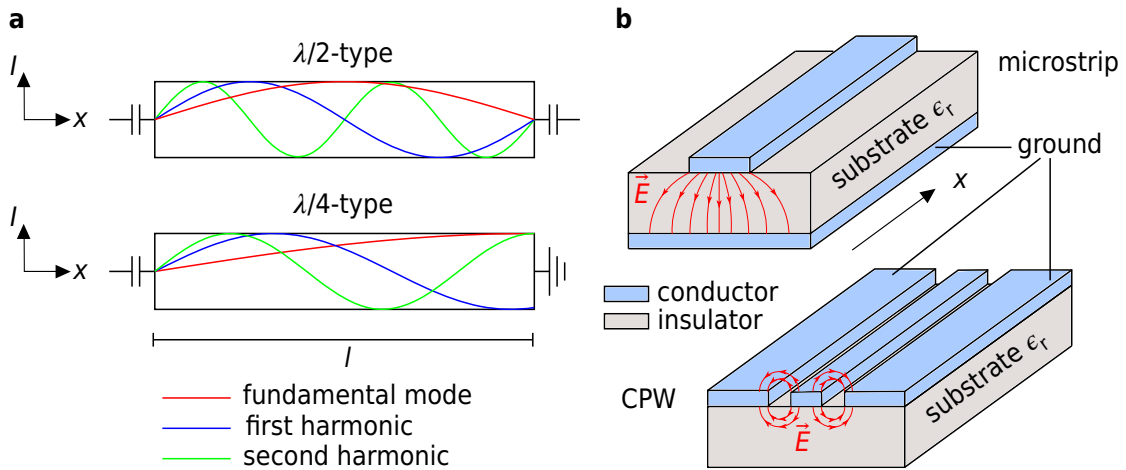


**Figure 2.9:** **a** At the top, a  $\lambda/2$ -type resonator is depicted. It is capacitively coupled to its environment at both ends where only current nodes of standing waves are allowed. At the bottom, a  $\lambda/4$ -type resonator is represented with one end connected to ground while the other is capacitively coupled to the environment. This allows for standing waves with a current node at the capacitively coupled end and an antinode at the grounded one. For both types, the current  $I$  distributions along the line axis  $x$  of the standing waves of the fundamental as well as first and second harmonic are given. **b** Two possible realizations for a microwave transmission line resonator are displayed; at the top, a microstrip geometry with backside metallization for grounding and at the bottom, a coplanar waveguide transmission line resonator where ground is put on both sides of the inner conducting line. Furthermore, the electric field  $\vec{E}$  distributions of the structures are displayed in red.

<sup>15</sup>Such resonators are called  $\lambda/2$ -resonators.

<sup>16</sup>Such resonators are called  $\lambda/4$ -resonators.

There are different possibilities how to design a transmission line resonator. In a *microstrip* geometry, the electric field distributes between the microstrip line and the ground on the backside of the substrate on which the structure is fabricated (see Fig. 2.9b). The thickness of the substrate, its dielectric permittivity  $\epsilon_r$  and the width of the microstrip determine the capacitance per unit length. The electric ground can also be put in coplanar design on both sides of the transmission line. Then, the capacitance per unit length is determined by the gap width between line and ground plane,  $\epsilon_r$  of the substrate and the width of the transmission line (see Fig. 2.9b). In such *coplanar waveguide (CPW)* resonator geometries, the electric field distributes between the transmission line, called inner conductor, and the ground planes.

### S-matrix description

In all measurements performed in this thesis, a microwave signal is evaluated which is transmitted from one port through the setup including the experiment under investigation to another. An intuitive representation for such a two-port network is given by the scattering matrix  $S$  which relates incident and reflected voltage waves at the two ports

$$\begin{pmatrix} V_1^- \\ V_2^- \end{pmatrix} = \begin{pmatrix} S_{11} & S_{12} \\ S_{21} & S_{22} \end{pmatrix} \begin{pmatrix} V_1^+ \\ V_2^+ \end{pmatrix}. \quad (2.69)$$

$V_j^+$  is defined as amplitude of the voltage wave incident on port  $j$  and  $V_j^-$  as the amplitude of the voltage wave reflected from port  $j$ . Thus, the transmission component  $S_{21}$  of the scattering matrix is defined as the ratio between the voltage wave amplitude reflected at port 2 and the voltage wave amplitude incident on port 1

$$S_{21} = \left. \frac{V_2^-}{V_1^+} \right|_{V_2^+}, \quad (2.70)$$

under the condition that there is no voltage wave incident on port 2.

### 2.4.3. Strong qubit-resonator coupling

In order to investigate coherent quantum phase slip in a QPSFQ, the qubit has to be strongly coupled to a microwave resonator. The resonator has a loss or decay rate  $\kappa$  while the qubit inherits a decay rate  $\gamma$  due to spontaneous emission. Strong coupling means that the coupling rate  $\tilde{g}$  has to be bigger than the loss rates,  $\tilde{g} \gg \gamma, \kappa$ . This means that a photon can be swapped faster from the resonator to a qubit excitation and back than either photon or excitation can decay. Such a coupling can be realized e. g. by galvanic coupling of the qubit's persistent current and the resonator current  $I_{\text{res}}$  via a shared piece of inductance  $L_{\text{coupl}}$ . In the persistent current basis, this is represented by

$$\hbar\tilde{g} = L_{\text{coupl}} I_{\text{res}} I_{\text{p}} \tilde{\sigma}_z. \quad (2.71)$$

A rotation of the coupling Hamiltonian into the qubit basis with Eq. (2.55) gives the interaction Hamiltonian

$$\hat{H}_{\text{int}} = \hbar g = L_{\text{coupl}} I_{\text{res}} I_{\text{p}} \left( \frac{E_s}{\hbar\omega_q} \sigma_x + \frac{2I_{\text{p}}\Phi_0(f-1/2)}{\hbar\omega_q} \sigma_z \right). \quad (2.72)$$

The standard way to describe such a coupled system in cQED is the Jaynes-Cummings-model [JC63]. The corresponding Hamiltonian consists of resonator, qubit and interaction Hamiltonian  $\hat{H}_{\text{r}}$ ,  $\hat{H}_{\text{q}}$  and  $\hat{H}_{\text{int}}$

$$\hat{H}_{\text{JC}} = \hat{H}_{\text{r}} + \hat{H}_{\text{q}} + \hat{H}_{\text{int}}, \quad (2.73)$$

$$= \hbar\omega_{\text{r}} \left( a^\dagger a + \frac{1}{2} \right) + \frac{\hbar}{2} \omega_{\text{q}} \sigma_z + \hat{H}_{\text{int}}. \quad (2.74)$$

The resonator Hamiltonian is written as that of an harmonic oscillator in terms of the photon creation and annihilation operators  $a^\dagger$ ,  $a$ . The qubit is defined as a spin 1/2 - particle with spin states up and down corresponding to ground state  $|0\rangle$  and excited state  $|1\rangle$  (see Eq. (2.56)).  $\omega_{\text{q}}$  denotes the transition frequency between these states. The interaction Hamiltonian can be expressed in terms of the qubit ladder operators  $\sigma^+$ ,  $\sigma^-$  and the resonator's creation and annihilation operators  $a^\dagger$ ,  $a$

$$\hat{H}_{\text{int}} = \hbar g (\sigma^+ + \sigma^-) (a^\dagger + a), \quad (2.75)$$

$$= \hbar g (\sigma^+ a^\dagger + \sigma^+ a + \sigma^- a^\dagger + \sigma^- a). \quad (2.76)$$

Taking the time-evolution of the operators into account, Eq. (2.76) reads

$$\hat{H}_{\text{int}} = \hbar g (\sigma^+ a^\dagger e^{i(\omega_{\text{q}} + \omega_{\text{r}})t} + \sigma^+ a e^{i(\omega_{\text{q}} - \omega_{\text{r}})t} + \sigma^- a^\dagger e^{i(-\omega_{\text{q}} + \omega_{\text{r}})t} + \sigma^- a e^{-i(\omega_{\text{q}} + \omega_{\text{r}})t}). \quad (2.77)$$

In typical cQED measurements, qubit and resonator are close-by in frequency,  $\omega_{\text{q}} \approx \omega_{\text{r}}$ , which can be used to simplify Eq. (2.77) by neglecting the fast oscillating terms  $\omega_{\text{q}} + \omega_{\text{r}}$

$$\hat{H}_{\text{int,RWA}} = \hbar g (\sigma^+ a + \sigma^- a^\dagger). \quad (2.78)$$

Due to coupling  $g$ , a photon exchange comes from either a swap of one photon from the resonator into a qubit excitation ( $\sigma^+ a$ ) or the qubit relaxation combined with the creation of a photon in the resonator ( $\sigma^- a^\dagger$ ). This is the *rotating wave approximation (RWA)* that transfers the coupled qubit-resonator system into a reference system rotating with the qubit Larmor frequency  $\omega_q$  under the condition that  $\omega_r \approx \omega_q$ .

So far, only a galvanic qubit-resonator coupling has been considered. However, Eq. (2.75) also accounts for other types of coupling such as capacitive or inductive dipole-dipole coupling.

Under RWA, exact diagonalization of Eq. (2.74) results in the system ground state  $|\downarrow, 0\rangle$ <sup>17</sup> and the system's dressed excited states

$$|+, n\rangle = \cos \theta_n |\uparrow, n-1\rangle + \sin \theta_n |\downarrow, n\rangle, \quad (2.79)$$

$$|-, n\rangle = \sin \theta_n |\uparrow, n-1\rangle - \cos \theta_n |\downarrow, n\rangle, \quad (2.80)$$

with the mixing angle

$$\theta_n = \frac{1}{2} \arctan \left( \frac{2g\sqrt{n+1}}{\omega_{rq}} \right). \quad (2.81)$$

The corresponding eigenenergies are

$$E_{\uparrow,0} = -\frac{\hbar}{2} \omega_{rq}, \quad (2.82)$$

$$E_{\pm,n} = (n+1)\hbar\omega_r \pm \frac{\hbar}{2} \sqrt{4g^2(n+1) + \omega_{rq}^2}. \quad (2.83)$$

It is obvious that the resonator-qubit detuning  $\omega_{rq} = \omega_q - \omega_r$  is a crucial parameter of the system.

## Zero qubit-resonator detuning

In case of *zero detuning*  $\omega_{rq} = 0$ , Eq. (2.79) and Eq. (2.80) reduce to a doublet of maximally entangled qubit-resonator states

$$|\pm, 0\rangle = \frac{1}{\sqrt{2}} (|\uparrow, 0\rangle + |\downarrow, 1\rangle), \quad (2.84)$$

with a degeneracy lifted by  $2g$ . This means that the system oscillates between states with excited qubit and zero photons and qubit in the ground state and one photon in the resonator. The frequency of this oscillation is the vacuum Rabi frequency  $g/\pi$ . In a transmission spectroscopy measurement, this can be observed as an avoided level crossing of qubit and resonator.

---

<sup>17</sup>  $|\downarrow\rangle$  ( $|\uparrow\rangle$ ) represents the qubit in its ground (excited) state and  $|n\rangle$  states that there are  $n$  photons in the resonator.

## Large qubit-resonator detuning

The case of *large detuning*  $\omega_{\text{rq}} \gg g$  is of great importance for cQED experiments. Applying the unitary transformation [Bla+04]

$$U = \exp\left(\frac{g}{\omega_{\text{rq}}}(\sigma^+ a - \sigma^- a^\dagger)\right), \quad (2.85)$$

sheds more light on the dynamics of the coupled system

$$U \hat{H} U^\dagger \approx \hbar \left( \omega_{\text{r}} + \frac{g^2}{\omega_{\text{rq}}} \sigma_z \right) a^\dagger a + \frac{\hbar}{2} \left( \omega_{\text{q}} + \frac{g^2}{\omega_{\text{rq}}} \right) \sigma_z. \quad (2.86)$$

The second term of the sum states that the qubit transition between ground and excited state is shifted due to the coupling by [AT55]

$$E_{+,n} - E_{-,n-1} = \hbar \omega_{\text{q}} + \frac{\hbar g^2}{\omega_{\text{rq}}}(2n + 1). \quad (2.87)$$

In case of electric interaction, this shift is called ac Stark shift and for magnetic interaction ac Zeeman shift <sup>18</sup>.

The first summand in Eq. (2.86) gives a shift of the resonator frequency due to coupling to the qubit

$$E_{\pm,n} - E_{\pm,n-1} = \hbar \omega_{\text{r}} \pm \frac{\hbar g^2}{\omega_{\text{rq}}}, \quad (2.88)$$

which is called *dispersive shift*. It can be used to probe the qubit state without direct measurement of the qubit. Since the qubit state is projected onto the resonator, the readout of the resonator represents a non-demolition measurement of the qubit, preserving its state.

---

<sup>18</sup>The basic concept for this shifts is the *Lamb shift*.

## 2.5. Recent experiments on quantum phase slip

### 2.5.1. Superconducting loops with QPS junctions

In 2012, O. V. Astafiev et al. were the first to observe coherent QPS [Ast+12] in a quantum phase slip flux qubit (QPSFQ) as described in Sec. 2.4.1. Several qubits were galvanically coupled to a superconducting microwave resonator as discussed in Sec. 2.4.3. Qubits and resonator were made from the same 20 nm disordered superconducting indium oxide (InOx) film and the width of the embedded nanowires was varied. Only for the narrowest wire with a width of 40 nm, *avoided level crossings* (anti-crossings) between resonator and qubit were observed when the qubit was tuned into resonance with the resonator by sweeping the external magnetic field. Astafiev et al. were furthermore able to trace the qubit transition up to 80 GHz. In a second work, J. T. Peltonen et al. presented similar observations for galvanically coupled QPSFQ made from disordered, 3 nm thin, superconducting niobium nitride (NbN) films [Pel+13].

In both works, one goal was to shed more light on the dependence of the QPS amplitude  $E_s$  on the width of the nanowire. As outlined in Sec. 2.2.2, several phenomenological approaches were made to derive this dependence theoretically. However, the results differ in their predictions. In order to exploit cQPS for e.g. quantum information processing, it is crucial to understand this dependence so that one is able to design and fabricate QPS junctions with certain properties. The conclusion is drawn that the theoretical predictions Eq. (2.26) and Eq. (2.29) have an unclear meaning due to the facts that the concept of normal-state resistance is not well-defined for strongly disordered superconductors and that the coherence length  $\xi$  cannot be well defined.

In contrast, it is suggested that in strongly disordered superconductors, electrons form localized pairs in the absence of global superconducting coherence. This implies that superconducting transport is taken by pair hopping from one localized state to another, a theoretical concept introduced by Feigelmann et al. [Fei+07; Fei+10; FIM10].

In this framework, the phase slip amplitude is derived as

$$E_s \approx \rho \sqrt{\frac{L}{d}} \exp(-d \sqrt{\rho \nu t}), \quad (2.89)$$

where  $\rho$  represents the phase stiffness per unit square,  $\nu$  the electron density of states,  $L$  and  $d$  length and width of the nanowire.  $\rho$  is directly related to the kinetic inductance per square

$$\rho = \frac{\hbar}{(2e)^2 L_k}. \quad (2.90)$$

In [Pel+13], the  $E_s$  vs.  $d$  dependence investigation indicated that  $E_s$  seems to be dominated by constrictions along the nanowire conforming to the theoretical approach described in Sec. 2.2.2.

## 2.5.2. Superconducting nanorings

Other QPS related circuits of both theoretical and experimental interest are superconducting nanorings. These are enclosed superconducting loops which have a conductor width that is much smaller than the coherence length of the superconductor  $d \ll \xi$ ; in other words, a long nanowire bent to a loop. For  $d \gg \xi$  instead, it is the system described in Sec. 2.1.2 which has an energy spectrum dependent on the number of flux quanta  $N$  inside the loop and the externally applied flux  $\Phi_{\text{ext}}$

$$E = \frac{\Phi_0^2}{2L} \left( \frac{\Phi_{\text{ext}}}{\Phi_0} - N \right)^2. \quad (2.91)$$

The differentiation of Eq. (2.91) with respect to  $\Phi_{\text{ext}}$  gives a saw-tooth like dependence of the persistent current  $I_p$  flowing inside the loop on the externally applied magnetic flux (see Fig. 2.10).

However for  $d \ll \xi$ , the behaviour of the persistent current changes dramatically. In 2002, K. A. Matveev, A. I. Larkin and L. I. Glazman theoretically modeled a superconducting nanoring as a chain of coupled superconducting grains represented by tunnel junctions with tunnelling energy  $E_J$  [MLG02]. The effective action of the chain is

$$S_{\text{CG}} = \int_0^{1/T} \sum_{n=1}^{N_J} \left( \frac{\dot{\theta}_n^2}{2E_c} + E_J(1 - \cos \theta_n(t)) \right) dt, \quad (2.92)$$

with the number of junctions  $N_J$  in the ring and the phase difference over the  $n$ th junction  $\theta_n(t)$ . Introducing QPS fluctuations, it is shown that for a large number of junctions  $N_J \gg 1$ , the dominant contribution to the energy of the system comes from the contact  $k$  at which the phase slip event takes place. For a sufficiently large quantum phase slip amplitude  $E_s$ , this contribution leads to an energy level repulsion at half-integer values of a flux quantum and therewith to a change of the persistent current dependence on flux from saw-tooth to sinusoidal (see dashed line in Fig. 2.10). In order to get from a chain of junctions to a long nanowire, the number of junctions  $N_J$  translates into the wire length  $L$ . The change of flux states inside the loop or in other words the quantum phase slip amplitude is predicted to be proportional to  $L$ . Additionally taking disorder into account or interference effects between different sites along the wire at which QPS events take place results in a suppression of  $E_s$ . Under these conditions,  $E_s$  is only proportional to  $L^{3/4}$ . Furthermore, they claim that the same applies for a superconducting nanowire which is shunted by a superconducting line forming a loop; hence what is described in Sec. 2.5.1.

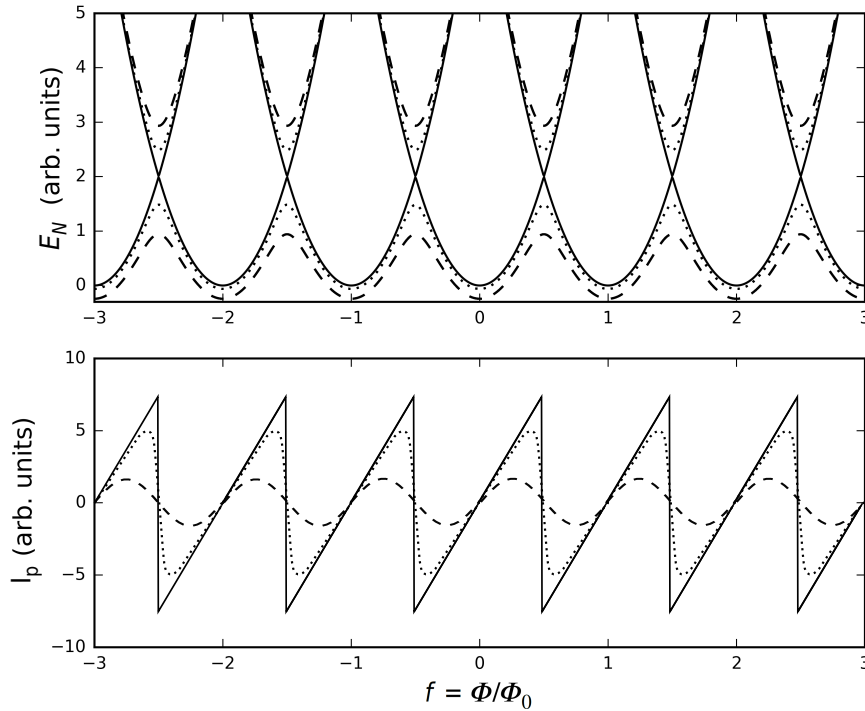


**Figure 2.10:** Energy and persistent current diagrams vs. applied frustration  $f = \Phi/\Phi_0$ . For zero phase slip amplitude, the energy spectrum  $E_N$  is given by parabolas while the persistent current  $I_p$  shows a saw-tooth like dependence on  $f$  (solid line). A small phase slip amplitude results in a lifting of the degeneracy of the energy spectrum at multiples of  $\Phi_0/2$  which leads to a rounding of the saw-tooth like dependence of the persistent current (dotted line). For large phase slip amplitude, the degeneracy is lifted even further and the persistent current shows a sinusoidal dependence on  $f$  (dashed line).

In 2012, K. Y. Arutyunov et al. observed a change in the persistent current behaviour with external flux depending on the width of the nanoring wire. The ring was connected with two Josephson junctions on opposite sides and the tunnel current through the junction-loop circuit was evaluated. Milling down the titanium nanoring in several steps changed the measured tunnel current dependence on externally applied magnetic flux from saw-tooth like for wider nanoring arms to sinusoidal for thinner ones similar to what is depicted in Fig. 2.10. This indicates that the nanorings exhibit quantum phase slip and that its amplitude is proportional to the width of the nanoring arm.

## 3. Experimental details

---

*"Two things are necessary for our work: relentless perseverance and the willingness to throw away something, in which one has invested a lot of time and effort."*

**Albert Einstein**

In Ch. 3, all information is drawn up which is necessary to understand how to experimentally realize (coherent) quantum phase slip. In Sec. 3.1, the superconducting thin film materials are discussed that are used for the experiments explained in Ch. 4. The fabrication techniques that were optimized as a major part of this work in order to obtain nanowires with dimensions deep in the sub- $\mu\text{m}$  regime are described in Sec. 3.2. Eventually, the continuous and pulsed microwave measurement methods performed at ultra-low temperatures depicted in Sec. 3.3 lead to the experimental findings.

## 3.1. Material

Indium oxide ( $\text{InO}_x$ ) thin films used in the first experiments that successfully detected coherent quantum phase slip (cQPS) behaviour [Ast+12] have the disadvantage of unstable disorder properties over time when kept at room temperature. The films degrade strongly. This makes them inappropriate for the realization of robust QPS samples. Thus, more robust superconductors have to be used and their applicability for quantum phase slip (QPS) has to be studied.

In this section, the strongly disordered superconductors are discussed which are used for the experiments throughout this thesis. Nanowires studied at Karlsruhe Institute of Technology (KIT) are made from sputter deposited granular aluminium or aluminium oxide ( $\text{AlO}_x$ ), respectively. The fabrication and characterization of these films is part of this work. Constrictions which were investigated in experiments at the Royal Holloway, University of London (RHUL), UK and the National Physical Laboratory (NPL), UK were patterned from strongly disordered niobium nitride ( $\text{NbN}$ ) thin films. These films were fabricated at the Leibniz Institute of Photonic Technology (IPHT), Jena, Germany.

### 3.1.1. Sputter deposited granular aluminium ( $\text{AlO}_x$ )

Granular aluminium ( $\text{AlO}_x$ ) films have been studied in detail already since the 1960s [ACC66; ACS67; CA68; Deu+73; Abe77; Zie+79] and are still of big interest in current research [Bac+13; Bac+15], e.g. due to their tunability towards the superconductor to insulator phase transition. Based on the granular structure,  $\text{AlO}_x$  is often referred to as *granular* aluminium or *porous* aluminium. An important parameter of such highly disordered films is their normalconducting sheet resistance which can vary between some ten  $\Omega$  to hundreds of  $\text{k}\Omega$ . Following Sec. 2.1.3, high sheet resistances mean high kinetic inductances for wires made from such films which still establish superconductivity when cooled through  $T_c$ .

While in former experimental investigations  $\text{AlO}_x$  thin films were deposited either by thermal evaporation of aluminium in an oxygen atmosphere at room temperature or post-oxidization of an porous aluminium thin film thermally evaporated on a strongly cooled substrate, in this work the  $\text{AlO}_x$  thin films are fabricated by reactive DC magnetron sputtering of pure aluminium in a slight oxygen atmosphere [Rot+17; Vos14] onto a 330 nm thick silicon substrate. In order to be able to control the sheet resistance reproducibly, the sputter chamber has to be pumped to a background pressure of  $10^{-8}$  mbar which removes all oxygen ( $\text{O}_2$ ) and water vapour from the chamber. As a non-reactive sputter gas, 35 – 40 sccm argon ( $\text{Ar}_2$ ) is introduced into the chamber (see Fig. 3.1b). Additionally, 2.5 sccm of an  $\text{Ar}_2:\text{O}_2$  mixture with a 9:1 ratio is added to provide the necessary  $\text{O}_2$ . A plasma is lit by applying a voltage between an anode and a cathode, where the latter is the

pure aluminium target. Electrons escape from the cathode, get accelerated on their way towards the anode, ionize the  $\text{Ar}_2$  atoms and create a plasma. The ions are accelerated and hit the target with a sufficient amount of energy to let Al atoms escape the metal target. On their way, they react with the  $\text{O}_2$  and eventually  $\text{AlO}_x$  is deposited on a substrate which is placed at the anode. The necessary sputter rate of 5–10 nm/min is achieved by applying a voltage of 350–400 V at a power of 100 W.

The goal was to achieve superconducting  $\text{AlO}_x$  films with normalconducting sheet resistances on the order of a few  $\text{k}\Omega$ . All  $\text{AlO}_x$  thin films used for the experiments in this thesis have a constant thickness of 20–22 nm since the sheet resistance shall not be changed by variation of the thickness. As can be seen in Fig. 3.1a, the sheet resistance is adjusted by varying either the  $\text{Ar}_2$  pressure in the chamber or the amount of  $\text{O}_2$  available for reaction [Rot+17; Vos14].

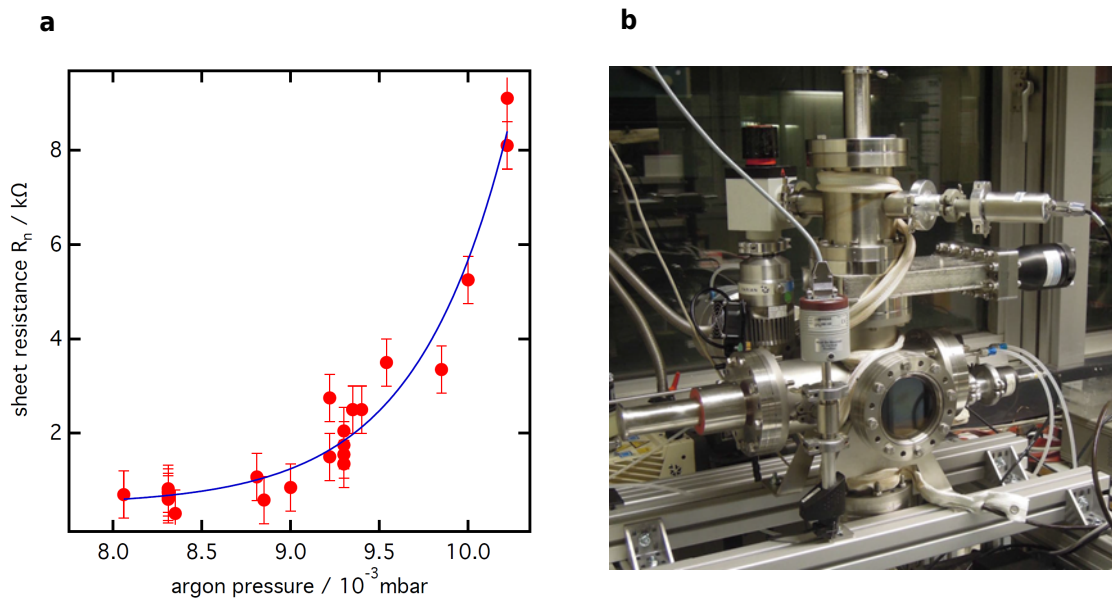


**Figure 3.1:** **a** Dependence of the  $\text{AlO}_x$  sheet resistance on the  $\text{Ar}_2$  pressure [Rot+17]. **b** Homemade sputter tool for the  $\text{AlO}_x$  deposition.

The reason for the observed exponential decrease of the sheet resistance with increasing  $\text{Ar}_2$  pressure (see Fig. 3.1) can be found by investigating the stoichiometry of the sputtered  $\text{AlO}_x$  films. As can be seen in a transmission electron microscope (TEM) image (see Fig. 3.2a), the above mentioned granularity is clearly visible. For the shown  $\text{AlO}_x$  thin film having a sheet resistance of 2  $\text{k}\Omega$ , pure aluminium grains (see Fig. 3.2b) with a diameter of 3–4 nm surrounded by an oxygen layer can be observed (see also the supplementary material of [Rot+17]). The measured grain size of the sputtered films are in good agreement with findings in [Deu+73]. Following [Deu+73], the coherence length  $\xi$  is of the order of the grain size  $\xi \approx 4$  nm. The grains can be considered as a tightly connected network of Josephson junctions. The oxide around the grain core represents the tunnel barrier. The tunnelling probability is exponentially dependent on the tunnel barrier

thickness. A higher  $O_2$  partial chamber pressure would translate into thicker oxide barriers. However, precisely adjusting the sheet resistance using the  $O_2$  flow was not possible because the flow could not be controlled at a scale necessary for this purpose. Instead, the  $O_2$  flow was kept constant and the  $Ar_2$  partial pressure was adjusted via the  $Ar_2$  flow, as can be seen in Fig. 3.1. An increase of the  $Ar_2$  partial pressure results in a reduced sputter rate because of the increased plasma density. Hence, the probability of the Al atoms to react with the  $O_2$  increases which leads to thicker oxide barriers in the film. This gives rise to the observed exponential dependence in Fig. 3.1.

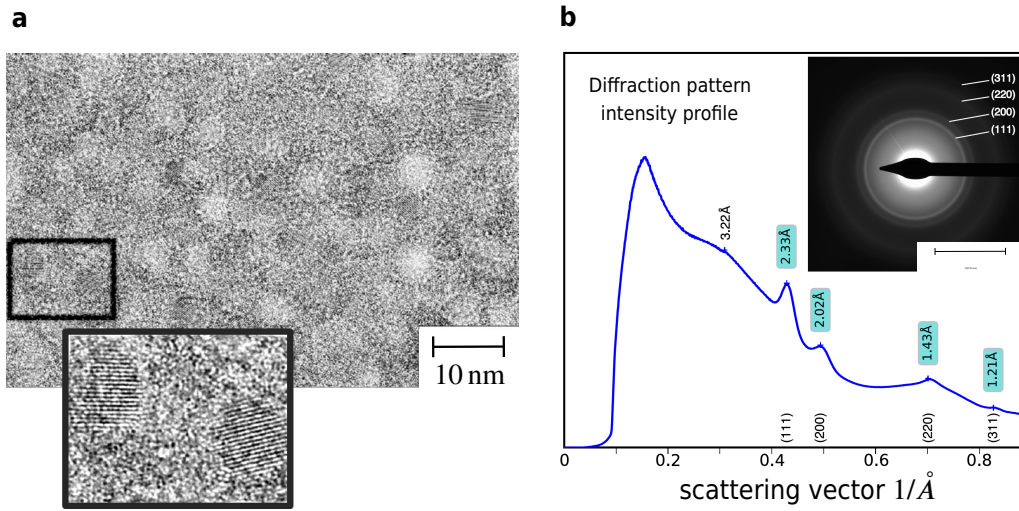


**Figure 3.2:** **a** TEM image of an  $AlO_x$  film with a thickness of 20 nm and a sheet resistance of 2  $k\Omega$ . A granular structure is visible with grains of a mean size of 3-4 nm. The inset is a zoom into the black framed rectangular in the main image. Here, the grains are clearly distinguishable. Inside the grains, aluminium atoms are lined up indicating a mono-crystalline structure surrounded by amorphous oxide. **b** Intensity profile and TEM diffraction pattern of the same film. The colourized labels mark the peaks that are in agreement with the corresponding lattice planes of the face-centred cubic lattice of bulk aluminium [Rot+17].

All  $AlO_x$  films presented in Fig. 3.1a show a superconducting transition similar to the one shown in Fig. 3.3. The superconducting transition temperature for  $AlO_x$  films with a sheet resistance of  $R_{\square} \approx 1 - 10 k\Omega$  is  $T_c \approx 1.6 - 2.0$  K, hence higher than the one of pure aluminium. The transition is broadened which is typical for a highly disordered superconductor [Rot+17; Vos14].

As mentioned in the beginning of this section, wires made from these superconducting  $AlO_x$  films exhibit high sheet kinetic inductances of 0.5–3 nH. This has been tested by fabricating superconducting microwave resonators from 20 nm thick  $AlO_x$  films with sheet resistances of 1–2  $k\Omega$ . With  $T_c \approx 1.9$  K, sheet kinetic inductances of  $L_{kin,\square} \approx 0.75 - 1.5$  nH could be expected from Eq. (2.15). The kinetic inductance of the resonators exceeded their geometric inductance by several orders of magnitude. The measured resonance frequencies of these resonators agreed well with the frequencies expected from the calculated sheet kinetic inductance values [Wil15]. Furthermore, the resonators showed high in-

intrinsic quality factors unexpected for films with such high oxide contamination [Wil15; Grü+18].

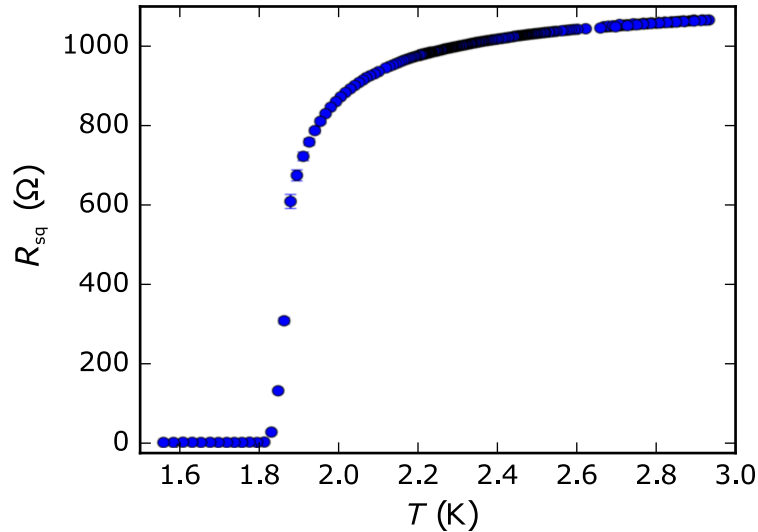


**Figure 3.3:** Broadened superconducting transition for a 22 nm thin  $\text{AlO}_x$  film [Wil15]. The sheet resistance  $R_{sq}$  is measured in a 4-probe way to remove cable resistance.

### 3.1.2. Atomic layer deposited niobium nitride (NbN)

Nanowires made from 3 – 4 nm thin niobium nitride films have already been proven to exhibit coherent quantum phase slip (cQPS) [Pel+13]. Furthermore, the material properties turned out to be stable over time. A further important aspect is the intrinsic film homogeneity. In order to ensure that thin films obtain a homogeneously disordered internal structure, NbN thin films fabricated by plasma enhanced atomic layer deposition (PEALD) were utilized in this thesis. This is in contrast to previous experiments where DC reactive magnetron sputtered NbN thin films were used [Pel+13].

In atomic layer deposition, thin films are grown on a substrate by exposing this substrate alternately with different *precursors* which are gaseous species of the material one wants to deposit. These precursors can only react with a limited amount of substrate sites resulting in a very precise control of layer growth on atomic scales. In this way, a film can be deposited nicely layer by layer.

The NbN films utilized for experiments in this thesis were deposited onto an undoped 250 nm thick silicon substrate in a standard OpAL ALD system by Oxford Instruments Plasma Technology which reaches a minimal chamber background pressure of 2 mTorr [Zie+13; Lin+17]. The system was upgraded by an ICP unit for the necessary plasma enhancement (PE) of the ALD process and by a nitrogen glove box to the open load system to reduce water contamination of the chamber. It is important to avoid oxygen and water

### 3. Experimental details

residuals in the chamber since niobium-oxygen (Nb-O) has a higher chemical binding energy than niobium-nitride (Nb-N).

As precursors for this PEALD process, the metal-organic compound (*tertbutylimido*)-*tris* (*diethylamino*)-*niobium* (TBTDEN) produced by Heraeus Precious Metals, Germany, and hydrogen in form of a plasma were chosen. One deposition cycle consists of four steps. It starts with the exposure of the substrate with TBTEN followed by a chamber purge with dry argon and nitrogen. As a third step, NbN is formed by hydrogen radicals originating from the ICP induced hydrogen plasma. In the last step, the chamber is again purged with dry argon and nitrogen. Such cycles result in a NbN growth rate of 0.046 nm/cycle [Zie+13; Lin+17]. The typical thickness of these films ranges between 3 – 80 nm and is deposited in 57 – 109 cycles. The lowest incorporation of oxygen is around 10 % within a 1:1 niobium to nitrogen composition. The films consist of NbN as well as Nb crystalline parts [Lin+17].

The deposited films exhibit sheet resistance values in the range of 0.1–5 k $\Omega$ . The thickness dependent critical temperature of these films is in the range of 4.5 – 14 K. The superconductor to insulator transition appears for films with a thickness in the range of 2.6 – 5 nm where the films start to show a transition into an insulating rather than into a superconducting state [Lin+17].

In Fig. 3.4a, the superconducting transition of a 3.3 nm NbN thin film with a sheet resistance of  $R_{sq} = 3$  k is shown.

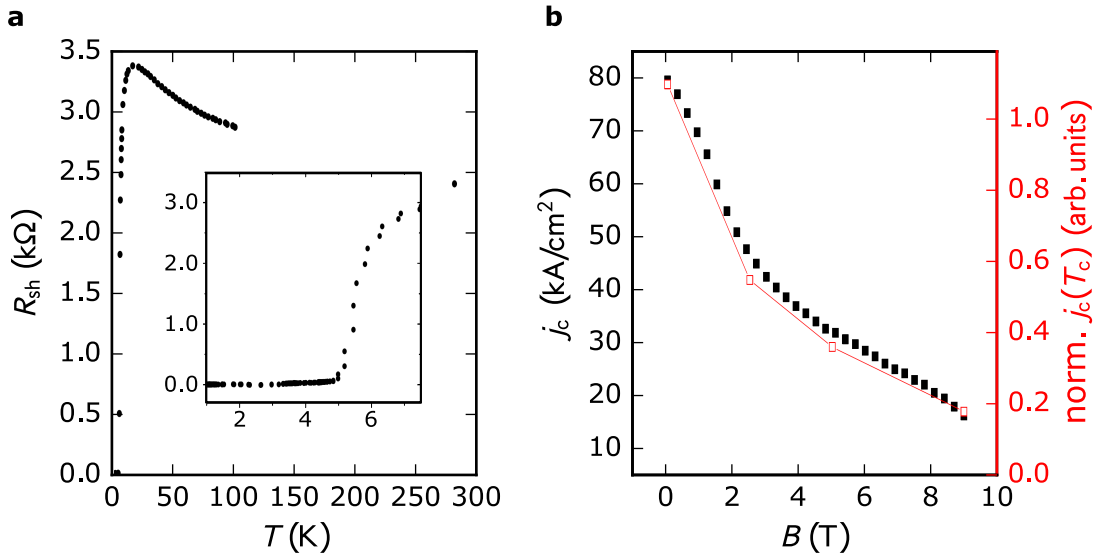


**Figure 3.4:** **a** Transport measurement of the sheet resistance versus temperature of a 3.3 nm thin NbN film. The inset shows a zoom into the low temperature region. **b** Critical current density of a 1  $\mu$ m wide wire, as a function of applied perpendicular magnetic field measured at 10 mK (solid markers) and the extracted scaling of the critical current density  $j_c(T_c)$  from measurements of  $T_c(B)$  (hollow squares and line) showing the same functional dependence (see Supplemental material of [Gra+18] for more details).

Atomic force microscopy (AFM) measurements indicate that the used NbN films have a granular structure with grain sizes on the order of 20 nm. Transport measurements (at  $T = 10$  mK) of a  $1\ \mu\text{m}$  wide structure made from a 3.3 nm thick NbN film showed a significant critical current density up to magnetic fields of 9 T (see Fig. 3.4b and Supplemental material of [Gra+18]). This suggests that the granular NbN films are homogeneous with a continuously varying, non-vanishing order parameter between the grains. Hence, the inter-grain-boundaries are strong but not formed by Josephson junctions. From the critical current measurements at high magnetic fields, a superconducting coherence length of  $\xi = 5$  nm for a 3.3 nm thin film could be extracted [Gra+18].

## 3.2. Fabrication

An important part of this thesis was to set up and optimize a fabrication method with which (quasi)one-dimensional nanowires were made from the disordered superconductors described in Sec. 3.1. The coherence lengths of these materials are on the order of  $\xi \approx 1 - 10$  nm. Following the theoretical considerations regarding the phase slip amplitude  $E_s$  in Sec. 2.2, the width of the nanowires has to be on the order of  $w \approx 10 - 50$  nm, i.e. on the order of the coherence length. Such dimensions cannot be realized by optical lithography due to its insufficient resolution. Thus, electron beam (e-beam) lithography had to be utilized for defining the nanowires followed by plasma etching techniques. The fabrication techniques presented below are nicely described and explained in literature. The reader may enquire about information in excess of the here-mentioned in [Cui16] and references therein.

### 3.2.1. Techniques

#### Optical lithography

Optical lithography or photolithography is a standard technique in semiconductor and microsystems technology. It is used to pattern structures like integrated circuits of thin films down to several tens of nanometres. The minimum feature size of an exposed line

$$d_{\min} = \frac{\lambda}{2A_N} \quad (3.1)$$

depends on the wavelength  $\lambda$  of the light source and the numerical aperture  $A_N$  of the lens. The light is shone through a photomask on a photoresist which was spun on a substrate and prebaked in advance. For the optical lithography in this thesis, the photoresist AZ@5214 E by Microchemicals GmbH is exposed by the ultraviolet light source of a MA6 maskaligner by SÜSS MicroTec. The combination of the light source with a wavelength of 400 nm and the resist with a thickness of  $d \approx 1 \mu\text{m}$  allow for a reliable minimal resolution of 1  $\mu\text{m}$ . This is fine for larger structures like on-chip ground planes or microwave feedlines having dimensions of at least a few micrometers.

In a standard positive optical exposure, the photoresist is spun with 6000 rpm for 60 s resulting in a film thickness of 1  $\mu\text{m}$ . Subsequently, the resist is baked at 115°C for 50 s before it is exposed for 7 s. All resist that was not covered by the chromium parts of the photomask is removed by the subsequent development step. The chip is immersed in the developer AZ@726 MIF by Microchemicals GmbH for 50 s, the development is stopped by placing the chip in demineralized water.

## Electron beam lithography

To obtain the minimal resolution achievable with electron beam (e-beam) lithography, several factors are crucial. Ideally, the e-beam resist can be spun on a substrate very thinly so that forward scattering of the electrons is reduced. Furthermore, minimum scattering is limited by the size of the resist molecules. For the e-beam lithography of nanowires and sub- $\mu\text{m}$  structures, the negative e-beam resist hydrogen silsesquioxane (HSQ) was utilized in this work <sup>1</sup>. HSQ is based on glassy  $\text{SiO}_2$  and its chemical formula is  $[\text{HSQ}_{3/2}]_n$  [CLR10]. It has been shown to provide all the above mentioned benefits [Nam+98a; Nam+98b; WAB03; Gri+07]. A resolution down to 10 nm can only be achieved with a suitable aspect ratio. By spinning the HSQ at 6000 rpm for 60 s, an HSQ film thickness of 50 nm can be realized. The film is baked at 150°C for 120 s before exposure.

The exposure is done in a 50 keV JEOL JBX-5500ZD e-beam machine. The width of the exposed structures is set by the exposure dose and the latter one has to be adjusted to the e-beam resist and the substrate properties because both of them affect the forward and the back scattering of the electrons. For 20 nm  $\text{AlO}_x$  films with sheet resistances of 1 – 3 k $\Omega$  on doped silicon substrates as well as for 3 – 4 nm NbN films with similar sheet resistances on undoped silicon substrates, the base dose was set to 900  $\mu\text{C}/\text{cm}^2$  <sup>2</sup>. All structures with larger linewidths than the nanowires are exposed with the base dose and a writing current of 1 nA. By applying a proximity correction, overexposure is avoided. Therefore, wider structures are defined by an area exposure which integrates maximum dose at the structure edges and a reduction of exposure dose inside the structure. This allows for sharp edges and an optimal exposure distribution.

The nanowires are defined by point exposure, i.e. single shots along a line with a step width of 4 nm with a writing current of 100 pA and much higher exposure doses. The width of the nanowire is set by factorizing the base dose. Reproducible wire widths could be achieved with the exposure values listed in Tab. 3.1

material	base dose ( $\mu\text{C}/\text{cm}^2$ )	dose multiplication factor							
$\text{AlO}_x$ / NbN	900/600	6	9	11	16	19	25	32	40
average wire width (nm $\pm$ 3 nm)		10	13	16	21	28	34	37	40

**Table 3.1:** Electron beam exposure parameters for reproducible definition of different wire widths in 50 nm HSQ on 20 nm  $\text{AlO}_x$  films on doped silicon substrate as well as 3-4 nm NbN films on undoped silicon substrate. The preparation of the HSQ is described in the text. The wire width values are averaged over many samples within an error range of  $\pm$  3 nm.

<sup>1</sup>To be precise, a 2 % HSQ version is used.

<sup>2</sup>In a second fabrication run, the base dose for the NbN samples was set to 600  $\mu\text{C}/\text{cm}^2$ , because the nanowires appeared to be 30 nm wider than expected. Comparing these nanowires, which had bias lines in close vicinity, with dose patterns with no additional structures around them, it became clear that large structures in close vicinity led to an overexposure.

After the exposure step, the HSQ is developed in AZ®726 MIF for 50 s. The solvent in AZ®726 MIF that is responsible for the removal of unexposed HSQ is tetramethylammonium hydroxide (TMAH). Since TMAH is an aluminium etchant, the  $\text{AlO}_x$  is in advance covered by a 5 nm niobium oxide ( $\text{NbO}_x$ ) layer that protects it against the etchant. For NbN, this procedure is not necessary.

## Plasma etching

Plasma etching is a dry etching technique since it abstains from the use of wet chemicals. The basic structure of a plasma etching unit is a parallel plate reactor where one electrode is grounded and the other is connected to a high frequency (HF) voltage source. For the removal of the NbN films, a modified plasma etch is utilized, namely *reactive ion etching* (RIE) in an Oxford Instruments Plasmalab 80 Plus RIE machine. For RIE, the sample to be etched is placed on the HF-coupled electrode. 2 sccm  $\text{Ar}_2$  and 20 sccm tetrafluoromethane ( $\text{CF}_4$ ) are used as reactive gas mixture. The applied HF results in positively charged  $\text{Ar}_2$  ions and  $\text{CF}_4$  chemical radicals in a plasma between the electrodes. The radicals lead to a material removal by chemical reaction while the accelerated ions etch physically with their kinetic energy. 20 s of RIE etching at a power of 210 W and a pressure of 100 mTorr is sufficient to remove the 3 – 4 nm thick NbN completely. Fluorine also etches HSQ but not as fast as the NbN and furthermore, the HSQ layer is an order of magnitude thicker than the NbN layer.

The  $\text{AlO}_x$  thin films are etched by a modified RIE technique, namely by *inductively coupled plasma etching* (ICP) in an Oxford Instruments Plasmalab 100 unit. While in a standard RIE process, the radical/ion density in the plasma and their kinetic energy are both dependent on the applied RIE power (and the gas pressure, of course), in an ICP process, the plasma density is increased via a second RF bias which is applied to an additional ICP coil. The electric field generated by this coil is perpendicular to the RIE electric field. Thus, higher densities can be achieved at the same RIE power and pressure in the chamber. The used RIE power is 100 W while the ICP power is set to 200 W. Furthermore, a different reactive gas mixture of 2 sccm  $\text{Ar}_2$  and 12 sccm pure chlorine  $\text{Cl}_2$  is used. The  $\text{Cl}_2$  has the advantage of a high selectivity between HSQ and  $\text{AlO}_x$ , i.e. it etches HSQ not even a bit. This guarantees for a homogeneous etching of a 20 nm  $\text{AlO}_x$  film within 60 s.

### 3.2.2. Procedure

In Fig. 3.5a, the deposition of the superconducting film is depicted, either  $\text{AlO}_x$  or NbN as explained in Sec. 3.2.1. Fig. 3.5b displays the e-beam lithographic step. In Fig. 3.6, the subsequent steps are presented including etching and optical lithography. The figure is divided into two columns, since the order of these steps is different for  $\text{AlO}_x$  (left) and NbN (right) samples.

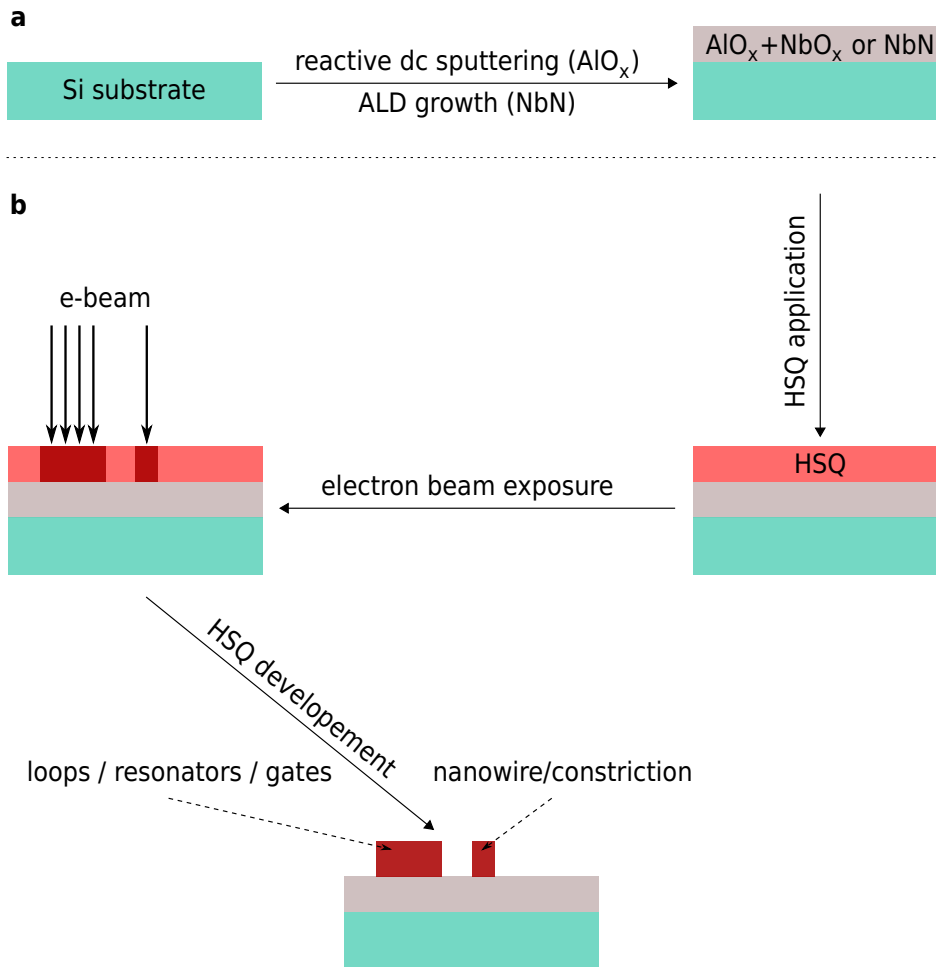


**Figure 3.5:** **a** Deposition of the strongly disordered superconducting film; either a 20 nm thick  $\text{AlO}_x$  film is deposited on a silicon (Si) substrate by reactive dc magnetron sputtering or a 3-4 nm thick NbN film by atomic layer (ALD) growth. The  $\text{AlO}_x$  film is covered by a 5 nm thick  $\text{NbO}_x$  passivation layer to protect it from the developer. **b** Application and patterning of the 50 nm thick negative electron beam (e-beam) resist hydrogen silsesquioxane (HSQ). As depicted, nanowires and constrictions are exposed in a different way than bigger structures like loops, resonators or gates (see text for more details).

### 3. Experimental details

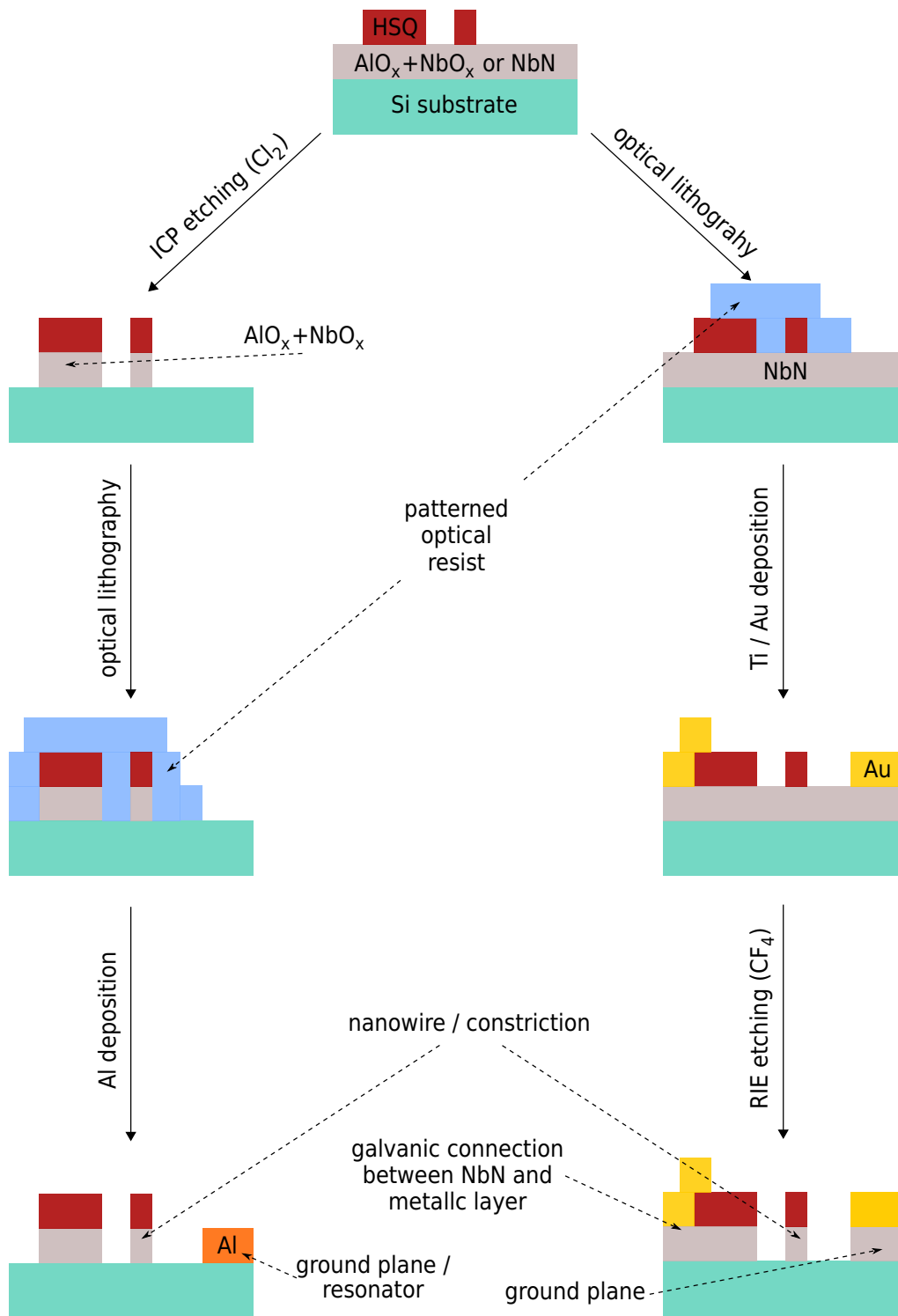


**Figure 3.6:** Fabrication scheme after the steps shown in Fig. 3.5. Left column for  $\text{AlO}_x$  samples and right column for NbN samples. Overall steps are the same but happen in a different order.

### 3.2.3. Results

Here, the results of the fabrication steps described in Sec. 3.2.2 are presented. In Fig. 3.7, structures fabricated from a 20 nm thick  $\text{AlO}_x$  film are shown. The left upper picture shows a loop with embedded 20 nm wide nanowire that is made with the  $\text{Cl}_2$  based ICP etch process. The loop arm is 1  $\mu\text{m}$  wide and exhibits sharp edges. This indicates good process parameters for the electron beam writing as well as for the etch process. In the right upper corner, the sample is presented in a lateral view in order to illustrate the layer composition of 50 nm HSQ (blue), 5 nm  $\text{NbO}_x$  + 20 nm  $\text{AlO}_x$  (red) and 50 nm silicon (green). The silicon pedestal on the bottom results from a slight over-etching due to the much higher etch rate of silicon in comparison to  $\text{AlO}_x$ .

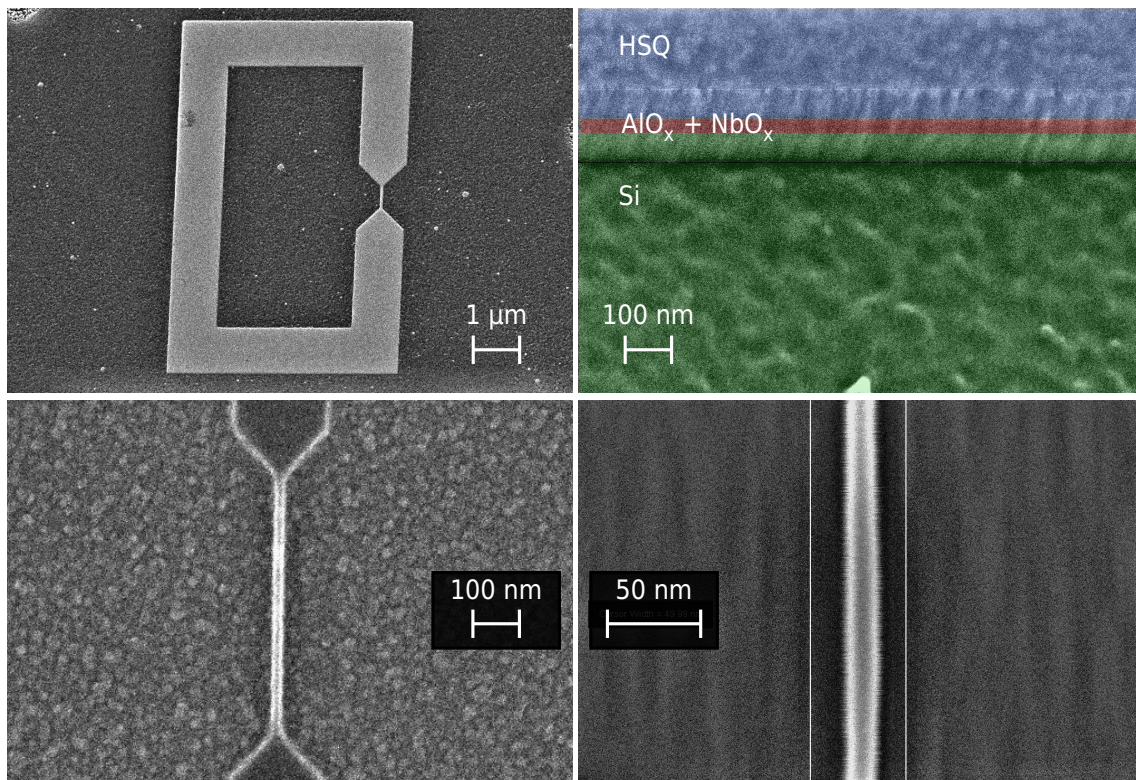


**Figure 3.7:**  $\text{AlO}_x$  sample etched with the  $\text{Cl}_2$  based ICP etch process. *Left top* Loop with nanowire. *Right top* Lateral profile of an etched stack of 50 nm HSQ (blue), 5 nm  $\text{NbO}_x$  + 20 nm  $\text{AlO}_x$  (red) and 50 nm silicon (green). *Left bottom* 500 nm long and 20 nm wide nanowire with triangular connection to the loop. *Right bottom* Zoom onto the 20 nm wide nanowire.

In the bottom left of Fig. 3.7, a homogeneous 500 nm long and 20 nm wide nanowire is shown with a zoom onto it in the bottom right corner. Such samples can be fabricated reproducibly with the steps described above.

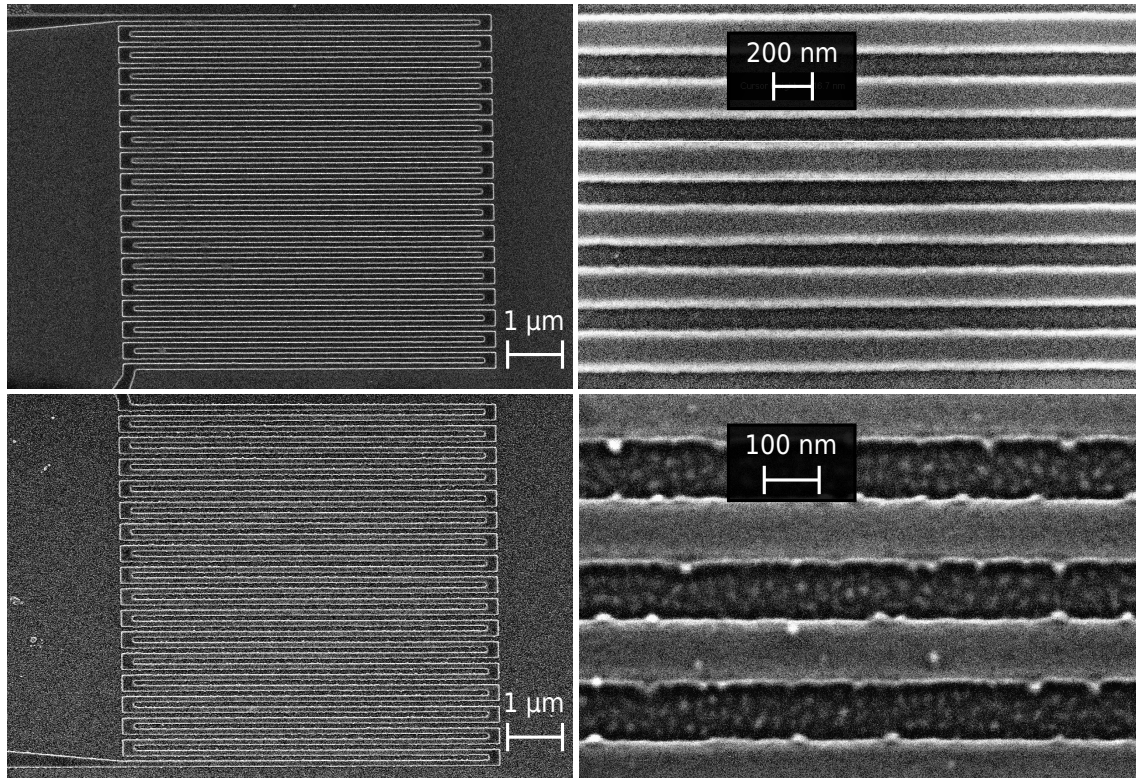


**Figure 3.8:** Comparison of different etch processes with a NbN sample. The different shades of grey represent areas with different electrical conductivity. *Left pictures* showing long meander with 100 nm wide wire arms and equal spacings in between. In the *right pictures* a zoom in is shown. The *upper row* represents the  $\text{Cl}_2$  based ICP etch process, while the *lower row* is the  $\text{CF}_4$  based RIE process. In particular in the zoomed pictures, one can see that the  $\text{CF}_4$  based RIE process results in rougher edges than the  $\text{Cl}_2$  based ICP etch process. The  $\text{CF}_4$  based RIE process attacks silicon which leads to the white dots.

In Fig. 3.8, structures fabricated from a 3 – 4 nm thick NbN film are presented. The upper row shows a meander with 100 nm wide wire arms and equal spacings in between which were etched by the  $\text{Cl}_2$  based ICP etch process. The bottom row shows the same structure but etched with the  $\text{CF}_4$  based RIE process. All structures look nice; in particular the equal wire arm and spacing width indicate correct electron beam doses. At a closer look, the  $\text{CF}_4$  RIE etched samples (bottom) seem to have rougher edges than the  $\text{Cl}_2$  ICP etched ones. This explained by the fact that HSQ is rather inert against  $\text{Cl}_2$  while it is etched by  $\text{CF}_4$ . However, both etching techniques work out and result in working samples.

Fig. 3.7 and Fig. 3.8 illustrate that the optimized etching techniques presented in Sec. 3.2.1 are suitable for the fabrication of nanowires with widths on the 20 nm scale from highly disordered superconducting thin films.

### 3.3. Experimental setup

In this section, the whole experimental apparatus is described which is used to perform the necessary measurements for this thesis. It is crucial to maintain the experiment at ultra-low temperatures. The techniques for this purpose are discussed in Sec. 3.3.1. Microwave measurements are the core techniques for superconducting circuit QED experiments and they resort to common methods developed and used in high-frequency technology. The setup for experiments with continuously applied wave signals is described in Sec. 3.3.2, followed by the explanation of the apparatus used for pulsed microwave signals in Sec. 3.3.3.

#### 3.3.1. Ultra-low temperature cryostats

The experiments within this PhD project have to be performed at ultra-low temperatures for various reasons. For quantum phase slip to happen, the temperature of the system has to be much lower than the transition temperature of the used superconducting films. This ensures that the experiments are not affected by thermally activated phase slips or even more general by thermally activated fluctuations of the whole superconducting circuit. Even more importantly, the frequency regime of the experiments is at a few GHz. To avoid thermal excitations at these frequencies, the system has to be maintained well below 100 mK. Possible cooling techniques for this purpose have been intensively studied since the 1950s and are well documented in literature. Details in excess of the here given can be found in [EH05] and in references therein.

A standard apparatus to reach and maintain such temperatures is a *dilution refrigerator* (DR) consisting of an outer part that is cooled to around 4 K which is used as a pre-cooling system for the inner part in which a mixture of the helium isotopes  $^4\text{He}/^3\text{He}$  is cycled to reach temperatures on the order of 10 mK. The outer part can be realized as *wet* type cooled by a liquid  $^4\text{He}$  bath. This bath also acts as a thermal shield protecting the inner part from external thermal radiation. Although the liquid  $^4\text{He}$  bath is shielded by a surrounding liquid nitrogen ( $\text{N}_2$ ) bath having a temperature of 77 K, evaporation of liquid  $^4\text{He}$  happens due to several reasons. Thus, the  $^4\text{He}$  has to be refilled. The same applies for the liquid  $\text{N}_2$  bath although it is surrounded by a vacuum shield.

Instead of an open system that needs cryogenic liquids to be refilled, a second closed cycle technique has been developed, namely the *pulse-tube cooler* or briefly pulse-tube (PT). The cooling effect originates from a periodic pressure variation applied to  $^4\text{He}$  by a compressor and from a displacement of the  $^4\text{He}$  in the PT. Heat can be extracted via a heat exchanging mechanism. Thus, a PT can reach temperatures of around 4 K and replaces the use of liquid  $^4\text{He}$  and  $\text{N}_2$  baths. Therefore, it is referred to as *dry* type cooler.

The inner dilution unit is a closed system that exploits the fact that a  $^4\text{He}/^3\text{He}$  mixture

undergoes a phase separation at very low temperatures<sup>3</sup>. This takes place in the so-called *mixing chamber* (MC) where a light  $^3\text{He}$  rich phase separates from a heavy  $^4\text{He}$  phase with a small amount of  $^3\text{He}$  diluted in it. Between the 4 K stage and the MC, a standard DR has a *still* and a counter flow heat exchanger. The mixture is circulated by pumping on the still. In the still, one finds  $^3\text{He}$  vapor atop a dilute  $^3\text{He}$  phase.  $^3\text{He}$  of that vapor is circulated through some cleaning traps, a condenser and the heat exchanger back into the upper light  $^3\text{He}$  rich phase in the MC. Depending on pressure and temperature,  $^3\text{He}$  dissolves then into the  $^4\text{He}$  phase. A tube from this lower phase in the MC connects it with the heat exchanger and the still closing the circle. The pumping on the still causes evaporation of mainly  $^3\text{He}$  out of the  $^4\text{He}$  phase which extracts thermal energy from the MC and leads to cooling. The cold  $^3\text{He}$  coming from the MC exchanges energy with the  $^3\text{He}$  going to the MC in the other line in the heat exchanger before entering the still. In the experiments described in Ch. 4, mainly dry, pulse-tube dilution refrigerators of type LD-400 by BlueFors cryogenics were used.

#### 3.3.2. Microwave measurement setup

A typical measurement setup which is used to perform microwave measurements in the lower GHz regime at ultra-low temperatures is shown in Fig. 3.9.

A *vector network analyzer* (VNA) sends a microwave signal via a coaxial line from port 1 through a directional coupler into a dilution refrigerator (DR). Inside the DR, the signal is damped via attenuators which are electrical elements in which a resistor is placed between inner and outer conductor. This resistive connection leads to a partial dissipation of the microwave signal power as well as to an extraction of thermal energy from the inner conductor. The attenuators connect the inner conductor with the cryostat at the 4 K stage as well as at the still and the mixing chamber (MC) (see Fig. 3.9). The dissipation of electrical power is needed since all measurements have to be performed at ultra-low power levels down to single photon microwave powers. The microwave coaxial cables are made from stainless steel that add some more frequency-dependent attenuation and provide sufficient thermal isolation between the various temperature stages due to its low temperature conduction. Subsequently, the microwave signal which travels from the VNA through this attenuated and thermalized line is directed through the experimental sample which is mounted inside a closed sample box that is thermalized at the MC stage. This ensures that the experiment is stabilized at ultra-low temperatures and protected from surrounding electromagnetic as well as thermal radiation. Furthermore, a combination of lead (Pb) and permalloy shields cover the sample box in order to protect it from stray magnetic fields. Additionally, the sample holder is equipped with a superconducting coil which allows one to apply a global magnetic field perpendicular to the sample.

---

<sup>3</sup>In such a mixture, the typical amount of  $^3\text{He}$  in  $^4\text{He}$  is on the order of 6%.

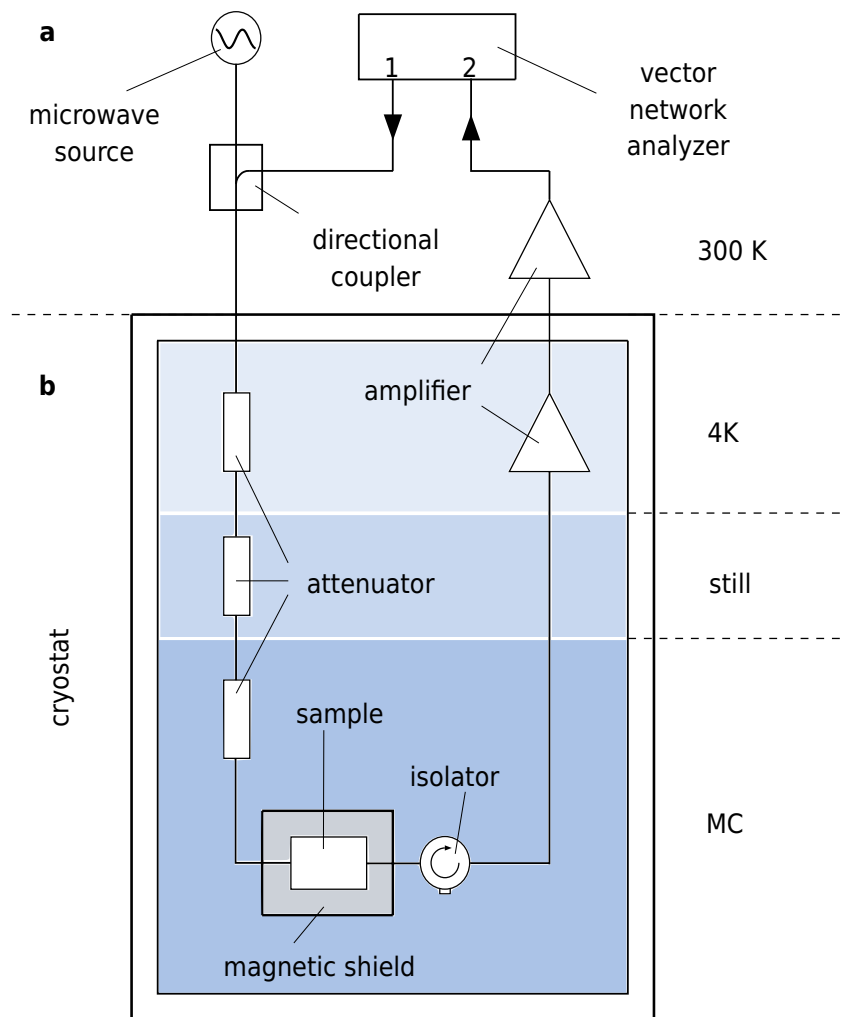


**Figure 3.9:** Ultra-low temperature continuous microwave measurement setup. **a** Room temperature part outside the cryostat where signals of a vector network analyser (VNA) and a microwave source are combined by a directional coupler and send into the cryostat on the ingoing signal line. On the line outgoing from the cryostat, the signal is amplified before it returns to the VNA. **b** Microwave setup part inside the cryostat. At the 4 K stage, the microwave signal is attenuated when entering and amplified before leaving the cryostat. The signal is further attenuated at the still and at the mixing chamber (MC) before reaching the sample. The sample has an additional magnetic shield. After the sample, the signal passes an isolator before reaching the amplifier at 4 K.

After interfering with the experiment, the microwave signal passes a microwave isolator and a superconducting coaxial cable before it is amplified by a low-temperature amplifier at 4 K<sup>4</sup>. The isolator allows the signal coming from the sample to pass while microwaves reflected from as well as thermal fluctuations coming from the amplifier are dissipated before reaching the sample. The superconducting cable leaves the signal un-attenuated and

<sup>4</sup>Typically, a so-called *hot electron mobility transistor* (HEMT) amplifier is used.

### 3. *Experimental details*

---

helps to thermally isolate the MC from the 4 K stage by utilizing the vanishing thermal conduction of superconductors. Amplification at low temperatures results in an increase of the signal amplitude before thermal noise is added at higher temperatures. The amplified signal travels from the amplifier through a coaxial cable made from stainless steel to the outgoing port of the dilution refrigerator. Again, the stainless steel leads to a sufficient thermal isolation of the 4 K stage from the room temperature port. At room temperature the signal gets further amplified by room temperature amplifiers before reaching port 2 of the VNA. The VNA evaluates the  $S_{21}$  signal (see Eq. (2.70)) transmitted from port 1 to port 2 which was described in Sec. 2.4.2. Each element is electrically matched to an impedance of  $50 \Omega$  which avoids loss of the signal by reflections at the connections.

In order to send additional microwave signals to the experimental chip, a microwave source is connected to the second port of the directional coupler mentioned in the beginning. This coupler provides a mixing of VNA and additional signals towards the sample but acts as a protection for the outgoing port 1 of the VNA from possible originating from the microwave source. For the experiments described in Ch. 4, different devices like amplifiers, attenuators or circulators are used. More details on these devices are presented in Tab. 3.2.

Device	KIT	RHUL	NPL
Network analyzer	Keysight <sup>®</sup> N5241 PNA-X 100 kHz – 13.56 GHz	Rohde&Schwarz <sup>®</sup> R&S ZNB20 9 kHz – 20 GHz	Rohde&Schwarz <sup>®</sup> R&S ZNB20 9 kHz – 20 GHz
Microwave source	Agilent <sup>®</sup> E8257D 250 kHz – 20 GHz	Rohde&Schwarz <sup>®</sup> R&S SMB100A 100 kHz – 20 GHz	Rohde&Schwarz <sup>®</sup> R&S SMB100A 100 kHz – 20 GHz
Directional coupler/ power combiner	Marki <sup>®</sup> C20-0R520 500 MHz – 20 GHz	Anritsu <sup>®</sup> K240C DC–20 GHz	1/16 resistive divider
Attenuators	Inmet <sup>®</sup> 18AH-20	Bluefors <sup>®</sup>	XMA <sup>®</sup> cryo
300 K	0 – 60 dB	0 – 40 dB	20 dB
4 K	20 dB	-	10 dB
still	20 dB	20 dB	20 dB
20 mK	20 dB		
Magnet	Homemade 500 turns 11.5 mT/A	Homemade 4000 turns 150.0 mT/A	Homemade 2000 turns 75.0 mT/A
Circulator/ isolator	Quinstar <sup>®</sup> QCY-060400CM00 4 – 8 GHz	Quinstar <sup>®</sup> QCI-080800XM00 4 – 20 GHz	2x Quinstar <sup>®</sup> QCI-080800XM00 4 – 20 GHz
Amplifiers	Low noise factory <sup>®</sup> LNF-LNC 1-12A 1 – 12 GHz	Low noise factory <sup>®</sup> LNF-LNC 1-12A 1 – 12 GHz	Low noise factory <sup>®</sup> LNF-LNC 1-12A 1 – 12 GHz
4 K			
300 K	2x Minicircuits <sup>®</sup> ZVA-213 S+ 800 MHz – 20 GHz	Low noise factory <sup>®</sup> LNF-LNR 1-15A 1 – 15 GHz	2x AtlantecRF <sup>®</sup> AOX-010120 1 – 12 GHz
Cryostat	Bluefors <sup>®</sup> LD400 20 mK	Bluefors <sup>®</sup> LD400 12 mK	Bluefors <sup>®</sup> LD400 15 mK

**Table 3.2:** List of different setups with all components used at Karlsruhe Institute of Technology (KIT), Royal Holloway, University of London (RHUL) and National Physical Laboratory (NPL).

### 3.3.3. Time domain setup

The setup presented in Sec. 3.3.2 evaluates microwave signals that are continuously sent from the VNA and the microwave source (see Fig. 3.9). However, for cQED measurements like Rabi oscillations or lifetime measurements as described in Sec. 2.4, it is necessary to send single microwave pulses for readout and drive of the experiment that need certain timings and synchronization. While the microwave setup inside the dilution refrigerator stays the same, the room temperature setup consisting of VNA and microwave source has to be replaced by the setup shown in Fig. 3.10.

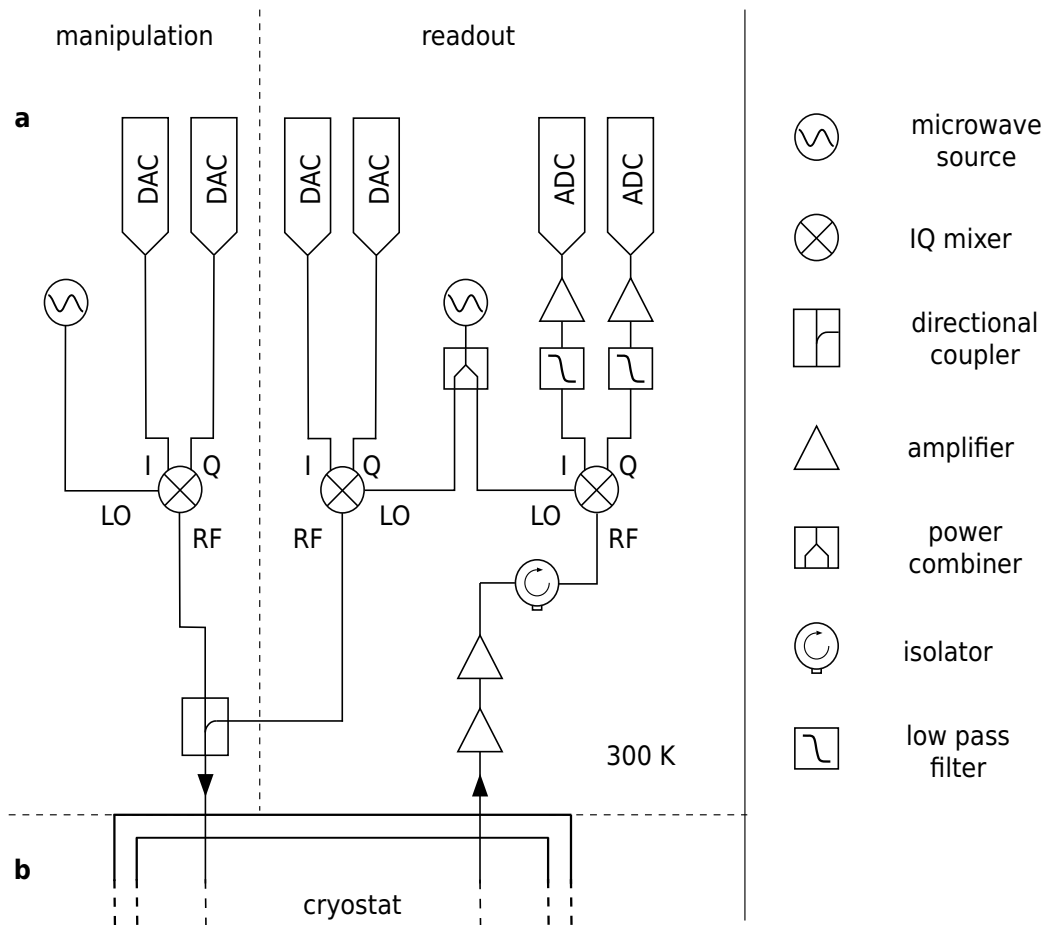


**Figure 3.10:** Pulsed microwave measurement setup with a legend of components on the right side. **a** Room temperature part outside the cryostat. A fast digital-to-analog converter (DAC) produces the manipulation signal that is combined with the readout pulse on the ingoing line while the outgoing line is downmixed and detected by a fast analog-to-digital converter card (ADC). **b** The part inside the cryostat is identical to Fig. 3.9b.

For the read out of the sample, the VNA is replaced by a microwave source here referred to as local oscillator (LO) whose signal is split into two tones by a power divider (PD). An IQ mixer subsequently modulates one part of the LO signal with the output of a fast

digital-to-analog converter (DAC). This provides the envelopes for the microwave signal. This signal is then amplified/attenuated to adjust to the necessary power level. This signal is combined via a directional coupler with a manipulation signal sequence that is generated by an arbitrary waveform generator (AWG) that switches a second microwave source via a second IQ mixer. The resulting signal is then fed into the cryostat. The second readout signal coming from the IQ mixer is mixed with the signal coming out of the cryostat which has been amplified before by two room temperature amplifiers. This results in I and Q signals with noise and RF signal leakage reduced by a low pass filter. Further amplification is added before the resulting signals are detected by an analog-to-digital converter (ADC) card.

Device	Model
Microwave source	Anritsu <sup>®</sup> MG3692C 2 – 20 GHz
Digital-to-analog converter (DAC)	Tabor Electronics <sup>®</sup> AWG WX2184C 10 kHz – 1 GHz
Analog-to-digital converter (ADC)	Spectrum <sup>®</sup> M41
IQ mixers	Marki <sup>®</sup> ML IQ0318L 3 – 18 GHz Marki <sup>®</sup> ML IQ0416L 4 – 16 GHz
Directional coupler	Marki <sup>®</sup> C20-0R520 0.5 – 20 GHz
Amplifiers	MiniCircuits <sup>®</sup> ZVA-183-S+ 0.7 – 18 GHz MiniCircuits <sup>®</sup> ZFL-1000H 10 MHz – 1 GHz
Power combiner	MiniCircuits <sup>®</sup> ZFRSC-123-S+ DC – 1 GHz
Isolator	Pasternack <sup>®</sup> PE8402 4 – 8 GHz
Low pass filter	MiniCircuits <sup>®</sup> SBLP-117+ DC – 65 MHz

**Table 3.3:** Components of the time domain setup for pulsed microwave measurements as shown in Fig. 3.10 used at KIT.

### *3. Experimental details*

---

It is necessary to synchronize output and input signals with a pulse generator that defines the repetition time between consecutive pulses as well as starts the AWG output on its trigger 1. The output of the DACs for the readout and the recording of the ADC card is started by the second trigger of the pulse generator. In order to ensure for phase and frequency stability, all mentioned devices are connected to a 10 MHz reference source. Variations of pulse lengths and distances that have to be executed during the pulse measurements lead to different waveforms in the AWG that have to be stored in the AWG prior to the measurement. All utilized components of the time domain setup are listed in Tab. 3.3.

## 4. Results

---

*"A scientist in his laboratory is not a mere technician: he is also a child confronting natural phenomena that impress him as though they were fairy tales."*

**Marie Skłodowska Curie**

In Ch. 4, the experiments are described which are based on the theories explained in Ch. 2 and realized with techniques that were explained in Ch. 3.

In Sec. 4.1, an experiment with a nanowire made from superconducting  $\text{AlO}_x$  is described. The nanowire is embedded into a superconducting loop. In Sec. 4.2, a similar system made from superconducting  $\text{NbN}$  is investigated. After understanding a system with a single nanowire in Sec. 4.2, the interference of two such nanowires is explored in Sec. 4.3.

## 4.1. Capacitively coupled nanowire loop with large inductance

In the following experiment, a nanowire is embedded into a loop with large kinetic inductance. The whole device is fabricated from an  $\text{AlO}_x$  thin film. The complete fabrication cycle is listed in A.1.1. The measurements were performed at the Physikalische Institut at the KIT.

The used superconducting  $\text{AlO}_x$  thin film is 20 nm thick and was deposited by the sputter technique outlined in Sec. 3.1.1. The film shows a superconducting transition at 1.8 K with a sheet resistance of  $\sim 1.0 \text{ k}\Omega$ . This stems from a strongly disordered superconducting film.

Referring to Eq. (2.15), the sheet kinetic inductance is

$$L_{\text{kin},\square} = 0.18 \frac{\hbar}{k_B} \cdot \frac{1.0 \text{ k}\Omega}{1.8 \text{ K}} = 0.758 \cdot 10^{-9} \text{ H} = 0.758 \text{ nH}. \quad (4.1)$$

The conclusion derived from preceding experiments where DC transport measurements on arrays of parallel  $\text{AlO}_x$  nanowires were performed [Pfi14] is that the critical current of 20–30 nm wide nanowires made from a film as described above is on the order of 100 nA. In the experiment presented in the following, it had to be ensured that the current flowing through the nanowire is much smaller than its critical current. Since a loop geometry is used into which the nanowire is embedded, this can be reached by increasing the total loop inductance which scales anti-proportionally with the persistent current  $I_p = \Phi_0/(2L_{\text{tot}})$  in the loop driven by an external magnetic field.

### 4.1.1. Sample design and setup

The aim to increase the total loop inductance and decrease the persistent current, respectively to  $L_{\text{tot}} \approx 100 \text{ nH}$  and  $I_p \approx 10 \text{ nA}$  is achieved by a loop with area  $A_{\text{loop}} = 10.4 \times 20.4 \mu\text{m}^2$  and a loop wire width of 400 nm (highlighted in blue in Fig. 4.1b) made from an  $\text{AlO}_x$  thin film. In this loop, a 250 nm long and 20 nm wide nanowire is embedded (highlighted in blue in Fig. 4.1c).

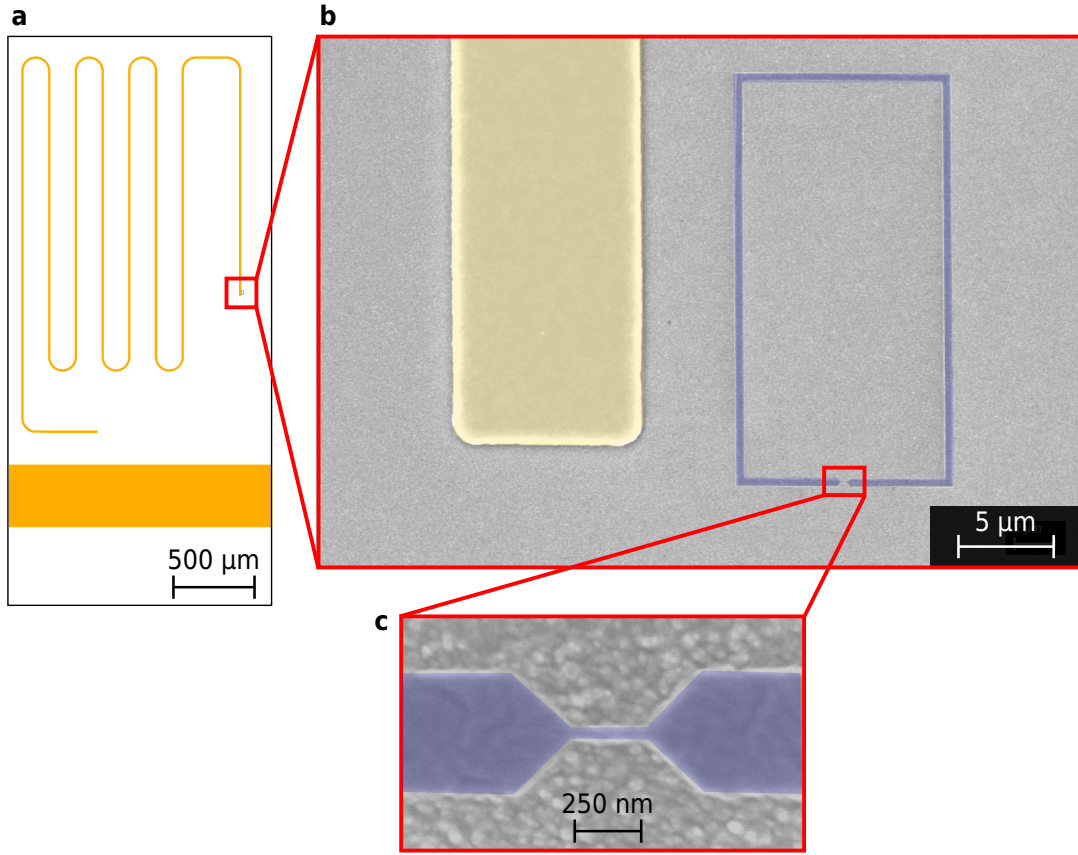


**Figure 4.1:** **a** Design sketch to scale of the meandered microstrip resonator coupled to the microwave feedline (horizontal) with a loop capacitively coupled to the end of the resonator. **b** SEM picture showing the end of the resonator (coloured in yellow) and the loop (coloured in blue). The loop contains a 250 nm long and 20 nm wide wire at the bottom. **c** Zoom onto the nanowire area (coloured in blue).

With the aforementioned  $\text{AlO}_x$  thin film parameters, the loop has a sheet kinetic inductance of  $L_{\text{kin},\square} = 0.758 \text{ nH}$ . Given a total number of squares  $N_{\text{tot}} = N_{\text{loop}} + N_{\text{wire}} = 152.4 + 12.5 = 164.9$ , which is the sum of squares of loop and nanowire, the total loop has a kinetic inductance of  $L_{\text{tot}} = 125 \text{ nH}$ . A simulation of the geometric inductance of the total loop performed with *femm* gives a  $L_{\text{geom}} = 56.4 \text{ pH}$ . Hence, the total loop inductance is dominated by the kinetic inductance and the geometric inductance can be neglected. In this loop, the persistent current is reduced to  $I_p = \Phi_0 / (2L_{\text{tot}}) = 8.27 \text{ nA}$ . This is far below the depairing current of the loop which is determined by the depairing current in the nanowire, the loop's weakest spot. However, this reduction holds a drawback for the coupling of the loop to a microwave readout resonator. The magnetic dipole moment created by the persistent current in the loop is very small which makes it difficult to couple the loop inductively (or galvanically) to the magnetic field mode (or the current mode) of a superconducting resonator. On the other side, the large total loop inductance determines

the loop impedance given by the inductive reactance

$$Z \approx |X_L| = |\omega L_{\text{tot}}| = 4.70 \text{ k}\Omega, \quad (4.2)$$

for a designed resonator frequency of 6 GHz. Due to such a high impedance, it becomes feasible to couple the loop capacitively to the electric field mode of a distributed microwave resonator. This can be seen in Fig. 4.1. The loop-wire circuit (highlighted in blue in Fig. 4.1b) is capacitively coupled to the end of a superconducting  $\lambda/2$  microstrip resonator (highlighted in yellow in Fig. 4.1b). On the other end, the resonator is capacitively coupled to a microstrip feedline through which transmission is measured.

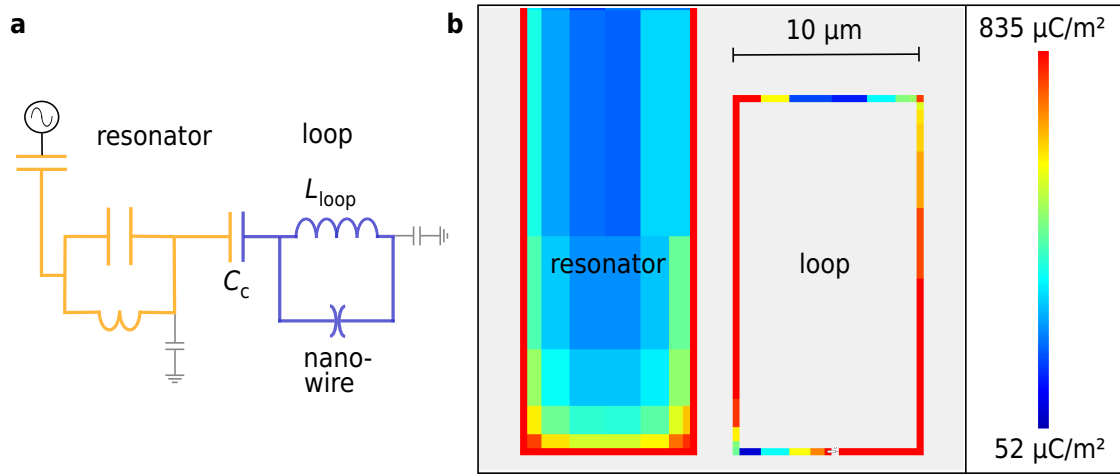


**Figure 4.2:** **a** Electrical equivalent circuit of the experiment containing the resonator (yellow) and the loop with embedded nanowire (blue). **b** Simulated charge distribution of the the end of the resonator and the loop at the resonator frequency. The simulation was performed with Sonnet<sup>®</sup>.

The electrical equivalent circuit of the experiment is given in Fig. 4.2a. Resonator and feedline are fabricated from an 80 nm thick aluminium film. A microstrip design is utilized for the resonator. This avoids a large coplanar ground plane close to the loop<sup>1</sup> which inheres electric field or charge fluctuations which might disturb the loop-resonator system. Due to its large impedance, the loop has a self-capacitance that can be evaluated to be around 0.5 fF. This leads to a charge separation in the loop induced by the AC electric field of the resonator which can be seen in Fig. 4.2b. It shows the charge distribution at the end of the resonator and in the loop simulated with Sonnet<sup>®</sup>. The loop represents an electric dipole to which the resonator electric field mode can capacitively couple.

As can be seen in Fig. 4.3a, the experimental chip is glued (with conducting silver paste) to a copper plated microwave printed circuit board (PCB)<sup>2</sup> with structured CPW feedlines through which the microwave transmission signal is provided to the experiment.

<sup>1</sup>The ground plane would be essential in a CPW design in order to get a  $50 \Omega$  matching to the environment.

<sup>2</sup>The PCB material is TMM<sup>®</sup>10i by Rogers Corporation.

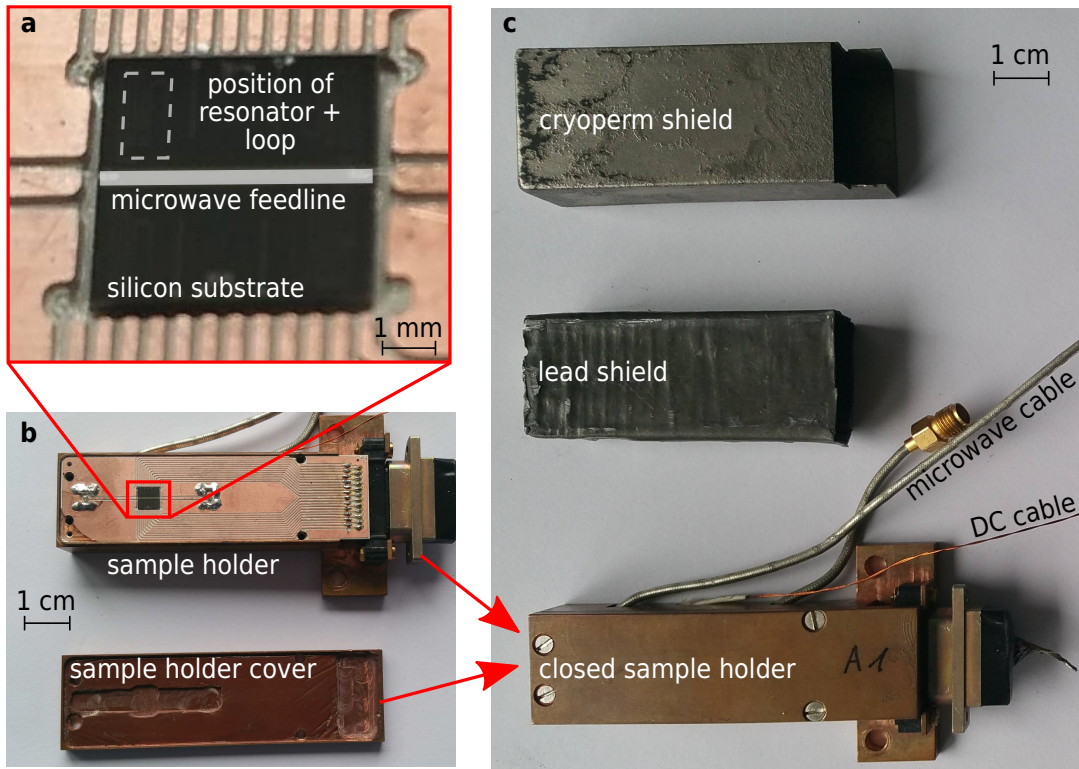


**Figure 4.3:** **a** Photograph of the silicon chip which contains the experiment (see dashed rectangle) shown in Fig. 4.1. In the centre, the aluminium microwave feedline is highlighted. The chip is glued onto the copper plated PCB. At left and right side, the feedline is bonded to the copper CPW microwave feedline of the PCB. DC lines at top and bottom were not used in the experiment. **b** The PCB is fixed on the rectangular copper sample holder (*top*). After mounting the PCB, the sample holder is closed with a copper cover (*bottom*). **c** The closed sampleholder (*bottom*) with SMA microwave and DC cables is subsequently covered by a lead shield (*mid*) and a cryoperm shield (*top*) in order to protect the experiment from stray magnetic fields.

The PCB is mounted to a copper sample holder (see Fig. 4.3**b**). This holder exhibits a homemade coil with 500 windings made from superconducting niobium-titanium wire. The perpendicular magnetic field at the place of the sample provided by this coil has been measured to 11.5 mT/A. It can be used to tune the persistent current in the loop. The sample holder is closed by a copper cover (see Fig. 4.3**b**) to avoid microwave radiation loss and it is placed into a lead (Pb) and a cryoperm shield (see Fig. 4.3**c**) to protect it from stray magnetic fields (see Fig. 4.3**c**). The shielded sample holder is mounted to the mixing chamber of a dilution refrigerator providing a temperature of  $T = 20$  mK. The sample holder is wired as shown in Fig. 3.9, with the components listed in column "KIT" in Tab. 3.2.

### 4.1.2. Microwave transmission spectroscopy

Measuring a microwave signal transmitted through the sample, the resonator shows a resonance dip at a frequency  $f_{\text{res}} = 6.22$  GHz as can be seen in Fig. 4.4.

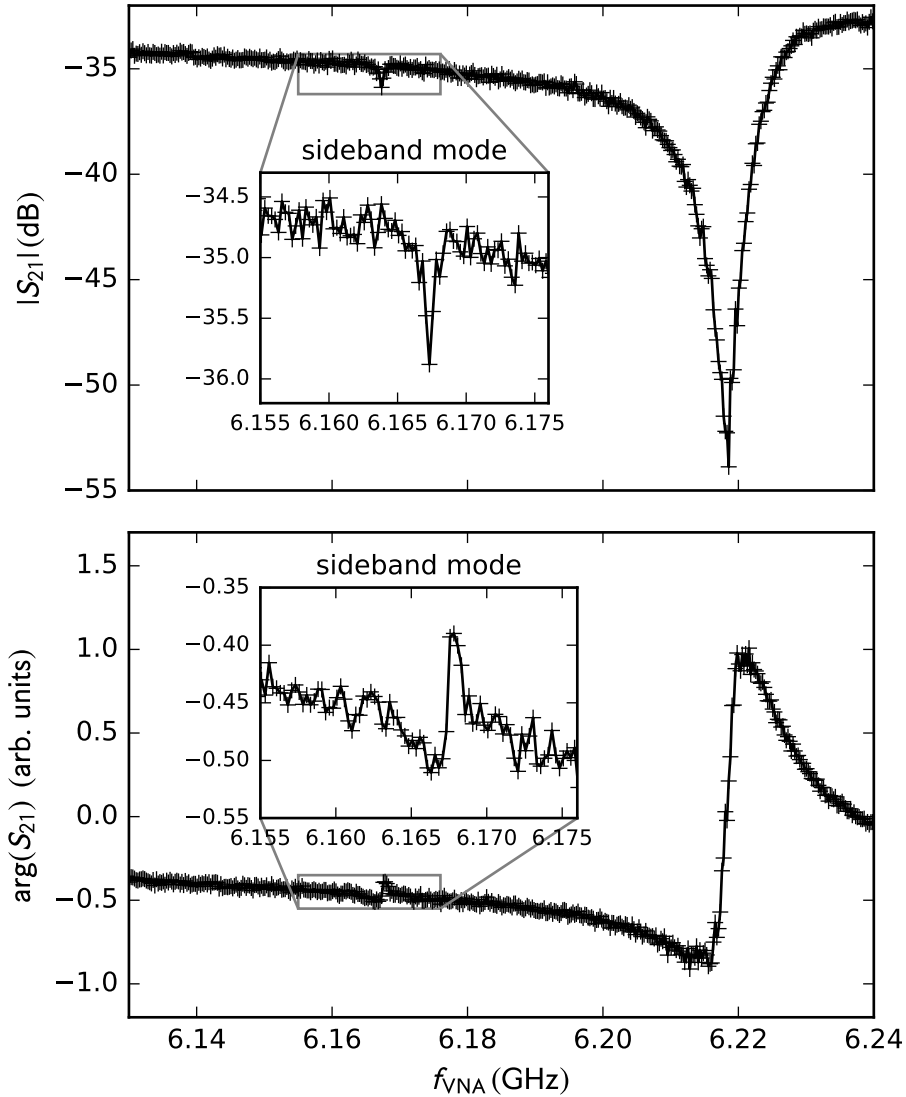


**Figure 4.4:** Transmission amplitude  $|S_{21}|$  (top) and phase  $\arg(S_{21})$  (bottom) signal plotted versus readout frequency of the VNA. The spectrum is measured at -115 dBm and 20 mK. A large resonance at 6.22 GHz is observed as well as a small one at 6.17 GHz. insets Zooms onto the small resonance which is a sideband mode of resonator and loop (see text).

At resonance, the resonator absorbs energy from the feedline which leads to a dip in the transmission spectrum. The resonator has a loaded quality factor  $Q_1 \approx 600$ . Furthermore,

a weaker resonance dip can be observed at 6.17 GHz (see Fig. 4.4 inset). Simulations showed that the loop's inductance and self-capacitance result in a loop self-resonance mode (see also [Vos17]). Together with the resonator mode, this self resonance mode creates a frequency sideband mode at

$$f_{\text{sb}} = f_{\text{loop}} - 2f_{\text{res}} = 6.17 \text{ GHz}. \quad (4.3)$$

This sideband mode is weaker coupled to the feedline and has a loaded quality factor of  $Q_1 \approx 5000$ .

The fact that the resonance at 6.22 GHz is the pure resonator mode while the resonance at 6.17 GHz is a sideband with the loop self-resonance becomes obvious when an external magnetic field is applied perpendicular to the sample. The pure resonator does not care for small applied magnetic fields because it is fabricated by a superconducting aluminium wire which has a critical magnetic field much larger than the applied one. This is different for the sideband mode as it is shown in Fig. 4.5. The sideband mode appears to be dominated by the critical current of the embedded nanowire made from the highly disordered  $\text{AlO}_x$  thin film. Driving a persistent current in the loop by applying an external field, leads to a drastic change of the resonance frequency of the sideband mode. The reason will be considered in detail in Sec. 4.1.4.

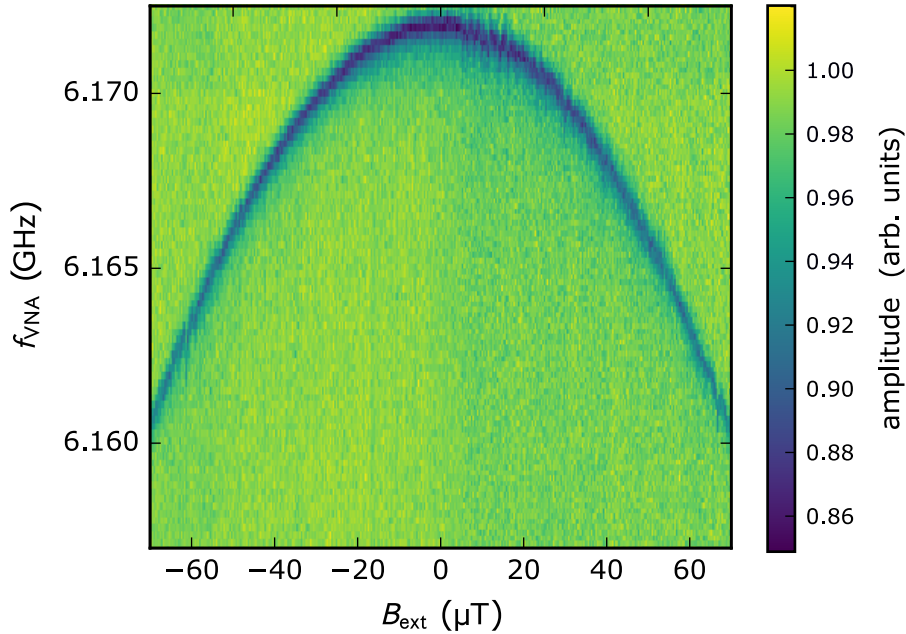


**Figure 4.5:** A first magnetic field scan after cooling down in zero magnetic field. The transmission amplitude of the sideband mode is plotted in colour versus the externally applied magnetic field.

### 4.1.3. Granular aluminium nanowire considered as QPS junction

If the nanowire acts as a quantum phase slip junction (QPSJ) and allows for coherent tunnelling of fluxoids into and out of the loop, the loop-nanowire circuit may act as a two-level system as explained in Sec. 2.3.3. Then, the two states are two adjacent fluxon states in the loop (see Fig. 4.6) or in other words the persistent current states that flow in clockwise and anti-clockwise direction in the loop. The two-level system is called quantum phase slip flux qubit (QPSFQ) [MH05] and was described in Sec. 2.3.3.

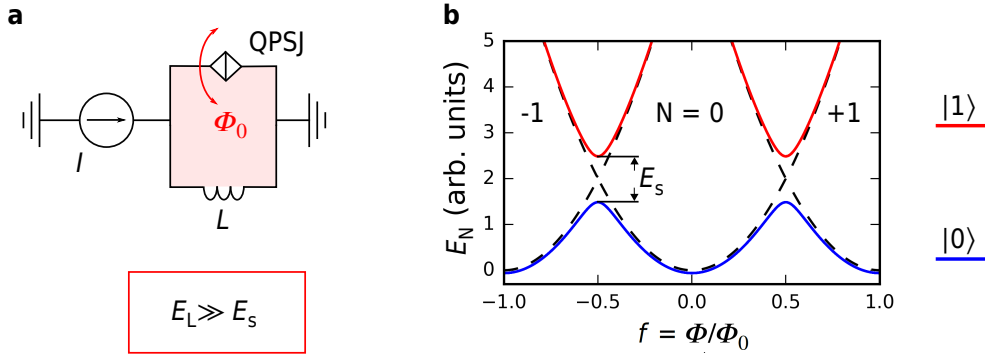


**Figure 4.6:** **a** Electrical circuit of the quantum phase slip flux qubit (QPSFQ). The number  $N$  of fluxoids ( $\Phi_0$ ) in the superconducting loop with inductance  $L$  and embedded QPS junction (QPSJ) can only change in discrete numbers under external flux bias. The QPSFQ is subject to the restriction  $E_L \gg E_s$ . **b** QPSFQ energy spectrum for  $N = -1, 0, +1$  fluxoids in the loop (dashed parabolae) as function of magnetic frustration  $f = \Phi/\Phi_0$ . The QPS tunnelling  $E_s$  lifts the degeneracy at half-integer values of  $f$ . The coherent tunnelling creates a two-level system with a ground state  $|0\rangle$  (blue) and an excited state  $|1\rangle$  (red).

Strong coupling - represented by the coupling coefficient  $g$  - of such a qubit to a microwave resonator leads to avoided level crossings when the level transition is tuned into resonance with the resonator (see Sec. 2.4.3) via a variation of the magnetic field. This is expressed through the Jaynes-Cummings Hamiltonian under rotating wave approximation (see Eq. (2.74))

$$\hat{H}_{\text{JC}} = \hat{H}_r + \hat{H}_q + \hat{H}_{\text{int}}, \quad (4.4)$$

$$= \hbar\omega_r \left( a^\dagger a + \frac{1}{2} \right) + \frac{\hbar}{2} \omega_q \sigma_z + \hbar g (\sigma^+ a + \sigma^- a^\dagger), \quad (4.5)$$

with the qubit frequency given by

$$f_q = \frac{\omega_q}{2\pi} = \frac{1}{\hbar} \sqrt{(2I_p \Phi_0 (f - 1/2))^2 + E_s^2}. \quad (4.6)$$

In resonance, qubit and resonator form a doublet of dressed states with a degeneracy that is lifted by two times the coupling coefficient  $g$  (see Sec. 2.4.3). In Fig. 4.7, the resonance

amplitude is plotted in colour versus the readout frequency of the vector network analyser (VNA) and the applied magnetic field. At around  $6 \mu\text{T}$ , the resonance frequency starts to drop for increasing magnetic field before it suddenly jumps to frequencies higher than the original  $6.17 \text{ GHz}$ . This is exactly the point where the two-level system is tuned into resonance with the monitored resonance mode according to Eq. (4.6); an avoided level crossing is observed. The observed pattern is symmetric to around  $8 \mu\text{T}$  where the two-level system reaches its lowest transition frequency before it increases again (see Eq. (4.6)). A fit of Eq. (4.5) to the anticrossing in Fig. 4.7, gives a coupling factor of

$$g = 49.60 \pm 0.50 \text{ MHz.} \quad (4.7)$$

The resonator mode also shows an avoided level crossing at the same magnetic field values but with much weaker coupling of  $g \approx 1, \text{ MHz}$ .

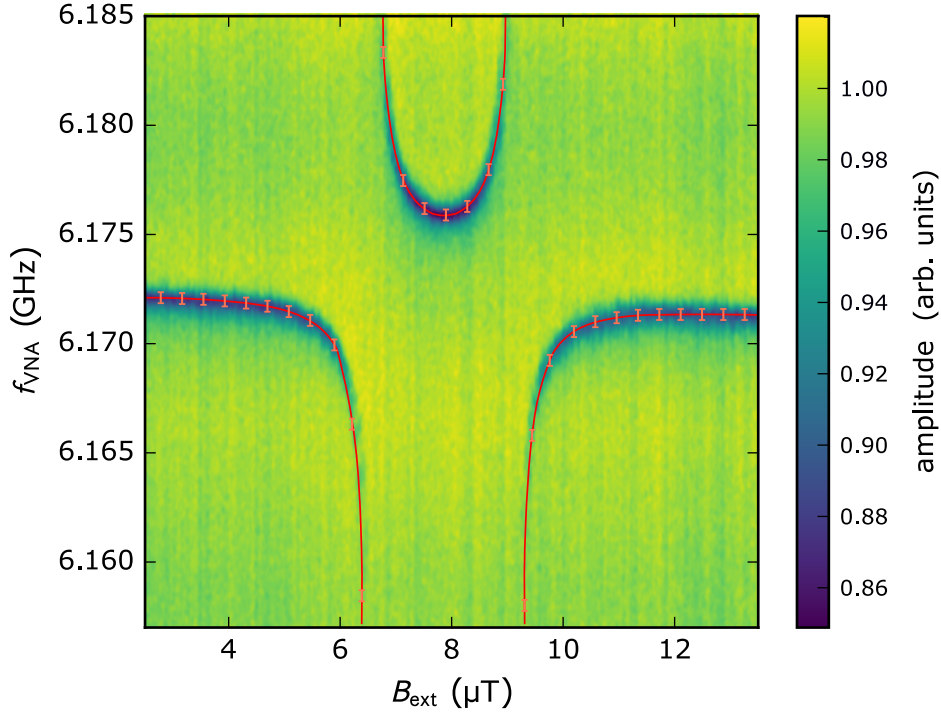


**Figure 4.7:** Avoided level crossing of the two-level system shown in Fig. 4.8 and resonator sideband mode displayed as colour coded microwave transmission amplitude versus probe frequency  $f_{\text{VNA}}$  and magnetic field  $B_{\text{ext}}$ . The red line is a fit by Eq. (4.5).

The capacitive coupling of the electric qubit dipole moment to the electric field of a resonance mode can be assessed by

$$hg_{\Phi} = C_c V_r V_q, \quad (4.8)$$

where  $g_\Phi$  represents the coupling strength in the flux eigenbasis,  $h$  is Planck's constant,  $C_c$  the coupling capacitance between resonator and loop,  $V_r$  the voltage drop at the end of the resonator and  $V_q$  the voltage drop over the loop.

The coupling capacitance  $C_c$  as presented in Fig. 4.2 is estimated as capacitance between two asymmetric coplanar lines (see [Sim01]), where one is the end of the resonator with a width of  $10\ \mu\text{m}$  while the other is the loop arm with a width of  $0.4\ \mu\text{m}$ . The coupling extends to  $20\ \mu\text{m}$  at most which is the length of the qubit loop arm. The distance between both lines is around  $4\ \mu\text{m}$ . This gives a maximal coupling capacitance of  $C_c = 1.33\ \text{fF}$ . Taking into account that the resonator current oscillates sinusoidally with the fundamental mode frequency  $f_r = 6.22\ \text{GHz}$ , the resonator voltage drop at the end can be calculated by  $V_r = \sqrt{hf_r/2C_r}$ . With a resonator capacitance  $C_r = 292\ \text{fF}$  (see [Bra13]), the resonator voltage drop is  $V_r = 2.7\ \mu\text{V}$ .

The loop's electric dipole moment results from the coherent tunnelling across the nanowire. It is the transition dipole between two adjacent states flux states. As such, the voltage drop over the loop can be assessed by  $V_q = \Phi_0 f_q$ , where  $\Phi_0$  is the distance in flux space between the neighbouring states and  $f_q$  is the transition frequency. In anticipation of Eq. (4.10),  $V_q = \Phi_0 \cdot 5.3\ \text{GHz} = 10.9\ \mu\text{V}$ .

Together this leads to a maximum coupling between resonator and loop of

$$g_\Phi \leq 58\ \text{MHz}. \quad (4.9)$$

However, it has to be stated that this coupling is most probably overestimated because the coupling capacitance might be dominated only by a fraction of the length of the loop arm and also the loop's capacitance to ground has to be taken into account. A safe estimate is rather a tenth, namely  $g_\Phi \approx 5\ \text{MHz}$  what agrees more with the experimental observation of around  $1\ \text{MHz}$ .

Since the loop resonance mode, which is monitored in Fig. 4.7, has a capacitance two orders of magnitude less than the pure resonator mode, the coupling of the loop to the sideband mode is estimated to be one order of magnitude higher (around  $50\ \text{MHz}$ ). This also agrees with Eq. (4.7). In other words, the coupling of the qubit to the sideband mode is stronger because it includes the loop dynamics.

In order to monitor the level transition in dependence of the applied magnetic flux as predicted by Eq. (4.6), the dispersive readout technique is utilized which is explained in Sec. 2.4.3. Fig. 4.8 shows the amplitude of the sideband resonance dip in color versus the applied magnetic frustration  $f$  under an additional microwave drive tone  $f_{\text{mw}}$ . Due to the coupling, the resonator experiences a dispersive shift when the additional drive excites the qubit according to Eq. (2.88). Hence, the resonance amplitude changes. A change of magnetic frustration  $f$  leads to a change of the transition frequency according to Eq. (4.6) and the drive frequency has to be changed to excite the qubit.

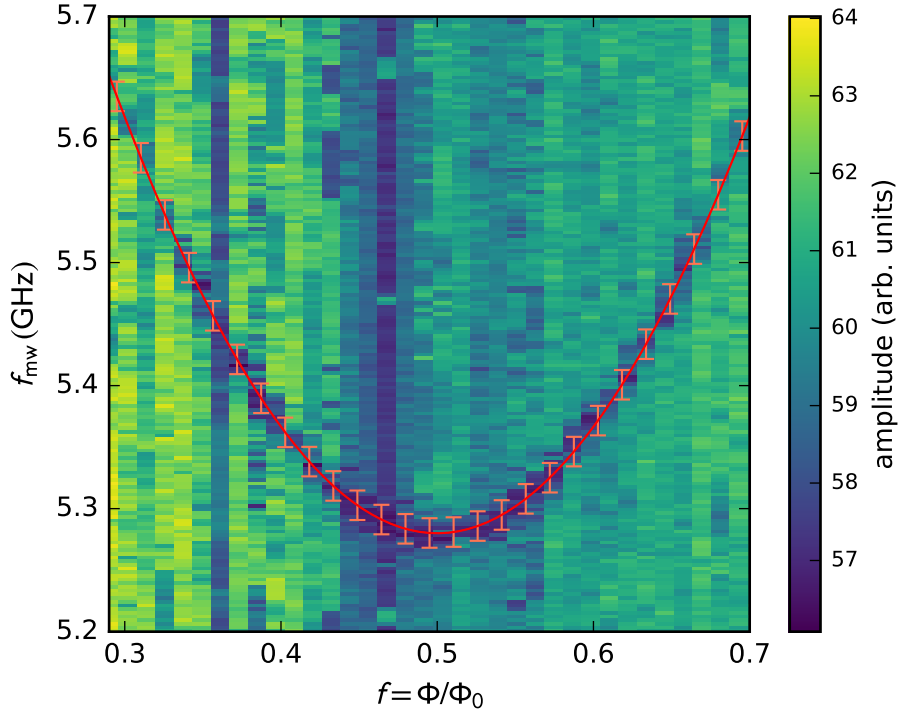


**Figure 4.8:** Dependence on magnetic frustration  $f = \Phi/\Phi_0$  of the transition of the two-level system participating in the anticrossing in Fig. 4.7 investigated by dispersive readout technique. The readout power level is at  $P_{\text{VNA}} = -122$  dBm while the drive power level is at  $P_{\text{mw}} = -97$  dBm (both including the setup attenuation). The microwave amplitude signal is plotted in color versus additional drive frequency  $f_{\text{mw}}$  and external magnetic frustration which is applied perpendicular to the sample. When  $f_{\text{mw}} = f_q(f)$ , the resonator experiences a dispersive shift due to coupling. The transition is fitted (red line) by Eq. (4.6).

Fitting (red line) the monitored transition in Fig. 4.8 with Eq. (4.6) gives a phase slip energy of

$$E_s = 5.28 \pm 0.01 \text{ GHz}, \quad (4.10)$$

and a persistent current of

$$I_p = 1.57 \pm 0.01 \text{ nA}. \quad (4.11)$$

However, this translates into a total loop inductance of  $L_{\text{fit}} = 656.89 \text{ nH}$  which exceeds the one calculated from design parameters and material properties by far. This indicates that the theoretical explanation involving just a two-level system based on coherent quantum phase slip in the nanowire is not consistent and seems unfeasible in this case.

Furthermore, as was seen in Fig. 4.5 which represents a first magnetic field sweep after the cooldown in zero magnetic field, the sideband mode showed no anticrossing at first. Also the resonator mode did not show any. Only after sweeping the magnetic field over a range of several times a magnetic flux quantum

$$\Delta B = \frac{\Phi_0}{A_{\text{loop}}} = 9.43 \text{ } \mu\text{T}, \quad (4.12)$$

with a given loop area  $A_{\text{loop}} = 10.4 \times 20.4 \text{ } \mu\text{m}^2 = 212.16 \text{ } \mu\text{m}^2$ , the avoided level crossing of the sideband mode in Fig. 4.7 is observed at a certain magnetic field value.

The fact that the magnetic field has to be swept over a large range before an anticrossing is observed does also not agree with the QPSFQ model. Under the condition of strong qubit-resonator coupling, anticrossings are expected at values of  $\Phi_0/2$  within a magnetic field sweep. Furthermore, as can be seen in Fig. 4.6, the energy spectrum of a QPSFQ predicts a periodic appearance of transitions with a  $\Phi_0$  per loop period in magnetic field. This then translates into a periodic appearance of anticrossings in the frequency spectrum of the sideband mode with a period of  $9.43 \text{ } \mu\text{T}$ . Such a periodicity has not been observed, however.

#### 4.1.4. Granular aluminium nanowire considered as Josephson weak link

In Sec. 4.1.2, the strong magnetic field dependence of the sideband mode (see Fig. 4.5) was shown. However, the frequency spectrum in Fig. 4.5 lacks an expected feature assuming the system to act as a QPSFQ as it was discussed in the previous section. In Fig. 4.5, no anticrossings are observed although the investigated magnetic field range is close to five times the equivalent of a fluxon in the loop. Nevertheless, it was shown in Fig. 4.8 that avoided level crossings do appear. However, fitting the energy spectrum with Eq. (4.6), did not match with the expected loop inductance value.

These circumstances trigger an alternative consideration of the nanowire taking its intrinsic structure into account. Subsequently, the nanowire is viewed as a Josephson weak link between two superconducting branches in which the Josephson effect is not suppressed (see Sec. 2.3.2). Picking up the reasoning in [Lik79], the important quantity in a weak link is its effective length  $L_{\text{eff}}$  that might drastically differ from its geometric length  $L$ . One reason can be the use of a dirty superconductor like the  $\text{AlO}_x$  thin film. Its granular structure results in monocrystalline Al grains with a coherence length of  $1.2 \mu\text{m}$ . The oxide barriers that connect the grains form a network of intrinsic Josephson junctions leading to a reduced overall coherence length of the  $\text{AlO}_x$  thin film.  $L_{\text{eff}}$  is determined by the length over which the nonlinear effect(s) take place in the weak link. If one assumes the oxide barrier between two grains of  $4 \text{ nm}$  diameter to be at least  $1 \text{ nm}$  thick (see Fig. 3.2a), the effective weak link length could be estimated to

$$L_{\text{eff}} \geq 1/5 \cdot L = 50 \text{ nm}. \quad (4.13)$$

According to [Lik79], it is possible that the nanowire forms a *long* ( $L_{\text{eff}} > \xi$ ) and *dirty* ( $l < L_{\text{eff}}$ ) weak link with an estimated electric mean free path of  $l \approx 0.01 \text{ nm}$  [Rot+17]. Following the Kulik-Omelyanchuk theory for dirty weak links [KO77; Lik79], the critical current of such a dirty weak link can be estimated to be

$$I_{\text{c, wl}} = 1.32 \left( \frac{3.52\pi k_{\text{B}} T_{\text{c}}}{4e} \right) \frac{1}{R_{\text{n}}} \approx 50 \text{ nA}, \quad (4.14)$$

for the  $250 \text{ nm}$  long and  $20 \text{ nm}$  wire with a sheet resistance of  $1 \text{ k}\Omega$  which results in a normal conducting resistance of  $R_{\text{n}} = 250 \text{ nm}/250 \text{ nm} \cdot 1 \text{ k}\Omega = 12.5 \text{ k}\Omega$ . The critical temperature of the  $\text{AlO}_x$  film is  $T_{\text{c}} = 1.8 \text{ K}$ . Except that, it could also be possible that at a certain spot in the wire a thicker oxide barrier was formed which leads to the formation of a spatially localized Josephson junction with similar critical current as given by Eq. (4.14).

As a Josephson weak link, the nanowire would have a non-linear inductance given by

$$L_{\text{wire}} = L_{\text{wl}} = \frac{\Phi_0}{2\pi I_{\text{c, wl}} \cos(\varphi_{\text{wl}})}, \quad (4.15)$$

where the phase drop over the weak link is given by  $\varphi_{wl} = 2\pi\Phi/\Phi_0 = 2\pi \cdot L_{wl}I/\Phi_0$  with the weak link inductance  $L_{wl}$  and the current  $I$  carried by the weak link.

Hence, the total loop inductance of the loop-nanowire system consists of the kinetic inductance of the loop plus the weak-link inductance

$$L_{tot} = L_{loop} + L_{wl}. \quad (4.16)$$

The sideband resonance mode would directly depend on the total inductance and would be given by

$$\begin{aligned} f_{sb} &= \frac{1}{2\pi} \frac{1}{\sqrt{L_{tot}C}} - 2f_{res} \\ &= \frac{1}{2\pi} \frac{1}{\sqrt{\left(L_{loop} + \frac{\Phi_0}{2\pi I_{c,wl} \cos(\varphi_{wl})}\right) \cdot C}} - 2f_{res}. \end{aligned} \quad (4.17)$$

Under the influence of an applied external magnetic flux  $\Phi_{ext}$ , the total superconducting phase of the system would split into two contributions

$$\varphi_{tot} = \varphi_{loop} + \varphi_{wl} = 2\pi\Phi_{ext} = 2\pi(L_{loop} + L_{wl}). \quad (4.18)$$

Due to the high total inductance, the persistent current  $I_p = \Phi_{ext}/L_{tot}$  which is driven by the external field is reduced. At such small currents, the loop inductance  $L_{loop}$  is linear. On the contrary, the weak-link inductance would scale with the cosine of its phase drop  $\varphi_{wl}$  already at small magnetic flux values (see Eq. (4.15)) which might lead to change in resonance frequency of the sideband mode as it is shown in Fig. 4.5.

Fig. 4.9 shows the same measurement as it was presented in Fig. 4.5. The amplitude  $|S_{21}|$  of the resonance signal is plotted in color versus the externally applied magnetic field. Using Eq. (4.18), a fit of Eq. (4.17) to Fig. 4.9 (red line) gives a critical current of the supposed weak link of

$$I_{c,wl} = 60 \pm 14 \text{ nA}, \quad (4.19)$$

as well as loop and weak link inductances of

$$L_{loop} = 121 \pm 2 \text{ nH}, \quad (4.20)$$

$$L_{wl} = 5.5 \pm 0.5 \text{ nH}. \quad (4.21)$$

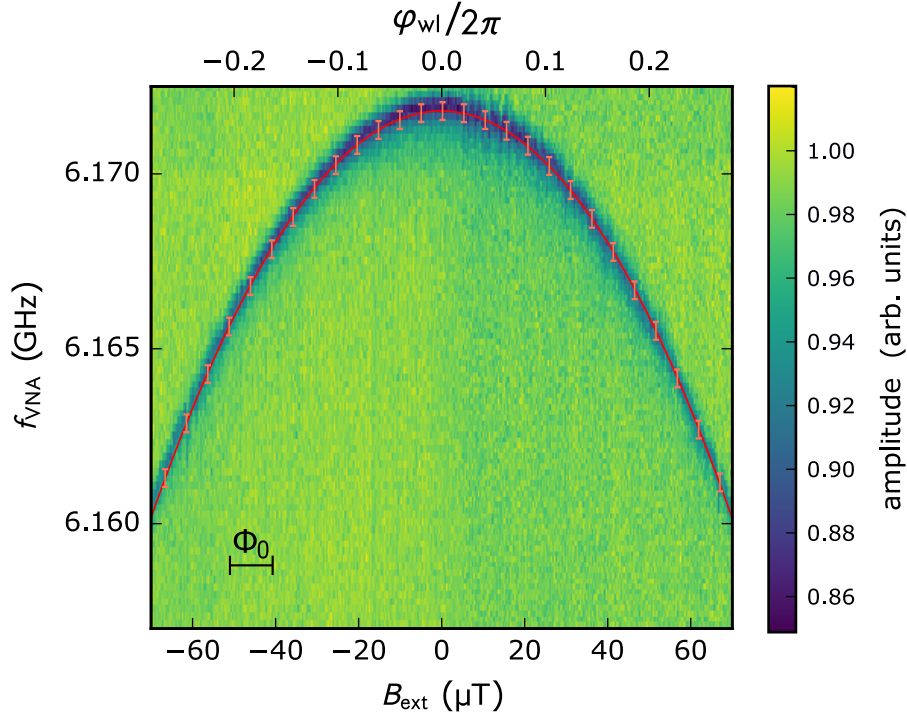


**Figure 4.9:** A first magnetic field scan after cooling down in zero magnetic field. The transmission amplitude of the sideband mode is plotted in colour versus the externally applied magnetic field. The red line presents a fit of the magnetic field dependence of the resonance frequency with Eq. (4.17).

This results in a basic loop parameter

$$\beta_L = \frac{2\pi I_{c,wl} L_{tot}}{\Phi_0} = \frac{L_{loop}}{L_{wl}} = 22 \pm 1. \quad (4.22)$$

$\beta_L$  is called normalized inductance [Lik79] and determines the phase relation between loop and weak link as

$$\varphi_{wl} = \varphi_{loop} - \beta_L \frac{I_p}{I_{c,wl}}. \quad (4.23)$$

$I_p = \Phi_0 / (2 L_{tot})$  is the persistent current in the loop driven by the externally applied magnetic field which impresses an external phase  $\varphi_e$ . This phase relation can be depicted nicely by taking into account that a Josephson weak link obeys the DC Josephson equation  $I_s = I_{c,wl} \sin(\varphi_{wl})$  (see Eq. (2.36)). Since the supercurrent in the loop is given by  $I_p$ , it can be replaced by  $I_s$  in Eq. (4.23) which then reads

$$\varphi_{wl} + \beta_L \sin(\varphi_{wl}) = \varphi_{loop}. \quad (4.24)$$

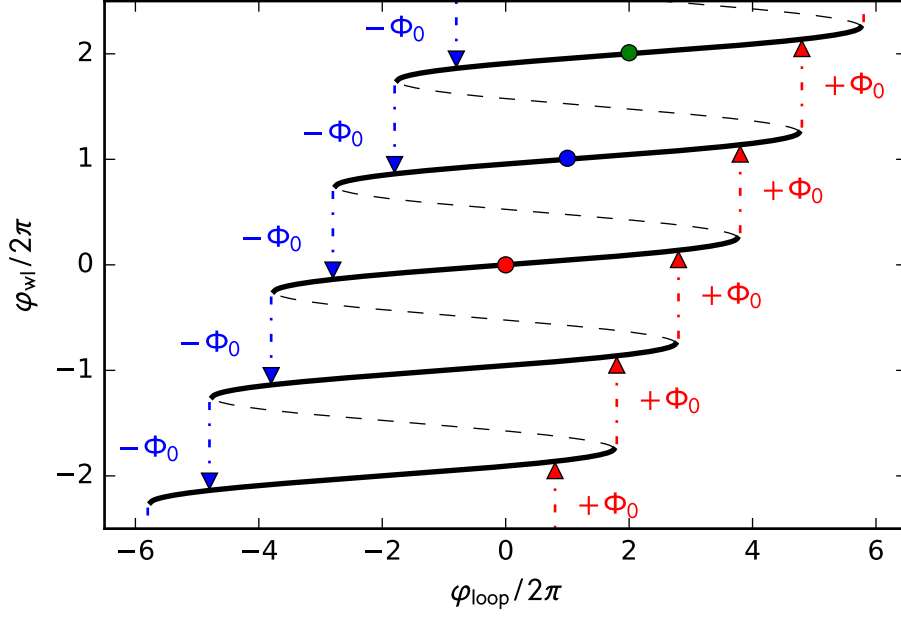


**Figure 4.10:** Relation between the loop phase  $\varphi_{\text{loop}}$  and the phase drop over the weak link  $\varphi_{\text{wl}}$ . Since the system is a closed superconducting loop the phase must always be a multiple of  $2\pi$  associated to a discrete number of fluxons in the loop. Due to the high  $\beta_L$  of the weak link, the system becomes multi-valued with metastable states (solid lines). The phase dynamics of the system can be represented as particle (circles) in a metastable state. The particle will stay in one state until the external phase exceeds a certain value and allows the system to occupy a higher ( $+\Phi_0$ ) or lower ( $-\Phi_0$ ) state. The red, blue and green circle correspond to 0, 1 or 2 fluxons in the loop.

In Fig. 4.10, Eq. (4.24) is plotted for  $\beta_L = 22$ . It can be directly seen that for such a large  $\beta_L$ , the system can be in multi-valued states (circles in Fig. 4.10). Every time the external phase exceeds more than plus (minus) four times  $2\pi$ , the system can change its state by plus (minus) one more flux quantum  $\Phi_0$  in the loop. This behaviour is well-known for a *radio-frequency Superconducting QUantum Interference Device* (RF-SQUID) which is formed by a superconducting loop with one embedded Josephson junction [Lik91; Tin04; Sch97]. The loop's characteristic energy scales are the assumed Josephson energy

$$E_J = E_{\text{wl}} = \frac{\Phi_0 I_{c,\text{wl}}}{2\pi} \approx h \cdot 30 \text{ GHz}, \quad (4.25)$$

the inductive energy

$$E_L = \frac{\Phi_0^2}{2L_{\text{tot}}} \approx h \cdot 30 \text{ GHz}, \quad (4.26)$$

and the assumed charging energy

$$E_C = \frac{e^2}{2C_{\text{tot}}} \approx h \cdot 30 \text{ GHz}. \quad (4.27)$$

The fact that the system gives rise to hysteretic behaviour as it is observable in Fig. 4.10 supposes that the flux might be the proper basis to describe the system's dynamics. This will be important in the following.

Fig. 4.11 shows a similar magnetic field sweep as presented in Fig. 4.9. While Fig. 4.9 was a first sweep after cooling down in zero magnetic field, Fig. 4.11 was recorded after a preceding magnetic field scan to more than five times a  $\Phi_0$  flux in the loop. Fig. 4.10 shows that for  $\beta_L = 22$  an externally applied flux of more than five times  $\Phi_0$  which corresponds to an externally impressed phase  $\varphi_{\text{loop}}$  more than five times  $2\pi$  brings the system into a higher metastable state (e.g. blue or green circle in Fig. 4.10). For a subsequent reduction of the magnetic field, the system will remain on this upper phase branch until the field is swept down so much that the system can reduce its state to a lower one.

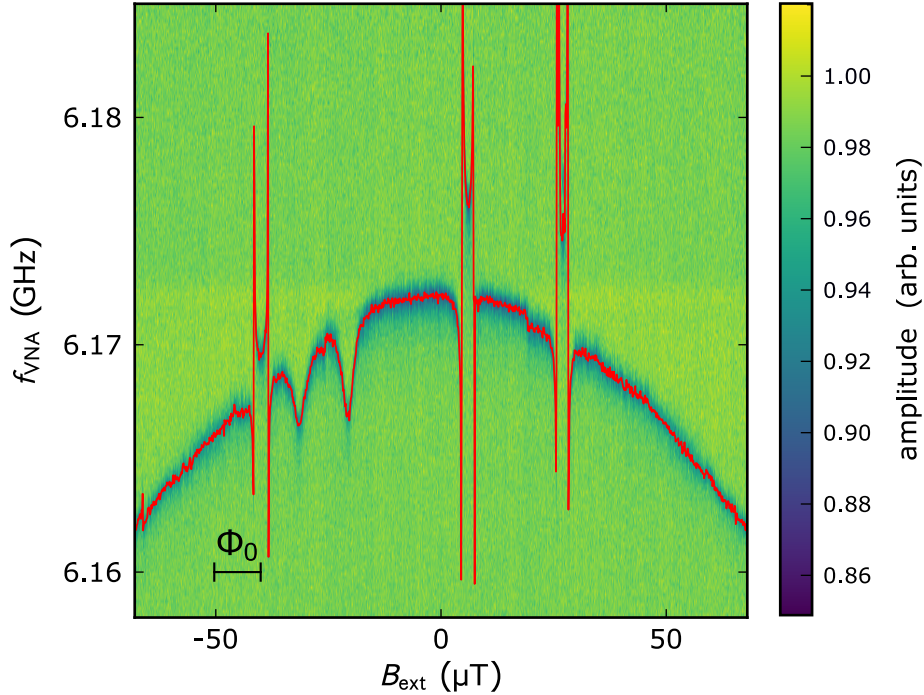


**Figure 4.11:** Magnetic field scan recorded after a preceding magnetic field sweep to more than five times a  $\Phi_0$  flux in the loop. The sideband mode resonance amplitude is plotted in colour versus the externally applied magnetic field. Several different anticrossings are visible including "bumps" in the resonance spectrum. The red line presents the resonance at minimum amplitude as a guide to the eye.

Deeper understanding of the system's dynamics can be gained by considering the magnetic energy  $E_L$  and the weak link's Josephson energy  $E_J$  which form the system's potential landscape [Fri+00; RHL95]

$$U(\Phi, \Phi_e) = U_0 \left[ \frac{1}{2} \left( \frac{2\pi(\Phi - \Phi_e)}{\Phi_0} \right)^2 - \beta_L \cos \left( 2\pi \frac{\Phi}{\Phi_0} \right) \right]. \quad (4.28)$$

Here,  $\Phi$  represents the metastable state or the number of fluxons in the loop respectively while  $\Phi_e$  is externally applied magnetic flux. The first summand of Eq. (4.28) represents the magnetic energy, the second one is the Josephson energy with  $U_0 = \Phi_0^2/(4\pi^2 L_{\text{tot}})$ . In case of  $\beta_L \ll 1$ , the Josephson energy term could be neglected. For  $\beta_L = 22$  however,  $E_J$  plays an important role for dynamics of the system and gives rise to hysteresis effects.

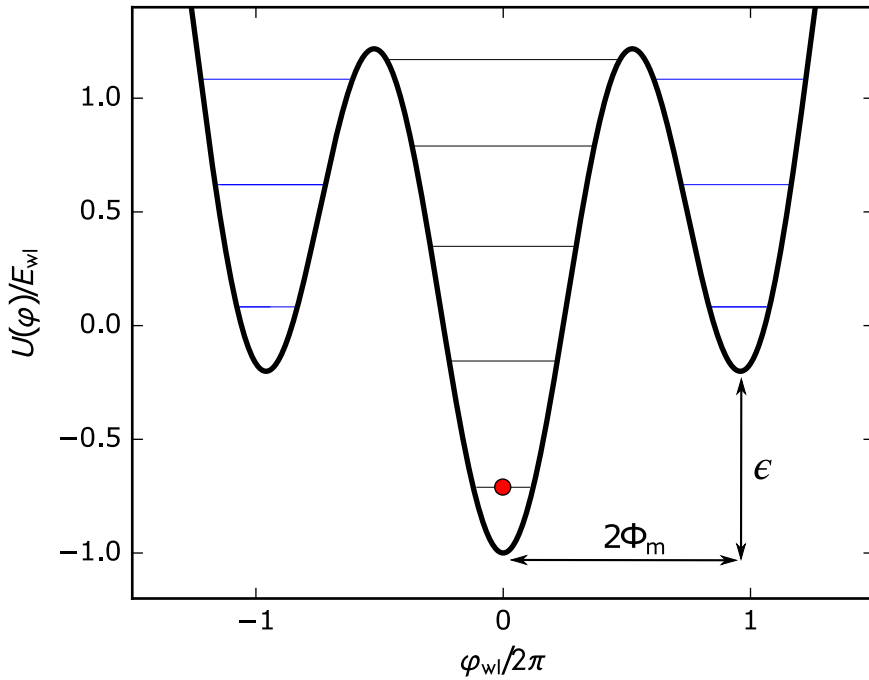


**Figure 4.12:** Potential Eq. (4.28) of the loop - weak link system plotted over the phase drop over the weak link  $\varphi_{wl}$  for zero magnetic field. The phase dynamics are represented by a particle (red circle) which is situated in the centre well. The energy levels in the centre as well as the adjacent wells are plotted (solid lines).  $\epsilon$  is the potential tilt,  $U_0$  is the barrier height between adjacent wells and  $\Phi_m$  represents the flux difference between two adjacent minima.

This can be seen clearly when plotting the potential Eq. (4.28) over the phase drop over the weak link  $\varphi_{wl}$  presented in Fig. 4.12. After cooling the system through  $T_c$  in zero magnetic field  $\Phi = \Phi_e = 0$ , the system resides in the ground state of the centre well of the potential. The wells result from the Josephson energy term and receive their depth by the large  $\beta_L$  parameter. As explained in Sec. 2.3.3, the system or more precisely its phase dynamics can be described as a particle that is localized in the centre well which is depicted in Fig. 4.12 as red circle. It corresponds to the red circle in Fig. 4.10. The

particle is in its ground state. The energetically higher excited states as well as the bound states in the adjacent wells are plotted. They are calculated by solving the Hamiltonian

$$H_{\text{loop,wl}} = 4E_C + U(\Phi, \Phi_e), \quad (4.29)$$

with  $E_C$  given by Eq. (4.27) and  $U(\Phi, \Phi_e)$  by Eq. (4.28).

The energy levels of the excited states are very high which makes them difficult to be populated in the experiment. However, the situation might change, when the magnetic field is increased. In Fig. 4.13, the potential is shown for applied magnetic fields of 0 (thin solid line),  $3\Phi_0$  (dashed dotted line) and  $5\Phi_0$  (thick solid line). The particle (red circle) cannot escape the well during the increase of applied flux (red dashed arrows) until the barrier to the adjacent well is low enough. For an applied flux of  $5\Phi_0$  the barrier to the next well has vanished. The particle can then "roll" down the potential (gray dashed arrows) until a well is deep enough to localize it. This is presented in Fig. 4.13 in the  $5\Phi_0$  potential as either blue circle when the particle reaches the next well or green circle when it arrives the second next well. The blue and green circles correspond to the ones in Fig. 4.10.

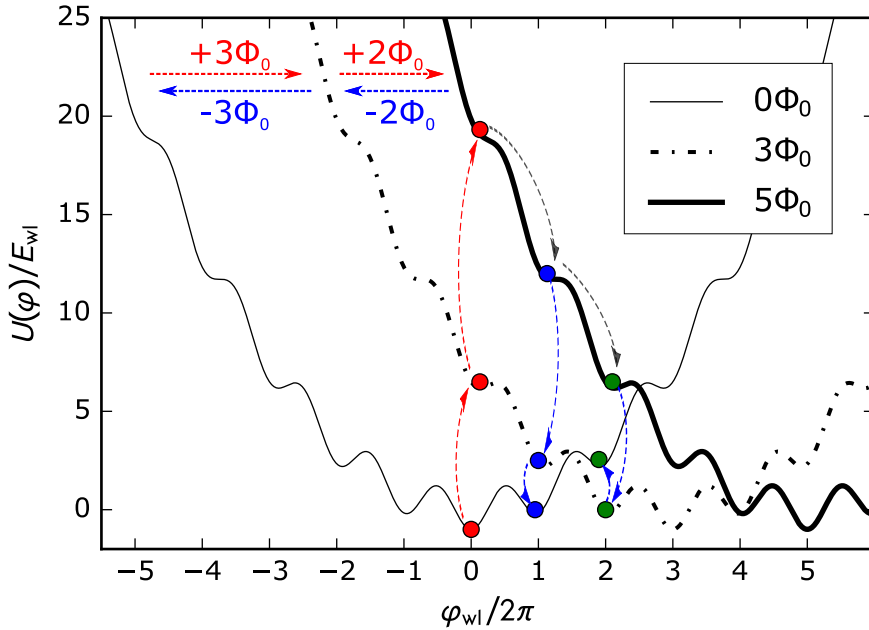


**Figure 4.13:** The potential given by Eq. (4.28) plotted over the phase drop over the weak link  $\varphi_{\text{wl}}$  for  $0\Phi_0$  (thin solid line),  $3\Phi_0$  (dashed dotted line) and  $5\Phi_0$  (thick solid line). The phase dynamics is represented by particles. Increasing the external flux (red horizontal arrows) tilts the potential. Increasing from  $0\Phi_0$ , the particle (red circle) is lifted up (red vertical arrows) as long as a barrier separates two neighbouring wells. Without barrier, the particle "rolls" down the potential (black arrows) until being trapped in a neighboring well (blue or green circle). During a subsequent reduction of the external flux (blue horizontal arrows), the particles remain in their occupied wells. The circle colors correspond to Fig. 4.10.

#### 4. Results

When the magnetic field is subsequently swept back, the system will stay in its new well. At certain magnetic field values, a situation can be on hand that is presented in Fig. 4.14a. In this situation, the particle cannot yet overcome the barrier to the next well but it can resonantly tunnel between the wells [Fri+00; RHL95] as depicted by the arrows. This tunnelling process can be coherent having a lifted degeneracy of states  $|0\rangle$ ,  $|1\rangle$  what is presented in Fig. 4.14b. The energy difference by which the degeneracy is lifted is given by [Fri+00; RHL95]

$$\Delta E = \sqrt{\epsilon^2 + \Delta^2}, \quad (4.30)$$

where the flux dependent tilt of the potential (see Fig. 4.14a) is  $\epsilon = 2U_0 4\pi^2 \Phi_m \Phi_e / \Phi_0^2$  and the tunnel coupling is represented by  $\Delta$  (see Fig. 4.14b).  $\Delta U_0$  gives the barrier height.

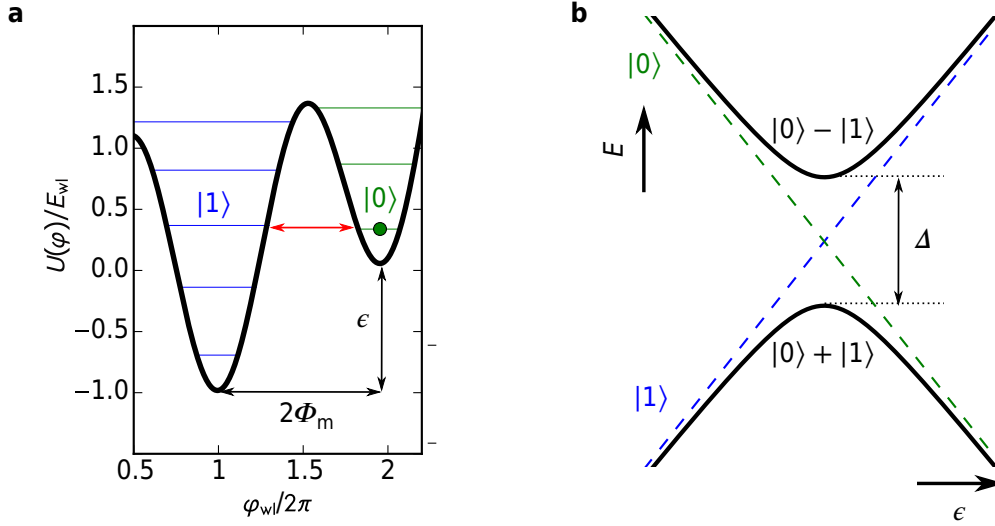


**Figure 4.14:** **a** Potential Eq. (4.28) plotted at an external flux of  $1.5 \Phi_0$  with the system occupying the second metastable state from zero (green circle, see Fig. 4.13 and Fig. 4.10). Under this conditions, coherent, resonant tunnelling can take place through the barrier between states  $|0\rangle$  and  $|1\rangle$  (double-sided arrow). **b** This system forms a two level system with a degeneracy that is lifted by  $\Delta$ . The energy difference between the two dressed states is given by Eq. (4.30).

Eq. (4.30) has the same form as Eq. (4.6) and therefore also fits to the appearance and shape of the transition spectrum in Fig. 4.8 and of the anticrossing in Fig. 4.7. The fit of the Jaynes-Cummings Hamiltonian Eq. (4.5) but now with a qubit energy (frequency) given by Eq. (4.30) instead of Eq. (4.6).

The anticrossing in Fig. 4.7 corresponds to the one in the center at around  $8 \mu\text{T}$  in Fig. 4.11 and as aforementioned is caused by the energy dependent transition presented in Fig. 4.8. Fitting of Eq. (4.30) to the transition in Fig. 4.8 would result in a tunnel coupling

$$\Delta = 5.28 \pm 0.01 \text{ GHz}, \quad (4.31)$$

and an energy tilt per frustration  $f = \Phi/\Phi_0$  of

$$\epsilon = 9.75 \pm 0.01 \text{ GHz.} \quad (4.32)$$

Nevertheless, this level-transition is not the only one that is observed. In Fig. 4.11 different anticrossings appear when the magnetic field is swept back over a big range. This can be explained considering the change of the potential with magnetic flux as presented in Fig. 4.13. For changing magnetic field, the well and therewith the localized levels in it would considerably change. This might give rise to coherent, resonant inter-well tunnelling between different states. As a result, different anticrossings can be observed in Fig. 4.11. For example the "bumps" in the frequency spectrum at  $-30$  to  $-40 \mu\text{T}$  in Fig. 4.11 are due to two-level systems with a minimum transition frequency of 6.5 GHz. All transitions that have been observed were fitted by Eq. (4.30). The results are listed in Tab. 4.1

$\Delta/h$ (GHz)	$\epsilon/h$ (GHz per $f = \Phi/\Phi_0$ )
4.19	34.69
5.28	9.75
6.5	15.02

**Table 4.1:** Parameters of the observed two-level systems taken from fits to Eq. (4.30).

Tab. 4.1 shows that not only the tunnel couplings vary but also the potential tilt. This might be explained by the fact that the different energy levels in a well depend differently on magnetic field. Close to the top of the barrier, the well's width increases stronger with magnetic field than deep in the well. This might lead to a stronger magnetic field transition of the resonant inter-well tunnelling.

Here, it has to be stated that the derivation of the capacitive coupling between either resonator mode or sideband mode and loop-nanowire system, which was done in Sec. 4.1.3 (see Eq. (4.8)), would also hold for the consideration in this section. In any case, the qubit's electric dipole moment would result from the tunnelling between adjacent fluxon states.

It is furthermore obvious that in a single magnetic field sweep, no transition appears with a periodicity of  $\Phi_0$  in the loop due to the form of the potential Eq. (4.28). It is however possible to get the transition presented in Fig. 4.8 again when the system is in another metastable fluxon state since the potential is the same for every integer of  $\Phi_0$  in the loop. It is only shifted by this  $n \cdot \Phi_0$ . After the detection of the transition presented in Fig. 4.8, the magnetic field is swept to around five times  $\Phi_0$  so that the system occupies the next higher metastable state. Reducing the field subsequently, the same transition appears at flux that is  $\Phi_0$  shifted from the one at which the transition was before. This is shown in Fig. 4.15.

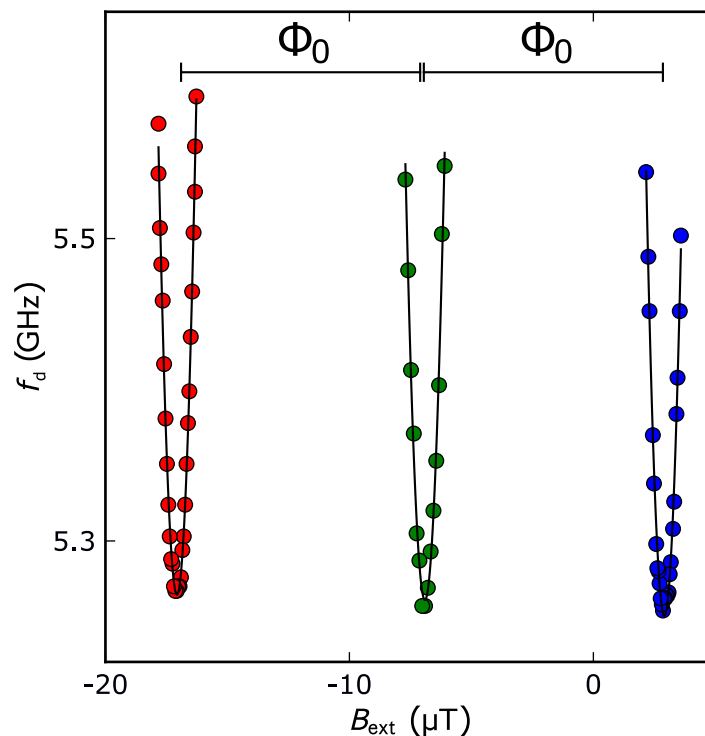


**Figure 4.15:** Magnetic field dependent two-level transitions as shown in Fig. 4.8 for 3 subsequent, hysteretic magnetic field cycles leading the system to occupy adjacent metastable fluxon states. The solid lines represent fits to Eq. (4.30) with the same parameters.

Reconsidering Fig. 4.14a, the question arises why the particle does coherent, resonant tunnelling with a state  $|1\rangle$  that is energetically so high up that it is likely to relax instantaneously into the ground state in its own well. A reason may be that the tunnelling rate is faster than the relaxation rate.

That the state is rather long living is backed up by the observation that an observed frequency spectrum like in Fig. 4.11 is stable over days as long as the magnetic flux is not swept so far that the system can occupy an adjacent metastable state. Very seldom ( $t \approx 1$  week), a sudden jump in the spectrum takes place during a sweep. This could correspond to a relaxation of a state  $|1\rangle$  into its ground state. Therefore, the system has to be able to switch to a lower metastable state resulting in an observed spectrum that is different to the one before the jump. This is observed many times.

### 4.1.5. AC Stark effect

The coupling of two-level system and resonator does not only result in a dispersive resonator frequency shift depending on the two-level system's state but also in a change of the transition frequency in dependence on the electric field strength or photon number in the resonator, respectively as it was explained in Sec. 2.4.3. In Fig. 4.16, the amplitude of the sideband resonance mode is plotted in colour at a fixed magnetic field value which corresponds to the minimum transition frequency point in Fig. 4.8. Using again the dispersive readout technique, the additional drive  $f_{\text{mw}}$  is used to drive the transition while the microwave power applied by the VNA to read out the resonance  $P_{\text{VNA}}$  is swept.

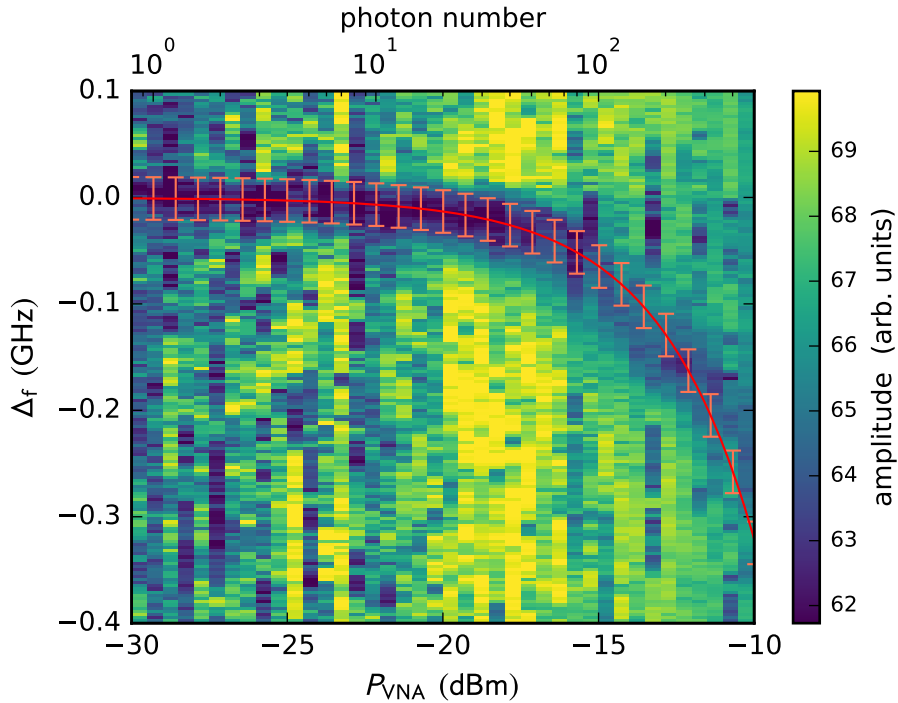


**Figure 4.16:** Dependence of the transition in Fig. 4.8 on the readout power  $P_{\text{VNA}}$ , here given without setup attenuation. The qubit transition is fixed at the sweet spot ( $\Delta E = \Delta$ ) and investigated via the dispersive readout technique. The change of the transition with  $P_{\text{VNA}}$  is fitted by Eq. (4.33) (red line). This is used to calibrate the average number of photons  $\langle n \rangle$  in the resonance mode with the applied microwave power. This calibrated photon number is displayed as upper x axis. The drive power level is at  $P_{\text{mw}} = -102$  dBm including setup attenuation.

It is observed that the dispersive shift of the sideband resonance mode and thus the transition frequency decreases for increasing readout power (see Fig. 4.16). The change in transition frequency is due to the changing AC electric field of the resonance mode or

its photon number, respectively. More photons in the resonator means a linear increase of the resonator decay rate. Due to coupling to all photons, the two-level system loses more energy and its frequency gets reduced, respectively. This effect is called AC Stark shift as explained in Sec. 2.4.3. The change of qubit transition frequency  $\Delta_f$  is given by Eq. (2.87)

$$\Delta_f = \frac{g^2}{f_r - f_q}(2n + 1). \quad (4.33)$$

Eq. (4.33) makes it possible to calibrate the applied readout power  $P_{\text{VNA}}$  given on the lower x-axis in Fig. 4.16 for the photon number in the readout resonator which is displayed at the upper x-axis. For an applied power of  $-30$  dBm (plus further 80 dB of attenuation in the line), a measurement is performed in the single photon regime. This means coupling of one microwave photon to a two-level system excitation.

#### 4.1.6. Driven Rabi oscillations

Since it is possible to drive the level transition with an external microwave signal, the next step is to perform a Rabi drive experiment. The level transition will be driven sinusoidally between ground and excited state as explained in Sec. 2.4.1.

For this purpose, the continuous microwave measurement setup displayed in Fig. 3.9 which was used so far is replaced by the pulsed microwave measurement setup shown in Fig. 3.10. This setup is necessary to send pulsed microwave signals to the sample and evaluate them afterwards. The loop-nanowire system is still monitored through the sideband resonance mode.

Applying a drive pulse is represented by the drive Hamiltonian Eq. (2.58)

$$\tilde{H}_d = A_d \cos(2\pi f_d t) \tilde{\sigma}_z, \quad (4.34)$$

with drive amplitude  $A_d$  and drive frequency  $f_d$  when the drive is tuned into resonance with the transition frequency  $f_q$ , it leads to oscillations between ground and excited state as it is shown in Fig. 4.17b.

The two-level system is in its ground state in the beginning. A drive is applied for a time  $\Delta t$  followed by a readout pulse that extracts the state of the two-level system (see Fig. 4.17a). By various measurements, in which  $\Delta t$  is increased measurement-wise, the two-level system oscillation under drive can be monitored.

Since now it is shown that the two-level system can be driven between ground and excited state, in the following it will be called a qubit.

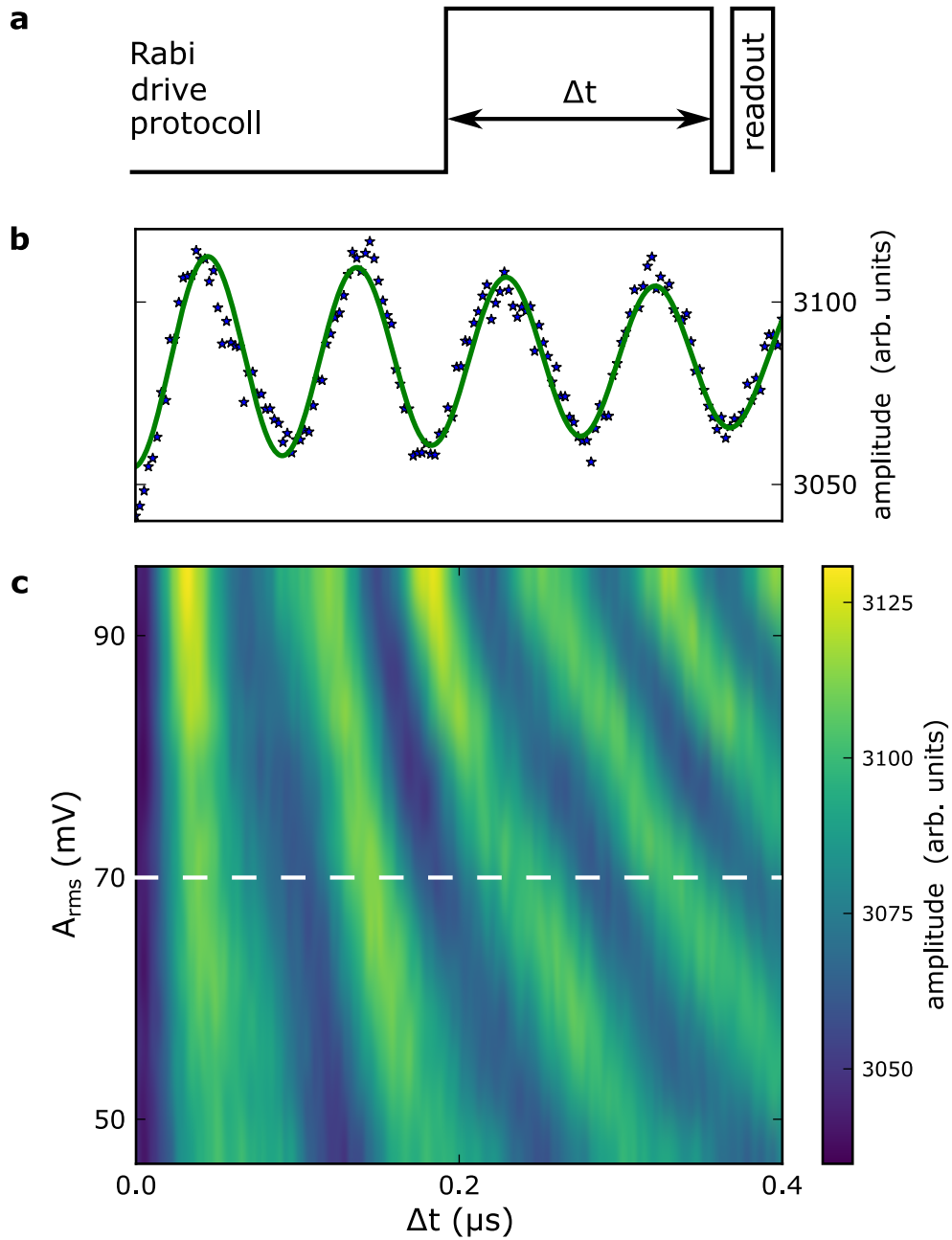


**Figure 4.17:** **a** Rabi drive protocol. After applying a drive (see Eq. (4.34)) for time  $\Delta t$  to the qubit, a readout pulse extracts the qubit state. **b** Subsequent measurements with varied drive pulse duration  $\Delta t$  (single stars) plotted over  $\Delta t$  gives the Rabi oscillation. The transmission amplitude  $|S_{21}|$  of the sideband resonance used to read out the qubit state dispersively is plotted versus  $\Delta t$ . The green solid line represents a fit by an exponentially damped cosine function. **c** Rabi oscillations like in **b** measured for different drive power amplitudes  $A_{\text{rms}}$ . The transmission amplitude  $|S_{21}|$  is plotted in color. The white dashed horizontal line corresponds to the drive power amplitude value at which the figure in **b** is taken.

As the next step, the dependence of the Rabi oscillations on the drive amplitude is investigated. According to Eq. (2.60)

$$\Omega_R = \frac{A}{\hbar^2} \frac{E_0}{\omega_q}, \quad (4.35)$$

the Rabi frequency is proportional to the amplitude of the drive signal. This is presented in Fig. 4.17c. There, the sideband resonance amplitude  $|S_{21}|$  is plotted in color versus drive amplitude  $A_{\text{rms}}$ <sup>3</sup> and the time  $\Delta t$  over which the drive is applied before the qubit state is read out. Each horizontal line in Fig. 4.17c represents a measurement like in Fig. 4.17b. The frequency of the Rabi oscillation that is visible horizontally in Fig. 4.17c decreases with decreasing drive amplitude.

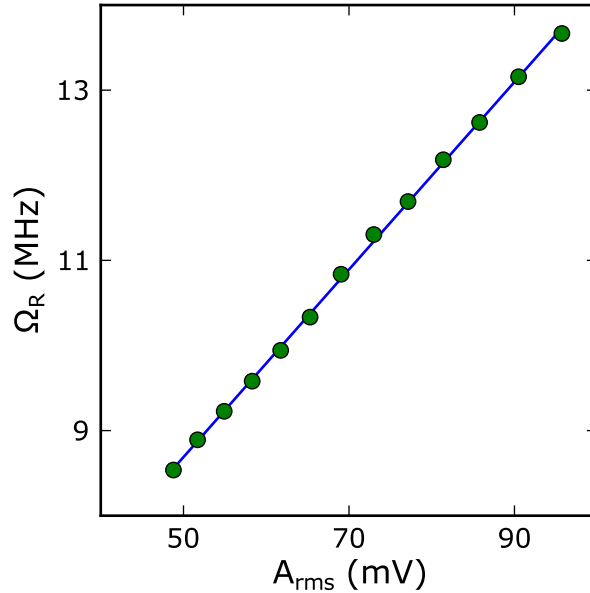


**Figure 4.18:** Rabi frequency values  $\Omega_R$  extracted from fits of Eq. (4.35) to each Rabi oscillation in Fig. 4.17c plotted versus the corresponding drive amplitude values  $A_{\text{rms}}$ . The linear dependence of  $\Omega_R$  on  $A_{\text{rms}}$  (solid line as guide to the eye) is in nice agreement with the expected behaviour (see Eq. (4.35)).

In Fig. 4.18, the Rabi frequency values  $\Omega_R$  extracted from the measurement in Fig. 4.17c are plotted versus the corresponding drive amplitude values  $A_{\text{rms}}$ . A linear dependence of  $\Omega_R$  on  $A_{\text{rms}}$  can be observed (solid line in Fig. 4.18 as guide to the eye). This is in nice agreement with theory (see Eq. (4.35)).

---

<sup>3</sup>“rms” stands for *root mean square*.

### 4.1.7. Qubit lifetimes

The driven Rabi oscillations proof that the qubit's spontaneous emission rate is sufficiently small to allow the qubit to stay in its excited state on the time scale a measurement is performed. If the emission rate was faster than the Rabi frequency, the qubit would decay faster than it would be coherently driven to its ground state. In order to evaluate the time span over which the qubit can remain in its excited state before decaying, a so-called  $T_1$  measurement is performed.

In the beginning of such a measurement, the qubit is prepared in its ground state. A short pulse is applied to excite the qubit. In the Bloch sphere representation (see Sec. 2.4.1), a pulse that brings the qubit vector from the ground state (pointing in positive  $z$  direction) to the excited state (pointing in negative  $z$  direction) represents a rotation of  $\theta = \pi$  around the  $y$  axis. Hence, it is called a  $\pi$ -pulse. After this  $\pi$ -pulse in the  $T_1$ -measurement, the qubit decays freely over a time  $\Delta t$  before a readout pulse is applied. This shows how far the qubit decayed during  $\Delta t$ . The complete pulse sequence is shown in Fig. 4.19b.

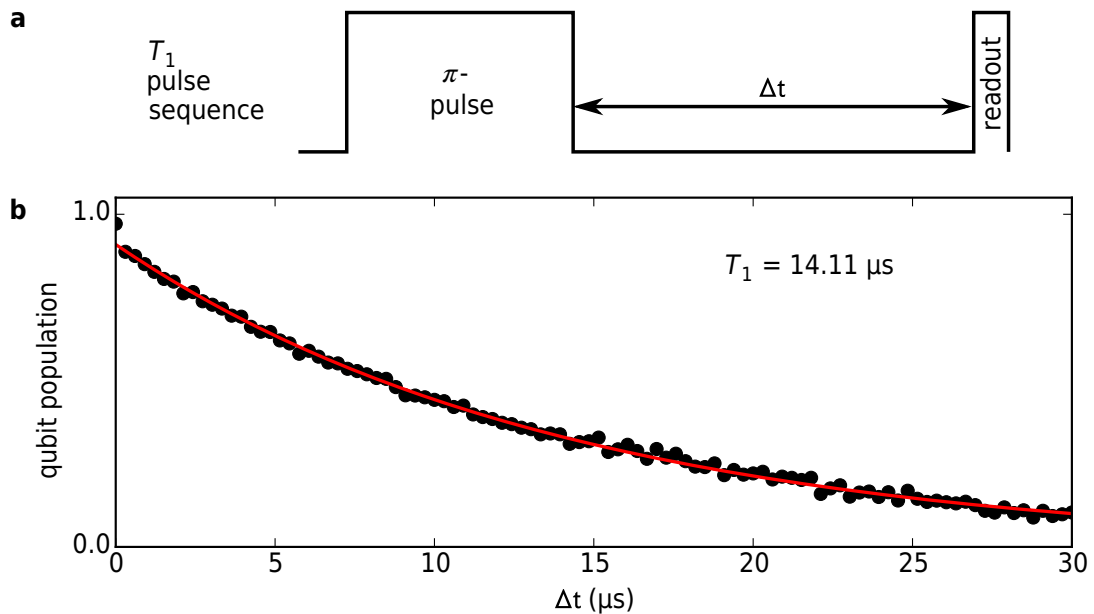


**Figure 4.19:** **a**  $T_1$  pulse sequence. Prepared in the ground state, the qubit is excited by a  $\pi$ -pulse. After a waiting time of  $\Delta t$ , the qubit state is read out by a readout pulse. **b** Repeating the pulse sequence with increasing waiting time  $\Delta t$ . Each circle including error bar represents a single measurement plotted over the corresponding  $\Delta t$  value. The measurement is fitted by an exponential decay (red solid line) giving the  $T_1$  lifetime of the qubit.

In Fig. 4.19b, the qubit decay is displayed. The qubit population is plotted over the waiting time  $\Delta t$ . 1.0 means the qubit is purely in the excited state, while for 0.0 it is in its ground

state. Fitting this exponential decay (solid line) results in a  $T_1$ -lifetime

$$T_1 = 14.11 \pm 0.30 \mu\text{s}. \quad (4.36)$$

In order to understand what limits the longitudinal relaxation time  $T_1$ , the so-called *Purcell effect* is considered [PTP46; Hou+08]. Due to their transversal coupling, the qubit can decay into the sideband mode. The decay rate of this process is given by [Hou+08]

$$\Gamma_{1,\text{Purcell}} = \left( \frac{g}{f_{\text{sb}} - f_{\text{q}}} \right)^2 \kappa = \left( \frac{g}{f_{\text{sb}} - f_{\text{q}}} \right)^2 \frac{2\pi f_{\text{sb}}}{Q_1}, \quad (4.37)$$

with sideband and qubit frequencies  $f_{\text{sb}}$  and  $f_{\text{q}}$ , coupling factor  $g$  and resonator decay rate  $\kappa$ .  $\kappa$  is determined by the coupling of the resonator to the feedline expressed by its loaded quality factor  $Q_1$ . It is obvious that the qubit decay depends on how strong it is coupled to the resonator and furthermore, how fast energy can decay from the resonator into the feedline. The Purcell limit of the  $T_1$  lifetime is given by the inverse loss rate and can be evaluated to

$$T_{1,\text{Purcell}} = \Gamma_{1,\text{Purcell}}^{-1} = \left( \frac{f_{\text{sb}} - f_{\text{q}}}{g} \right)^2 \frac{Q_1}{2\pi f_{\text{sb}}} \approx \left( \frac{6170 - 5290}{49.6} \right)^2 \frac{5000}{2\pi \cdot 6170} \mu\text{s} = 42.5 \mu\text{s}. \quad (4.38)$$

So, the measured  $T_1$  lifetime is a factor of three lower than it would be due to the Purcell limitation by coupling to the sideband mode. It is not clear yet, which further transversal decay channels are present in the system. The coupling to the main resonator mode at 6.22 GHz with a coupling strength of only  $g \approx 1$  MHz is too small to explain the  $T_1$  limit.

Except the longitudinal relaxation due to transversal coupling, the qubit can furthermore lose energy by longitudinal coupling to parasitic systems, e.g. on the surface of the circuit or intrinsically in the material. This is tested by a *Ramsey* or  $T_2^*$ -measurement.

In the beginning of such a measurement, the qubit is again prepared in its ground state. Then, a short  $\frac{\pi}{2}$ -pulse rotates the qubit vector around the x axis to the equator of the Bloch sphere. The qubit is kept there for a time  $\Delta t$  before another  $\frac{\pi}{2}$ -pulse rotates it back to the ground state. Directly after this pulse, a readout pulse is sent that will show how much the qubit decayed during the waiting time at the equator. The complete pulse sequence is shown in Fig. 4.20a.

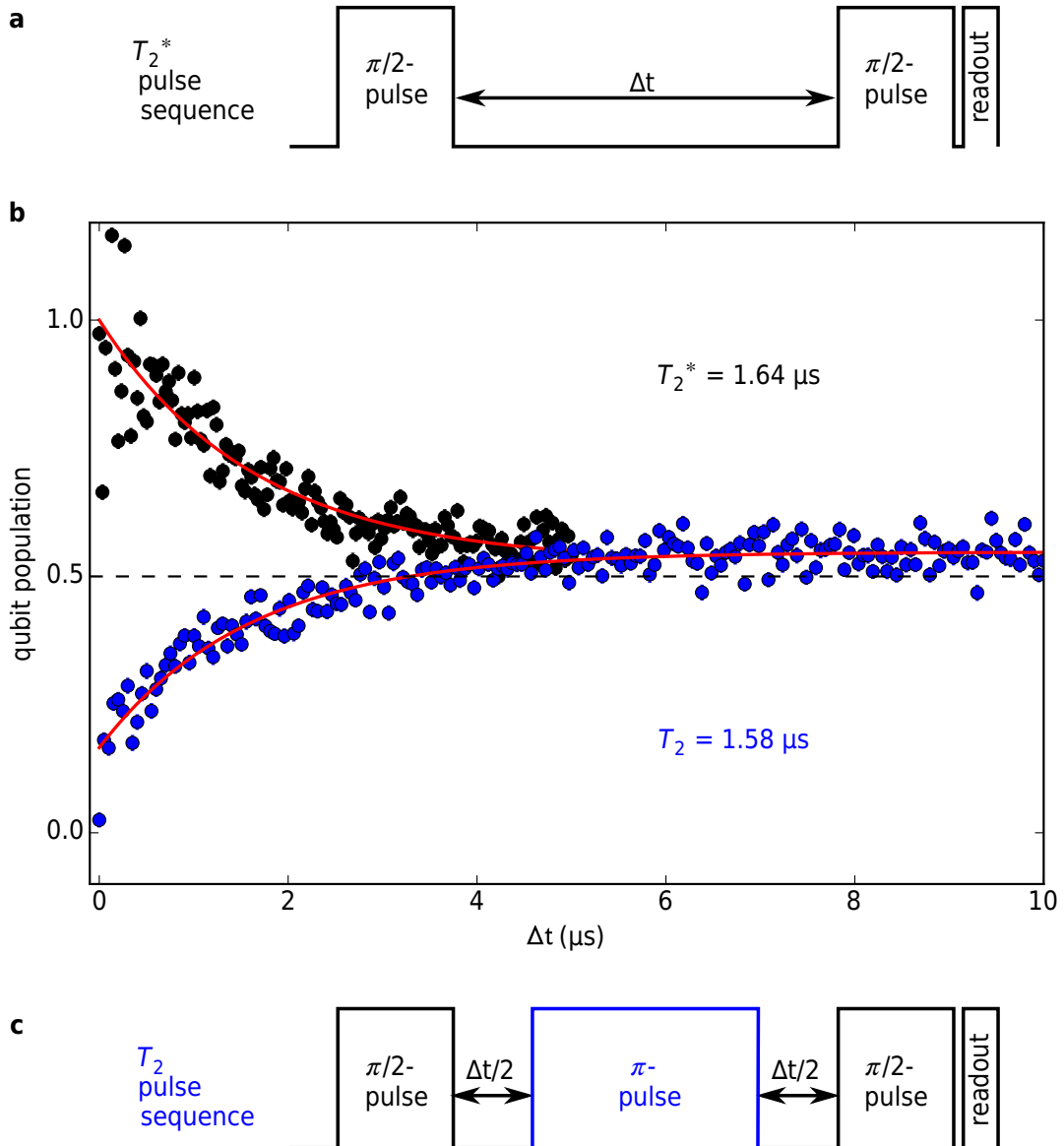


**Figure 4.20:** **a**  $T_2^*$  (Ramsey) pulse sequence. Prepared in the ground state, the qubit is excited by a  $\pi/2$ -pulse. After a waiting time of  $\Delta t$ , another  $\pi/2$ -pulse rotates it back to the ground state, where the qubit state is extracted by a readout pulse. **b** Repeating the pulse sequence from **a** with increasing waiting time  $\Delta t$ . Each black circle including error bar represents a single measurement plotted over the corresponding  $\Delta t$  value. The measurement is fitted by an exponential decay (upper red line) giving the  $T_2^*$  lifetime of the qubit. Repeating the pulse sequence from **c** with increasing waiting time  $\Delta t$ . Each blue circle including error bar represents a single measurement plotted over the corresponding  $\Delta t$  value. The measurement is fitted by an exponential decay (lower red line) giving the  $T_2$  lifetime of the qubit. **c**  $T_2$  (spin-echo) pulse sequence. The waiting time of  $\Delta t$  in the  $T_2^*$  (Ramsey) pulse sequence is interrupted by an additional  $\pi$ -pulse that rotates the qubit to the other side of the equator. This leads to refocussing before the qubit is rotated back to the ground state where the qubit state is extracted by a readout pulse.

The black circles in Fig. 4.20b represent the outcome of such a  $T_2^*$ -measurement. The qubit population is plotted versus the waiting time  $\Delta t$ . The qubit population is the same as in the  $T_1$  measurement presented in Fig. 4.19. Fitting this exponential decay (upper red line) results in a  $T_2^*$ -lifetime

$$T_2^* = 1.64 \pm 0.19 \mu\text{s}. \quad (4.39)$$

Two  $\frac{\pi}{2}$ -pulses are equivalent to the  $\pi$ -pulse which brings the qubit to its excited state in the aforementioned  $T_1$ -measurement. This is why in Fig. 4.20b the black circles start from a qubit population of around 1.0. The decay ends at a qubit population of around 0.5, which represents the point, where the excited and the ground state are equally populated.

It is clearly visible that  $T_2^* \ll T_1$  or not so-called  $T_1$ -limited. This means the qubit lost energy during the waiting time at the equator what can be caused by coupling to defect systems (e. g. intrinsically) or background noise. In order to get rid of this so-called *dephasing*, the Ramsey protocol can be enhanced by an additional  $\pi$ -pulse (blue in Fig. 4.20c) in the middle between the two  $\frac{\pi}{2}$ -pulses. The additional  $\pi$ -pulse projects the qubit vector to the opposite side of the equator in the Bloch sphere. This represents a reverse of time which then leads to a reverse of the dephasing. This reversal is called *refocussing*. The enhancement of the Ramsey measurement by a further  $\pi$ -pulse is called a *spin-echo* or  $T_2$ -experiment. Its complete pulse sequence is shown in Fig. 4.20c. Such a  $T_2$ -measurement was performed on the the presented system represented by the blue circles in Fig. 4.20b. Again the qubit population is plotted versus the waiting time  $\Delta t$ .

In comparison to the the  $T_2^*$ -measurement, the excess  $\pi$ -pulse brings the qubit back to the ground state. This is why in Fig. 4.20b the blue circles start from a qubit population of around 0.0. Also here the decay approaches 0.5. That it actually exceeds 0.5 can be due to the fact that pulses did not bring the qubit perfectly to the equator. The decay resulted in a  $T_2$ -lifetime of

$$T_2 = 1.58 \pm 0.08 \mu\text{s} \approx T_2^*, \quad (4.40)$$

taken from the exponential fit (lower red line). This means the refocussing  $\pi$ -pulse did not compensate the dephasing. This indicates that the frequency cut-off that is given by halving the time  $\Delta t$  with the  $\pi$ -pulse is lower than the noise frequency that causes the dephasing.

### 4.1.8. Discussion and Conclusion

The experiment presented in this section was intended to show coherent quantum phase slip (cQPS) in a very thin wire made from granular aluminium ( $\text{AlO}_x$ ). Although the nanowire was designed to act as a quantum phase slip junction (QPSJ) as suggested in [MN06] forming a quantum phase slip flux qubit (QPSFQ) when embedded into a loop, as it was theoretically predicted in [MH05] and experimentally realized in [Ast+12; Pel+13], the measurements suggest that the Josephson effect - the dual to the QPS effect [MN06] - was still dominating over the nanowire.

$\text{AlO}_x$  was chosen because of its high normal conducting sheet resistance which can be adjusted during its fabrication process [Rot+17]. The high normal conducting sheet resistance of a wire allows for high kinetic inductance in the superconducting state, a prerequisite for quantum phase slip to occur. The second important constraint that had to be met was a wire diameter on the order of the superconducting coherence length of the  $\text{AlO}_x$  thin film.

For the present experiment, a nanowire with a width of 20 nm and a length of 250 nm was embedded into a loop, both made from the same  $\text{AlO}_x$  thin film. Due to the large loop size, the persistent current in the loop, which is driven by the external magnetic field, is lower than the critical current of the nanowire. This was a further prerequisite of the experiment. The loop-nanowire system was capacitively coupled to the electric field mode of the resonator. As suggested by the observations in the experiment, the resonator and the loop created a sideband resonance mode besides the fundamental resonator mode. The sideband mode appeared to be the more interesting candidate to investigate the loop-nanowire system's properties rather than the resonator because the coupling to the sideband mode was much stronger.

Although the prerequisites were met, the nanowire seemed to have formed a long, dirty Josephson weak link [Lik79] rather than a QPSJ. Possibly, a width of 20 nm was still too wide and due to its intrinsic granular structure, the nanowire might have formed a Josephson weak link junction. Embedding the nanowire into the loop, an RF SQUID system seemed to be made up similar to experiments like [Fri+00; RHL95]. The system gave rise to metastable fluxon states in the loop and therewith hysteretic behaviour. The system's potential landscape was modelled by the quadratic dependence of the magnetic energy on flux with deep wells caused by the sinusoidal weak link energy dependence on flux. Using certain preparation, the system could be prepared into configurations where coherent tunnelling between fluxon states took place. Based on this, a tunnelling two-level system was formed which coupled strongly to the sideband resonance mode. At resonance, two-level system and sideband mode exhibited anticrossings. Via a dispersive readout technique, the magnetic field dependence of the level transition could be subsequently monitored.

Further investigation revealed that the two-level system's transition energy depends on the

electric field strength of the resonance sideband mode. This is well known as AC Stark effect. Furthermore, Rabi oscillations could be successfully performed on the two-level system. This proved that the system represents a qubit with distinct lifetime. Time domain measurements disclosed that the two-level system exhibits interesting coherence properties given a longitudinal relaxation time of  $T_1 = 14.11 \mu\text{s}$ . The qubit was clearly subject to dephasing since its transversal  $T_2^*$ -lifetime was not  $T_1$ -limited but an order of magnitude lower ( $T_2^* = 1.64 \mu\text{s}$ ). Even spin-echo experiments with the aim of reducing the dephasing effect by a refocussing pulse did not improve the transversal lifetime ( $T_2 \approx T_2^*$ ). The reason for the dephasing in the system has to be investigated in the future and might shed light on the intrinsic properties of the granular thin film.

It also remained for further studies to find out the conditions which have to be met to have coherent quantum phase slips dominating the wire dynamics. Potential perspectives are further reduction of the wire diameter and/or a consequent increase of the normal conducting sheet resistance of the  $\text{AlO}_x$  films. The latter would bring the material closer to the superconductor to insulator transitions. Both perspectives are favourable for cQPS to occur.

## 4.2. Galvanically coupled constriction loop

In the following, experiments on coherent quantum phase slip (cQPS) in NbN constrictions are presented. The measurements were performed at the Royal Holloway, University of London (RHUL), Egham, UK, as part of an internship in the group of Prof. Dr. O. Astafiev.

The superconducting, granular NbN thin film used in the following experiments is 3.3 nm thick and was deposited by the PEALD technique outlined in Sec. 3.1.2 in 72 cycles. The film shows a superconducting transition at 4.7 K with a sheet resistance of 2.0 k $\Omega$ .

Referring to Eq. (2.15), this leads to a sheet kinetic inductance of

$$L_{\text{kin},\square} = 0.18 \frac{\hbar}{k_{\text{B}}} \cdot \frac{2.0 \text{ k}\Omega}{4.7 \text{ K}} = 0.585 \cdot 10^{-9} \text{ H} = 0.585 \text{ nH}. \quad (4.41)$$

The idea for the following experiment originates in the experimental findings in [Pel+13]. The major idea is to observe a dependence of the QPS energy  $E_{\text{s}}$  on the width of the phase slip element. While in [Pel+13] nanowires with lengths of few hundreds of nm were used, here constrictions with a length of only 60 nm are embedded to enhance the controllability of  $E_{\text{s}}$  as discussed in Sec. 2.2.2.

### 4.2.1. Sample design and measurement setup

As can be seen in Fig. 4.21, 16 loops with one constriction per loop are galvanically coupled to the centre of a CPW  $\lambda/2$ -resonator which is capacitively coupled at each end to a microwave feedline. The loops are designed with different loop areas and the constriction width is varied in such a way that there is always a pair of loops with the same constriction width. Thus, 8 different constriction widths are under investigation. The exact design parameters of all loops and constrictions can be found in Tab. 4.2.

The loops are placed in the centre of the resonator where it has its maximum current for odd resonance modes. Due to the galvanic coupling of loops and resonator, this current is superposed by the persistent current circulating in the loops induced by an external magnetic field.

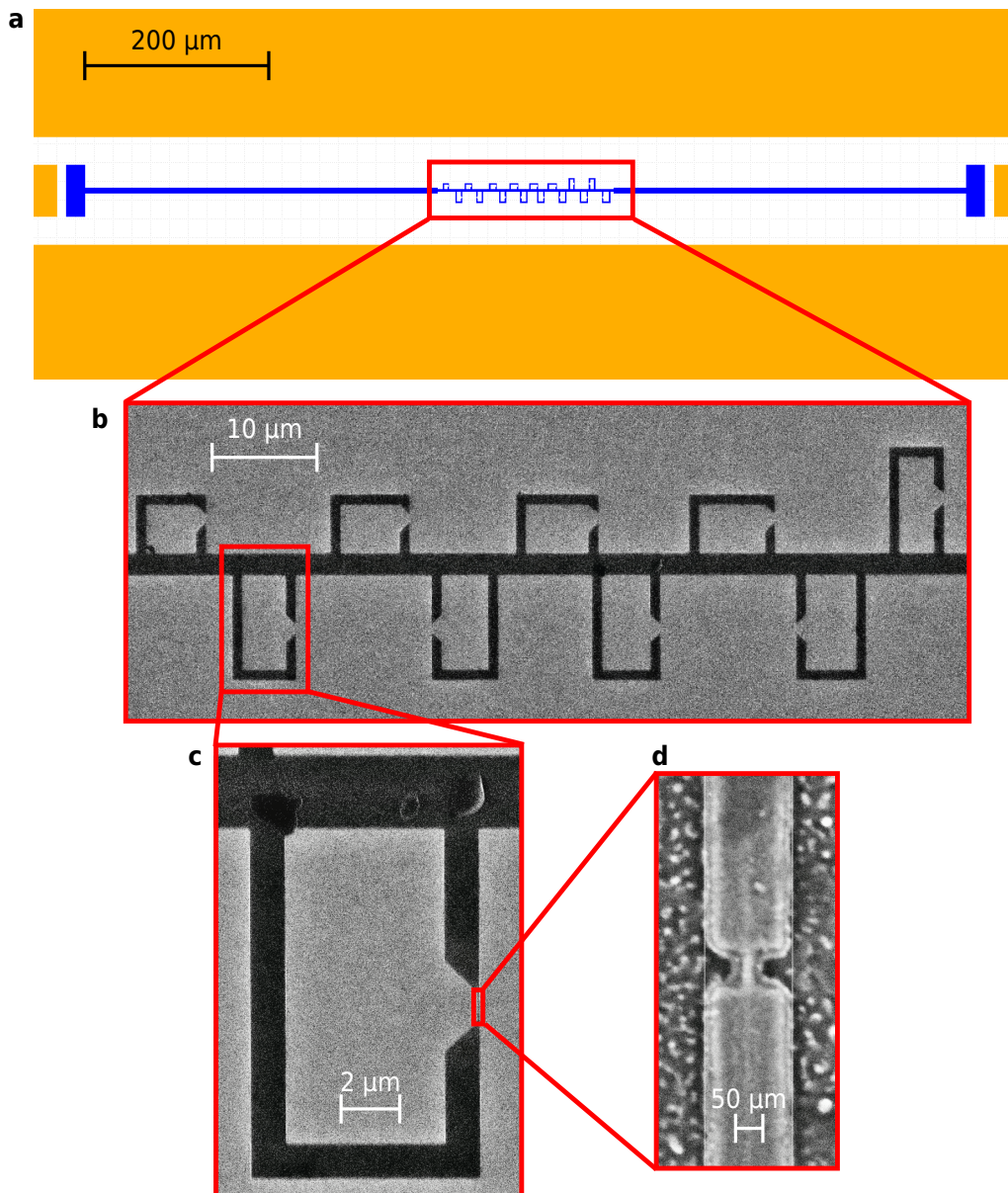


**Figure 4.21:** **a** 16 different loops with constrictions galvanically coupled to the center of a CPW  $\lambda/2$ -resonator (blue). Above and below, there are ground planes, left and right, microwave connection pads are placed (all yellowish). **b** A SEM picture of the 9 inner loops presenting the variation of loop sizes and shared coupling inductances. **c** Zoom onto a single loop. The loop wire width is 1.2  $\mu\text{m}$ . **d** Further zoom onto the constriction with a width of 51 nm. It can be seen that the complete structure shows an additional surrounding which is due to overexposure in the e-beam process. As mentioned in Sec. 3.2.3, the  $\text{CF}_4$  based RIE process attacks silicon which leads to the white dots around the constriction. The different shades of grey represent areas with different electrical conductivity.

#### 4.2. Galvanically coupled constriction loop

position	loop	inner loop area ( $\mu\text{m}^2$ )	mid loop area ( $\mu\text{m}^2$ )	no. loop squares	no. coupling squares	coupling (%)	test $w_{\text{constr}}$ (nm)	actual $w_{\text{constr}}$ (nm)
top	1	23.18	38.11	26.32	2.54	9.65	12	48
left	2	28.89	45.83	26.69	2.99	11.20	16	56
	3	31.21	48.93	27.26	3.14	11.52	18	59
	4	37.21	57.03	28.67	3.6	12.56	21	59
	5	39.06	59.57	29.05	3.75	12.91	28	62
	6	41.56	62.83	29.51	3.9	13.22	34	65
top	7	43.19	64.30	34.05	2.5	7.34	36	73
right	8	46.79	68.54	35.56	2.66	7.48	40	75
bottom	9	49.13	71.28	35.79	2.73	7.63	40	75
left	10	51.14	73.64	36.03	2.81	7.80	36	73
	11	53.15	76.01	36.3	2.88	7.93	34	65
	12	57.08	80.61	36.74	3.03	8.25	28	62
	13	59.09	82.98	36.97	3.11	8.41	21	59
	14	61.53	85.84	37.2	3.19	8.58	18	59
bottom	15	67.15	92.44	37.9	3.41	9.00	16	56
right	16	68.74	94.31	38.13	3.49	9.15	12	50

**Table 4.2:** Design parameters of all 16 loops and constrictions that are coupled to the CPW  $\lambda/2$ -resonator. The test  $w_{\text{constr}}$  is the width of a test constriction structure which is on the same chip as the actual  $w_{\text{constr}}$ . The difference in widths between them results from overexposure due to bigger structures surrounding the actual constrictions. The depicted width values are within an error margin of  $\pm 10\%$ .

In Fig. 4.21b, it is shown how the single loops differ from each other in loop size and shared coupling inductance. The loop wire width of all loops is  $1.2\mu\text{m}$ . Fig. 4.21d depicts a single constriction with a width of  $51\text{nm}$ . One can see that it consists of an inner structure surrounded by some additional area. This additional part results from an e-beam overexposure due to the bigger structures surrounding the constriction. This is why the measured or actual constrictions in Tab. 4.2 are wider than the test constrictions which are on the same chip but have no surrounding structures. The fabrication details of the experimental chip are listed in A.1.2.

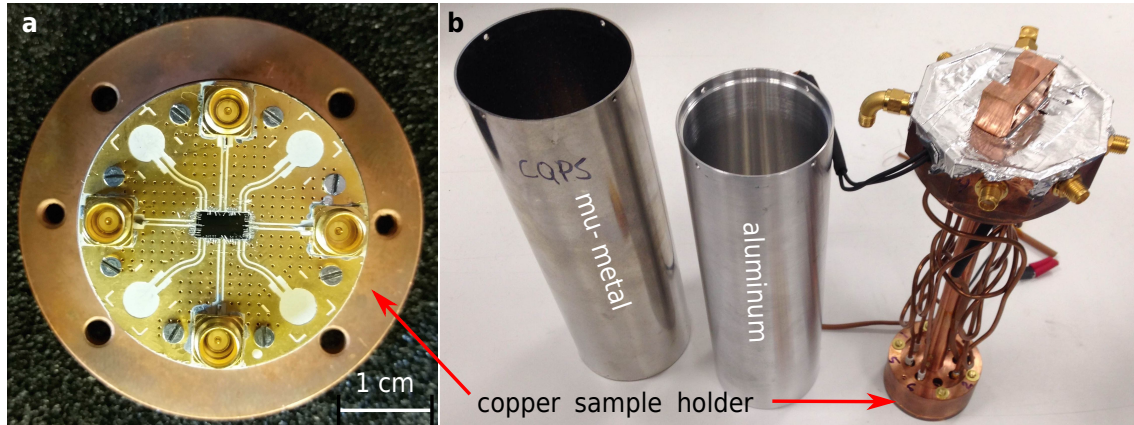


**Figure 4.22:** **a** On-chip experiment (black) glued in the centre of a gold coated PCB. The left and right PCB connection ports are used for the transmission measurement. Contacts between chip and PCB are done via aluminium wire bonds. The PCB is mounted on a copper holder. **b** The copper holder is covered by a copper cover incorporating a solenoid coil (right bottom). The closed copper holder is mounted onto a post which is fixed at the mixing chamber of the cryostat. Cryoperm (left) from muShield and superconducting aluminium (mid) shield will protect the mounted post (right) against stray magnetic fields.

As can be seen in Fig. 4.22a, the chip (see Fig. 4.21a) is glued onto a microwave printed circuit board (PCB)<sup>4</sup> which is structured with CPW feedlines matched to  $50 \Omega$ . The PCB is gold coated to ensure high conductivity. The contact between on-chip microwave feedline and PCB feedlines as well as between on-chip and PCB ground planes is done by  $25 \mu\text{m}$  wide aluminium bond wires. Since the on-chip microwave connectors are also matched to  $50 \Omega$ , power loss due to strong reflections can be avoided. The PCB is mounted onto a copper holder. This holder can be closed by a copper cover to reduce microwave radiation losses into open space (see Fig. 4.22b). In this round cover a solenoid coil made from niobium titanium wire is integrated which supplies the necessary global perpendicular magnetic field for the experiment. By preceding characterization, the magnetic field of this coil per applied current at the position of the loops was determined to  $154 \text{ mT/A}$ . The closed sample box is mounted at the cryostat's base plate and placed inside a cryoperm shield (see Fig. 4.22) to avoid influences by stray magnetic fields. All CQUID measurements following from here were done at  $T = 12 \text{ mK}$ . Details on the microwave components and cryostat utilized in this setup can be found in Tab. 3.3.

<sup>4</sup>The PCB material is TMM®10i by Rogers Corporation.

### 4.2.2. Frequency spectroscopy

The sample is cooled down to 12 mK and measured at a microwave power level of  $-115$  dBm. In Fig. 4.23, the frequency spectrum of the microwave signal transmitted through the experimental chip, which is installed in the described setup, is displayed (black line).

The red line shows a simulation of the resonator fundamental frequency using a sheet kinetic inductance value of  $0.55$  nH. The fundamental resonator frequency mode at  $4.15$  GHz agrees well between measurement and simulation. The value of  $0.55$  nH differs from  $0.585$  nH (see Eq. (4.41)) calculated from the superconducting transition by about  $6\%$ . For all further measurements, either the fundamental mode or the second harmonic is used. The loaded quality factor  $Q_1$  of the fundamental mode is around  $600$  and of the second harmonic is even lower. This points out that the resonator is strongly coupled to the signal line. It has to be further stated that the fundamental resonance peak is split into two parts. For the subsequent described measurements, the left part of the peak at  $4.15$  GHz shows no magnetic field dependence while the right one at  $4.3$  GHz does. The reason is not completely clear but it could be due to the resonator-loop coupling which will be explained in the following.

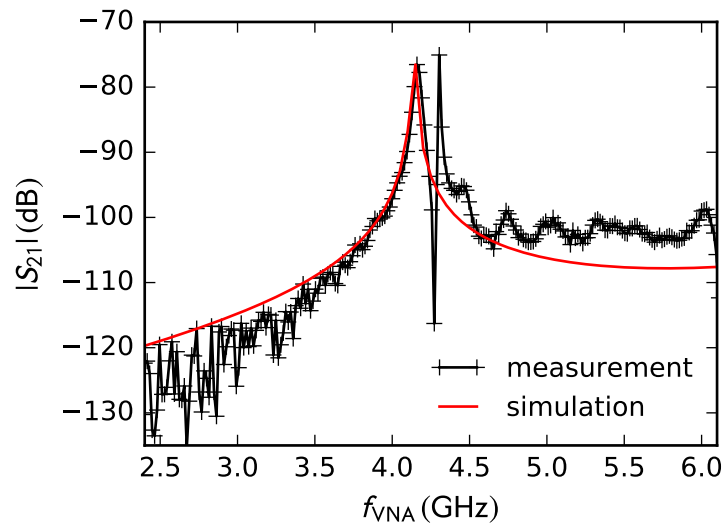


**Figure 4.23:** Transmission amplitude  $|S_{21}|$  plotted versus frequency. The spectrum is measured at  $-115$  dBm and  $12$  mK (black line). For the fundamental resonance mode, a simulation with a kinetic sheet inductance of  $0.55$  nH (red line) is in very good agreement with the measurement.

### 4.2.3. Magnetic field spectroscopy

For the subsequent measurement, the magnetic field perpendicular to the loops is swept over more than  $154\ \mu\text{T}$  in steps of  $60\ \text{nT}$  and the resonance frequency of the fundamental mode is monitored. In Fig. 4.24, the phase value at the resonance frequency is plotted versus the applied magnetic field. At a specific magnetic field value the phase starts to decrease with increasing magnetic field which in this case translates into a decreasing resonance frequency (see Fig. 4.26). The phase decreases until it abruptly jumps to a value much higher than it originally started with. This means that the resonance frequency jumps to a higher value than it initially had and stays around there up to the dashed line. In one of the coupled loops, the constriction allows for magnetic fluxons to coherently tunnel between two adjacent fluxon states. As shown in Sec. 2.4, the loop then forms a quantum phase slip flux qubit (QPSFQ) in which the transition frequency between two adjacent fluxon states depends on the externally applied magnetic field (see Eq. (2.56)). It has to be noted that in the following, the two-level systems that are formed by the loops with embedded constrictions, are synonymously called qubits. Although no Rabi oscillations could be performed due to short lifetimes and setup limitations, recent experiments with similar QPSFQ systems have shown Rabi oscillations [Pel+16].

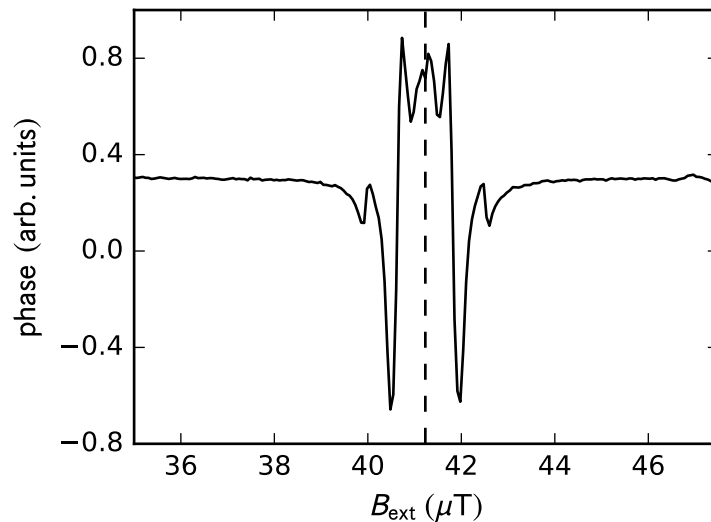


**Figure 4.24:** Resonator phase signal at resonance plotted versus applied magnetic field. An avoided level crossing between qubit and resonator can be observed with virtual mirror axis (dashed line). The measurement is performed at  $-115\ \text{dBm}$  and  $12\ \text{mK}$ .

As a result of strong coupling, qubit and resonator will avoid each other when their eigenstates become equal. In other words, they form degenerate dressed states. In Fig. 4.24, such an *avoided level crossing* or *anti-crossing* respectively is observed where the qubit transition frequency equalizes with the resonator frequency. This leads to the observed

frequency decrease and the jump at certain magnetic field values [Ast+12; Pel+13]. This indicates coupling between resonator and qubit.

The fact that for a further increase of the magnetic field, a behavior mirrored to the aforementioned takes place is due to the fact that at the virtual mirror axis (dashed line in Fig. 4.24), the qubit reaches its minimum transition frequency or sweet spot<sup>5</sup>, respectively (see Eq. (2.56)). Afterwards it increases again and crosses the resonator frequency a second time.

As described in Sec. 2.4, for a QPSFQ, the pattern seen in Fig. 4.24 has to repeat with further increasing magnetic field with a  $\Phi_0$  periodicity. In Fig. 4.25*top*, it is clearly visible that the pattern recurs with a period of 54.1  $\mu\text{T}$ . Furthermore, a much smaller periodic feature can be observed. This can be seen more clearly in Fig. 4.25*bottom*.

Its period is much smaller, namely 21.8  $\mu\text{T}$ . Since the effect on the phase or the resonance frequency respectively is much smaller than for the first pattern, it can be assumed that the coupling of this second qubit is weaker than of the first one. This will be discussed shortly.

For each loop, the periodicity in magnetic field is given by

$$\Phi_0 = B_{\text{ext}} \cdot A_{\text{loop}}, \quad (4.42)$$

where  $B_{\text{ext}}$  is the externally applied magnetic field and  $A_{\text{loop}}$  is the loop area. Calculating the loop areas from the measured magnetic field periodicities, gives

$$A_{\text{loop},1} = \frac{\Phi_0}{54.1 \mu\text{T}} = 38.22 \mu\text{m}^2,$$

$$A_{\text{loop},2} = \frac{\Phi_0}{21.8 \mu\text{T}} = 94.85 \mu\text{m}^2.$$

As explained in Sec. 2.1.2, to calculate the magnetic flux enclosed in the loop, the path inside the superconducting ring has to be taken. Hence, the calculated loop areas have to be compared with the *mid loop areas* in Tab. 4.2.  $A_{\text{loop},1}$  is in excellent agreement with **loop 1** while  $A_{\text{loop},2}$  nicely agrees with **loop 16** both with less than 1 % deviation. In particular,  $A_{\text{loop},2}$  shows that the *inner loop area* presented in Tab. 4.2 cannot explain the periodicity.

---

<sup>5</sup>At the minimum transition frequency, the transition is minimally affected by magnetic field fluctuations. This improves the qubit lifetime, which makes this a *sweet spot* to measure the qubit.

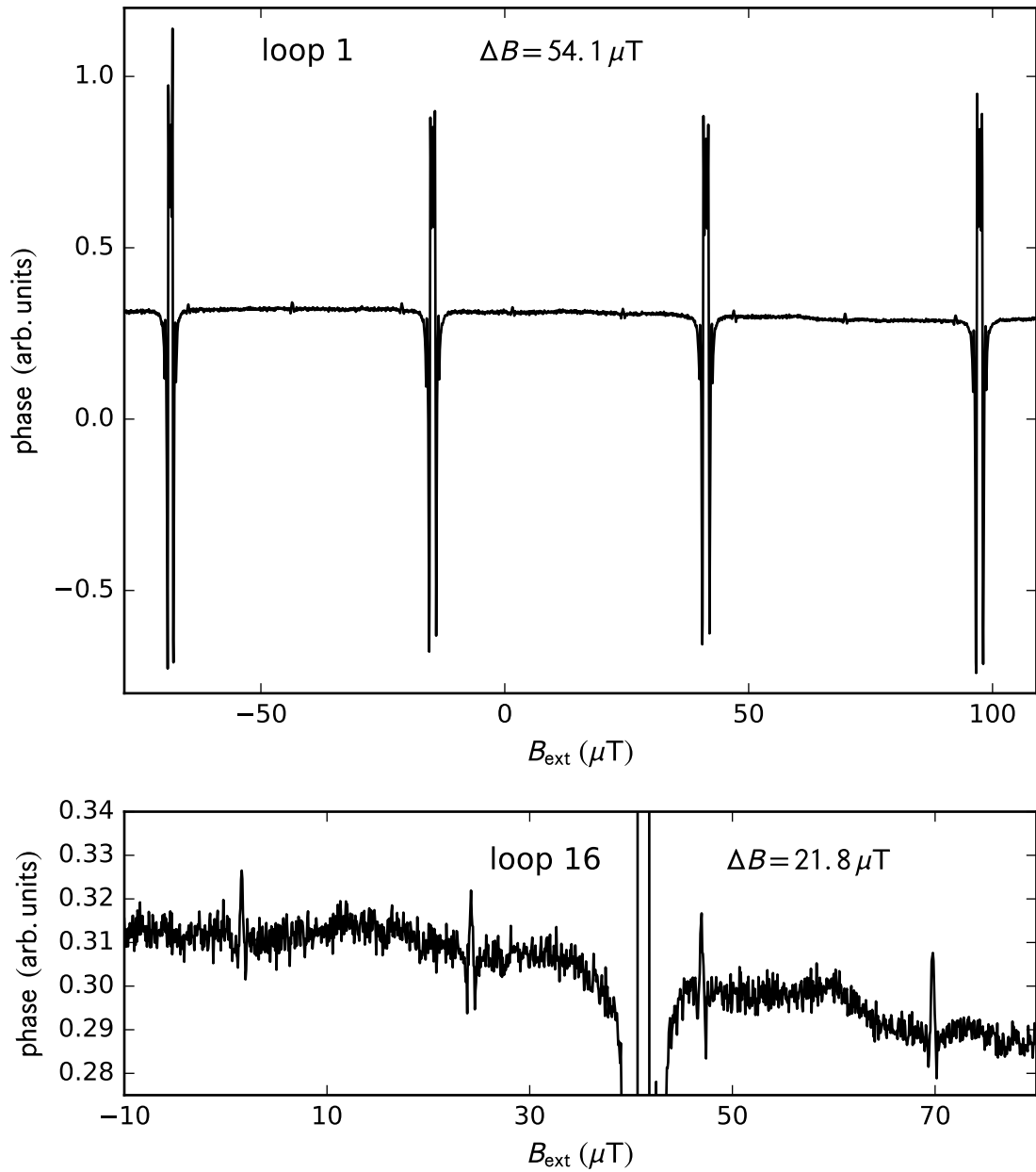


**Figure 4.25:** The same measurement as shown in 4.24 performed over a large magnetic field range (black line). *top* Four anti-crossings with a periodicity in magnetic field of  $54.1 \mu\text{T}$  can be observed. *bottom* Zoom onto a much smaller periodic pattern. It has a magnetic field periodicity of  $21.8 \mu\text{T}$ .

#### 4.2.4. Coupling strength

In anticipation of the qubit transition which is mapped in the subsequent subsection and with the knowledge of the design parameters, one can evaluate the qubit-resonator coupling strength. The qubit is galvanically coupled to the resonator by a shared piece of inductance or through shared currents, respectively. In the flux eigenbasis, the coupling of the QPSFQ with its Hamiltonian (see Eq. (2.50)) to the resonator can be expressed by [Ast+12; Pel+13]

$$hg_{\Phi} = MI_r I_p, \quad (4.43)$$

where  $g_{\Phi}$  represents the coupling strength in the flux eigenbasis,  $h$  is Planck's constant,  $M$  the mutual inductance between resonator and loop,  $I_r$  the current in the resonator and  $I_p$  the persistent current in the loop. Here, the mutual inductance simply is the shared inductance  $L_{\text{coupl}} = N_{\text{coupl}} \cdot L_{\text{kin},\square} = 2.54 \cdot 0.585 \text{ nH} = 1.49 \text{ nH}$ . Taking into account that the resonator current oscillates sinusoidally with the fundamental mode frequency  $f_r = 4.30 \text{ GHz}$ , the resonator current can be calculated by  $I_r = \sqrt{hf_r/2L_r}$  [Tza+07]. The resonator frequency is completely dominated by the resonator's kinetic inductance. With a number of squares of  $N_r = 400$ , this leads to an inductance of  $L_r = N_r \cdot L_{\text{kin},\square} = 400 \cdot 0.585 \text{ nH} = 234 \text{ nH}$  and a resonator current of  $I_r = 2.47 \text{ nA}$ . With a persistent current of  $I_p = 66.76 \text{ nA}$  taken from the fit in Fig. 4.27, the coupling in the flux frame calculates to

$$\frac{g_{\Phi}}{h} = 1.49 \text{ nH} \cdot 2.47 \text{ nA} \cdot 66.76 \text{ nA}/h = 370.65 \text{ MHz}. \quad (4.44)$$

However, the presented measurements are not performed in the flux frame but in the qubit frame. The qubit frame Hamiltonian can be derived by diagonalizing the Hamiltonian in the flux eigenbasis consisting of the qubit (see Eq. (2.50)), the resonator and the coupling energy  $g_{\Phi}$

$$H = \frac{hf_q}{2}\sigma_z + hf_r a^{\dagger}a + hg(a^{\dagger} + a)\sigma_x. \quad (4.45)$$

$f_q$  and  $f_r$  are the qubit and resonator frequencies,  $a^{\dagger}$ ,  $a$  are the photon creation and annihilation operators and  $\sigma_{x,z}$  are the Pauli matrices. The qubit-resonator coupling  $g$  in the qubit frame is then given by [Oel+10]

$$\frac{g}{h} = \frac{g_{\Phi}}{h} \cdot \frac{E_s}{E_q}. \quad (4.46)$$

Here,  $E_s$  is the tunnelling energy and  $E_q$  the flux-dependent qubit energy.

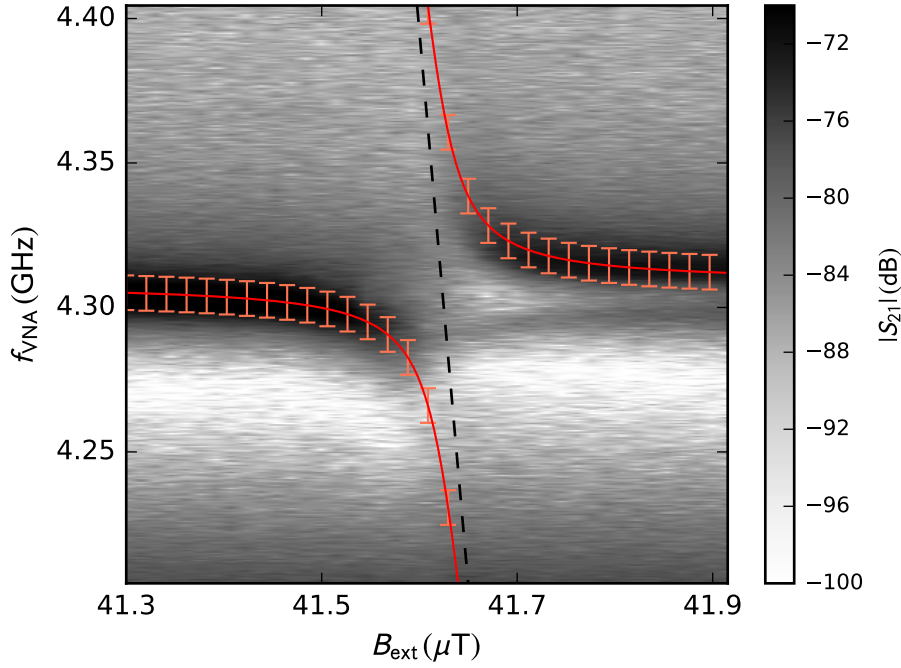


**Figure 4.26:** Avoided level crossing of qubit 1 and resonator fundamental mode displayed as grey-scale coded microwave transmission amplitude versus probe frequency and magnetic field. The red line is the fit of Eq. (4.45) while the black dashed line represents the qubit transition observed in Fig. 4.27.

Fig. 4.26 presents a measurement of the anti-crossing of qubit 1 and the resonator fundamental mode. In contrast to Fig. 4.24, here the microwave amplitude  $|S_{21}|$  is plotted in grey-scale versus magnetic field and frequency. The microwave power level of the vector network analyser (VNA) is at  $-125$  dBm. The aforementioned shift of the resonator peak (black) down to lower frequencies with increasing magnetic field and the abrupt jump to higher frequencies are clearly visible. This anticrossing is fitted by Eq. (4.45) taking into account the fitted parameters from the qubit spectroscopy. This results in a coupling of

$$\frac{g}{h} = 63.68 \pm 1.30 \text{ MHz}. \quad (4.47)$$

With a qubit sweet spot frequency  $f_{\text{sweet}} = E_s/h = 940$  MHz and a qubit energy  $E_q$  which equals the resonator energy  $E_r = h_r = 4.30$  GHz - since the coupling energy is evaluated at the anti-crossing - the coupling is calculated to

$$\frac{g}{h} = \frac{g\Phi}{h} \cdot \frac{f_{\text{sweet}}}{f_r} = 370.65 \text{ MHz} \cdot \frac{0.94 \text{ GHz}}{4.30 \text{ GHz}} = 81.02 \text{ MHz}. \quad (4.48)$$

This value is in agreement with the condition for strong qubit-resonator coupling, namely that the coupling  $g$  has to be larger than the resonator decay rate  $\kappa = f_{\text{res}}/Q \approx 7$  MHz. Since the same condition demands  $g$  to be larger than the qubit decay rate  $\gamma$ , this gives an upper estimate for the qubit decay time of roughly 10 ns. This is in agreement with [Pel+16].

Eq. (4.48) is based on the assumption that there are no microwave photons in the resonator. Hence,  $I_r = \sqrt{hf_r/2L_r}$  can be derived from the average quantum fluctuations in the resonator [Tza+07]. The coupling dependence on the photon number  $n$  in the resonator can be expressed by [Oel+10]

$$g_n = \frac{g_0}{\sqrt{n+1}}, \quad (4.49)$$

where  $g_0$  is the coupling strength at zero photons in the resonator given by Eq. (4.46). An increasing number of photons in the resonator leads to decreasing coupling strength in the qubit frame. This is obvious if one imagines a large number of photons in the resonator or a large resonator current, respectively. In such a case, the resonator sees the persistent current only as very weak perturbation. The anti-crossing will be suppressed for increasing resonator currents resulting in a decreased observed coupling strength. Using Eq. (4.50), the calculated number of photons in the resonator is

$$n = \left(\frac{g_0}{g_n}\right)^2 - 1 = \left(\frac{81.02 \text{ MHz}}{63.68 \text{ MHz}}\right)^2 - 1 = 0.62. \quad (4.50)$$

This indicates, that the measurement is performed with around a single photon in the resonator.

### 4.2.5. Transition spectroscopy

In order to measure the transition frequency of a qubit, an additional microwave *drive tone* is transmitted to the sample. The signal of the VNA is fixed to the resonator frequency and used solely to read out the resonator. In the following, it is called *readout tone*. When the drive tone is close to the transition frequency of the qubit, it coherently drives periodic Rabi oscillations between the qubit states (see Sec. 2.4.1). This leads to a modulation of the resonator with the Rabi frequency (see Eq. (2.61)) and hence a dispersive shift of the resonator, as explained in Sec. 2.4.3. This shift can be measured by monitoring the probe tone.

In Fig. 4.27, such a dispersive shift measurement of loop 1 is presented. The phase signal of the resonator at resonance is displayed in grayscale versus microwave drive frequency  $f_{\text{mw}}$  and externally applied magnetic field  $B_{\text{ext}}$ . Where the microwave drive equalizes the qubit transition, a dispersive shift of the resonator and hence a change in the phase signal is caused. According to Eq. (2.56), the qubit transition frequency  $f_{\text{q}}$  depends on the externally applied magnetic field  $B_{\text{ext}}$  or magnetic flux  $\Phi$ , respectively

$$f_{\text{q}} = \frac{1}{h} \sqrt{(2I_{\text{p}}\delta\Phi)^2 + E_{\text{s}}^2}. \quad (4.51)$$

The red line in Fig. 4.27 represents a fit of Eq. (4.51) to the observed qubit transition. It gives a phase slip energy of

$$E_{\text{s}}/h = 940.26 \pm 37.60 \text{ MHz}, \quad (4.52)$$

mentioned above as the sweet spot frequency  $f_{\text{sweet}}$  and a persistent current of

$$I_{\text{p}} = 66.76 \pm 2.67 \text{ nA}. \quad (4.53)$$

Considering a number of squares of the qubit loop of  $N_{\text{loop}} = 26.32$  (see Tab. 4.2), this leads to a sheet kinetic inductance of

$$L_{\text{kin},\square} = \frac{\Phi_0}{2I_{\text{p}}N_{\text{loop}}} = 0.586 \text{ nH}, \quad (4.54)$$

which is in good agreement with Eq. (4.41) and the resonator frequency simulation.

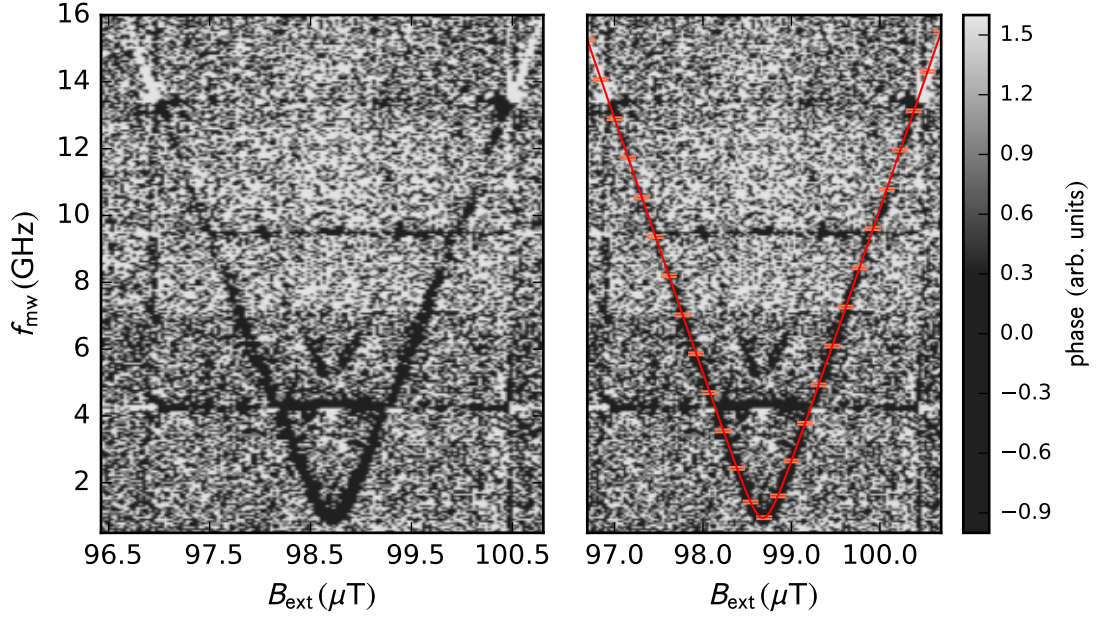


**Figure 4.27:** Dependence of the transition of qubit 1 on magnetic field investigated by dispersive readout technique. The readout power level is at  $P_{\text{VNA}} = -115$  dBm while the drive power level is at  $P_{\text{mw}} = -75$  dBm both including setup attenuation. *left* The phase signal at the second harmonic resonance of the resonator is plotted in grayscale versus additional drive frequency  $f_{\text{mw}}$  and external magnetic field  $B_{\text{ext}}$  which is applied perpendicular to the sample. When  $f_{\text{mw}} = f_{\text{q}}(B_{\text{ext}})$ , the resonator experiences a dispersive shift due to coupling. *right* The transition is fitted (red line) by Eq. (4.51).

In Fig. 4.28, the same measurement is presented for loop 16. A fit of the transition with Eq. (4.51) gives a QPS energy of  $E_{\text{s}} = 300.18 \pm 9.00$  MHz with a persistent current of  $I_{\text{p}} = 46.29 \pm 1.39$  nA carried by the loop. Under consideration of the loop's number of squares  $N = 38.13$ , this leads to a kinetic sheet inductance of  $L_{\text{kin},\square} = 0.584$  nH which is in nice agreement with qubit 1.

In Tab. 4.3, the important parameters of the two measured qubits are listed again.

qubit	$E_{\text{s}}/h$ (MHz)	$I_{\text{p}}$ (nA)	$L_{\text{kin},\square}$ (nH)	$w_{\text{con}}$ (nm)
1	940.26	66.76	0.586	51 ( $\pm 2-5\%$ )
16	300.18	46.29	0.584	51 ( $\pm 2-5\%$ )

**Table 4.3:** Important parameters of the two measured qubits.

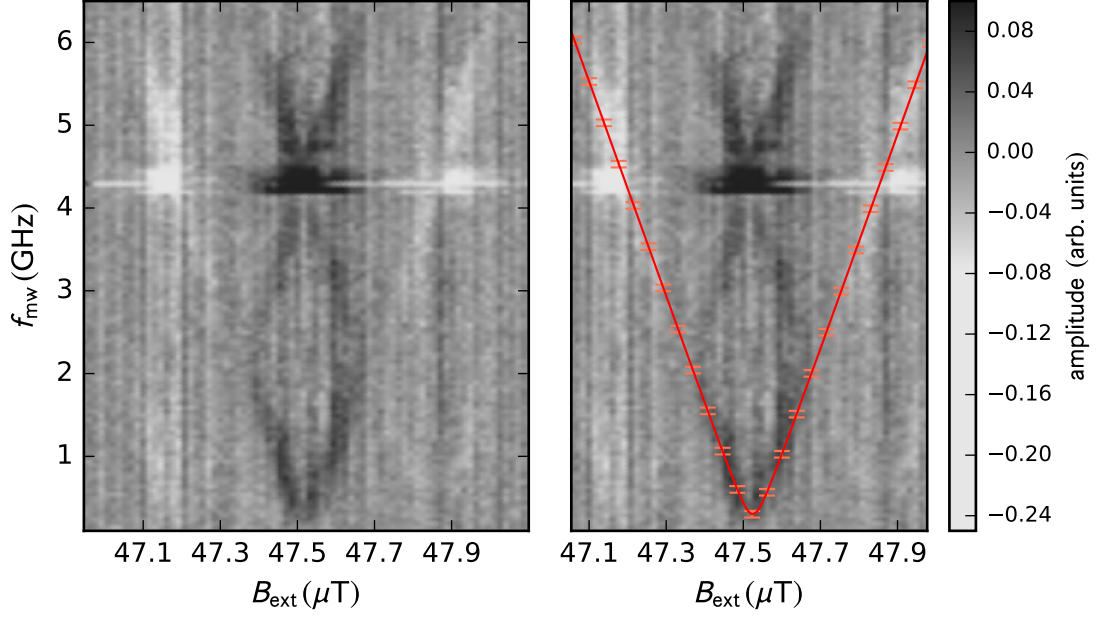


**Figure 4.28:** Dependence of the transition of qubit 16 on magnetic field investigated by dispersive readout technique. The readout power level is at  $P_{\text{VNA}} = -115$  dBm while the drive power level is at  $P_{\text{mw}} = -75$  dBm both including setup attenuation. *left* The amplitude signal at the fundamental resonance of the resonator is plotted in grayscale versus additional drive frequency  $f_{\text{mw}}$  and external magnetic field  $B_{\text{ext}}$  which is applied perpendicular to the sample. When  $f_{\text{mw}} = f_{\text{q}}(B_{\text{ext}})$ , the resonator experiences a dispersive shift due to coupling. *right* The transition is fitted (red line) by Eq. (4.51).

In the following the measured coherent QPS amplitudes (see Tab. 4.3) are compared with theoretical estimations. To calculate  $E_s$  theoretically, Eq. (2.29) is used

$$E_s = \beta \Delta \sqrt{\frac{R_q}{R_\xi}} \frac{L}{\xi} \exp\left(-\alpha \frac{R_q}{R_\xi}\right). \quad (4.55)$$

Here, the coefficients  $\alpha$  and  $\beta$  are introduced which are on the order of unity. They are theoretically derived to be  $\alpha = 0.36$  and  $\beta = 0.32$  (see Sec. 2.2.2 and [VN12]) under certain assumptions for the nanowire.

The superconducting gap of the NbN thin film is given by  $\Delta = 1.746k_B T_c$  (see Eq. (2.1)) with  $T_c = 4.7$  K.  $R_\xi = R_\square \xi / w_{\text{nw}}$  is the resistance of a piece of wire with the length of the coherence length  $\xi = 5$  nm (see Sec. 3.1.2), the width  $w_{\text{nw}}$  (as given in Tab. 4.2) and a film sheet resistance  $R_\square = 2$  k $\Omega$ . The length of the nanowires is  $L \approx 60$  nm.

In Fig. 4.29, the measured values of the coherent QPS amplitudes  $E_s/h$  of the two observed qubits are plotted versus their nanowire widths  $w_{\text{nw}}$ . Taking all known nanowire proper-

ties into account, but leaving  $\alpha$  and  $\beta$  free parameters on the order of unity, Eq. (4.55) is fitted to the data points (see green solid line). This results in  $\alpha = 0.34$  and  $\beta = 0.97$ . Since only two data points are fitted, this is not a claim of perfect agreement with the theoretical prediction. But considering that all nanowire properties are gained from different experiments, it indicates that theory and experiment might converge. The dashed lines in Fig. 4.29 indicate the uncertainty range of  $E_s/h$  due to the limitation to define the widths of the nanowires (see error in x).

Fig. 4.29 might give an explanation why only two out of sixteen qubits could have been observed in the experiment. The two identified loops are the ones with the narrowest constrictions of around 50 nm. The other loops had wider constrictions (see Tab. 4.2). Fig. 4.29 shows that for these wider constrictions the QPS amplitude is too low to be observed or might already be suppressed at all. Furthermore, Fig. 4.29 points out that in the detection band of  $\leq h \cdot 10$  GHz of the used setup/experiment, the range of usable nanowire widths is around 35 – 50 nm.

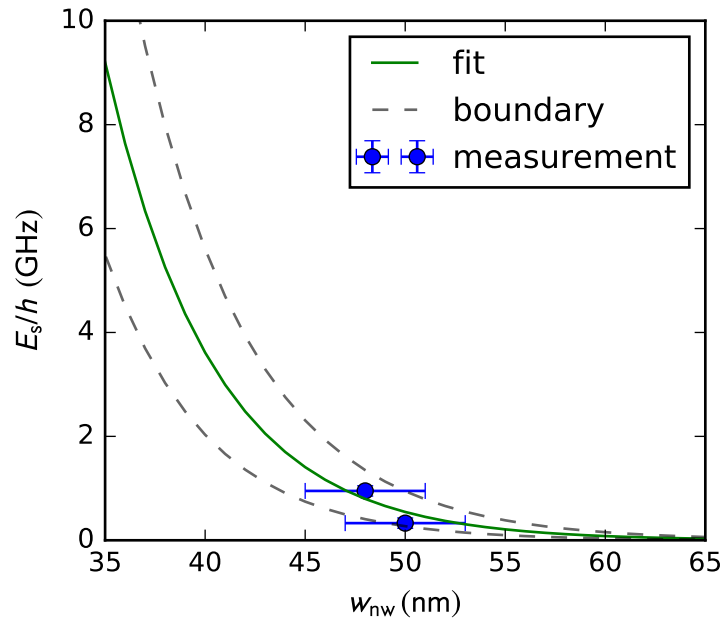


**Figure 4.29:** Coherent QPS amplitudes of the two observed qubits plotted versus their nanowire widths (blue circles). The errors in x are due to the limitations in measuring the widths. The data is fitted by Eq. (4.55) with fit parameters  $\alpha$  and  $\beta$  on the order of unity (green solid line). The dashed lines represent the uncertainty range due to the error in widths.

## Power dependence

The strong qubit-resonator coupling becomes manifest in a further effect discussed in Sec. 2.4.3. Not only the resonator experiences a dispersive shift when the qubit becomes excited as shown in Sec. 4.2.5. According to Eq. (2.87)

$$f_q = E_s/\hbar + \frac{g^2}{f_q - f_r}(2n + 1), \quad (4.56)$$

also the qubit becomes dispersively shifted with a change of the power that is applied to the resonator or the number of photons  $n$  in the resonator, respectively. For the measurement presented in Fig. 4.30, the qubit transition is fixed at the sweet spot. For an increasing readout power  $P_{\text{VNA}}$  applied via the vector network analyser (VNA), the qubit becomes excited at decreasing drive frequencies  $f_{\text{mw}}$ .

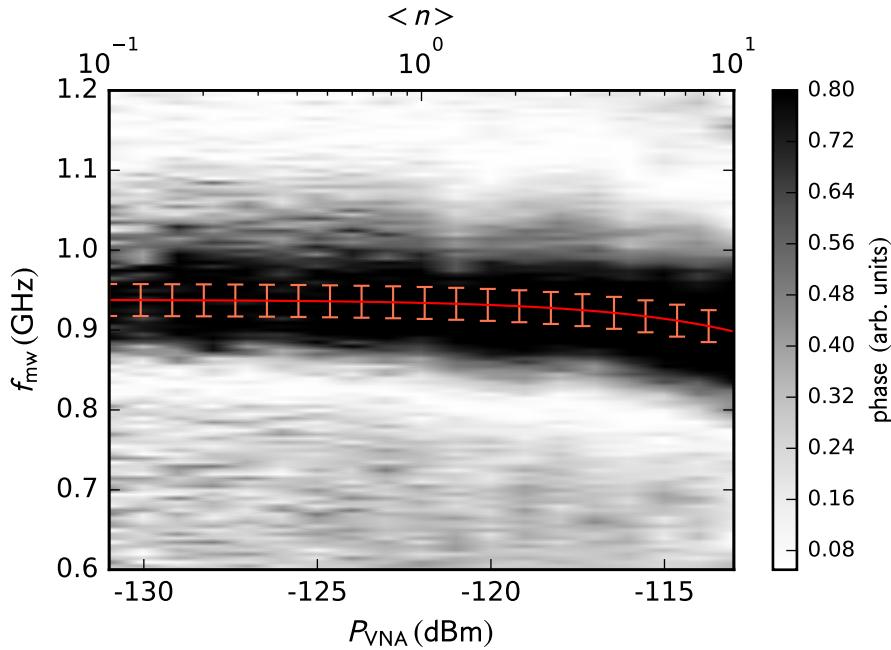


**Figure 4.30:** Dependence of the transition of qubit 1 on the readout power  $P_{\text{VNA}}$  applied via the vector network analyser (VNA). The qubit transition is fixed at the sweet spot and investigated via the dispersive readout technique. The change of the transition with  $P_{\text{VNA}}$  is fitted with Eq. (4.56) (red line). The result is utilized to calibrate the average number of photons  $\langle n \rangle$  in the resonance mode with the applied microwave power. This calibrated photon number is displayed as upper x axis. The drive power level is at  $P_{\text{mw}} = -90$  dBm including setup attenuation.

With Eq. (4.56), this shift can be utilized to calibrate the average number of photons  $\langle n \rangle$  in the resonance mode with the applied microwave power. This calibrated photon number is displayed in Fig. 4.30 at the upper x axis.

### 4.2.6. Multiphoton transitions

In Fig. 4.27 as well as in Fig. 4.28, additional transitions despite the aforementioned ones are visible. These transitions are marked in Fig. 4.31. As can be seen in Fig. 4.32, they occur at higher drive power levels (around  $-75$  dBm). The reason for the appearance of these transitions is the strong qubit-resonator coupling. As evaluated in Sec. 4.2.4, the coupling strength between qubit 1 and the resonator is  $g_\phi = 370.65$  MHz. Compared to the resonator frequency, this is a fraction of

$$\frac{g_\phi}{f_r} = \frac{0.37 \text{ GHz}}{4.15 \text{ GHz}} = 8.9\%. \quad (4.57)$$

For such strong coupling, the rotating wave approximation, which neglects terms in the interaction Hamiltonian Eq. (2.77) that rotate faster ( $\omega_q + \omega_r$ ), breaks down. These terms are called *counter-rotating* terms.

Hence in the full interaction Hamiltonian Eq. (2.77)

$$\hat{H}_{\text{int}} = \hbar g(\sigma^+ a^\dagger e^{i(\omega_q + \omega_r)t} + \sigma^+ a e^{i(\omega_q - \omega_r)t} + \sigma^- a^\dagger e^{i(-\omega_q + \omega_r)t} + \sigma^- a e^{-i(\omega_q + \omega_r)t}), \quad (4.58)$$

the first term which represents a qubit excitation in combination with the creation of a photon ( $\sigma^+ a^\dagger$ ) and the fourth term which is a qubit relaxation together with the loss of a photon ( $\sigma^- a$ ) lead to a new set of qubit-resonator ground and doublet of dressed excited states<sup>67</sup> [For+16]

$$|\downarrow, 0\rangle, \quad (4.59)$$

$$\begin{aligned} |+, n\rangle &= \cos \phi_n (|\uparrow, n-1\rangle + \lambda \sqrt{n-1} |\downarrow, n-2\rangle) + \\ &\quad + \sin \phi_n (|\downarrow, n\rangle + \lambda \sqrt{n+1} |\uparrow, n+1\rangle), \end{aligned} \quad (4.60)$$

$$\begin{aligned} |-, n\rangle &= \sin \phi_n (|\uparrow, n-1\rangle + \lambda \sqrt{n-1} |\downarrow, n-2\rangle) \\ &\quad - \cos \phi_n (|\downarrow, n\rangle + \lambda \sqrt{n+1} |\uparrow, n+1\rangle). \end{aligned} \quad (4.61)$$

<sup>6</sup>See Sec. 2.4.3 for comparison

<sup>7</sup> $|\downarrow\rangle(|\uparrow\rangle)$  represents the qubit in its ground(excited) state and  $|n\rangle$  states that there are  $n$  photons in the resonator.

Here, the new mixing angle is  $\phi_n = 1/2 \arctan\left(2g\sqrt{n}/(\omega_{\text{rq}} + 2ng^2/(\omega_r + \omega_q))\right)$  and the measure of how much the counter-rotating terms act on the dressed states is given by  $\lambda = g/(\omega_r + \omega_q)$ .

The regime in which the counter-rotating terms in the interaction Hamiltonian play a role is the quantum *Bloch-Siegert* regime or because the reason is the very strong coupling it is called the *ultrastrong coupling* regime.

Other than in [For+16], the here presented resonator has not only a fundamental mode but also several harmonics. This means that the system Hamiltonian gets extended by a sum over the resonator mode spectrum  $\hat{H}_r = \sum_n \hbar\omega_n(a_n^\dagger a_n + 1/2)$  and a sum over coupling to all the modes  $\hat{H}_{\text{int}} = \sum_n \hbar g_{\phi,n}(a_n^\dagger + a_n + 1/2)\tilde{\sigma}_z$ . Here,  $n$  represents the  $n$ -th resonator mode and  $\tilde{\sigma}_z$  the Pauli matrix in the flux frame [Che+17]. Under these circumstances, additional transitions appear under strong enough drive at drive frequencies

$$f_{\text{mw}} = f_q \pm s \cdot f_r, \quad (4.62)$$

where  $f_q$  is the qubit's base transition ( $s = 0$ ) and  $f_r$  is the fundamental resonator frequency.

$s$  gives the higher-order modes of the resonator. Since the  $+$  in Eq. (4.62) leads to transitions with higher frequency, they are called the  $s$ -th order *blue-sideband* transitions while the  $-$  leads to the  $s$ -th order *red-sideband* transitions.

In Fig. 4.31*top*, the first order blue-sideband transition (blue line) above the fundamental resonator frequency (yellow dashed line) is observed for qubit 16 at a drive power of  $-75$  dBm. Using the nomenclature of Eq. (4.59), this is the  $|\downarrow, 0\rangle \leftrightarrow |-, 2\rangle$  transition which can only be a result of the first term in Eq. (4.58). The other transition of qubit 16 below the fundamental resonator frequency (yellow dashed line) is its first order red-sideband transition  $|-, 1\rangle \leftrightarrow |+, 1\rangle$ . For the fits, the parameters from Tab. 4.3 are taken.

In Fig. 4.31*bottom*, the first order blue-sideband transition (blue line) above the fundamental resonator frequency (yellow dashed line) is observed for qubit 1 at a drive power of  $-75$  dBm. It has to be mentioned that the transition  $f_{\text{mw}} = f_q + 1 \cdot 4.3$  GHz is observed although the spectroscopy is performed with the resonator's second harmonic. However, it is intuitively understandable that a photon in the resonator with three times the fundamental frequency can be considered as three photons with the fundamental frequency leading to the observed side-band [Che+17].

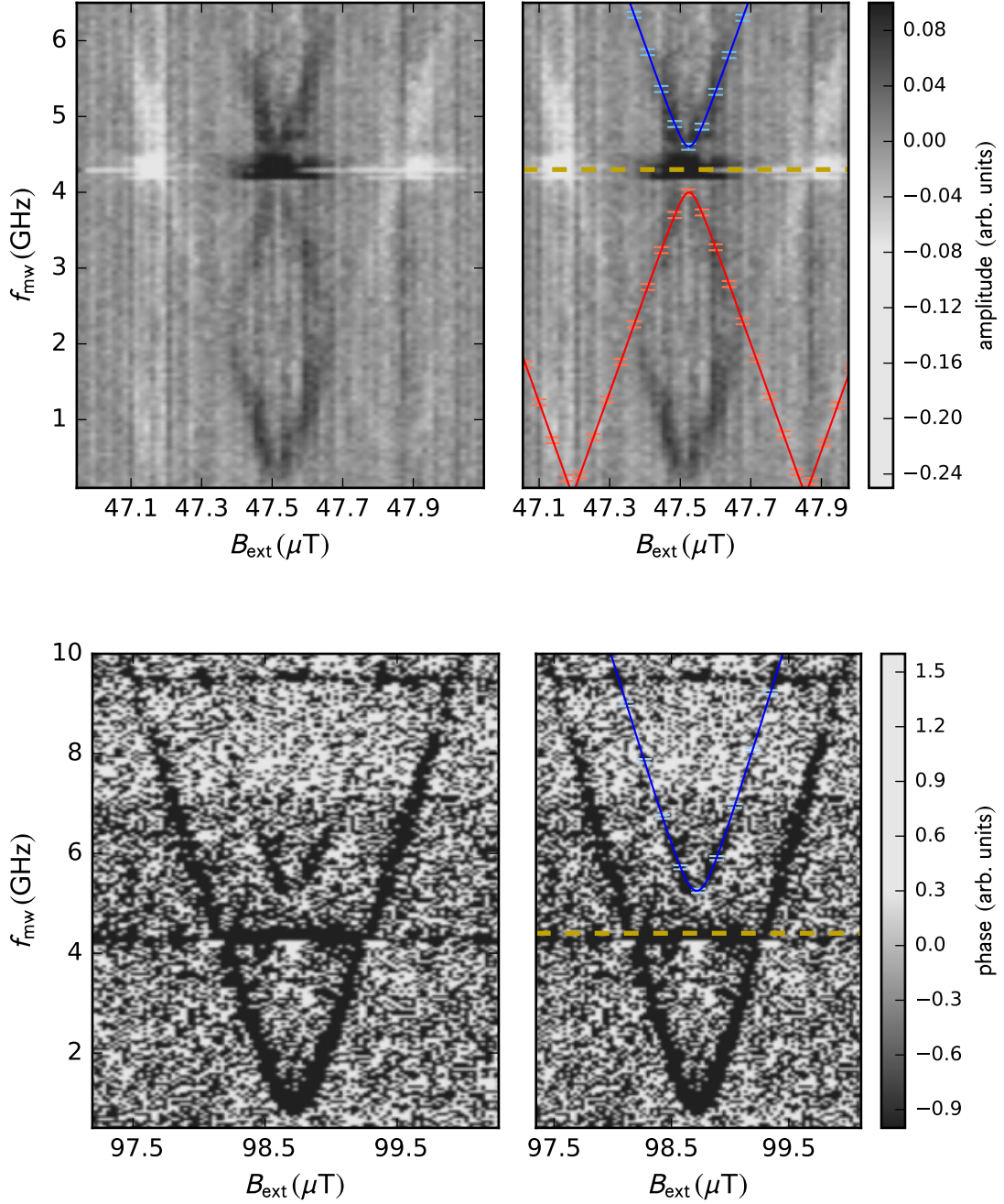


**Figure 4.31:** *top* Transition of qubit 16 measured by dispersive readout as shown in Fig. 4.28. *right* Here, the first blue-sideband transition  $f_q + 1 \cdot f_r$  (blue line) above the resonator fundamental mode  $f_r$  (dashed line, yellow) as well as the first red-sideband  $f_q - 1 \cdot f_r$  (red line) below  $f_r$  are fitted. The fits by Eq. (4.51) are done with the parameters taken from Tab. 4.3. *bottom* Transition of qubit 1 measured by dispersive readout as shown in Fig. 4.27. *right* Here, the first blue-sideband transition  $f_q + 1 \cdot f_r$  (blue line) above the resonator fundamental mode  $f_r$  (dashed line, yellow) is fitted by Eq. (4.51) with the parameters taken from Tab. 4.3.

The fact that the sideband-transitions have to be driven strongly in order to observe them (given by the factor  $\lambda$  in Eq. (4.60) and Eq. (4.61)) is shown in Fig. 4.32 for qubit 1. While the fundamental transition at 0.94 GHz can be observed for very low drive power levels  $P_{\text{mw}}$ , the first order blue sideband at 5.24 GHz needs a lot higher drive power levels to be driven. Both transitions show a power broadening with increasing drive power levels because for higher power levels more photons can populate the excited level.

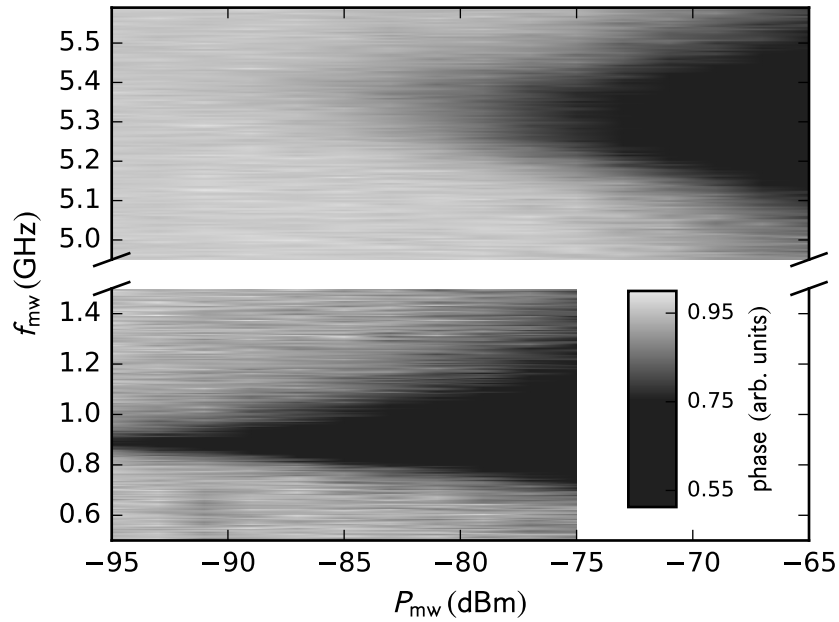


**Figure 4.32:** Dependence of the transition of qubit 1 (*bottom*) as well as its first blue-sideband transition (*top*) as shown in Fig. 4.31 on applied qubit drive power  $P_{\text{mw}}$ . The readout power level is at  $P_{\text{VNA}} = -120$  dBm including setup attenuation. For low drive power levels only the qubit's transition from ground to excited state is populated. Only for higher drive power levels also the blue-sideband transition can be driven. Both transitions show a power broadening with increasing drive power levels.

### 4.2.7. Conclusion

In the experiment presented in this section, coherent quantum phase slip could successfully be demonstrated in a system consisting of a superconducting loop and a nanowire with a nano-fabricated constriction in it. Several superconducting loops with embedded constrictions were galvanically coupled to a CPW  $\lambda/2$ -resonator. Loops and resonators were made from the same superconducting thin film with high normal conducting sheet resistance that allows for high kinetic inductance in the superconducting regime. The technical realization of constriction widths of a few tens of nm allowed for quantum phase slips (QPS) in the constrictions. This again allowed the magnetic fluxons enclosed in the superconducting loops to tunnel out of and into the loop through the constrictions. By that, the loops acted as two-level systems that were coupled to the resonator or a photon field, respectively.

Experimentally observed avoided-level crossings with certain magnetic field periodicities (see Fig. 4.26 and Fig. 4.25) suggested strong coupling between resonator and two-level system and allowed to identify the different loops. Spectroscopy of the two-level transitions by dispersive readout technique (see Fig. 4.27 and Fig. 4.28) validated the expected magnetic field dependence of the two-level systems. They behaved as theoretically predicted quantum phase slip flux qubits (QPSFQ) where QPS (and therewith fluxon tunnelling) could coherently be driven by microwave driving. The findings are in good agreement with similar findings for loops with long nanowires as well as short constrictions [Ast+12; Pel+13; Pel+16].

A full set of additional investigations substantiate the strong qubit-resonator coupling. Hence, a dispersive qubit transition shift with resonator photon number or drive power level, respectively could be experimentally observed (see Fig. 4.30). And furthermore, the appearance of multiphoton sideband transitions (see Fig. 4.31) at high drive power levels (see Fig. 4.32) furnishes evidence that the qubit-resonator coupling is on the edge to the ultrastrong coupling regime.

However, it has to be mentioned that only two out of sixteen loops could be experimentally observed. Thus, the goal to observe a scaling of QPS energy  $E_s$  with constriction width could only partially be reached. The important fact is that the two identified loops are the ones with the narrowest constrictions of around 50 nm. All other loops had wider constrictions which would translate into reduced QPS energy  $E_s$ . Since the observed ones are already rather low ( $< h \cdot 1$  GHz), this might simply mean that QPS is suppressed in the wider constrictions due to the exponential dependence of  $E_s$  on the constriction width (see Fig. 4.29). This is supported by the fact that the two observed transitions are already a factor of 3 apart although they are designed and fabricated to be equal. Nevertheless, an uncertainty in the constriction width of 3 – 5 nm remains with the presented fabrication method. This slight variation could be the reason for the factor 3 and for suppression of QPS in all other loops. A subsequent experiment with constriction widths  $\leq 50$  nm also supported this assumption since it only showed transitions for loops with a constriction

width of 50 nm ( $E_s \approx h \cdot 1 \text{ GHz}$ ) but none for narrower wires where transitions might already be out of the setup's detection band of  $\leq h \cdot 10 \text{ GHz}$  (see Fig. 4.29).

Going to thin films with higher normal conducting sheet resistances may help to reduce the sensitivity on the constriction width in future experiments as  $E_s$  also depends exponentially on the sheet resistance.

### 4.3. A charge quantum interference device based on two constrictions in series

While the measurements presented in Sec. 4.2 were performed at the Royal Holloway, University of London (RHUL), Egham, UK, the measurements which are discussed in the following were done at the National Physical Laboratory (NPL), Teddington, UK as part of the same internship in the group of Prof. Dr. O. Astafiev.

In Sec. 4.2, it is shown that quantum phase slip (QPS) can be coherently driven in a QPS junction (QPSJ) which is a continuous superconducting wire with a narrow constriction to control the QPS energy. Based on these findings, the motivation of the experiment presented in the following is the interference of two such QPS junctions. To be more precise, the interference of fluxon trajectories tunnelling through the two junctions and therewith compassing a statically charged island between the junctions (see Fig. 4.33). This effect has theoretically been derived by Y. Aharonov and A. Casher in 1984 [AC84]. Travelling along a path around a static charge with electric field  $E$ , the fluxon with magnetic moment  $\vec{\mu}$  picks up a phase shift

$$\phi_{AC} = \frac{1}{hc} \oint \vec{\mu} \times \vec{E} d\vec{r}. \quad (4.63)$$

This phase shift has been experimentally observed in particle and solid-state systems [Cim+89; Eli+93; San+93; Kön+06] as well as in Josephson junction (JJ) arrays [Pop+12; Bel+16]. Regarding the phase-charge duality that underlies the duality between QPSJ and JJ as described in Sec. 2.3, the dual to the Aharonov-Casher effect is the Aharonov-Bohm effect [AB59]. Here, a particle with charge  $q$  gains a phase shift while compassing a magnetic field with non-zero magnetic vector potential  $\vec{A}$

$$\phi_{AB} = \frac{q}{hc} \oint \vec{A} d\vec{r}. \quad (4.64)$$

For Cooper pairs tunnelling through JJs while circumferencing a magnetic field, this interference has already been studied 50 years ago [Cha60]. The device in which the interference takes place is a superconducting ring with two embedded JJs. It is the well known *Superconducting QUantum Interference Device (SQUID)* (see Fig. 4.33). Comparing Fig. 4.33a with **b**, one can see that the device with two QPSJs which is investigated in the following is the exact dual to the JJ based SQUID.

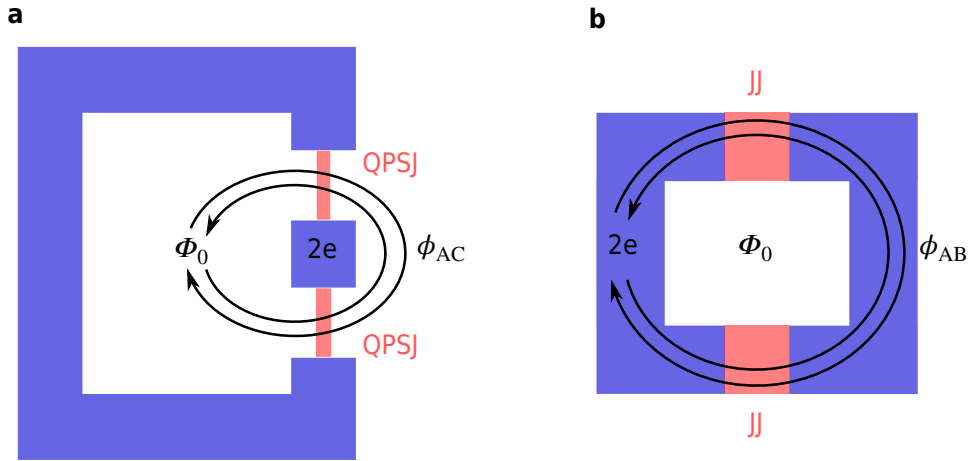


**Figure 4.33:** Comparison of the Aharonov-Casher and the Aharonov-Bohm effect in devices. **a** In the Aharonov-Casher effect, a fluxon  $\Phi_0$  which encircles a charge  $2e$  picks up a phase shift  $\phi_{AC}$ . The device is a superconducting loop with two QPS junctions (QPSJ, red). The loop holds the fluxon inside except the QPSJ allows the fluxon to tunnel in and out along a path around the island with charge  $2e$ . **b** In the Aharonov-Bohm effect, a charge of  $2e$  which encircles a fluxon  $\Phi_0$  picks up a phase shift  $\phi_{AB}$ . The device is the well-known Superconducting QUantum Interference Device (SQUID), a superconducting loop with two Josephson junctions (JJ, red). The charge  $2e$  encircles the fluxon  $\Phi_0$ . On its path it tunnels through the JJs.

### 4.3.1. Sample design

As depicted in Fig. 4.33, the two constrictions are embedded in series into a loop. The complete circuit is made from the same superconducting, granular NbN thin film. To utilize coherent fluxon tunnelling through the QPS junctions, the sample design of the preceding experiment (see Sec. 4.2) is used. It is extended by a second constriction in the loop. The two constrictions are separated by a wider wire section (see Fig. 4.34). As can be seen here, a gate capacitor is connected to this island between the constrictions (see Fig. 4.34*bottom*). It allows to change the island's offset charge. This island is made wide enough to suppress phase slipping while it is small enough to minimize its self-capacitance. The gate is used to manipulate the electric field of the island and  $\phi_{AC}$  (see Eq. (4.63)), respectively. The principle measurement setup is equivalent to the one utilized in the preceding experiment (see Fig. 4.22 and corresponding text) though partially other components are utilized (see Tab. 3.3). Additionally, a filtered line is used for the charge gate. It is a thermocoax® line with 1 MHz low pass cutoff which is furthermore equipped with a homemade LC LP filter with 15 MHz at the mixing chamber. This helps to reduce charge noise which would eventually affect the experiment. Again, 16 loops with but now with 2 constrictions each are galvanically coupled to a CPW  $\lambda/2$ -resonator which is made in the same fabrication step as the loops and constrictions. The fabrication details of the experiment are listed in A.1.2.

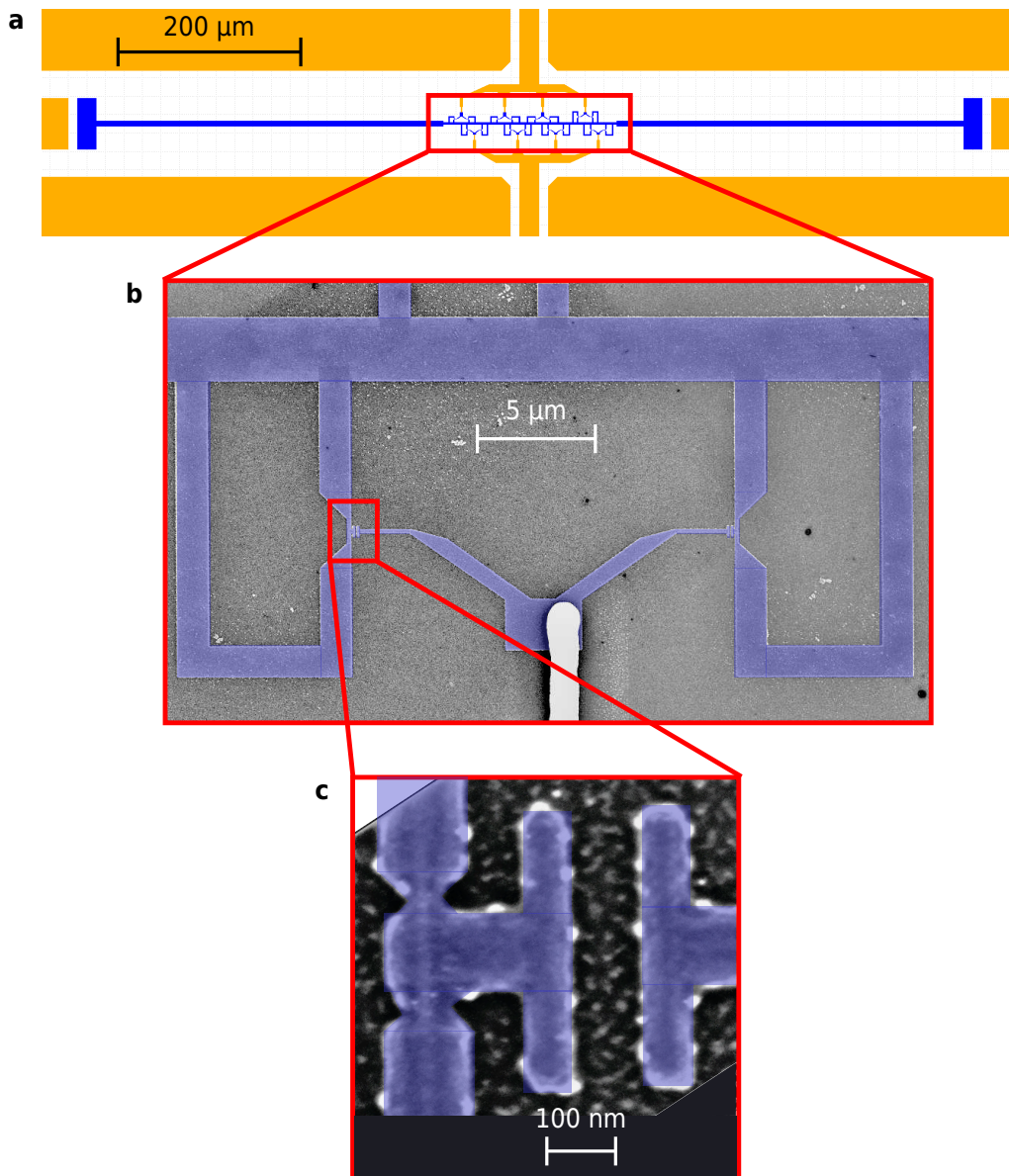


**Figure 4.34:** **a** 16 different loops with two constrictions in series per loop. The loops are galvanically coupled to the center of a CPW  $\lambda/2$ -resonator (blue). Above and below, there are ground planes as well as voltage bias lines, and left and right, microwave connection pads are placed (all yellowish). **b** A SEM picture of 2 inner loops with a voltage bias line that splits up to both loops. The loop wire width is 1.2  $\mu\text{m}$ . **c** Zoom onto the two constrictions in series (left). The island between them (right) is connected to a parallel line gate capacitor.

### 4.3.2. Frequency and magnetic field spectroscopy

In the microwave transmission frequency spectrum, resonance peaks with a fundamental mode frequency of 3.74 GHz and higher modes at 7.32 GHz and 11.01 GHz can be observed. The loaded quality factor of the fundamental mode is  $Q_1 \approx 600$  while the higher order modes have lower ones.

Monitoring the fundamental resonance while sweeping the magnetic field strength perpendicular to the sample, it can be observed that the resonance mode passes through five different anticrossings (see Fig. 4.35).

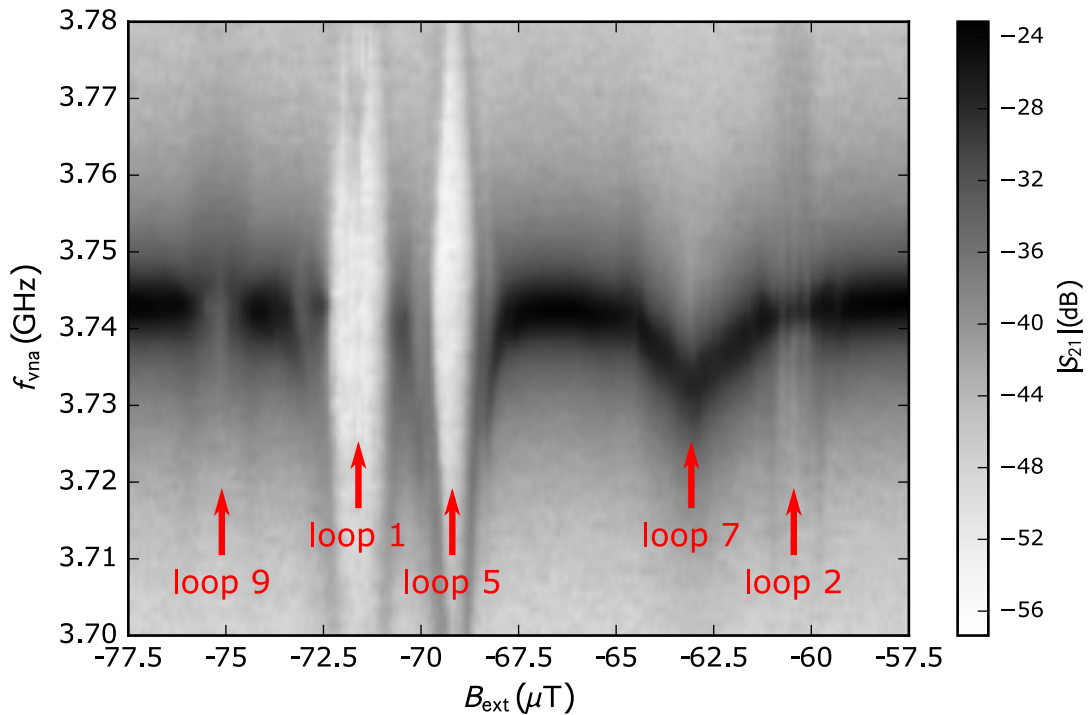


**Figure 4.35:** Avoided level crossings of loops 1,2,5,7,9 (red arrows) and the resonator fundamental mode displayed as grey-scale coded microwave transmission amplitude versus probe frequency and externally applied magnetic field. The loops are identified by their different periodicities in magnetic field (not visible here).

This is due to the coherent fluxon tunnelling through the constrictions in the individual loops and the loop-resonator coupling. As explained in Sec. 4.2.3, the loop-constriction circuit acts as a quantum phase slip flux qubit (QPSFQ) with a magnetic field dependent transition frequency. Due to coupling, resonator and qubit form dressed states when their frequencies match. The dressed states are degenerate by  $2g$ , where  $g$  is the coupling strength or coefficient, respectively. An anticrossing can be observed as a change of the monitored resonator frequency at certain magnetic fields. At these magnetic fields, the qubit's transition frequency matches the resonator frequency. This is in accordance to the observations

presented in Fig. 4.24 and Fig. 4.26.

In Fig. 4.35, it is visible that the coupling strengths of the five qubits are different. As explained in Sec. 4.2.4, the galvanic coupling depends on the inductance which is shared by loop and resonator. Since this inductance is varied for all loops (see Tab. 4.2), the coupling strength must vary and the anticrossings appear differently strong in the magnetic field spectrum.

With further increase of the magnetic field, each anticrossing reappears at an individual periodicity that is used to determine which loops are observed. With Tab. 4.2, *loop 1*, *loop 2*, *loop 5*, *loop 7* and *loop 9* can be identified.

### 4.3.3. Transition spectroscopy

Having identified the loops which exhibit coherent quantum phase slip (CQPS), the next step is to monitor the transitions and their dependence on magnetic field. This is done by utilizing the aforementioned dispersive readout technique. While the resonator frequency is monitored with the vector network analyser (VNA), a second microwave drive tone  $f_{\text{mw}}$  is applied. When the drive frequency matches the qubit (loop) transition frequency, the qubit becomes excited. Due to strong coupling, this excitation leads to a dispersive shift of the resonator frequency. According to

$$f_{\text{q}} = \frac{1}{h} \sqrt{(2I_{\text{p}} \delta \Phi)^2 + E_{\text{s}}^2}, \quad (4.65)$$

the qubit frequency will change with magnetic field. In Fig. 4.36, Fig. 4.37 and Fig. 4.38, this is shown for all five qubits. Here, the phase signal corresponding the resonance peak is plotted in grey-scale versus applied drive frequency  $f_{\text{mw}}$  and magnetic field  $B$ .

In Tab. 4.4, the evaluated parameters of the five qubits shown Fig. 4.36, Fig. 4.37 and Fig. 4.38 are listed including periodicities.

loop	$E_{\text{s}}/h$ (GHz)	$I_{\text{p}}$ (nA)	$\Delta B$ ( $\mu\text{T}$ )
1	3.00	36.70	40.75
2	1.45	31.70	32.90
5	5.01	31.00	23.55
7	7.52	34.20	21.25
9	0.55	33.40	18.88

**Table 4.4:** Important parameters of the five measured qubits.

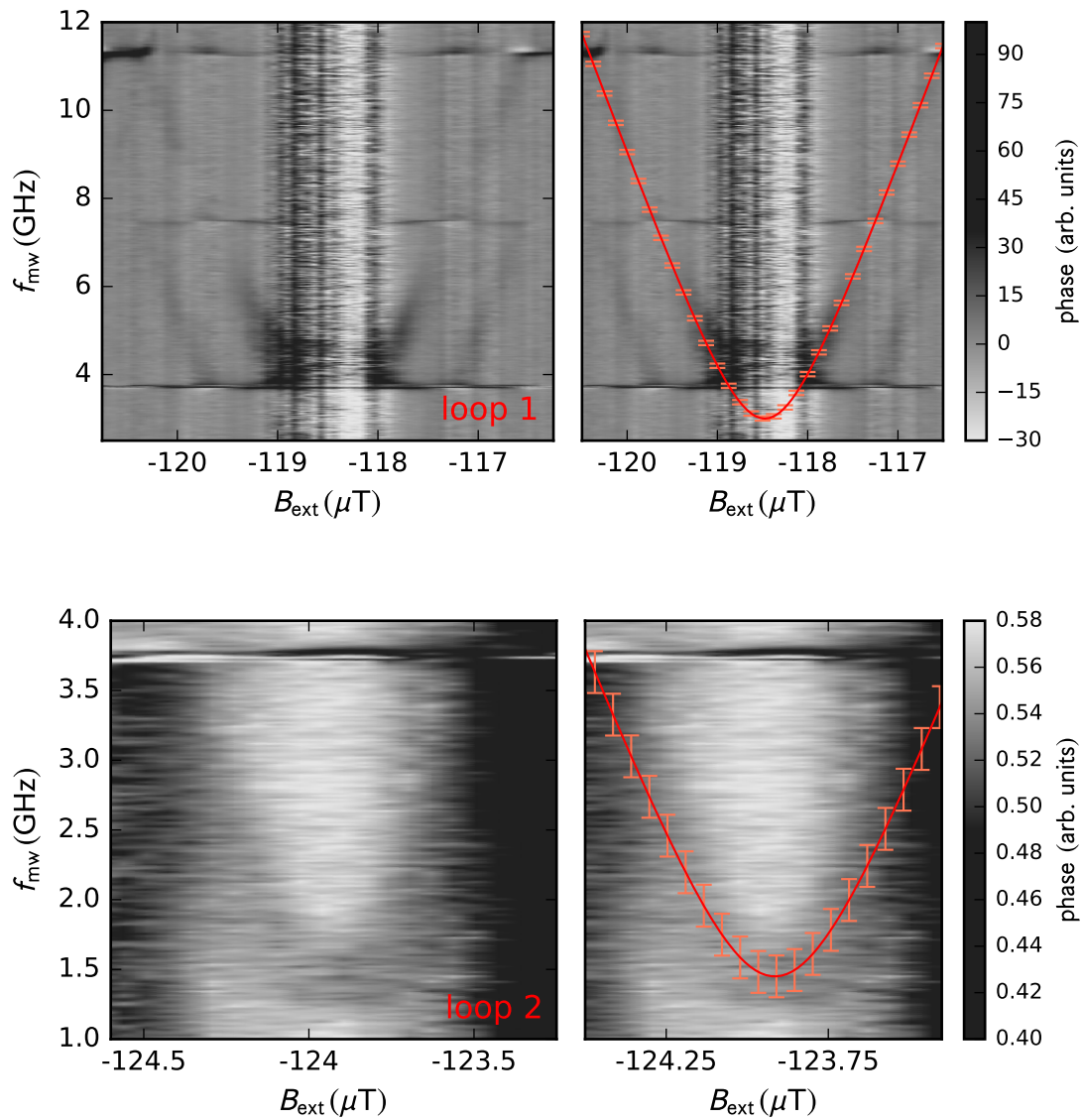


**Figure 4.36:** Dependence of the transition on magnetic field investigated by dispersive readout technique. *top* Loop 1: The phase signal at the fundamental resonance of the resonator is plotted in grey-scale versus additional drive frequency  $f_{\text{mw}}$  and external magnetic field  $B_{\text{ext}}$  which is applied perpendicular to the sample. When  $f_{\text{mw}} = f_{\text{q}}(B_{\text{ext}})$ , the resonator experiences a dispersive shift due to coupling. The transition is fitted (red line) by Eq. (4.65). *bottom* The same as in the upper plots but now for loop 2.

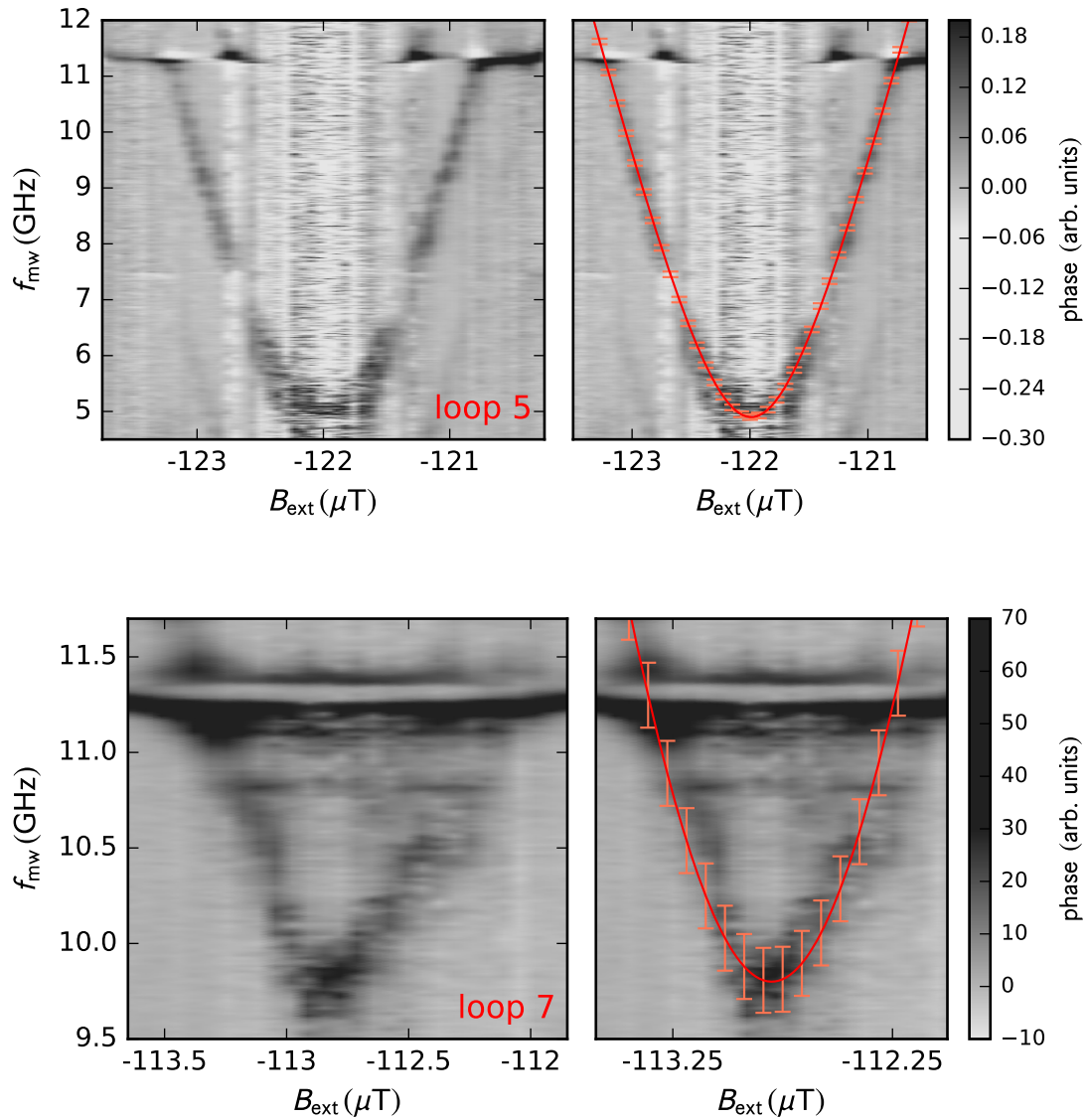


**Figure 4.37:** Dependence of the transition on magnetic field investigated by dispersive readout technique. *top* Loop 5: The phase signal at the fundamental resonance of the resonator is plotted in grey-scale versus additional drive frequency  $f_{\text{mw}}$  and external magnetic field  $B_{\text{ext}}$  which is applied perpendicular to the sample. When  $f_{\text{mw}} = f_{\text{q}}(B_{\text{ext}})$ , the resonator experiences a dispersive shift due to coupling. The transition is fitted (red line) by Eq. (4.65). *bottom* The same as in the upper plots but now for loop 7.

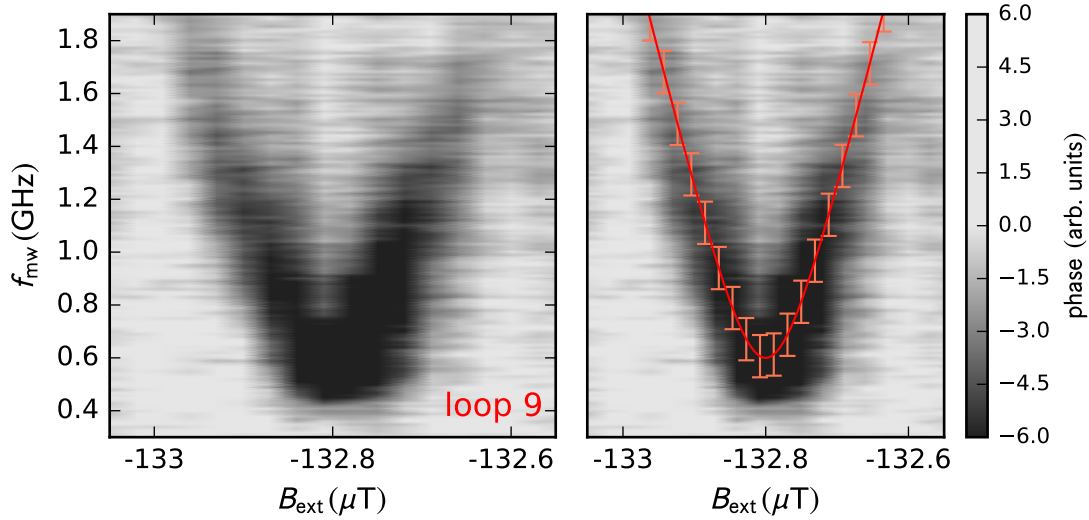


**Figure 4.38:** Dependence of the transition on magnetic field investigated by dispersive readout technique here for loop 9. The phase signal at the fundamental resonance of the resonator is plotted in grey-scale versus additional drive frequency  $f_{\text{mw}}$  and external magnetic field  $B_{\text{ext}}$  which is applied perpendicular to the sample. When  $f_{\text{mw}} = f_{\text{q}}(B_{\text{ext}})$ , the resonator experiences a dispersive shift due to coupling. The transition is fitted (red line) by Eq. (4.65).

#### 4.3.4. Electric gate charge dependence

Having found that the loops with two constrictions show similar behaviour as loops with only one constriction, the foundation stone for checking an interference of the two constrictions is laid. So far, the similar behaviour may solely result from coherent QPS happening in one of the two constrictions with the other one working as additional inductance. The case of two constrictions where both of them allow for coherent QPS can be tested by applying a voltage bias on the charge gate at the island between the constrictions (see beginning of this section).

In Fig. 4.39, the transition dependence on magnetic field of loop 1 measured by dispersive readout is displayed for two different applied gate voltages or island charge values, namely  $q = -0.14 \times 2e$  and  $q = -0.55 \times 2e$ . In each plot, two transitions are marked that behave completely opposite to each other with varied island charge. While the lower transition decreases in frequency with decreasing island charge, the upper one increases. The reason for this opposite behaviour will be explained in Sec. 4.3.5.

In the following, the measurements are performed at the sweet spot or minimum transition point of both transitions. Considering Eq. (4.65), this is the point where the transition energy is solely determined by the quantum phase slip energies  $E_{\text{S}}$  of the two QPS junctions.

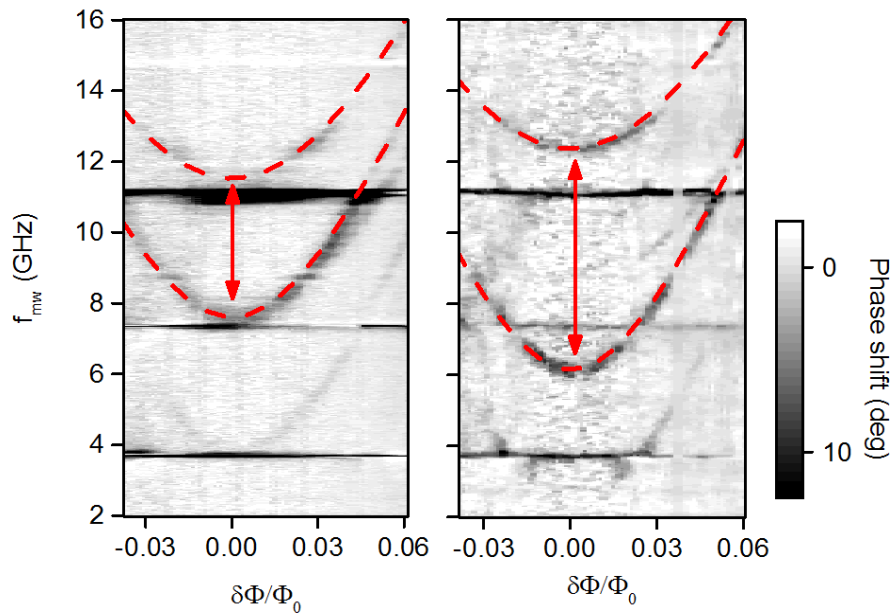


**Figure 4.39:** Transition spectroscopy of loop 1 by dispersive readout technique for two different island charge values  $q = -0.14 \times 2e$  (left) and  $q = -0.55 \times 2e$  (right). The dashed lines are fits by Eq. (4.65). The appearance of two transitions in each plot will be explained in Sec. 4.3.5. Double-sided arrows mark the sweet spots of the transitions (see Fig. 4.40) [Gra+18].

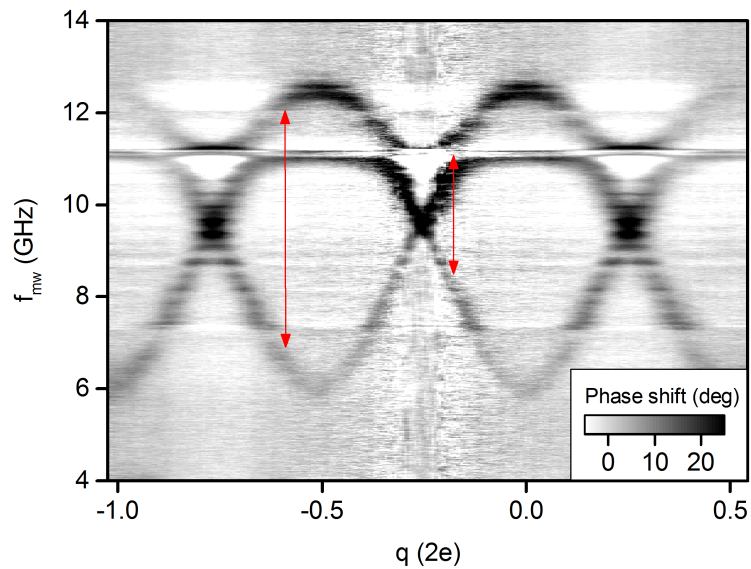


**Figure 4.40:** Monitoring the sweet spots of the transitions in Fig. 4.39 in dependence on the island charge. Double-sided arrows mark the same working points as in Fig. 4.39 [Gra+18].

A continuous variation of the gate charge between the junctions leads to the observation in Fig. 4.40. Both transitions vary periodically with applied gate charge but completely out of phase. At first, the periodic dependence is explained while in Sec. 4.3.5, the appearance of two transitions is discussed.

The periodic dependence on the gate charge can be understood in terms of interference of the two constrictions both allowing for flux to tunnel coherently across them. By tunnelling, the fluxon encircles the island with charge  $q$  that creates an electric field  $E$ . According to Eq. (4.63), the flux gains a phase dependent on the island charge.

By introducing a second constriction in series to the first one with a wider section between them, Eq. (4.65) becomes [Pop+12; FA02; MLG02]

$$f_q = \frac{1}{h} \sqrt{(2I_p \delta\Phi)^2 + h^2 |v_1 + v_2 e^{-i2\pi q}|^2}, \quad (4.66)$$

under the condition that both constrictions exhibit coherent QPS with phase slip amplitudes  $v_{1,2}$ . The interference of both constrictions due to the Aharonov-Casher effect is mediated by the overall island charge  $q$  (normalized to  $2e$ ). This results in a  $q = 2e$ -periodic oscillation of the transition when the island charge is varied via the gate capacitor (as it is observed in Fig. 4.40).

The case of  $v_1 = v_2$  is called symmetric and would lead to a  $|\cos(\pi q)|$  dependence of the level transition on gate charge  $q$ . At the sweet spot in magnetic field ( $\delta\Phi = 0$ ), the transition would decrease to zero.

As can be seen in Fig. 4.40 however, the transition remains at a finite minimum value of 6 GHz. This is the case when the phase slip rates differ significantly from each other ( $v_1 \gg v_2$ ).

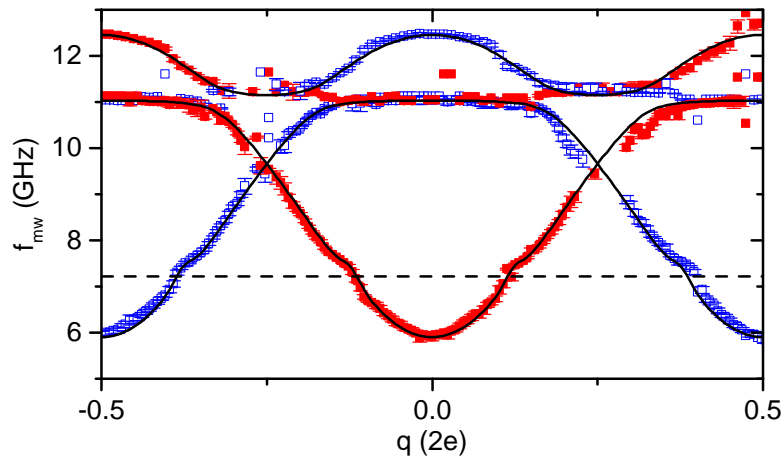


**Figure 4.41:** Transition frequencies for both transitions extracted from Fig. 4.40. The solid lines are fits to Eq. (4.66). As will be explained in Sec. 4.3.5, the blue points represent even and the red ones odd charge parity [Gra+18].

In Fig. 4.41, the transition data is extracted from fits to individual peaks in the phase shift versus frequency plot in Fig. 4.40 and fitted by Eq. (4.66). The fit gives phase slip rates of  $\nu_1 = 9.2$  GHz and  $\nu_2 = 3.3$  GHz which supports the argument of largely unequal rates in the two constrictions. This considerable variation in phase slip rates of a factor of 3 despite equal fabrication parameters for both constrictions agrees with the findings in loops with one constriction (see Sec. 4.2.5). The phase slip rates depend exponentially on the constriction width which can be controlled by fabrication to a precision of  $\pm 2-5$  nm.

So far, the tuning of the transition by charge was only investigated at the sweet spot  $\delta\Phi = 0$ . According to Eq. (4.66), the maximum transition tunability with charge has to reduce away from the sweet spot since there the inductive energy term is not negligible and superposes the charge tuning effect which exclusively affects the QPS amplitude  $E_s$ .

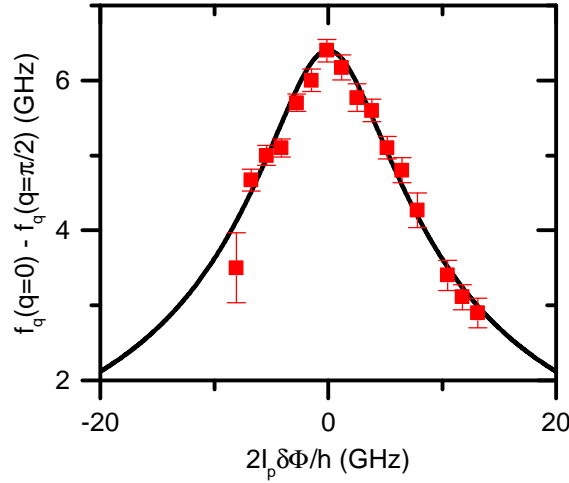


**Figure 4.42:** Observed maximum detuning by charge for a variation for different magnetic flux values.  $\delta\Phi = 0$  is the sweet spot. The black line is a fit to Eq. (4.66) [Gra+18].

In Fig. 4.42, the maximum detuning by charge is plotted versus a variation in magnetic field or flux, respectively. This is a result of many measurements just like that in Fig. 4.40, repeated for different values of flux bias around the sweetspot. The observation agrees well with the expected reduction of detuning by charge away from the sweet spot. The data points are taken from measurements at different flux values and fitted by Eq. (4.66).

### 4.3.5. Quasiparticles and charge parity

As aforementioned, in this section the appearance of two transitions in Fig. 4.39, Fig. 4.40 and Fig. 4.41 which are out of phase in regard to the applied gate charge is discussed. Out

of phase means that the second transition is  $\pi$ -shifted with respect to the first one. With  $q$  normalized to  $2\pi$ , i. e. a shift of charge  $q' = e$ . In a superconducting film far away from its critical temperature, critical current or critical magnetic field, such a charge can only be carried by quasiparticles. These are electron pair states that are occupied by only one electron [Tin04]. The origin of these quasiparticles is unclear for the presented device. However, the appearance of quasiparticles in superconducting thin-film devices is rather common even at very low temperatures.

If it is allowed for quasiparticles to enter the island between the constrictions, the island can have odd or even charge parity depending on the overall number of quasiparticles. The fluctuations of the island charge parity can be understood by considering the nature of the junctions in the device. Since the used short nanowire constrictions are formed by a continuous superconducting wire with minimal charging energy (compared to Josephson junctions, which have a substantial charging energy due to the junction capacitance), quasiparticles can enter the island without paying any additional charging energy. Hence, the time, which a quasiparticle spends on the island, is determined by the normal state resistance of the constriction. This time can be estimated to around 2 ns (see [Gra+18]). In case of a large amount of quasiparticles in the system, a rapidly fluctuating number of quasiparticles on the island is expected. This leads to a behaviour of equal probabilities for the two parities over the much longer measurement timescale as it is observed in Fig. 4.43. It is clearly visible, that both states  $q = 0$  (blue solid line) and  $q = 1e$  (red dashed line) have identical populations. The two peaks visible differ in height because the two modes couple differently strong to the resonator mode. Furthermore the observation shows that charge is not quantized on the island. This can be mapped with direct duality arguments to the SQUID, where flux threading its loop is not quantized, unlike the flux in a continuous superconducting ring.

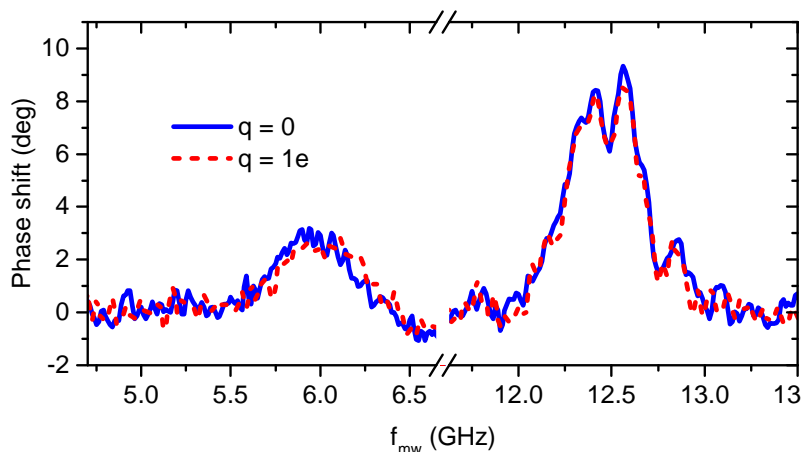


**Figure 4.43:** Phase response taken from Fig. 4.40 for island charge values of  $q = 0$  (solid line) and  $q = 1e$  (dashed line). The level population is equal for both parity states. The difference in height of the two peaks visible for each parity state results from differently strong coupling to the resonator mode [Gra+18].

### 4.3.6. Conclusion

In the experiment presented in this section, the interference of two quantum phase slip junctions (QPSJ), which were embedded into a superconducting loop, was successfully proven. The utilized device is directly based on the experiments in the preceding section Sec. 4.2. While in Sec. 4.2 the loops had only one constriction each, in this experiment a second constriction was placed in series to the existing one. The islands or pieces of superconducting wire between the constrictions were connected to gate capacitors that allow to tune the charge on the island.

That a loop with one constriction can act like a flux qubit based on the fact that QPS can coherently be driven in a constriction had been shown in Sec. 4.2 and was directly utilized here. For two constrictions which both permit QPS associated fluxon tunnelling the overall tunnelling rate is determined by the interference of both constrictions. In five loops, coherent QPS (cQPS) could be confirmed by observing a magnetic field dependent level transition (see Fig. 4.36 to Fig. 4.38). Due to strong coupling, these transitions caused avoided level crossings with the resonator mode when tuned into resonance (see Fig. 4.35).

By tunnelling, the fluxon determined by the superconducting loop, encircles the charged island. According to the Aharonov-Casher (AC) effect, the fluxon gains a phase shift on its trajectory which depends on the island charge. Such phase shift would change the level transition energy. This was observed in this experiment (see Fig. 4.39 to Fig. 4.41). The observation of a qubit transition tunable by the island charge is a direct proof of the interference of the fluxon trajectories (and cQPS in both constrictions, respectively) and of the AC effect. The periodic dependence of the qubit transition on the island charge is in good agreement with theoretical predictions (see Fig. 4.41). The shown device represents the exact dual to the well known Superconducting Quantum Interference Device (SQUID) where Cooper pair (charge) trajectories interfere with each other. This interference is determined by the magnetic flux which the Cooper pairs encircle based on the Aharonov-Bohm effect, the dual to the AC effect (see Fig. 4.33). The device presented in this section was therefore named *Charge Quantum Interference Device (CQUID)*.

In the experiment, a second transition was observed which behaved in the same way as the expected one but was completely out of phase in its dependence on the gate charge (see Fig. 4.39 to Fig. 4.41). This transition results from the existence of superconducting quasiparticles on the island. Two different charge parity states of the system - even for Cooper pairs and even numbers of quasiparticles and odd for odd numbers of quasiparticles - were observed and studied (see Fig. 4.43).



## 5. Conclusions and Outlook

---

*"Experiments always tell the truth. The misconceptions are in the interpretations."*

**Hans-Jürgen Quadbeck-Seeger**

In this final chapter, the conclusion will be drawn on the research work which was described throughout this thesis. Understood experimental observations will be summarized and unanswered questions will be touched.

In this thesis, several experiments were performed with the aim of investigating coherent quantum phase slips (QPS). According to theoretical predictions, certain prerequisites have to be fulfilled in order to observe coherent QPS in experiment. The QPS process is predicted to appear in wires made from highly-disordered superconducting thin films when the wire cross-section is reduced down to the scale set by the coherence length. Furthermore, the wire has to be cooled to temperatures which are much lower than the critical temperature of the superconducting film.

The high disorder in the films results in high sheet resistance values above the critical temperature and high kinetic inductance values below it. In this thesis, two superconducting materials were utilized for the realization of QPS, namely granular aluminium ( $\text{AlO}_x$ ) and niobium nitride (NbN). The first milestone in this thesis dealt with the optimization of a fabrication method for highly-disordered  $\text{AlO}_x$  thin films. Using DC magnetron sputtering in an oxygen atmosphere,  $\text{AlO}_x$  thin films with sheet resistances of 1 – 10  $\text{k}\Omega$  were realized that showed superconducting transitions at critical temperatures around 1.9 K. In the films, tightly-connected networks of mono-crystalline aluminium grains separated by oxide barriers were formed. The sheet resistance values of the  $\text{AlO}_x$  films with a constant thickness of 20 nm were adjusted via the oxygen partial pressure in the sputter process. By fabricating microwave resonators out of these films, the expected kinetic inductance values, which were expected from the sheet resistances of the films, were confirmed. The NbN thin films were provided by a collaboration with the IPTH Jena. They were fabricated by an atomic layer deposition technique and their sheet resistance values of several  $\text{k}\Omega$  were adjusted via the film thickness.

The second important stepping stone of this thesis was to realize wire cross sections on the order of the superconducting coherence. For the  $\text{AlO}_x$  as well as the NbN films the coherence length is on the order of 5 nm. Hence, an electron beam (e-beam) lithography technique was adapted in which so-called spin-on glass was used as hard mask on top of the superconducting films. By consequent optimization, the patterned structure size was reproducibly brought down to minimally 10 nm. The hard mask structure protected the superconducting thin films against subsequent chlorine based chemical plasma etching which patterned the nm-scaled structures. The developed fabrication technique proved to be successful for different highly-disordered superconducting thin films.

To demonstrate coherent QPS in the fabricated nanowires, the concept of a so-called quantum phase slip flux qubit (QPSFQ) was utilized. This circuit has been theoretically proposed by Mooij and Harmans in 2005 [MH05] and experimentally demonstrated for the first time by Astafiev et al. in 2012 [Ast+12]. A QPSFQ consists of a superconducting loop, in which the magnetic flux only appears in multiples of the flux quantum  $\Phi_0$  due to flux quantization, and an embedded nanowire. The number of fluxons in the loop cannot change unless the nanowire exhibits QPS which allows the fluxons to tunnel across the wire. In case of coherent QPS, which leads to coherent tunnelling of fluxons, the circuit forms a two-level system or quantum bit (qubit) where the two classically localized states are the adjacent fluxon states in the loop.

In the experiments presented in this thesis, several of these loop-nanowire devices were electromagnetically coupled to superconducting microwave resonators. Due to their strong coupling, the qubit, which can be considered an artificial atom, and the resonator, which can be understood as a microwave photon field, did interact with each other. The interaction allowed for dispersive readout of the two-level systems with the resonators, which is well understood in terms of circuit quantum electrodynamics (cQED) [Bla+04]. To characterize the two-level systems, several experiments were performed such as magnetic field dependent level transitions as well as energy dependent multiphoton transitions, driven Rabi oscillations and lifetime measurements. In a further experiment, a charge quantum interference device due to the interference of coherent QPS of two nanowires in series could be successfully realized for the first time.

While the dynamics of the nanowires made from NbN agreed well with the concept of coherent QPS, the experiment utilizing a nanowire made from  $\text{AlO}_x$  suggests that the nanowire formed a Josephson weak-link rather than a QPS nanowire. This opened up the interesting question whether the nanowire cross section was not sufficiently small to allow for coherent QPS or the intrinsic structure of the material played a more sophisticated role than just resulting in the aimed high sheet resistance. As a promising future experiment to clarify this question, the method presented in this thesis can be used. One major change is to reduce the width of the embedded nanowire which can be achieved with the established fabrication technique. This might bring the nanowire into the QPS and out of the Josephson weak link regime. Then, the circuit should show - inter alia - the clear behaviour of a quantum phase flux qubit with a clear periodicity in flux. As a second helpful change, the loop arm facing the resonator could be made wider to increase the coupling so that it might couple stronger to the bare resonator mode. This facilitates the readout and measurement directly with the readout resonator. Another experiment is to use the design, which was utilized to characterize the QPSFQs made from NbN, and adapt it for granular aluminium. With appropriate wire widths, the devices are expected to show QPSFQ behaviour. If both suggested experiments did not show QPSFQ behaviour, this would imply that the intrinsic structure of granular aluminium would result in some unexpected behaviour making it interesting for further investigations.



# Bibliography

- [AB59] Y. Aharonov and D. Bohm. “Significance of Electromagnetic Potentials in the Quantum Theory”. In: *Phys. Rev.* 115 (3 1959), pp. 485–491. DOI: [10 . 1103/PhysRev . 115 . 485](https://doi.org/10.1103/PhysRev.115.485) (cit. on p. 115).
- [Abe77] B. Abeles. “Effect of charging energy on superconductivity in granular metal films”. In: *Phys. Rev. B* 15 (5 1977), pp. 2828–2829. DOI: [10 . 1103 / PhysRevB . 15 . 2828](https://doi.org/10.1103/PhysRevB.15.2828) (cit. on pp. 3, 40).
- [AC84] Y. Aharonov and A. Casher. “Topological Quantum Effects for Neutral Particles”. In: *Phys. Rev. Lett.* 53 (4 1984), pp. 319–321. DOI: [10 . 1103 / PhysRevLett . 53 . 319](https://doi.org/10.1103/PhysRevLett.53.319) (cit. on p. 115).
- [ACC66] B. Abeles, R. W. Cohen, and G. W. Cullen. “Enhancement of Superconductivity in Metal Films”. In: *Phys. Rev. Lett.* 17 (12 1966), pp. 632–634. DOI: [10 . 1103/PhysRevLett . 17 . 632](https://doi.org/10.1103/PhysRevLett.17.632) (cit. on p. 40).
- [ACS67] B. Abeles, R. W. Cohen, and W. R. Stowell. “Critical Magnetic Fields of Granular Superconductors”. In: *Phys. Rev. Lett.* 18 (21 1967), pp. 902–905. DOI: [10 . 1103/PhysRevLett . 18 . 902](https://doi.org/10.1103/PhysRevLett.18.902) (cit. on p. 40).
- [AGZ08] K. Y. Arutyunov, D. S. Golubev, and A. D. Zaikin. “Superconductivity in one dimension”. In: *Physics Reports* 464.1-2 (2008), pp. 1–70. DOI: [101016/ jphysrep200804009](https://doi.org/10.1016/j.physrep.2008.04.009) (cit. on p. 2).
- [Ast+12] O. V. Astafiev, L. B. Ioffe, S. Kafanov, Y. A. Pashkin, K. Y. Arutyunov, D. Shahar, O. Cohen, and J. S. Tsai. “Coherent quantum phase slip”. In: *Nature* 484.7394 (2012), pp. 355–358. DOI: [10 . 1038/nature10930](https://doi.org/10.1038/nature10930) (cit. on pp. 3, 36, 40, 91, 99, 101, 113, 130).
- [AT55] S. H. Autler and C. H. Townes. “Stark Effect in Rapidly Varying Fields”. In: *Phys. Rev.* 100 (2 1955), pp. 703–722. DOI: [10 . 1103/PhysRev . 100 . 703](https://doi.org/10.1103/PhysRev.100.703) (cit. on p. 35).
- [Bac+13] N. Bachar, S. Lerer, S. Hacothen-Gourgy, B. Almog, and G. Deutscher. “Kondo-like behavior near the metal-to-insulator transition of nanoscale granular aluminum”. In: *Phys. Rev. B* 87 (21 2013), p. 214512. DOI: [10 . 1103/PhysRevB . 87 . 214512](https://doi.org/10.1103/PhysRevB.87.214512) (cit. on p. 40).

- [Bac+15] N. Bachar, U. S. Pracht, E. Farber, M. Dressel, G. Deutscher, and M. Scheffler. “Signatures of Unconventional Superconductivity in Granular Aluminum”. In: *Journal of Low Temperature Physics* 179.1 (2015), pp. 83–89. DOI: [10.1007/s10909-014-1244-z](https://doi.org/10.1007/s10909-014-1244-z) (cit. on p. 40).
- [BCS57] J. Bardeen, L. N. Cooper, and J. R. Schrieffer. “Theory of Superconductivity”. In: *Physical Review* 108 (5 1957), pp. 1175–1204. DOI: [10.1103/PhysRev.108.1175](https://doi.org/10.1103/PhysRev.108.1175) (cit. on pp. 2, 6).
- [Bel+16] M. T. Bell, W. Zhang, L. B. Ioffe, and M. E. Gershenson. “Spectroscopic Evidence of the Aharonov-Casher Effect in a Cooper Pair Box”. In: *Phys. Rev. Lett.* 116 (10 2016), p. 107002. DOI: [10.1103/PhysRevLett.116.107002](https://doi.org/10.1103/PhysRevLett.116.107002) (cit. on p. 115).
- [BGB04] H. P. Büchler, V. B. Geshkenbein, and G. Blatter. “Quantum Fluctuations in Thin Superconducting Wires of Finite Length”. In: *Phys. Rev. Lett.* 92 (6 2004), p. 067007. DOI: [10.1103/PhysRevLett.92.067007](https://doi.org/10.1103/PhysRevLett.92.067007) (cit. on pp. 2, 15).
- [Bla+04] A. Blais, R.-S. Huang, A. Wallraff, S. M. Girvin, and R. J. Schoelkopf. “Cavity quantum electrodynamics for superconducting electrical circuits: An architecture for quantum computation”. In: *Phys. Rev. A* 69 (6 2004), p. 062320. DOI: [10.1103/PhysRevA.69.062320](https://doi.org/10.1103/PhysRevA.69.062320) (cit. on pp. 27, 35, 131).
- [BLT00a] A. Bezryadin, C. N. Lau, and M. Tinkham. “Quantum suppression of superconductivity in ultrathin nanowires”. In: *Nature* 404.6781 (2000), pp. 971–974. DOI: [10.1038/35010060](https://doi.org/10.1038/35010060) (cit. on p. 3).
- [BLT00b] A. Bezryadin, C. N. Lau, and M. Tinkham. “Quantum suppression of superconductivity in ultrathin nanowires”. In: *Nature* 404 (2000), pp. 971–974. DOI: [10.1038/35010060](https://doi.org/10.1038/35010060) (cit. on p. 13).
- [Bra13] J. Braumüller. “Development of a tunable transmon qubit in microstrip geometry”. MA thesis. Department of Physics, Karlsruhe Institute of Technology, 2013 (cit. on p. 70).
- [Bur+17] J. Burnett, J. Sagar, O. W. Kennedy, P. A. Warburton, and J. C. Fenton. “Low-Loss Superconducting Nanowire Circuits Using a Neon Focused Ion Beam”. In: *Phys. Rev. Applied* 8 (1 2017), p. 014039. DOI: [10.1103/PhysRevApplied.8.014039](https://doi.org/10.1103/PhysRevApplied.8.014039) (cit. on p. 14).
- [CA68] R. W. Cohen and B. Abeles. “Superconductivity in Granular Aluminum Films”. In: *Phys. Rev.* 168 (2 1968), pp. 444–450. DOI: [10.1103/PhysRev.168.444](https://doi.org/10.1103/PhysRev.168.444) (cit. on p. 40).
- [Cha60] R. G. Chambers. “Shift of an Electron Interference Pattern by Enclosed Magnetic Flux”. In: *Phys. Rev. Lett.* 5 (1 1960), pp. 3–5. DOI: [10.1103/PhysRevLett.5.3](https://doi.org/10.1103/PhysRevLett.5.3) (cit. on p. 115).

- [Che+17] Z. Chen, Y. Wang, T. Li, L. Tian, Y. Qiu, K. Inomata, F. Yoshihara, S. Han, F. Nori, J. S. Tsai, and J. Q. You. “Single-photon-driven high-order sideband transitions in an ultrastrongly coupled circuit-quantum-electrodynamics system”. In: *Phys. Rev. A* 96 (1 2017), p. 012325. DOI: [10.1103/PhysRevA.96.012325](https://doi.org/10.1103/PhysRevA.96.012325) (cit. on p. 110).
- [Cim+89] A. Cimmino, G. I. Opat, A. G. Klein, H. Kaiser, S. A. Werner, M. Arif, and R. Clothier. “Observation of the topological Aharonov-Casher phase shift by neutron interferometry”. In: *Phys. Rev. Lett.* 63 (4 1989), pp. 380–383. DOI: [10.1103/PhysRevLett.63.380](https://doi.org/10.1103/PhysRevLett.63.380) (cit. on p. 115).
- [CL81] A. O. Caldeira and A. J. Leggett. “Influence of Dissipation on Quantum Tunneling in Macroscopic Systems”. In: *Physical Review Letters* 46 (4 1981), pp. 211–214. DOI: [10.1103/PhysRevLett.46.211](https://doi.org/10.1103/PhysRevLett.46.211) (cit. on p. 12).
- [CLR10] D. B. Cordes, P. D. Lickiss, and F. Rataboul. “Recent Developments in the Chemistry of Cubic Polyhedral Oligosilsesquioxanes”. In: *Chemical Reviews* 110.4 (2010), pp. 2081–2173. DOI: [10.1021/cr900201r](https://doi.org/10.1021/cr900201r) (cit. on p. 47).
- [Cui16] Z. Cui. *Nanofabrication: Principles, Capabilities and Limits*. 2. ed. Springer, 2016. ISBN: 978-3319393599; 3319393596 (cit. on p. 46).
- [Deu+73] G. Deutscher, H. Fenichel, M. Gershenson, E. Grünbaum, and Z. Ovadyahu. “Transition to zero dimensionality in granular aluminum superconducting films”. In: *Journal of Low Temperature Physics* 10.1 (1973), pp. 231–243. DOI: [10.1007/BF00655256](https://doi.org/10.1007/BF00655256) (cit. on pp. 40, 41).
- [EH05] C. Enss and S. Hunklinger. *Low-Temperature Physics*. Springer, 2005. ISBN: 978-3540231646 (cit. on p. 53).
- [Eli+93] W. J. Elion, J. J. Wachters, L. L. Sohn, and J. E. Mooij. “Observation of the Aharonov-Casher effect for vortices in Josephson-junction arrays”. In: *Phys. Rev. Lett.* 71 (14 1993), pp. 2311–2314. DOI: [10.1103/PhysRevLett.71.2311](https://doi.org/10.1103/PhysRevLett.71.2311) (cit. on p. 115).
- [FA02] J. R. Friedman and D. V. Averin. “Aharonov-Casher-Effect Suppression of Macroscopic Tunneling of Magnetic Flux”. In: *Phys. Rev. Lett.* 88 (5 2002), p. 050403. DOI: [10.1103/PhysRevLett.88.050403](https://doi.org/10.1103/PhysRevLett.88.050403) (cit. on p. 124).
- [Fei+07] M. V. Feigel’man, L. B. Ioffe, V. E. Kravtsov, and E. A. Yuzbashyan. “Eigenfunction Fractality and Pseudogap State near the Superconductor-Insulator Transition”. In: *Phys. Rev. Lett.* 98 (2 2007), p. 027001. DOI: [10.1103/PhysRevLett.98.027001](https://doi.org/10.1103/PhysRevLett.98.027001) (cit. on p. 36).
- [Fei+10] M. V. Feigel’man, L. B. Ioffe, V. E. Kravtsov, and E. Cuevas. “Fractal superconductivity near localization threshold”. In: *Annals of Physics* 325.7 (2010), pp. 1390–1478. DOI: [10.1016/j.aop.2010.04.001](https://doi.org/10.1016/j.aop.2010.04.001) (cit. on p. 36).

- [FIM10] M. V. Feigel'man, L. B. Ioffe, and M. Mézard. "Superconductor-insulator transition and energy localization". In: *Phys. Rev. B* 82 (18 2010), p. 184534. DOI: [10.1103/PhysRevB.82.184534](https://doi.org/10.1103/PhysRevB.82.184534) (cit. on p. 36).
- [For+16] P. Forn-Diaz, G. Romero, C. J. P. M. Harmans, E. Solano, and J. E. Mooij. "Broken selection rule in the quantum Rabi model". In: *Scientific reports* 6 (2016), 26720 EP - (cit. on pp. 109, 110).
- [Fri+00] J. R. Friedman, V. Patel, W. Chen, S. K. Tolpygo, and J. E. Lukens. "Quantum superposition of distinct macroscopic states". In: *Nature* 406.6791 (2000), pp. 43–46. DOI: [10.1038/35017505](https://doi.org/10.1038/35017505) (cit. on pp. 77, 80, 91).
- [Gio88] N. Giordano. "Evidence for Macroscopic Quantum Tunneling in One-Dimensional Superconductors". In: *Physical Review Letters* 61 (18 1988), pp. 2137–2140. DOI: [10.1103/PhysRevLett.61.2137](https://doi.org/10.1103/PhysRevLett.61.2137) (cit. on pp. 3, 12).
- [Gra+18] S. E. de Graaf, S. T. Skacel, T. Hönigl-Decrinis, R. Shaikhdarov, H. Rotzinger, S. Linzen, M. Ziegler, U. Hübner, H.-G. Meyer, V. Antonov, E. Il'ichev, A. V. Ustinov, A. Y. Tzalenchuk, and O. V. Astafiev. "Charge quantum interference device". In: *Nature Physics* 14.6 (2018), pp. 590–594. DOI: [10.1038/s41567-018-0097-9](https://doi.org/10.1038/s41567-018-0097-9) (cit. on pp. 44, 45, 123–126).
- [Gri+07] A. E. Grigorescu, M. C. van der Krogt, C. W. Hagen, and P. Kruit. "10Nm Lines and Spaces Written in HSQ, Using Electron Beam Lithography". In: *Microelectron. Eng.* 84.5-8 (2007), pp. 822–824. DOI: [10.1016/j.mee.2007.01.022](https://doi.org/10.1016/j.mee.2007.01.022) (cit. on p. 47).
- [Grü+18] L. Grünhaupt, N. Maleeva, S. T. Skacel, M. Calvo, F. Levy-Bertrand, A. V. Ustinov, H. Rotzinger, A. Monfardini, G. Catelani, and I. M. Pop. "Loss Mechanisms and Quasiparticle Dynamics in Superconducting Microwave Resonators Made of Thin-Film Granular Aluminum". In: *Phys. Rev. Lett.* 121 (11 2018), p. 117001. DOI: [10.1103/PhysRevLett.121.117001](https://doi.org/10.1103/PhysRevLett.121.117001) (cit. on p. 43).
- [GZ08] D. S. Golubev and A. D. Zaikin. "Thermally activated phase slips in superconducting nanowires". In: *Physical Review B* 78 (14 2008), p. 144502. DOI: [10.1103/PhysRevB.78.144502](https://doi.org/10.1103/PhysRevB.78.144502) (cit. on p. 12).
- [Hou+08] A. A. Houck, J. A. Schreier, B. R. Johnson, J. M. Chow, J. Koch, J. M. Gambetta, D. I. Schuster, L. Frunzio, M. H. Devoret, S. M. Girvin, and R. J. Schoelkopf. "Controlling the Spontaneous Emission of a Superconducting Transmon Qubit". In: *Phys. Rev. Lett.* 101 (8 2008), p. 080502. DOI: [10.1103/PhysRevLett.101.080502](https://doi.org/10.1103/PhysRevLett.101.080502) (cit. on p. 88).
- [HZ12] T. T. Hongisto and A. B. Zorin. "Single-Charge Transistor Based on the Charge-Phase Duality of a Superconducting Nanowire Circuit". In: *Phys. Rev. Lett.* 108 (9 2012), p. 097001. DOI: [10.1103/PhysRevLett.108.097001](https://doi.org/10.1103/PhysRevLett.108.097001) (cit. on p. 3).

- [JC63] E. T. Jaynes and F. W. Cummings. “Comparison of quantum and semiclassical radiation theories with application to the beam maser”. In: *Proceedings of the IEEE* 51.1 (1963), pp. 89–109. DOI: 10.1109/PROC.1963.1664 (cit. on p. 33).
- [Jos62] B. D. Josephson. “Possible new effects in superconductive tunnelling”. In: *Physics Letters* 1 (1962), pp. 251–253. DOI: 10.1016/0031-9163(62)91369-0 (cit. on p. 17).
- [Kam11] H. Kamerlingh Onnes. “Further experiments with liquid helium. G. On the electrical resistance of pure metals, etc. VI. On the sudden change in the rate at which the resistance of mercury disappears.” In: *Comm. Phys. Lab. Univ. Leiden* 124c (1911) (cit. on pp. 2, 6).
- [KO77] I. Kulik and A. Omel’yanchuk. “Properties of superconducting microbridges in the pure limit”. In: *Sov. J. Low Temp. Phys. (Engl. Transl.); (United States)* 3:7 (1977) (cit. on p. 73).
- [Kön+06] M. König, A. Tschetschetkin, E. M. Hankiewicz, J. Sinova, V. Hock, V. Daumer, M. Schäfer, C. R. Becker, H. Buhmann, and L. W. Molenkamp. “Direct Observation of the Aharonov-Casher Phase”. In: *Phys. Rev. Lett.* 96 (7 2006), p. 076804. DOI: 10.1103/PhysRevLett.96.076804 (cit. on p. 115).
- [LA67] J. S. Langer and V. Ambegaokar. “Intrinsic Resistive Transition in Narrow Superconducting Channels”. In: *Physical Review* 164 (2 1967), pp. 498–519. DOI: 10.1103/PhysRev.164.498 (cit. on p. 11).
- [Lau+01] C. N. Lau, N. Markovic, M. Bockrath, A. Bezryadin, and M. Tinkham. “Quantum Phase Slips in Superconducting Nanowires”. In: *Physical Review Letters* 87 (2001), p. 217003. DOI: 10.1103/PhysRevLett.87.217003 (cit. on p. 13).
- [Leh+12] J. S. Lehtinen, T. Sajavaara, K. Y. Arutyunov, M. Y. Presnjakov, and A. L. Vasiliev. “Evidence of quantum phase slip effect in titanium nanowires”. In: *Phys. Rev. B* 85 (9 2012), p. 094508. DOI: 10.1103/PhysRevB.85.094508 (cit. on p. 3).
- [Lik79] K. K. Likharev. “Superconducting weak links”. In: *Rev. Mod. Phys.* 51 (1 1979), pp. 101–159. DOI: 10.1103/RevModPhys.51.101 (cit. on pp. 2, 73, 75, 91).
- [Lik91] K. K. Likharev. *Dynamics of Josephson junctions and circuits*. 2nd pr. Philadelphia, Pa. [u.a.]: Gordon and Breach, 1991. ISBN: 2-88124-042-9 (cit. on pp. 6, 76).

- [Lin+17] S. Linzen, M. Ziegler, O. V. Astafiev, M. Schmelz, U. Hübner, M. Diegel, E. Il'ichev, and H.-G. Meyer. “Structural and electrical properties of ultra-thin niobium nitride films grown by atomic layer deposition”. In: *Superconductor Science and Technology* 30.3 (2017), p. 035010. DOI: [10.1088/1361-6668/aa572a](https://doi.org/10.1088/1361-6668/aa572a) (cit. on pp. 43, 44, 152, 156).
- [Lit67] W. A. Little. “Decay of Persistent Currents in Small Superconductors”. In: *Physical Review* 156 (2 1967), pp. 396–403. DOI: [10.1016/S0031-8914\(35\)90097-0](https://doi.org/10.1016/S0031-8914(35)90097-0) (cit. on p. 10).
- [LL35] F. London and H. London. “Supraleitung und Diamagnetismus”. In: *Physica* 2 (1-12 1935), pp. 341–354. DOI: [10.1016/S0031-8914\(35\)90097-0](https://doi.org/10.1016/S0031-8914(35)90097-0) (cit. on p. 6).
- [Man+12] V. E. Manucharyan, N. A. Masluk, A. Kamal, J. Koch, L. I. Glazman, and M. H. Devoret. “Evidence for coherent quantum phase slips across a Josephson junction array”. In: *Phys. Rev. B* 85 (2 2012), p. 024521. DOI: [10.1103/PhysRevB.85.024521](https://doi.org/10.1103/PhysRevB.85.024521) (cit. on p. 2).
- [MH05] J. E. Mooij and C. J. P. M. Harmans. “Phase-slip flux qubits”. In: *New Journal of Physics* 7.1 (2005), p. 219. DOI: [10.1088/1367-2630/7/1/219](https://doi.org/10.1088/1367-2630/7/1/219) (cit. on pp. 3, 23, 68, 91, 130).
- [MH70] D. E. McCumber and B. I. Halperin. “Time Scale of Intrinsic Resistive Fluctuations in Thin Superconducting Wires”. In: *Physical Review B* 1 (3 1970), pp. 1054–1070. DOI: [10.1103/PhysRev.164.498](https://doi.org/10.1103/PhysRev.164.498) (cit. on p. 11).
- [Mil+14] S. A. Mills, N. E. Staley, J. J. Wisser, C. Shen, Z. Xu, and Y. Liu. “Single-crystal superconducting nanowires of NbSe<sub>2</sub> fabricated by reactive plasma etching”. In: *Applied Physics Letters* 104.5 (2014), p. 052604. DOI: [10.1063/1.4864158](https://doi.org/10.1063/1.4864158) (cit. on p. 14).
- [MLG02] K. A. Matveev, A. I. Larkin, and L. I. Glazman. “Persistent Current in Superconducting Nanorings”. In: *Phys. Rev. Lett.* 89 (9 2002), p. 096802. DOI: [10.1103/PhysRevLett.89.096802](https://doi.org/10.1103/PhysRevLett.89.096802) (cit. on pp. 37, 124).
- [MN06] J. E. Mooij and Y. V. Nazarov. “Superconducting nanowires as quantum phase-slip junctions”. In: *Nat Phys* 2.3 (2006), pp. 169–172. DOI: [10.1038/nphys234](https://doi.org/10.1038/nphys234) (cit. on pp. 2, 15, 91).
- [MO33] W. Meissner and R. Ochsenfeld. “Ein neuer Effekt bei Eintritt der Supraleitfähigkeit”. In: *Naturwissenschaften* 21 (44 1933), pp. 787–788. DOI: [10.1007/BF01504252](https://doi.org/10.1007/BF01504252) (cit. on p. 6).
- [Moo+15] J. E. Mooij, G. Schön, A. Shnirman, T. Fuse, C. J. P. M. Harmans, H. Rotzinger, and A. H. Verbruggen. “Superconductor-insulator transition in nanowires and nanowire arrays”. In: *New Journal of Physics* 17.3 (2015), p. 033006. DOI: [10.1088/1367-2630/17/3/033006](https://doi.org/10.1088/1367-2630/17/3/033006) (cit. on p. 20).

- [Mor+14] T. Morgan-Wall, H. J. Hughes, N. Hartman, T. M. McQueen, and N. Marković. “Fabrication of sub-15nm aluminum wires by controlled etching”. In: *Applied Physics Letters* 104.17 (2014), p. 173101. DOI: [10.1063/1.4874137](https://doi.org/10.1063/1.4874137) (cit. on p. 14).
- [Nam+98a] H. Namatsu, T. Yamaguchi, M. Nagase, K. Yamazaki, and K. Kurihara. “Nano-patterning of a hydrogen silsesquioxane resist with reduced linewidth fluctuations”. In: *Microelectronic Engineering* 41.Supplement C (1998), pp. 331–334. DOI: [https://doi.org/10.1016/S0167-9317\(98\)00076-8](https://doi.org/10.1016/S0167-9317(98)00076-8) (cit. on p. 47).
- [Nam+98b] H. Namatsu, Y. Takahashi, K. Yamazaki, T. Yamaguchi, M. Nagase, and K. Kurihara. “Three-dimensional siloxane resist for the formation of nanopatterns with minimum linewidth fluctuations”. In: *Journal of Vacuum Science & Technology B: Microelectronics and Nanometer Structures Processing, Measurement, and Phenomena* 16.1 (1998), pp. 69–76. DOI: [10.1116/1.589837](https://doi.org/10.1116/1.589837) (cit. on p. 47).
- [NBT72] R. S. Newbower, M. R. Beasley, and M. Tinkham. “Fluctuation Effects on the Superconducting Transition of Tin Whisker Crystals”. In: *Phys. Rev. B* 5 (3 1972), pp. 864–868. DOI: [10.1103/PhysRevB.5.864](https://doi.org/10.1103/PhysRevB.5.864) (cit. on p. 12).
- [Oel+10] G. Oelsner, S. H. W. van der Ploeg, P. Macha, U. Hübner, D. Born, S. Anders, E. Il’ichev, H.-G. Meyer, M. Grajcar, S. Wünsch, M. Siegel, A. N. Omelyanchouk, and O. Astafiev. “Weak continuous monitoring of a flux qubit using coplanar waveguide resonator”. In: *Phys. Rev. B* 81 (17 2010), p. 172505. DOI: [10.1103/PhysRevB.81.172505](https://doi.org/10.1103/PhysRevB.81.172505) (cit. on pp. 101, 103).
- [Ott+99] A. van Otterlo, D. Golubev, A. Zaikin, and G. Blatter. “Dynamics and effective actions of BCS superconductors”. In: *The European Physical Journal B - Condensed Matter and Complex Systems* 10.1 (1999), pp. 131–143. DOI: [10.1007/s100510050836](https://doi.org/10.1007/s100510050836) (cit. on p. 12).
- [Pel+13] J. T. Peltonen, O. V. Astafiev, Y. P. Korneeva, B. M. Voronov, A. A. Korneev, I. M. Charaev, A. V. Semenov, G. N. Golt’sman, L. B. Ioffe, T. M. Klapwijk, and J. S. Tsai. “Coherent flux tunneling through NbN nanowires”. In: *Phys. Rev. B* 88 (22 2013), p. 220506. DOI: [10.1103/PhysRevB.88.220506](https://doi.org/10.1103/PhysRevB.88.220506) (cit. on pp. 3, 36, 43, 91, 93, 99, 101, 113).
- [Pel+16] J. T. Peltonen, Z. H. Peng, Y. P. Korneeva, B. M. Voronov, A. A. Korneev, A. V. Semenov, G. N. Golt’sman, J. S. Tsai, and O. V. Astafiev. “Coherent dynamics and decoherence in a superconducting weak link”. In: *Phys. Rev. B* 94 (18 2016), p. 180508. DOI: [10.1103/PhysRevB.94.180508](https://doi.org/10.1103/PhysRevB.94.180508) (cit. on pp. 98, 103, 113).

- [Pfi14] M. Pfirrmann. “Fabrication and transport measurements of parallel arrays of nanowires”. MA thesis. Department of Physics, Karlsruhe Institute of Technology, 2014 (cit. on p. 62).
- [Pop+12] I. M. Pop, B. Douçot, L. Ioffe, I. Protopopov, F. Lecocq, I. Matei, O. Buisson, and W. Guichard. “Experimental demonstration of Aharonov-Casher interference in a Josephson junction circuit”. In: *Phys. Rev. B* 85 (9 2012), p. 094503. DOI: [10 . 1103 / PhysRevB . 85 . 094503](https://doi.org/10.1103/PhysRevB.85.094503) (cit. on pp. 115, 124).
- [PTP46] E. M. Purcell, H. C. Torrey, and R. V. Pound. “Resonance Absorption by Nuclear Magnetic Moments in a Solid”. In: *Phys. Rev.* 69 (1-2 1946), pp. 37–38. DOI: [10 . 1103 / PhysRev . 69 . 37](https://doi.org/10.1103/PhysRev.69.37) (cit. on p. 88).
- [RB03] A. Rogachev and A. Bezryadin. “Superconducting properties of polycrystalline Nb nanowires templated by carbon nanotubes”. In: *Applied Physics Letters* 83.3 (2003), pp. 512–514. DOI: [10 . 1063 / 1 . 1592313](https://doi.org/10.1063/1.1592313) (cit. on p. 14).
- [RB05] M. Remeika and A. Bezryadin. “Sub-10 nanometre fabrication: molecular templating, electron-beam sculpting and crystallization of metallic nanowires”. In: *Nanotechnology* 16.8 (2005), p. 1172 (cit. on p. 14).
- [RHL95] R. Rouse, S. Han, and J. E. Lukens. “Observation of Resonant Tunneling between Macroscopically Distinct Quantum Levels”. In: *Phys. Rev. Lett.* 75 (8 1995), pp. 1614–1617. DOI: [10 . 1103 / PhysRevLett . 75 . 1614](https://doi.org/10.1103/PhysRevLett.75.1614) (cit. on pp. 77, 80, 91).
- [Rot+17] H. Rotzinger, S. T. Skacel, M. Pfirrmann, J. N. Voss, J. Münzberg, S. Probst, P. Bushev, M. P. Weides, A. V. Ustinov, and J. E. Mooij. “Aluminium-oxide wires for superconducting high kinetic inductance circuits”. In: *Superconductor Science and Technology* 30.2 (2017), p. 025002. DOI: [10 . 1088 / 0953 - 2048 / 30 / 2 / 025002](https://doi.org/10.1088/0953-2048/30/2/025002) (cit. on pp. 40–42, 73, 91).
- [San+93] K. Sangster, E. A. Hinds, S. M. Barnett, and E. Riis. “Measurement of the Aharonov-Casher phase in an atomic system”. In: *Phys. Rev. Lett.* 71 (22 1993), pp. 3641–3644. DOI: [10 . 1103 / PhysRevLett . 71 . 3641](https://doi.org/10.1103/PhysRevLett.71.3641) (cit. on p. 115).
- [Sch97] V. V. Schmidt. *The physics of superconductors : introduction to fundamentals and applications; with 51 problems with solutions*. Ed. by P. [ Müller. Berlin: Springer, 1997. ISBN: 3-540-61243-2; 978-3-642-08251-1 (cit. on pp. 6, 76).
- [Sim01] R. N. Simons. *Coplanar waveguide circuits, components, and systems*. Wiley series in microwave and optical engineering. New York, NY: Wiley-Interscience, 2001. ISBN: 0-471-16121-7 (cit. on p. 70).

- [SM89a] S. Saito and Y. Murayama. “Effect of dissipation on macroscopic quantum tunneling in thin superconducting wires”. In: *Physics Letters A* 139 (1989), pp. 85–90. DOI: [10.1016/0375-9601\(89\)90614-2](https://doi.org/10.1016/0375-9601(89)90614-2) (cit. on p. 13).
- [SM89b] S. Saito and Y. Murayama. “Macroscopic quantum tunneling in thin superconducting wires”. In: *Physics Letters A* 135 (1989), pp. 55–58. DOI: [10.1016/0375-9601\(89\)90727-5](https://doi.org/10.1016/0375-9601(89)90727-5) (cit. on p. 13).
- [Tin04] M. Tinkham. *Introduction to superconductivity*. 2. ed. Dover books on physics. Mineola, NY: Dover Publ., 2004. ISBN: 0-486-43503-2; 978-0-486-43503-9 (cit. on pp. 2, 6, 76, 126).
- [Tza+07] T. L. Tzalenchuk, C. H. Webster, J. E. Healey, M. S. Colclough, C. M. Muirhead, and A. Ya. “Circuit QED with a flux qubit strongly coupled to a coplanar transmission line resonator”. In: *Superconductor Science and Technology* 20.8 (2007), p. 814. DOI: [10.1088/0953-2048/20/8/016](https://doi.org/10.1088/0953-2048/20/8/016) (cit. on pp. 101, 103).
- [VN12] M. Vanević and Y. V. Nazarov. “Quantum Phase Slips in Superconducting Wires with Weak Inhomogeneities”. In: *Phys. Rev. Lett.* 108 (18 2012), p. 187002. DOI: [10.1103/PhysRevLett.108.187002](https://doi.org/10.1103/PhysRevLett.108.187002) (cit. on pp. 14, 106).
- [Vos14] J. N. Voss. “Fabrication and Characterization of Metallic Aluminium Oxide Films”. Bachelor Thesis. Department of Physics, Karlsruhe Institute of Technology, 2014 (cit. on pp. 40–42).
- [Vos17] J. N. Voss. “Nonlinear effects in superconducting granular aluminium oxide nanowires”. MA thesis. Department of Physics, Karlsruhe Institute of Technology, 2017 (cit. on p. 67).
- [WAB03] M. J. Word, I. Adesida, and P. R. Berger. “Nanometer-period gratings in hydrogen silsesquioxane fabricated by electron beam lithography”. In: *Journal of Vacuum Science & Technology B: Microelectronics and Nanometer Structures Processing, Measurement, and Phenomena* 21.6 (2003), pp. L12–L15. DOI: [10.1116/1.1629711](https://doi.org/10.1116/1.1629711) (cit. on p. 47).
- [Wil15] M. Wildermuth. “Temperature and power dependence of superconducting aluminum oxide microwave resonators”. Bachelor Thesis. Department of Physics, Karlsruhe Institute of Technology, 2015 (cit. on pp. 42, 43).
- [Zai+97] A. D. Zaikin, D. S. Golubev, A. v. Otterlo, and G. T. Zimányi. “Quantum Phase Slips and Transport in Ultrathin Superconducting Wires”. In: *Physical Review Letters* 78 (1997), pp. 1552–1555. DOI: [10.1103/PhysRevLett.78.1552](https://doi.org/10.1103/PhysRevLett.78.1552) (cit. on p. 13).
- [Zgi+08] M. Zgirski, K.-P. Riikonen, V. Touboltsev, and K. Y. Arutyunov. “Quantum fluctuations in ultranarrow superconducting aluminum nanowires”. In: *Phys. Rev. B* 77 (5 2008), p. 054508. DOI: [10.1103/PhysRevB.77.054508](https://doi.org/10.1103/PhysRevB.77.054508) (cit. on p. 3).

- [Zie+13] M. Ziegler, L. Fritsch, J. Day, S. Linzen, S. Anders, J. Toussaint, and H.-G. Meyer. “Superconducting niobium nitride thin films deposited by metal organic plasma-enhanced atomic layer deposition”. In: *Superconductor Science and Technology* 26.2 (2013), p. 025008. DOI: [10 . 1088 / 0953 - 2048/26/2/025008](https://doi.org/10.1088/0953-2048/26/2/025008) (cit. on pp. 43, 44).
- [Zie+79] P. Ziemann, O. Meyer, G. Heim, and W. Buckel. “Low temperature self-ion irradiation of pure and granular aluminium-films”. In: *Zeitschrift für Physik B Condensed Matter* 35.2 (1979), pp. 141–149. DOI: [10 . 1007 / BF01321240](https://doi.org/10.1007/BF01321240) (cit. on p. 40).

# List of Publications

Published:

1. L. Grünhaupt, M. Spiecker, D. Gusenkova, N. Maleeva, *S. T. Skacel*, I. Takmakov, F. Valenti, P. Winkel, H. Rotzinger, W. Wernsdorfer, A. V. Ustinov, and I. M. Pop. "Granular aluminium as a superconducting material for high-impedance quantum circuits", *Nature Materials* (2019)
2. F. Valenti, F. Henriques, G. Catelani, N. Maleeva, L. Grünhaupt, U. v. Lüpke, *S. T. Skacel*, P. Winkel, A. Bilmes, A. V. Ustinov, J. Goupy, M. Calvo, A. Benoît, F. Levy-Bertrand, A. Monfardini, and I. M. Pop. "Interplay Between Kinetic Inductance, Nonlinearity, and Quasiparticle Dynamics in Granular Aluminum Microwave Kinetic Inductance Detectors", *Physical Review Applied* **11**, 054087 (2019)
3. S. E. de Graaf, *S. T. Skacel*, T. Hoenigl-Decrinis, R. Shaikhaidarov, H. Rotzinger, S. Linzen, M. Ziegler, U. Hübner, H.-G. Meyer, V. Antonov, E. Il'ichev, A. V. Ustinov, A. Ya. Tzalenchuk, and O. V. Astafiev. "Charge Quantum Interference Device", *Nature Physics* **14**, 590–594 (2018).
4. L. Grünhaupt, N. Maleeva, *S. T. Skacel*, M. Calvo, F. Levy-Bertrand, A. V. Ustinov, H. Rotzinger, A. Monfardini, G. Catelani, and I. M. Pop. "Loss Mechanisms and Quasiparticle Dynamics in Superconducting Microwave Resonators Made of Thin-Film Granular Aluminum", *Physical Review Letters* **121**, 117001 (2018).
5. S. Richer, N. Maleeva, *S. T. Skacel*, I. M. Pop, and D. DiVincenzo. "Inductively shunted transmon qubit with tunable transverse and longitudinal coupling", *Physical Review B* **96**, 174520 (2017).
6. L. Grünhaupt, U. v. Lüpke, D. Gusenkova, *S. T. Skacel*, N. Maleeva, S. Schlör, A. Bilmes, H. Rotzinger, A. V. Ustinov, M. Weides, and I. M. Pop. "An ion beam milling process for native  $\text{AlO}_x$  layers enabling coherent superconducting contacts", *Applied Physics Letters* **111**, 072601 (2017).
7. H. Rotzinger, *S. T. Skacel*, M. Pfirrmann, J. N. Voss, J. Münzberg, S. Probst, P. Bushev, M. P. Weides, A. V. Ustinov, and J. E. Mooij. "Aluminium-oxide wires for superconducting high kinetic inductance circuits", *Superconductor Science and Technology* **30**, 025002 (2017).

8. *S. T. Skacel*, Ch. Kaiser, S. Wuensch, H. Rotzinger, A. Lukashenko, M. Jerger, G. Weiss, M. Siegel, and A. V. Ustinov. "Probing the density of states of two-level tunneling systems in silicon oxide films using superconducting lumped element resonators", *Applied Physics Letters* **106**, 022603 (2015).
9. J. Braumüller, J. Cramer, S. Schlör, H. Rotzinger, L. Radtke, A. Lukashenko, P. Yang, *S. T. Skacel*, S. Probst, M. Marthaler, L. Guo, A. V. Ustinov, and M. Weides. "Multiphoton dressing of an anharmonic superconducting many-level quantum circuit", *Physical Review B* **91**, 054523 (2015).
10. A. Bruno, *S. T. Skacel*, Ch. Kaiser, S. Wünsch, M. Siegel, A. V. Ustinov, and M. P. Lisitskiy. "Investigation of Dielectric Losses in Hydrogenated Amorphous Silicon (a-Si:H) thin Films Using Superconducting Microwave Resonators", *Physics Procedia* **36**, 245-249 (2012).
11. Ch. Kaiser, *S. T. Skacel*, S. Wünsch, R. Dolata, B. Mackrodt, A. Zorin, and M. Siegel. "Measurement of dielectric losses in amorphous thin films at gigahertz frequencies using superconducting resonators", *Superconductor Science and Technology* **23**, 075008 (2010).

In preparation:

1. Yannick Schön, J. N. Voss, M. Wildermuth, A. Schneider, *S. T. Skacel*, I. Pop, M. P. Weides, J. H. Cole, H. Rotzinger, and A. V. Ustinov, "Rabi oscillations in disordered superconducting nanowire circuits", *in preparation* (2019).

# Appendix



# A. Fabrication details

In the following, the parameters are listed which were used in the fabrication of the different samples. Furthermore, some precautions are mentioned that had to be taken in order to guarantee for reproducibility.

Of not mentioned differently, the fabrication steps are performed at the Karlsruhe Institute for Technology.

## A.1. Samples

### A.1.1. Chip A0102

Sample A0102 contains the experiment discussed in Sec. 4.1. The fabrication procedure is visualized in Fig. 3.5 and Fig. 3.5 **left** column.

### $\text{AlO}_x$ thin film application

The application takes place in the home made "SAPHIR" sputter tool.

Chip name	Date	$t_{\text{psp}} /$ $t_{\text{msp}}$ (min)	$P_{\text{psp}} /$ $P_{\text{msp}}$ (W)	$V_{\text{psp}} /$ $V_{\text{msp}}$ (V)	$I_{\text{psp}} /$ $I_{\text{msp}}$ (mA)
A (no. 54)	2014/12/15	3 : 00 / 3 : 32	100	350 / 350	285 / 285
$P_{\text{mc,psp}} /$ $P_{\text{mc,msp}}$ ( $\mu\text{bar}$ )	$\text{flow}_{\text{Ar,psp}} /$ $\text{flow}_{\text{Ar,msp}}$ (sccm)	$\text{flow}_{\text{Ar/O,psp}} /$ $\text{flow}_{\text{Ar/O,msp}}$ (sccm)	Thickness (nm)	R ( $k\Omega$ )	Comment
7.65 / 7.41	40.6 / 40.6	2.0 / 2.0	22	3 over chip (2016/03/03)	pulsed process, rotation, silicon wafer

The abbreviations "psp" and "msp" stand for *pre-sputter* and *main sputter process*.  
"mc" stands for *main chamber* while "Ar" represents *argon* and "O" *oxygen*.

### **NbO<sub>x</sub> passivation layer application**

The application takes place in a commercial PLASSYS MEB 550 S evaporation tool.

Chip name	Date	Deposition rate (nm/s)	Thickness (nm)	Angle (°)	P <sub>mc,base</sub> (mbar)
A	2015/09/15	0.004	5	0	$2.5 \cdot 10^{-8}$

"mc" stands for *main chamber*.

### **HSQ (e-beam resist) application**

The application is done in a standard spincoater, namely a POLOS Wafer Spinner.

Chip name	Date	Resist	v <sub>ramp</sub> (rpm)	t <sub>ramp</sub> (s)
A	2016/03/03	HSQ 2%	300	4
a <sub>ramp</sub> (rpm/s)	v <sub>spin</sub> (rpm)	t <sub>spin</sub> (s)	T <sub>hp</sub> (°C)	t <sub>hp</sub> (s)
7500	4000	60	150	120

"hp" stands for *hot plate*.

### **e-beam lithography of HSQ**

The lithography is performed in a 50 keV JEOL JBX-5500ZD e-beam machine.

Chip name	Date	Beam dose ( $\mu\text{C}/\text{cm}^2$ )	t <sub>exp</sub> (h)	Comment
A	2016/03/03	900	2	Pattern E0059, wire doses 9.5, 14, 18

"exp" stands for *exposure*.

## Development of exposed HSQ

Chip name	Date	Developer	$t_{\text{dev}}$ (s)	Rinse
A	2016/03/03	MIF 726	50	60 s in H <sub>2</sub> O.

"dev" stands for *development*.

## HSQ and AlO<sub>x</sub> etching

The etching is performed with an Oxford Plasma Technology Plasmalab 100 ICP 180.

Chip name	Date	Recipe	$p_{\text{set}}/p_{\text{real}}$ (mTorr)	Gases
A	2016/03/24	HR-Ar-Cl	10 / 9.6	Ar / Cl
flow <sub>gas</sub> (sccm)	$P_{\text{RIE}}$ (W)	$P_{\text{ICP}}$ (W)	$t_{\text{etch}}$ (s)	Comment
2 / 12	100	200	80	15 min precond.

"Ar" and "Cl" stand for *argon* and *chlorine*. "RIE" and "ICP" stand for *reactive ion etching* and *inductively coupled plasma*. "precond." is abbreviated for *preconditioning*.

## Optical resist application

The application is done in a standard spincoater, namely a POLOS Wafer Spinner.

Chip name	Date	Resist	$v_{\text{ramp}}$ (rpm)	$t_{\text{ramp}}$ (s)
A	2016/03/29	AZ 5214E	500	3
$a_{\text{ramp}}$ (rpm/s)	$v_{\text{spin}}$ (rpm)	$t_{\text{spin}}$ (s)	$T_{\text{hp}}$ (°C)	$t_{\text{hp}}$ (s)
7500	6000	60	110	50

"hp" stands for *hot plate*.

In order to allow for a good contact of the resist on the etched surface, Hexamethyldisilazane (HMDS) was used prior to resist application.

## Optical lithography

The lithography is performed with a MA6 maskaligner unit by SÜSS MicroTec. The pattern is provided by a chromium mask. The resist is applied before the metal layer since a lift-off technique is used.

Chip name	Date	$I_{\text{exp}}$ (mW/cm <sup>2</sup> )	$P_{\text{exp}}$ (W)	$t_{\text{exp}}$ (s)	Mode
A	2016/03/29	5.0	343	7.0	Hard contact

"exp" stands for *exposure*.

## Development of exposed optical resist

Chip name	Date	Developer	$t_{\text{dev}}$ (s)	Rinse
A	2016/03/29	AZ Developer : H <sub>2</sub> O 1 : 1	45	60 s in H <sub>2</sub> O.

"dev" stands for *development*.

## Aluminium thin film application

The application takes place in a commercial PLASSYS MEB 550 S evaporation tool.

Chip name	Date	Deposition rate (nm/s)	Thickness (nm)	Angle (°)	$P_{\text{mc,base}}$ (mbar)
A	2016/03/29	0.2	30 (5 rpm rotation) 300 (no rotation)	20 / 0	$6.6 \cdot 10^{-8}$

"mc" stands for *main chamber*.

Steps of 5 s descum at 200 V and 10 mA plus 20 s cleaning with Ar plasma at  $-20^\circ$ , 200 V, 15 mA and 5 rpm planetary rotation were performed prior to application in order to sufficiently clean the surface from water and resist residuals.

### **Stripping of aluminium thin film**

Chip name	Date	Remover	Ultrasonic bath level	$t_{\text{lift-off}}$	Rinse in
A	2016/03/29	NEP	0 – 1	10	Isopropanol, H <sub>2</sub> O

### A.1.2. Chip A0105

Sample A0105 contains the experiments discussed in Sec. 4.2 and Sec. 4.2. The fabrication procedure is visualized in Fig. 3.5 and Fig. 3.5 **right** column.

### NbN thin film application

The application takes place as described in Sec. 3.1.2 and in [Lin+17] at the IPTH Jena. A resistance of 6–7 k $\Omega$  at the diagonal of a 20 $\times$ 20 mm<sup>2</sup> has been measured before starting subsequent steps.

### HSQ (e-beam resist) application

The application is done in a standard spincoater, namely a POLOS Wafer Spinner.

Chip name	Date	Resist	$v_{\text{ramp}}$ (rpm)	$t_{\text{ramp}}$ (s)
A	2016/03/24	HSQ 2%	300	4
$a_{\text{ramp}}$ (rpm/s)	$v_{\text{spin}}$ (rpm)	$t_{\text{spin}}$ (s)	$T_{\text{hp}}$ (°C)	$t_{\text{hp}}$ (s)
7500	4000	60	150	120

"hp" stands for *hot plate*.

### e-beam lithography of HSQ

The lithography is performed in a 50 keV JEOL JBX-5500ZD e-beam machine.

Chip name	Date	Beam dose ( $\mu\text{C}/\text{cm}^2$ )	$t_{\text{exp}}$ (h)	Comment
A	2016/03/24	900	2	Pattern E0060, 8 wire doses

"exp" stands for *exposure*.

## Development of exposed HSQ

Chip name	Date	Developer	$t_{dev}$ (s)	Rinse
A	2016/03/24	MIF 726	50	60 s in H <sub>2</sub> O.

"dev" stands for *development*.

## Optical resist application

The application is done in a standard spincoater, namely a POLOS Wafer Spinner.

Chip name	Date	Resist	$v_{ramp}$ (rpm)	$t_{ramp}$ (s)
A	2016/04/01	AZ 5214E	500	3
$a_{ramp}$ (rpm/s)	$v_{spin}$ (rpm)	$t_{spin}$ (s)	$T_{hp}$ (°C)	$t_{hp}$ (s)
7500	6000	60	110	50

"hp" stands for *hot plate*.

## Optical lithography

The lithography is performed with a MA6 maskaligner unit by SÜSS MicroTec. The pattern is provided by a chromium mask. The resist is applied before the metal layer since a lift-off technique is used.

Chip name	Date	$I_{exp}$ (mW/cm <sup>2</sup> )	$P_{exp}$ (W)	$t_{exp}$ (s)	Mode
A	2016/04/01	5.0	347	7.0	Hard contact, pattern M0021 MIC <sub>Res_v1</sub>

"exp" stands for *exposure*.

## Development of exposed optical resist

Chip name	Date	Developer	$t_{\text{dev}}$ (s)	Rinse
A	2016/04/01	AZ Developer : H <sub>2</sub> O 1 : 1	50	60 s in H <sub>2</sub> O.

"dev" stands for *development*.

## Titanium and gold thin film application

The application takes place in a commercial PLASSYS MEB 550 S evaporation tool. The 5 nm titanium (Ti) layer serves as sticking layer between the NbN and the gold (Au) layer.

Chip name	Date	Deposition rate (nm/s)	Thickness (nm)	Angle (°)	$P_{\text{mc,base}}$ (mbar)
A	2016/04/01	0.2	5 (Ti, no rotation)/ 80 (Au) (no rotation)	0/ 0	$6.6 \cdot 10^{-8}$

"mc" stands for *main chamber*.

No cleaning steps were done in order to avoid any risk for the thin NbN film.

## Stripping of Ti/Au thin films

Chip name	Date	Remover	Ultrasonic bath level	$t_{\text{lift-off}}$	Rinse in
A	2016/03/29	NEP	0 – 1	10	Isopropanol, H <sub>2</sub> O

## HSQ and NbN etching

The etching is performed with an Oxford Plasma Technology Plasmalab 100 at the Royal Holloway, University of London.

Chip name	Date	Recipe	$P_{\text{set}}/P_{\text{real}}$ (mTorr)	Gases
A	2016/04/20	TiN Etch	100 / 100.1	Ar / CF <sub>4</sub>
flow <sub>gas</sub> (sccm)	$P_{\text{RIE}}$ (W)	$P_{\text{ICP}}$ (W)	$t_{\text{etch}}$ (s)	Comment
2 / 20	210	No ICP	20	5 min oxygen plasma

"Ar" and "CF<sub>4</sub>" stand for *argon* and *tetrafluoromethane*. "RIE" and "ICP" stand for *reactive ion etching* and *inductively coupled plasma*.

### A.1.3. Chip A0109

Since it became clear that the constrictions were wider than we had aimed at (see Sec. 4.2), sample A0109 was fabricated with a lowered overall e-beam dose. The base dose of  $1000 \mu\text{C}/\text{cm}^2$  was higher than before, but therefore the dose factors were reduced. The reason for that were machine requirements since the wire dose factors spanned over a large range. The sample eventually showed the originally sighted widths.

### NbN thin film application

The application takes place as described in Sec. 3.1.2 and in [Lin+17] at the IPTH Jena. A resistance of  $4-5 \text{ k}\Omega$  at the diagonal of a  $20 \times 20 \text{ mm}^2$  has been measured before starting subsequent steps.

### HSQ (e-beam resist) application

The application is done in a standard spincoater, namely a POLOS Wafer Spinner.

Chip name	Date	Resist	$v_{\text{ramp}}$ (rpm)	$t_{\text{ramp}}$ (s)
A	2016/05/24	HSQ 2%	300	4
$a_{\text{ramp}}$ (rpm/s)	$v_{\text{spin}}$ (rpm)	$t_{\text{spin}}$ (s)	$T_{\text{hp}}$ (°C)	$t_{\text{hp}}$ (s)
7500	4000	60	150	120

"hp" stands for *hot plate*.

## e-beam lithography of HSQ

The lithography is performed in a 50 keV JEOL JBX-5500ZD e-beam machine.

Chip name	Date	Beam dose ( $\mu\text{C}/\text{cm}^2$ )	$t_{\text{exp}}$ (h)	Comment
A	2016/05/24	1000	2	Pattern E0061b, 8 wire doses

"exp" stands for *exposure*.

## Development of exposed HSQ

Chip name	Date	Developer	$t_{\text{dev}}$ (s)	Rinse
A	2016/05/24	MIF 726	50	60 s in $\text{H}_2\text{O}$ .

"dev" stands for *development*.

## Optical resist application

The application is done in a standard spincoater, namely a POLOS Wafer Spinner.

Chip name	Date	Resist	$v_{\text{ramp}}$ (rpm)	$t_{\text{ramp}}$ (s)
A	2016/05/24	AZ 5214E	500	3
$a_{\text{ramp}}$ (rpm/s)	$v_{\text{spin}}$ (rpm)	$t_{\text{spin}}$ (s)	$T_{\text{hp}}$ ( $^{\circ}\text{C}$ )	$t_{\text{hp}}$ (s)
7500	6000	60	110	50

"hp" stands for *hot plate*.

## Optical lithography

The lithography is performed with a MA6 maskaligner unit by SÜSS MicroTec. The pattern is provided by a chromium mask. The resist is applied before the metal layer since a lift-off technique is used.

Chip name	Date	$I_{\text{exp}}$ (mW/cm <sup>2</sup> )	$P_{\text{exp}}$ (W)	$t_{\text{exp}}$ (s)	Mode
A	2016/05/25	5.0	347	7.0	Hard contact, pattern M0024 RHUL <sub>K</sub> IT2

"exp" stands for *exposure*.

## Development of exposed optical resist

Chip name	Date	Developer	$t_{\text{dev}}$ (s)	Rinse
A	2016/05/25	AZ Developer : H <sub>2</sub> O 1 : 1	50	60 s in H <sub>2</sub> O.

"dev" stands for *development*.

## Titanium and gold palladium thin film application

The application takes place in a commercial PLASSYS MEB 550 S evaporation tool. The 5 nm titanium (Ti) layer serves as sticking layer between the NbN and the gold palladium (AuPd) layer.

Chip name	Date	Deposition rate (nm/s)	Thickness (nm)	Angle (°)	$P_{\text{mc,base}}$ (mbar)
A	2016/05/25	0.2	5 (Ti, no rotation)/ 80 (AuPd) (no rotation)	0/ 0	$6.6 \cdot 10^{-8}$

"mc" stands for *main chamber*.

No cleaning steps were done in order to avoid any risk for the thin NbN film.

## Stripping of Ti/Au thin films

Chip name	Date	Remover	Ultrasonic bath level	$t_{\text{lift-off}}$	Rinse in
A	2016/05/25	NEP	0 – 1	10	Isopropanol, H <sub>2</sub> O

## HSQ and NbN etching

The etching is performed with an Oxford Plasma Technology Plasmalab 100 at the Royal Holloway, University of London.

Chip name	Date	Recipe	$P_{\text{set}}/P_{\text{real}}$ (mTorr)	Gases
A	2016/06/06	TiN Etch	100 / 100.1	Ar / CF <sub>4</sub>
flow <sub>gas</sub> (sccm)	$P_{\text{RIE}}$ (W)	$P_{\text{ICP}}$ (W)	$t_{\text{etch}}$ (s)	Comment
2 / 20	210	No ICP	15	5 min oxygen plasma

"Ar" and "CF<sub>4</sub>" stand for *argon* and *tetrafluoromethane*. "RIE" and "ICP" stand for *reactive ion etching* and *inductively coupled plasma*.

## A.2. General precautions

In this section, the precautions are discussed that had to be taken during the fabrication processes.

### HSQ (e-beam resist) application

This step is error-prone due to the low boiling point of the HSQ in combination with the minor film thickness of 50 nm that it is spun on. For decent spin-on results, the chip has to be cleaned in a resist stripper like N-Methyl-2-pyrrolidone (NMP) at very soft ultrasound for around 5 min. After that, the chip is directly immersed in isopropanol and subsequently blown dry with a nitrogen gun.

The HSQ has to be stored in a standard refrigerator at any time. This keeps it usable for around 3-4 months before one of its main ingredients Methyl isopropyl keton (MIPK) is evaporated and the HSQ becomes jelly. In order to store it for a longer time, it has to be frozen at  $-18^{\circ}\text{C}$ .

For the spin-on process, the HSQ has to be warmed up to around  $20^{\circ}\text{C}$ . Leaving a small bottle at room temperature for 20 min does this job. The ramp time should not be increased above 3 – 4 s. Otherwise the HSQ starts to solidify before spinning takes place.

It has to be avoided to place the chip on a cold surface (e.g. a cold hot plate) immediately after the resist baking on the hot plate. Placing the chip on a tissue or in a carrier is the best.

### Development of exposed HSQ

For HSQ on  $\text{AlO}_x$  plus  $\text{NbO}_x$ , the maximum development time is around 90 s. Above that, the passivation layer  $\text{NbO}_x$  becomes permeable and the developer starts to etch the  $\text{AlO}_x$ .

### HSQ and $\text{AlO}_x$ etching

With the Oxford Plasma Technology Plasmalab 100 ICP 180 at the Karlsruhe Institute of Technology, reproducible etching results from a step of 15 min of preconditioning which means running the plasma without sample first.

With the Oxford Plasma Technology Plasmalab 100 at the Royal Holloway, University of London, reproducible etching results from a step of 5 min of oxygen plasma without sample first.

15 min preconditioning, 120s test etch with broken vacuum, etch time was set to 80s. Chip was etched through.

### **Optical resist application**

In order to allow for a good contact of the resist on the etched surface, Hexamethyldisilazane (HMDS) was used on chip A0102 prior to resist application.

All chips rest for 30 s before taken on the hot plate to allow for a *reflow* of the resist after spinning.

### **Aluminium thin film application**

Steps of 5 s descum at 200 V and 10 mA plus 20 s cleaning with Ar plasma at  $-20^{\circ}$ , 200 V, 15 mA and 5 rpm planetary rotation were performed prior to application in order to sufficiently clean the surface from water and resist residuals.



# List of Figures

2.1.	<p>The superconducting order parameter <math>\psi</math> plotted in the complex plane along the wire axis <math>x</math>. Each turn of the helix represents a phase change by <math>2\pi</math>. <b>a</b> Before the event of a phase slip, the wire carries <math>n</math> phase turns (here <math>n = 7</math>). <b>b</b> During the phase slip event, the amplitude of the order parameter <math> \psi </math> fluctuates to zero. A voltage drop occurs over the wire and thus the wire becomes resistive. <b>c</b> After re-establishing superconductivity, the nanowire only carries <math>n-1</math> phase turns (here <math>n = 6</math>). . . . .</p>	11
2.2.	<p><b>a</b> Two superconducting electrodes (blue) connected by a superconducting nanowire forming a quantum phase slip (QPS) junction (not to scale). The amplitudes of the two superconducting wavefunctions do not overlap over the the nanowire because its length is bigger than the coherence length <math>L \gg \xi</math>. Under this condition, quantum phase slips can happen. The spiral represents the superconducting phase turns over the nanowire. <b>b</b> In an electrical circuit, a QPS junction is represented by a diamond with a bar. . . . .</p>	15
2.3.	<p><b>a</b> Two superconducting electrodes (blue) separated by an isolating barrier (red) forming a Josephson junction (not to scale). The amplitudes of the two superconducting wavefunctions <math> \psi _{1,2}^2</math> decay exponentially over the barrier (dashed lines). Their overlap (grey) provides coupling between them. <b>b</b> In an electrical circuit, a Josephson junction is represented by a cross referring to its non-linear current properties. . . . .</p>	17
2.4.	<p>Two superconductors are weakly linked by a superconducting bridge. The length <math>L</math> of the link has to be smaller than the superconducting coherence length <math>\xi</math> in order to get an overlap of the superconducting wavefunctions <math>\Psi_{1,2}</math>. . . . .</p>	19

2.5. **a** A QPS junction (QPSJ) connected in series with a resistance  $R$  and an inductance  $L$ . The voltage  $V$  distributes over the different circuit elements ( $V_1, V_2, V_3$ ). **b** A Josephson junction (JJ) shunted by a resistance  $R$  and a capacitance  $C$ . The current  $I$  splits up into  $I_1, I_2$  and  $I_3$  (see Eq. (2.46)) obeying Kirchhoff's current law. **c** Current-voltage characteristic of the voltage-biased QPS circuit shown in **a**. There is no current flowing through the junction for increasing applied voltage until a critical voltage  $V_c$  is reached and the junction becomes resistive. For more details on stages i, ii and iii please refer to the text. **d** Current-voltage characteristic of the current-biased Josephson junction circuit shown in **b**. There is no voltage drop over the junction for increasing current until a critical current  $I_c$  is reached and the junction becomes resistive. For more details on stages i, ii and iii please refer to the text. . . . . 21

2.6. **a** Electrical circuit of the quantum phase slip flux qubit (QPSFQ). The number  $N$  of fluxoids ( $\Phi_0$ ) in the superconducting loop with inductance  $L$  and embedded QPS junction QPSJ can only change in discrete numbers under external flux bias. **b** Electrical circuit of the Cooper pair box (CPB). The number  $N$  of Cooper pairs ( $2e$ ) on the island (red) formed by gate capacitor  $C$  and the Josephson junction JJ can only change in discrete numbers under bias of the gate voltage  $V$ . **c** QPSFQ energy spectrum for  $N = -1, 0, +1$  fluxoids in the loop (dashed parabolas) as a function of magnetic frustration  $f = \Phi/\Phi_0$ . The QPS tunnelling  $E_s$  lifts the degeneracy at half-integer values of  $f$ . **d** CPB energy spectrum for  $N = -1, 0, +1$  Cooper pairs on the island (dashed parabolas) as a function of offset gate charge  $N_g = CV/2e$  in units of  $2e$ . The Josephson tunnelling  $E_J$  lifts the degeneracy at half-integer values of  $N_g$ . **c+d** In both cases, coherent tunnelling creates a two-level system with a ground state  $|0\rangle$  (blue) and an excited state  $|1\rangle$  (red). . . . . 24

2.7. Complete duality picture for Josephson and quantum phase slip (QPS) junction recapturing the different energetic regimes and typical systems as discussed in this section. . . . . 26

2.8. Bloch sphere representation of a two-level system or qubit, respectively. The ground state  $|0\rangle$  points in positive  $z$  direction while the excited state  $|1\rangle$  points to the opposite. Any qubit state  $\psi$  is represented as a point on the surface of the sphere given by spherical coordinates as in Eq. (2.57) with the Euler angles  $\theta$  and  $\phi$ . . . . . 28

2.9. **a** At the top, a  $\lambda/2$ -type resonator is depicted. It is capacitively coupled to its environment at both ends where only current nodes of standing waves are allowed. At the bottom, a  $\lambda/4$ -type resonator is represented with one end connected to ground while the other is capacitively coupled to the environment. This allows for standing waves with a current node at the capacitively coupled end and an antinode at the grounded one. For both types, the current  $I$  distributions along the line axis  $x$  of the standing waves of the fundamental as well as first and second harmonic are given. **b** Two possible realizations for a microwave transmission line resonator are displayed; at the top, a microstrip geometry with backside metallization for grounding and at the bottom, a coplanar waveguide transmission line resonator where ground is put on both sides of the inner conducting line. Furthermore, the electric field  $\vec{E}$  distributions of the structures are displayed in red. . . . . 31

2.10. Energy and persistent current diagrams vs. applied frustration  $f = \Phi/\Phi_0$ . For zero phase slip amplitude, the energy spectrum  $E_N$  is given by parabolas while the persistent current  $I_p$  shows a saw-tooth like dependence on  $f$  (solid line). A small phase slip amplitude results in a lifting of the degeneracy of the energy spectrum at multiples of  $\Phi_0/2$  which leads to a rounding of the saw-tooth like dependence of the persistent current (dotted line). For large phase slip amplitude, the degeneracy is lifted even further and the persistent current shows a sinusoidal dependence on  $f$  (dashed line). . . . . 38

3.1. **a** Dependence of the  $\text{AlO}_x$  sheet resistance on the  $\text{Ar}_2$  pressure [Rot+17]. **b** Homemade sputter tool for the  $\text{AlO}_x$  deposition. . . . . 41

3.2. **a** TEM image of an  $\text{AlO}_x$  film with a thickness of 20 nm and a sheet resistance of 2  $\text{k}\Omega$ . A granular structure is visible with grains of a mean size of 3-4 nm. The inset is a zoom into the black framed rectangular in the main image. Here, the grains are clearly distinguishable. Inside the grains, aluminium atoms are lined up indicating a mono-crystalline structure surrounded by amorphous oxide. **b** Intensity profile and TEM diffraction pattern of the same film. The colourized labels mark the peaks that are in agreement with the corresponding lattice planes of the face-centred cubic lattice of bulk aluminium [Rot+17]. . . . . 42

3.3. Broadened superconducting transition for a 22 nm thin  $\text{AlO}_x$  film [Wil15]. The sheet resistance  $R_{\text{sq}}$  is measured in a 4-probe way to remove cable resistance. . . . . 43



3.9.	Ultra-low temperature continuous microwave measurement setup. <b>a</b> Room temperature part outside the cryostat where signals of a vector network analyser (VNA) and a microwave source are combined by a directional coupler and send into the cryostat on the ingoing signal line. On the line outgoing from the cryostat, the signal is amplified before it returns to the VNA. <b>b</b> Microwave setup part inside the cryostat. At the 4 K stage, the microwave signal is attenuated when entering and amplified before leaving the cryostat. The signal is further attenuated at the still and at the mixing chamber (MC) before reaching the sample. The sample has an additional magnetic shield. After the sample, the signal passes an isolator before reaching the amplifier at 4 K. . . . .	55
3.10.	Pulsed microwave measurement setup with a legend of components on the right side. <b>a</b> Room temperature part outside the cryostat. A fast digital-to-analog converter (DAC) produces the manipulation signal that is combined with the readout pulse on the ingoing line while the outgoing line is downmixed and detected by a fast analog-to-digital converter card (ADC). <b>b</b> The part inside the cryostat is identical to Fig. 3.9 <b>b</b> . . . . .	58
4.1.	<b>a</b> Design sketch to scale of the meandered microstrip resonator coupled to the microwave feedline (horizontal) with a loop capacitively coupled to the end of the resonator. <b>b</b> SEM picture showing the end of the resonator (coloured in yellow) and the loop (coloured in blue). The loop contains a 250 nm long and 20 nm wide wire at the bottom. <b>c</b> Zoom onto the nanowire area (coloured in blue). . . . .	63
4.2.	<b>a</b> Electrical equivalent circuit of the experiment containing the resonator (yellow) and the loop with embedded nanowire (blue). <b>b</b> Simulated charge distribution of the the end of the resonator and the loop at the resonator frequency. The simulation was performed with Sonnet <sup>®</sup> . . . . .	64
4.3.	<b>a</b> Photograph of the silicon chip which contains the experiment (see dashed rectangle) shown in Fig. 4.1. In the centre, the aluminium microwave feedline is highlighted. The chip is glued onto the copper plated PCB. At left and right side, the feedline is bonded to the copper CPW microwave feedline of the PCB. DC lines at top and bottom were not used in the experiment. <b>b</b> The PCB is fixed on the rectangular copper sample holder ( <i>top</i> ). After mounting the PCB, the sample holder is closed with a copper cover ( <i>bottom</i> ). <b>c</b> The closed sampleholder ( <i>bottom</i> ) with SMA microwave and DC cables is subsequently covered by a lead shield ( <i>mid</i> ) and a cryoperm shield ( <i>top</i> ) in order to protect the experiment from stray magnetic fields. . . . .	65
4.4.	Transmission amplitude $ S_{21} $ ( <i>top</i> ) and phase $\arg(S_{21})$ ( <i>bottom</i> ) signal plotted versus readout frequency of the VNA. The spectrum is measured at -115 dBm and 20 mK. A large resonance at 6.22 GHz is observed as well as a small one at 6.17 GHz. <i>insets</i> Zooms onto the small resonance which is a sideband mode of resonator and loop (see text). . . . .	66

4.5.	A first magnetic field scan after cooling down in zero magnetic field. The transmission amplitude of the sideband mode is plotted in colour versus the externally applied magnetic field. . . . .	67
4.6.	<b>a</b> Electrical circuit of the quantum phase slip flux qubit (QPSFQ). The number $N$ of fluxoids ( $\Phi_0$ ) in the superconducting loop with inductance $L$ and embedded QPS junction (QPSJ) can only change in discrete numbers under external flux bias. The QPSFQ is subject to the restriction $E_L \gg E_c$ . <b>b</b> QPSFQ energy spectrum for $N = -1, 0, +1$ fluxoids in the loop (dashed parabolas) as function of magnetic frustration $f = \Phi/\Phi_0$ . The QPS tunnelling $E_c$ lifts the degeneracy at half-integer values of $f$ . The coherent tunnelling creates a two-level system with a ground state $ 0\rangle$ (blue) and an excited state $ 1\rangle$ (red). . . . .	68
4.7.	Avoided level crossing of the two-level system shown in Fig. 4.8 and resonator sideband mode displayed as colour coded microwave transmission amplitude versus probe frequency $f_{\text{VNA}}$ and magnetic field $B_{\text{ext}}$ . The red line is a fit by Eq. (4.5). . . . .	69
4.8.	Dependence on magnetic frustration $f = \Phi/\Phi_0$ of the transition of the two-level system participating in the anticrossing in Fig. 4.7 investigated by dispersive readout technique. The readout power level is at $P_{\text{VNA}} = -122$ dBm while the drive power level is at $P_{\text{mw}} = -97$ dBm (both including the setup attenuation). The microwave amplitude signal is plotted in color versus additional drive frequency $f_{\text{mw}}$ and external magnetic frustration which is applied perpendicular to the sample. When $f_{\text{mw}} = f_q(f)$ , the resonator experiences a dispersive shift due to coupling. The transition is fitted (red line) by Eq. (4.6). . . . .	71
4.9.	A first magnetic field scan after cooling down in zero magnetic field. The transmission amplitude of the sideband mode is plotted in colour versus the externally applied magnetic field. The red line presents a fit of the magnetic field dependence of the resonance frequency with Eq. (4.17). . . . .	75
4.10.	Relation between the loop phase $\varphi_{\text{loop}}$ and the phase drop over the weak link $\varphi_{\text{wl}}$ . Since the system is a closed superconducting loop the phase must always be a multiple of $2\pi$ associated to a discrete number of fluxons in the loop. Due to the high $\beta_L$ of the weak link, the system becomes multi-valued with metastable states (solid lines). The phase dynamics of the system can be represented as particle (circles) in a metastable state. The particle will stay in one state until the external phase exceeds a certain value and allows the system to occupy a higher ( $+\Phi_0$ ) or lower ( $-\Phi_0$ ) state. The red, blue and green circle correspond to 0, 1 or 2 fluxons in the loop. . . . .	76

- 
- 4.11. Magnetic field scan recorded after a preceding magnetic field sweep to more than five times a  $\Phi_0$  flux in the loop. The sideband mode resonance amplitude is plotted in colour versus the externally applied magnetic field. Several different anticrossings are visible including "bumps" in the resonance spectrum. The red line presents the resonance at minimum amplitude as a guide to the eye. . . . . 77
- 4.12. Potential Eq. (4.28) of the loop - weak link system plotted over the phase drop over the weak link  $\varphi_{wl}$  for zero magnetic field. The phase dynamics are represented by a particle (red circle) which is situated in the centre well. The energy levels in the centre as well as the adjacent wells are plotted (solid lines).  $\epsilon$  is the potential tilt,  $U_0$  is the barrier height between adjacent wells and  $\Phi_m$  represents the flux difference between two adjacent minima. . . . . 78
- 4.13. The potential given by Eq. (4.28) plotted over the phase drop over the weak link  $\varphi_{wl}$  for  $0 \Phi_0$  (thin solid line),  $3 \Phi_0$  (dashed dotted line) and  $5 \Phi_0$  (thick solid line). The phase dynamics is represented by particles. Increasing the external flux (red horizontal arrows) tilts the potential. Increasing from  $0 \Phi_0$ , the particle (red circle) is lifted up (red vertical arrows) as long as a barrier separates two neighbouring wells. Without barrier, the particle "rolls" down the potential (black arrows) until being trapped in a neighboring well (blue or green circle). During a subsequent reduction of the external flux (blue horizontal arrows), the particles remain in their occupied wells. The circle colors correspond to Fig. 4.10. . . . . 79
- 4.14. **a** Potential Eq. (4.28) plotted at an external flux of  $1.5 \Phi_0$  with the system occupying the second metastable state from zero (green circle, see Fig. 4.13 and Fig. 4.10). Under this conditions, coherent, resonant tunnelling can take place through the barrier between states  $|0\rangle$  and  $|1\rangle$  (double-sided arrow). **b** This system forms a two level system with a degeneracy that is lifted by  $\Delta$ . The energy difference between the two dressed states is given by Eq. (4.30). . . . . 80
- 4.15. Magnetic field dependent two-level transitions as shown in Fig. 4.8 for 3 subsequent, hysteretic magnetic field cycles leading the system to occupy adjacent metastable fluxon states. The solid lines represent fits to Eq. (4.30) with the same parameters. . . . . 82
- 4.16. Dependence of the transition in Fig. 4.8 on the readout power  $P_{VNA}$ , here given without setup attenuation. The qubit transition is fixed at the sweet spot ( $\Delta E = \Delta$ ) and investigated via the dispersive readout technique. The change of the transition with  $P_{VNA}$  is fitted by Eq. (4.33) (red line). This is used to calibrate the average number of photons  $\langle n \rangle$  in the resonance mode with the applied microwave power. This calibrated photon number is displayed as upper x axis. The drive power level is at  $P_{mw} = -102$  dBm including setup attenuation. . . . . 83

- 4.17. **a** Rabi drive protocol. After applying a drive (see Eq. (4.34)) for time  $\Delta t$  to the qubit, a readout pulse extracts the qubit state. **b** Subsequent measurements with varied drive pulse duration  $\Delta t$  (single stars) plotted over  $\Delta t$  gives the Rabi oscillation. The transmission amplitude  $|S_{21}|$  of the sideband resonance used to read out the qubit state dispersively is plotted versus  $\Delta t$ . The green solid line represents a fit by an exponentially damped cosine function. **c** Rabi oscillations like in **b** measured for different drive power amplitudes  $A_{\text{rms}}$ . The transmission amplitude  $|S_{21}|$  is plotted in color. The white dashed horizontal line corresponds to the drive power amplitude value at which the figure in **b** is taken. . . . . 85
- 4.18. Rabi frequency values  $\Omega_R$  extracted from fits of Eq. (4.35) to each Rabi oscillation in Fig. 4.17c plotted versus the corresponding drive amplitude values  $A_{\text{rms}}$ . The linear dependence of  $\Omega_R$  on  $A_{\text{rms}}$  (solid line as guide to the eye) is in nice agreement with the expected behaviour (see Eq. (4.35)). 86
- 4.19. **a**  $T_1$  pulse sequence. Prepared in the ground state, the qubit is excited by a  $\pi$ -pulse. After a waiting time of  $\Delta t$ , the qubit state is read out by a readout pulse. **b** Repeating the pulse sequence with increasing waiting time  $\Delta t$ . Each circle including error bar represents a single measurement plotted over the corresponding  $\Delta t$  value. The measurement is fitted by an exponential decay (red solid line) giving the  $T_1$  lifetime of the qubit. . . . 87
- 4.20. **a**  $T_2^*$  (Ramsey) pulse sequence. Prepared in the ground state, the qubit is excited by a  $\pi/2$ -pulse. After a waiting time of  $\Delta t$ , another  $\pi/2$ -pulse rotates it back to the ground state, where the qubit state is extracted by a readout pulse. **b** Repeating the pulse sequence from **a** with increasing waiting time  $\Delta t$ . Each black circle including error bar represents a single measurement plotted over the corresponding  $\Delta t$  value. The measurement is fitted by an exponential decay (upper red line) giving the  $T_2^*$  lifetime of the qubit. Repeating the pulse sequence from **c** with increasing waiting time  $\Delta t$ . Each blue circle including error bar represents a single measurement plotted over the corresponding  $\Delta t$  value. The measurement is fitted by an exponential decay (lower red line) giving the  $T_2$  lifetime of the qubit. **c**  $T_2$  (spin-echo) pulse sequence. The waiting time of  $\Delta t$  in the  $T_2^*$  (Ramsey) pulse sequence is interrupted by an additional  $\pi$ -pulse that rotates the qubit to the other side of the equator. This leads to refocussing before the qubit is rotated back to the ground state where the qubit state is extracted by a readout pulse. . . . . 89

4.21. **a** 16 different loops with constrictions galvanically coupled to the center of a CPW  $\lambda/2$ -resonator (blue). Above and below, there are ground planes, left and right, microwave connection pads are placed (all yellowish). **b** A SEM picture of the 9 inner loops presenting the variation of loop sizes and shared coupling inductances. **c** Zoom onto a single loop. The loop wire width is 1.2  $\mu\text{m}$ . **d** Further zoom onto the constriction with a width of 51 nm. It can be seen that the complete structure shows an additional surrounding which is due to overexposure in the e-beam process. As mentioned in Sec. 3.2.3, the  $\text{CF}_4$  based RIE process attacks silicon which leads to the white dots around the constriction. The different shades of grey represent areas with different electrical conductivity. . . . . 94

4.22. **a** On-chip experiment (black) glued in the centre of a gold coated PCB. The left and right PCB connection ports are used for the transmission measurement. Contacts between chip and PCB are done via aluminium wire bonds. The PCB is mounted on a copper holder. **b** The copper holder is covered by a copper cover incorporating a solenoid coil (right bottom). The closed copper holder is mounted onto a post which is fixed at the mixing chamber of the cryostat. Cryoperm (left) from muShield and superconducting aluminium (mid) shield will protect the mounted post (right) against stray magnetic fields. . . . . 96

4.23. Transmission amplitude  $|S_{21}|$  plotted versus frequency. The spectrum is measured at -115 dBm and 12 mK (black line). For the fundamental resonance mode, a simulation with a kinetic sheet inductance of 0.55 nH (red line) is in very good agreement with the measurement. . . . . 97

4.24. Resonator phase signal at resonance plotted versus applied magnetic field. An avoided level crossing between qubit and resonator can be observed with virtual mirror axis (dashed line). The measurement is performed at -115 dBm and 12 mK. . . . . 98

4.25. The same measurement as shown in 4.24 performed over a large magnetic field range (black line). *top* Four anti-crossings with a periodicity in magnetic field of 54.1  $\mu\text{T}$  can be observed. *bottom* Zoom onto a much smaller periodic pattern. It has a magnetic field periodicity of 21.8  $\mu\text{T}$ . . . . . 100

4.26. Avoided level crossing of qubit 1 and resonator fundamental mode displayed as grey-scale coded microwave transmission amplitude versus probe frequency and magnetic field. The red line is the fit of Eq. (4.45) while the black dashed line represents the qubit transition observed in Fig. 4.27. 102

- 4.27. Dependence of the transition of qubit 1 on magnetic field investigated by dispersive readout technique. The readout power level is at  $P_{\text{VNA}} = -115$  dBm while the drive power level is at  $P_{\text{mw}} = -75$  dBm both including setup attenuation. *left* The phase signal at the second harmonic resonance of the resonator is plotted in grayscale versus additional drive frequency  $f_{\text{mw}}$  and external magnetic field  $B_{\text{ext}}$  which is applied perpendicular to the sample. When  $f_{\text{mw}} = f_{\text{q}}(B_{\text{ext}})$ , the resonator experiences a dispersive shift due to coupling. *right* The transition is fitted (red line) by Eq. (4.51). . . . . 105
- 4.28. Dependence of the transition of qubit 16 on magnetic field investigated by dispersive readout technique. The readout power level is at  $P_{\text{VNA}} = -115$  dBm while the drive power level is at  $P_{\text{mw}} = -75$  dBm both including setup attenuation. *left* The amplitude signal at the fundamental resonance of the resonator is plotted in grayscale versus additional drive frequency  $f_{\text{mw}}$  and external magnetic field  $B_{\text{ext}}$  which is applied perpendicular to the sample. When  $f_{\text{mw}} = f_{\text{q}}(B_{\text{ext}})$ , the resonator experiences a dispersive shift due to coupling. *right* The transition is fitted (red line) by Eq. (4.51). . . . . 106
- 4.29. Coherent QPS amplitudes of the two observed qubits plotted versus their nanowire widths (blue circles). The errors in x are due to the limitations in measuring the widths. The data is fitted by Eq. (4.55) with fit parameters  $\alpha$  and  $\beta$  on the order of unity (green solid line). The dashed lines represent the uncertainty range due to the error in widths. . . . . 107
- 4.30. Dependence of the transition of qubit 1 on the readout power  $P_{\text{VNA}}$  applied via the vector network analyser (VNA). The qubit transition is fixed at the sweet spot and investigated via the dispersive readout technique. The change of the transition with  $P_{\text{VNA}}$  is fitted with Eq. (4.56) (red line). The result is utilized to calibrate the average number of photons  $\langle n \rangle$  in the resonance mode with the applied microwave power. This calibrated photon number is displayed as upper x axis. The drive power level is at  $P_{\text{mw}} = -90$  dBm including setup attenuation. . . . . 108
- 4.31. *top* Transition of qubit 16 measured by dispersive readout as shown in Fig. 4.28. *right* Here, the first blue-sideband transition  $f_{\text{q}} + 1 \cdot f_{\text{r}}$  (blue line) above the resonator fundamental mode  $f_{\text{r}}$  (dashed line, yellow) as well as the first red-sideband  $f_{\text{q}} - 1 \cdot f_{\text{r}}$  (red line) below  $f_{\text{r}}$  are fitted. The fits by Eq. (4.51) are done with the parameters taken from Tab. 4.3. *bottom* Transition of qubit 1 measured by dispersive readout as shown in Fig. 4.27. *right* Here, the first blue-sideband transition  $f_{\text{q}} + 1 \cdot f_{\text{r}}$  (blue line) above the resonator fundamental mode  $f_{\text{r}}$  (dashed line, yellow) is fitted by Eq. (4.51) with the parameters taken from Tab. 4.3. . . . . 111

- 4.32. Dependence of the transition of qubit 1 (*bottom*) as well as its first blue-sideband transition (*top*) as shown in Fig. 4.31 on applied qubit drive power  $P_{\text{mw}}$ . The readout power level is at  $P_{\text{VNA}} = -120$  dBm including setup attenuation. For low drive power levels only the qubit's transition from ground to excited state is populated. Only for higher drive power levels also the blue-sideband transition can be driven. Both transitions show a power broadening with increasing drive power levels. . . . . 112
- 4.33. Comparison of the Aharonov-Casher and the Aharonov-Bohm effect in devices. **a** In the Aharonov-Casher effect, a fluxon  $\Phi_0$  which encircles a charge  $2e$  picks up a phase shift  $\phi_{\text{AC}}$ . The device is a superconducting loop with two QPS junctions (QPSJ, red). The loop holds the fluxon inside except the QPSJ allows the fluxon to tunnel in and out along a path around the island with charge  $2e$ . **b** In the Aharonov-Bohm effect, a charge of  $2e$  which encircles a fluxon  $\Phi_0$  picks up a phase shift  $\phi_{\text{AB}}$ . The device is the well-known Superconducting QUantum Interference Device (SQUID), a superconducting loop with two Josephson junctions (JJ, red). The charge  $2e$  encircles the fluxon  $\Phi_0$ . On its path it tunnels through the JJs. . . . . 116
- 4.34. **a** 16 different loops with two constrictions in series per loop. The loops are galvanically coupled to the center of a CPW  $\lambda/2$ -resonator (blue). Above and below, there are ground planes as well as voltage bias lines, and left and right, microwave connection pads are placed (all yellowish). **b** A SEM picture of 2 inner loops with a voltage bias line that splits up to both loops. The loop wire width is  $1.2 \mu\text{m}$ . **c** Zoom onto the two constrictions in series (left). The island between them (right) is connected to a parallel line gate capacitor. . . . . 117
- 4.35. Avoided level crossings of loops 1,2,5,7,9 (red arrows) and the resonator fundamental mode displayed as grey-scale coded microwave transmission amplitude versus probe frequency and externally applied magnetic field. The loops are identified by their different periodicities in magnetic field (not visible here). . . . . 118
- 4.36. Dependence of the transition on magnetic field investigated by dispersive readout technique. *top* Loop 1: The phase signal at the fundamental resonance of the resonator is plotted in grey-scale versus additional drive frequency  $f_{\text{mw}}$  and external magnetic field  $B_{\text{ext}}$  which is applied perpendicular to the sample. When  $f_{\text{mw}} = f_{\text{q}}(B_{\text{ext}})$ , the resonator experiences a dispersive shift due to coupling. The transition is fitted (red line) by Eq. (4.65). *bottom* The same as in the upper plots but now for loop 2. . . . 120

4.37. Dependence of the transition on magnetic field investigated by dispersive readout technique. <i>top</i> Loop 5: The phase signal at the fundamental resonance of the resonator is plotted in grey-scale versus additional drive frequency $f_{\text{mw}}$ and external magnetic field $B_{\text{ext}}$ which is applied perpendicular to the sample. When $f_{\text{mw}} = f_q(B_{\text{ext}})$ , the resonator experiences a dispersive shift due to coupling. The transition is fitted (red line) by Eq. (4.65). <i>bottom</i> The same as in the upper plots but now for loop 7. . . . .	121
4.38. Dependence of the transition on magnetic field investigated by dispersive readout technique here for loop 9. The phase signal at the fundamental resonance of the resonator is plotted in grey-scale versus additional drive frequency $f_{\text{mw}}$ and external magnetic field $B_{\text{ext}}$ which is applied perpendicular to the sample. When $f_{\text{mw}} = f_q(B_{\text{ext}})$ , the resonator experiences a dispersive shift due to coupling. The transition is fitted (red line) by Eq. (4.65). . . . .	122
4.39. Transition spectroscopy of loop 1 by dispersive readout technique for two different island charge values $q = -0.14 \times 2e$ ( <i>left</i> ) and $q = -0.55 \times 2e$ ( <i>right</i> ). The dashed lines are fits by Eq. (4.65). The appearance of two transitions in each plot will be explained in Sec. 4.3.5. Double-sided arrows mark the sweet spots of the transitions (see Fig. 4.40) [Gra+18]. . . . .	123
4.40. Monitoring the sweet spots of the transitions in Fig. 4.39 in dependence on the island charge. Double-sided arrows mark the same working points as in Fig. 4.39 [Gra+18]. . . . .	123
4.41. Transition frequencies for both transitions extracted from Fig. 4.40. The solid lines are fits to Eq. (4.66). As will be explained in Sec. 4.3.5, the blue points represent even and the red ones odd charge parity [Gra+18]. . . . .	124
4.42. Observed maximum detuning by charge for a variation for different magnetic flux values. $\delta\Phi = 0$ is the sweet spot. The black line is a fit to Eq. (4.66) [Gra+18]. . . . .	125
4.43. Phase response taken from Fig. 4.40 for island charge values of $q = 0$ (solid line) and $q = 1e$ (dashed line). The level population is equal for both parity states. The difference in height of the two peaks visible for each parity state results from differently strong coupling to the resonator mode [Gra+18]. . . . .	126

# List of Tables

3.1.	Electron beam exposure parameters for reproducible definition of different wire widths in 50 nm HSQ on 20 nm $\text{AlO}_x$ films on doped silicon substrate as well as 3-4 nm NbN films on undoped silicon substrate. The preparation of the HSQ is described in the text. The wire width values are averaged over many samples within an error range of $\pm 3$ nm. . . . .	47
3.2.	List of different setups with all components used at Karlsruhe Institute of Technology (KIT), Royal Holloway, University of London (RHUL) and National Physical Laboratory (NPL). . . . .	57
3.3.	Components of the time domain setup for pulsed microwave measurements as shown in Fig. 3.10 used at KIT. . . . .	59
4.1.	Parameters of the observed two-level systems taken from fits to Eq. (4.30).	81
4.2.	Design parameters of all 16 loops and constrictions that are coupled to the CPW $\lambda/2$ -resonator. The test $w_{\text{constr}}$ is the width of a test constriction structure which is on the same chip as the actual $w_{\text{constr}}$ . The difference in widths between them results from overexposure due to bigger structures surrounding the actual constrictions. The depicted width values are within an error margin of $\pm 10\%$ . . . . .	95
4.3.	Important parameters of the two measured qubits. . . . .	105
4.4.	Important parameters of the five measured qubits. . . . .	119



# Acknowledgements

I would like to thank Prof. Alexey Ustinov for giving me the possibility to work on this challenging project for my PhD thesis and being my first advisor. I have to thank him for his input and feedback and for always lending me an ear.

I would like to thank Prof. Oleg Astafiev for being the second advisor of this thesis, and for having me as part of his team during my internship at the Royal Holloway, University of London. I have to thank him for our detailed discussions, for sharing his knowledge and experience and for his hospitality.

I have to thank Dr. Hannes Rotzinger for being my direct project supervisor, for having laid the first stepping stones when I started my PhD project, for his input and support, and for carefully proof reading this manuscript. We had to muster our perseverance during some discouraging times in this ambitious project. That we did not always concur with all points helped to scrutinize all important aspects of the project.

Furthermore, I thank all AIO<sub>x</sub> team members, Marco Pfirrmann, Jan Nicolas Voss, Micha Wildermuth, Julian Münzberg, for their contributions to the project and the friendly team atmosphere.

I would like to gratefully thank Dr. Sebastian de Graaf and Dr. Jürgen Lisenfeld for very helpful discussions and for their careful proof reading of this manuscript.

I would like to thank the team at RHUL and NPL, Dr. Rais Shaikhaidarov, Teresa Hoenigl-Decrinis, Dr. Sebastian de Graaf, Dr. Vladimir Antonov, Ilya Antonov and Massimo Venti for their generous hospitality and technical as well as scientific support, which lead to very fruitful experiments. I especially appreciated the hiking trips to the countryside with Rais.

I would like to thank Prof. Jared Cole, Dr. Nicolas Vogt, Dr. Clemens Müller, and Prof. Alexander Shnirman for our discussions and their support regarding the theoretical framework of this thesis.

I am very thankful to Dr. Silvia Diewald for her help in the electron beam fabrication of the nanowires as well as to Lucas Radtke for all his generous help in all matters of fabrication.

I am very grateful to Hans-Willi Pensl and Andre Vetter for their help - even at short notice - concerning liquid helium, vacuum pump and cryostat maintenance.

## *Acknowledgements*

---

I would like to deeply thank Michael Meyer and Roland Jehle as well as their teams in the mechanical and electronic workshop. The work of these teams is invaluable for the presented research.

I gratefully thank Steffi Baatz, Birgit Schelske, and Ilona Brosch for all their immediate support with administrative issues even on short notice. Their work is indispensable.

I would like to thank Dr. Oleksandr Lukashenko for helping me with all cryostat matters, for sharing all his experience of cryogenics and always having a good story to tell.

Special thanks go to my room mates Jochen Braumüller, Alexander Bilmes, and Marco Pfirrmann for our informal and always cheerful office atmosphere.

I am very grateful to Dr. Ioan Pop for supporting me in difficult times in the past year. I am very happy to be part of his team now.

There I would like to thank Dr. Natasha Maleeva, Lukas Grünhaupt, Daria Gusenkova, Martin Spieker, and Francesco Valenti for creating a most valuable working atmosphere. Extra thanks to Natasha for all our discussions.

I would like to thank my friends Sebastian Probst, Jochen Braumüller, and Marco Pfirrmann for all the fun we had during conference travels. Our discussions and your support meant a lot to me.

Deep thanks to all present and past group members, in particular Andre Schneider, Patrick Winkel, Alexander Stehli, Dr. Sebastian Probst, Dr. Susanne Butz, and Dr. Philipp Jung for the worthwhile times we shared.

Furthermore, I am very grateful to all members of the Physikalische Institut for creating a very pleasant working atmosphere.

I would like to thank the Heinrich Boell Foundation for supporting my PhD project with a generous PhD scholarship including financial support for research travels to conferences in Russia and the USA.

Special thanks go to Dr. Jutta Helm, and Dr. Tamara Or, for always supporting me with all scholarship concerns, as well as to the whole Boell team.

I am grateful to the Boell council of scholars, the Boell section board for new scholars and the Promovierenden-Initiative which I was affiliated with during the last years as well as all friends that I got to know in the Boell context for their open-mindedness, friendliness, for always offering a shelter and invigoratingly different views.

Furthermore, I would like to thank the Karlsruhe House of Young Scientists (KHYS) for the financial support of my internship at the Royal Holloway, University of London within the framework of KHYS Research Travel Grant.

I deeply thank my parents Monika Skacel and Werner Mülhaupt for your loving kindness and your undying support. Without you I would not have made it to where I am today. I love you.

My deepest thanks go to my beloved Damaris "Gem" Kröger for everything you have given to me in the past decade. We shared so many unforgettable moments. You are my best friend and my sunshine. I love you.

Deep thanks to my true friend Alexander Keilmann for all our evenings, discussions and your support. To many more years.

I would like to thank Carolin Lange for our invaluable workshops and our arts/science book project. I am looking forward to more exciting projects.

I would like to thank my true Egham friends Rima Chai, Wayne Sarten, Shahram Mossayebi, and Michael Ignatz for our great moments, our priceless discussions and the shelter during my internship at the Royal Holloway.

My true thanks go to Dominic Hennig for giving me extraordinarily valuable advices.